Analysis of SNL/MSU/DOE Fatigue Database Trends for Wind Turbine Blade Materials, 2010-2015

John F. Mandell[1], Daniel D. Samborsky[1], and David A. Miller[2],
Pancasatya Agastra[1] and Aaron T. Sears[2]
[1]Department of Chemical and Biological Engineering,
[2]Department of Mechanical Engineering,
Montana State University, Bozeman, MT, 59717, USA

Sandia Technical Managers: Joshua Paquette and Brian Naughton

Sandia National Laboratories

Analysis of SNL/MSU/DOE Fatigue Database Trends for Wind Turbine Blade Materials, 2010-2015

John F. Mandell[1], Daniel D. Samborsky[1], and David A. Miller[2],
Pancasatya Agastra[1] and Aaron T. Sears[2]
[1]Department of Chemical and Biological Engineering,
[2]Department of Mechanical Engineering,
Montana State University, Bozeman, MT, 59717, USA

Sandia Technical Managers: Joshua Paquette and Brian Naughton
Wind Energy Technologies Department
Sandia National Laboratories
P.O. Box 5800
Albuquerque, New Mexico 87185-1124

Abstract

Wind turbine blades are designed to several major structural conditions, including tip deflection, strength and buckling during severe loading, as well as very high numbers of fatigue cycles and various service environments. The MSU Database Program has, since 1989, addressed the broad range of properties needed for current and potential blade materials through static and fatigue testing and test development in cooperation with Sandia National Laboratories and wind industry and supplier partners. This report is the latest in a series, giving test results and analysis for the period 2010-2015. Program data are compiled in a public database [1] and other reports and publications given in the cited references.

The report begins with an executive summary and introductory material including background discussion of previous related studies. Section 3 describes experimental methods including processing, test methods, instrumentation and test development. Section 4 provides static tension, compression and shear stress-strain properties in three directions using coupons sectioned from a thick infused unidirectional glass/epoxy laminate. The nonlinear, shear dominated static properties were characterized with loading-unloading-reloading (LUR) tests in tension and compression to increasing load levels, for ±45O laminates. Section 5 explores the origins of tensile fatigue sensitivity in glass fiber dominated laminates with variations in fabric architecture including specially prepared fabrics and aligned strand laminates. Several types of resins are considered, with variations in resin toughness and bonding to fibers, as well as cure cycle variations for an epoxy. Conclusions are drawn as to the limits of tensile fatigue resistance

and the effects of resin type and fabric architecture, including the behavior of a commercial aligned glass strand product.

Interactions between cyclic fatigue response and creep are addressed for off-axis ($\pm$45O) glass/epoxy laminates in Section 6. The nonlinear fatigue and creep stress-strain and cumulative strain response are characterized in tension and compression as a function of stress level, cycles and cumulative time, using square and sinewave loading over a broad range of frequency. The results are analyzed in terms of the cycles and cumulative time under load. A cumulative strain failure criterion is established, and used to construct shear and tension constant life diagrams (CLD's) with data for nine R-values. The effects of a more ductile urethne resin are also explored.

A previous study of thick adhesives testing is extended to mixed mode fracture mechanics testing in Section 7. Mechanisms of static and fatigue crack extension near the laminate adherend interface are reported in detail. Data are presented for mixed mode adhesive fracture, compared to mixed mode fracture in ply delamination. Fatigue crack growth exponents are also developed for a mixed mode cracked lap shear coupon. The data for fatigue trends and relative failure strains and exponents are compared for various blade component materials in Section 8. The effects of temperature and seawater saturation are considered for selected materials of interest for wind and hydrokinetic turbine blades in Section 9. Section 10 gives detailed conclusions for each section.

Acknowledgements

Intentionally Left Blank

Contents

List of Figures

12

List of Tables

Intentionally Left Blank

1. Executive Summary

1.1 Overview

Wind turbine blades are designed to several major structural conditions, including tip deflection, strength and buckling during severe loading, as well as very high numbers of fatigue cycles and various service environments. The Montana State University (MSU) Database Program has, since 1989, addressed the broad range of properties needed for current and potential blade materials through static and fatigue testing and test development in cooperation with Sandia National Laboratories and wind industry and supplier partners. This report is the latest in a series, giving test results and analysis for the period 2010-2015. Program data are compiled in a public database [1] and other reports and publications given in the cited references. This section provides an overview of the findings of the study, separated into several primary technical topic areas as well as background information and experimental methods for each.

1.2 Static Properties: Thick Laminates and LUR Tests

Static strength and stiffness properties are not widely available for thick infused laminates in the three primary directions, particularly cases with strong nonlinear response which affects the cyclic stress-strain behavior. These properties are essential for refined blade design and analysis, and also as a basis for establishing the complex creep/fatigue interactions of shear dominated off-axis laminates. Test methodology and results are given in Section 4 for tension, compression and shear coupons sectioned from a 93 mm thick epoxy infused baseline unidirectional fabric laminate for which internal curing temperature was monitored and controlled to prevent exothermal heating effects. Thickness-direction properties are shown to be deficient relative to the transverse direction properties which are generally assumed to approximately represent them.

Loading-unloading-reloading (LUR) tests of $\pm45^0$ laminates have been conducted over a range of increasing tension and compression and reversed direction loads to explore the nonlinear stress-strain (and permanent strain) response, with the results also reduced to shear stress-strain curves. The results are extended to cyclic loading fatigue tests in Section 6.

1.3 Fatigue of Glass Fiber Dominated Laminates: Fabric Architecture, Aligned Strands and Resin Effects

The MSU/SNL Fatigue Program has previously explored the fatigue of a broad range of glass and carbon fiber laminates under many loading conditions of interest for wind blades. The greatest fatigue sensitivity for glass fiber materials has been found to occur for loading cycles with a strong tensile component along the primary fiber direction [2]. Thus, considerable testing has been done for this condition for a variety of blade industry materials systems, with the goal of better understanding the sensitivity and improving the material performance. Section 5 presents results for a range of glass fiber laminates tested at the same tensile fatigue loading condition, exploring the effects of fabric architecture and resin type. The particular fatigue sensitivity for this loading condition is found to relate to the resin cracking at the unidirectional fabric backing strands, and is very sensitive to the type of resin. Polyesters and most vinyl esters are the most sensitive, epoxies less so. For epoxy resins there is little sensitivity to the fabric

details including fabric weight, strand size, stitching and backing structure. An extreme example of reinforcement structure, aligned strands with no backing, provides both higher fiber content, improving static properties like modulus, and outstanding tensile fatigue resistance for laminates with all three resin types. An application of the aligned strand concept, Neptco RodPack precured glass/epoxy rods, show excellent fatigue resistance when incorporated into infused laminates.

1.4 Creep/Fatigue Interactions of ±45° Laminates

Wind turbine blade structures typically include significant quantities of ±45° double bias (DB) fabric material in the shells and webs, to resist torsion and buckling, and in the root, to build up the thickness. While not considered the primary structure, represented by unidirectional (UD) plies oriented along the blade axis (0°) in spars, the DB laminates and plies must perform without significant damage or failure at the strain levels and environments experienced by the blade in service. Edgewise, reversed loading in large blades is carried substantially by the shell, which may contain some fraction of unidirectional plies for this purpose; often, additional unidirectional fabric reinforcement is added at the trailing edge.

The off-axis orientation of the ±45° fibers introduces strong material nonlinearity to the static response, as well as significant damage accumulation, creep and strength and stiffness loss prior to total failure in fatigue. Bending loads produce the highest strains at the outermost fibers, which are usually DB fabric in the shell. Thus, the DB materials must resist the maximum blade strains under static and fatigue loads without failure or softening enough to reduce the blade stiffness or overload adjacent UD material. DB laminates have received relatively little attention in studies compared with UD and multidirectional (MD) laminates, and creep effects in blade laminates have not been well characterized despite their obvious relevance.

The creep and fatigue behavior of double bias (±45°) glass/epoxy laminates have been explored with a variety of tests, including conventional sine-wave fatigue loading at nine loading conditions (R-values), residual property stress-strain tests, square wave fatigue tests and creep tests. The fatigue results are presented as a strain-based constant life diagram (CLD) representing a 50% strain increase failure criterion which correlates with a transition to rapid strain increase and failure. Reversed loading effects are explored in detail, and show a substantial creep response during both the tensile and compressive parts of the wave-form; the creep response relates to the resin viscoelastic shear response. The off-axis laminate cyclic lifetime data can be correlated through a cumulative time under load criterion as opposed to a cumulative cycle criterion which correlates fiber dominated (UD) laminate fatigue data. The baseline epoxy resin is compared with a urethane resin, showing the effects of a tougher but more creep sensitive resin on the creep and fatigue resistance for ±45° laminates.

1.5 Adhesive and Core Material Fatigue

The major components of wind blades are commonly adhesively bonded with relatively thick paste adhesives. Previous efforts have explored a wide range of parameters which influence adhesive joint strength and fatigue resistance under tension, compression and reversed loading [1, 2]. Work reported here extends these studies to a fracture mechanics context which is more

applicable to largescale blade failure. Test development and analysis of crack growth under mixed shear and opening modes has resulted in data similar to those for laminate ply delamination, as well as detailed microscopy of crack growth along adhesive/laminate interfaces. Crack resistance under mixed mode flexural loading is used to compare laminate ply delamination and adhesive crack propagation over a complete range from pure shear to pure opening crack modes which may be experienced in blade joints. Mixed mode fatigue crack growth has been studied using a modified crack-lap shear test configuration.

Core materials are commonly used to stiffen thin laminate areas such as shells and webs against buckling. Like adhesives, core materials can fail under various modes or by crack growth along the laminate interface. Exploratory testing reported here has resulted in data for the fatigue resistance of sandwich coupons subjected to flexural fatigue loading, comparing four core materials.

1.6 Comparison of Fatigue Trends for Various Blade Materials

Composite structures like blades are complex in geometry and construction, containing ply drops for thickness tapering as well as other material transitions such as core materials and close-outs and intersections of spar-caps, webs and shells, and root connections. A multiplicity of failure modes is possible for each blade component material and material transition. Coupon testing can include only a limited range of details, usually under uniaxial loading and with machined edges. Simulations of damage development and progression may be based on the response of the individual materials and interfaces under characteristic external loading, and using full or subscale structure testing for validation. Potential damage initiation sites under structure fatigue loading may be approximated by the properties of each component material or transition area, coupled with a detailed stress analysis. Section 8 compiles and compares the static and fatigue damage conditions and trends for materials in the database [1] for various levels of coupon complexity, such as UD laminates, MD laminates, laminates containing ply drops, etc.

1.7 Environmental Effects on Properties

Section 9 addresses the effects of environmental factors including seawater and temperature changes on strength, stiffness and fatigue properties for a narrow range of database [1] materials. Included are UD laminates of glass fabric H infused epoxy (EP-1) and vinyl ester (VE-7) resins (Table 3), and a UD prepreg carbon/epoxy, Gurit SparPreg UC600. The glass laminates are representative of typical infused blade laminates with resins of different moisture affinity. The carbon prepreg provides a comparison to a higher performance material with a higher temperature epoxy resin. To address more complex structure, data are also presented for seawater effects on a baseline adhesive joint coupon where laminate, adhesive and interface effects could be present. Moisture effects were investigated for synthetic seawater fully saturated conditions (50°C conditioning) except for the adhesive joint, where the conditioning time was the saturation time for the laminate adherend. A more fundamental treatment of environmental effects and their modeling is available from an associated program [3].

Intentionally Left Blank

2. Introduction and Background

2.1 Introduction

This report presents results from the Montana State University (MSU) program on the fatigue of composite materials for wind turbine blades for the time period 2010-2015. Test results are included in the SNL/MSU/DOE Fatigue of Composite Materials Database [1] which is updated annually. Composite material designations, fabric and resin nomenclature is also detailed in the Database [1]. This is the most recent report in the overall over all series [2,4-10], which has summarized test results since program inception in 1989. Contractor report [11] also provides test data generated in part under this program. This report contains results which have also been presented in several conference proceedings in recent years [12-17]. Many additional results are given in cited references as well as student theses, all of which can be found under publications on the program website www.montana.edu/composites/.

2.2 Background

2.2.1 Overview
Wind turbine blades are designed to several major structural conditions, including tip deflection, strength and buckling during severe loading, as well as very high numbers of fatigue cycles during operation, varying between tension, compression and reversed tension-compression loads according to the particular loads spectrum for the turbine and wind conditions. An overview of blade design, manufacturing and materials considerations can be found in [18]. The major static strength and stiffness properties depend primarily on fiber type, content, and orientation, following composite mechanics predictions widely available in the literature. Coverage of the fatigue resistance of various types of composite materials can be found in [19]. The fatigue of specialized types of composite laminates appropriate for wind turbine blades has been the topic of research studies for more than two decades; a general review of this area can be found in [20], with an overview of topics directly relating to this report in [21]. Public databases for fatigue properties of wind blade types of laminates include [1] and [22].

2.2.2 Infusion Processed Blade Laminate Structure
Resin infusion processing of laminates involves assembly of a dry preform with plies of fabrics stacked in the selected orientation sequence. A vacuum is then drawn on the assembly, and resin (with catalyst or curing agent) infused into the assembly, as described in more detail later. The resulting laminate is then cured with or without the addition of external heat, and possibly subjected to additional post-curing steps. The resulting fabric based laminate is heterogeneous compared to some laminates from processes such as prepreg, where the individual fibers may be relatively uniformly distributed within a ply. A typical relatively high density unidirectional (UD) fabric is shown in Figure 1, with aligned strands of several thousand fibers each on the front side, and irregular transverse and random backing strands to which the main strands are stitched, on the back. The various levels of fiber packing are illustrated in Figure 2 for a low density fabric with no backing material. The relatively large inter-strand spaces with low density fabrics provide channels for enhanced resin flow, but result in lower fiber contents Figure 3 depicts the cross-section of a laminate with high density fabrics typical of most blades.
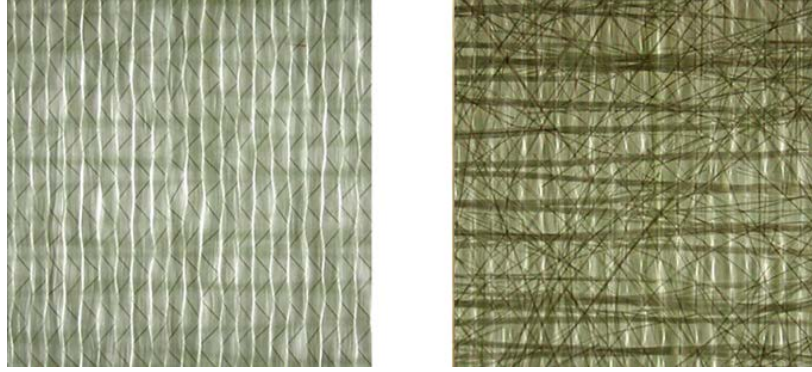
Figure 1. Front and back views of UD fabric H [1].
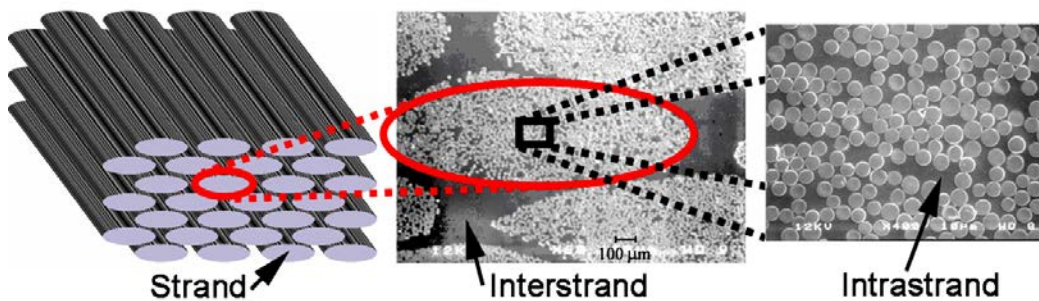
Figure 2. Exploded view of low density fabric A composite showing strand packing, inter-strand channels and intra-strand structure with individual glass fiber packing evident [2].

2.45 mm (+/-45°)

9.66 mm (0°)

0.69 mm (+/-45°)
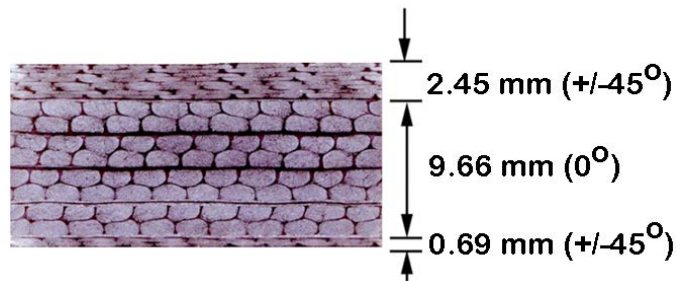
Figure 3. Infusion processed laminate with outer ±45° ply stacks sandwiching eight 0° UD plies (high fiber density fabric D [1]), where individual unidirectional (UD) plies are stacked back-to-back in pairs, and showing in-situ nesting of strands.

2.2.3 Static Properties

Static stress-strain properties have been widely reported for in-plane directions, but through-thickness data are uncommon, particularly for thick molded sections typical of blades. Shear and transverse compression stress-strain response is typically sufficiently non-linear to require special treatment in loading-unloading situations. A novel testing approach termed loading-unloading-reloading (LUR) has been reported in reference [25], used in conjunction with fatigue modeling. The LUR approach is discussed in Section 3, with results in Section 4.

2.2.4 Fatigue of UD dominated laminates

Reports [2] and [5] present fatigue data for a broad range of infused laminates with materials of current interest, while report [6] gives results for earlier types of fabrics and polyester resins. Test results are given for a broad range of materials parameters and loading conditions. Reinforcing stitched fabrics included in these studies are mostly glass fiber unidirectional (UD) or double bias DB ($\pm 45^o$, sometimes termed "biaxial" in these reports). Multidirectional (MD) laminates are composed of combinations of UD and DB fabrics. The fabrics are infusion molded with various resins to form laminates. Earlier laminates [6] had relatively low fiber volume fractions typical of hand lay-up processing, which could be varied in the process. More recent results [2, 5] were obtained for more dense fabrics which naturally produce fiber contents in the range of 50%-60% fiber by volume with vacuum infusion molding.

Fatigue results have been reported for a range of (uniaxial) loading conditions ranging through tension-tension, tension-compression and compression-compression [2, 5, 6]. For UD glass fiber laminates and MD laminates including significant 0° ply contents, the critical loading for damage is in tensile fatigue, or for cycles with a significant tensile component like reversed loading [2]. This is different for DB laminates or for carbon fibers.

The bar graph in Figure 4 compares a range of polyester, vinyl ester and epoxy resin MD laminates on the basis of million cycle fatigue strain (the initial test strain which can be withstood for 10^6 cycles before failure, as determined from a power-law curve fit to the maximum strain-log cycles data [2].) Early data [6] at low fiber contents typical of hand lay-up showed nearly identical tensile fatigue sensitivity (million-cycle strain) for polyester, vinyl ester and epoxy resins with low density UD fabric A[6]. More recent testing using higher density fabrics [2, 5] show distinctly better performance for epoxy resin than for polyester, with vinyl esters intermediate, as shown on the right side of Figure 4. The differences are noteworthy; as illustrated on the strain plot, the million cycle strain for the polyester resin laminate falls 39% below the corresponding epoxy laminate value. Million cycle strain values for all of the higher fiber content laminates fall significantly below corresponding values on the left for the lower fiber content laminates.

The foregoing indicates that tensile fatigue resistance is significantly impacted by interactions between resin, fabric and fiber content. The early data for low fiber content multidirectional laminates included in Figure 4 (left) show no effect of the type of resin. These low density fabrics were also molded over a broad range of fiber contents with two-sided molds. The million cycle strain trend with fiber content is given in Figure 5 for multidirectional, unidirectional and DB laminates with polyester resin. The unidirectional laminate million cycle fatigue strain gradually decreases with increasing fiber content; the DB initial strain also decreases gradually with fiber content, but in a much lower strain range. For the multidirectional laminates, the million cycle strain follows the unidirectional strain at lower fiber content, then transitions to near the DB strain above about 45% fiber volume (plotted as DD-series in Figure 3). The DD-series laminates are about 70% unidirectional material, 30% DB; at higher fiber contents the multidirectional laminates fail when the DB plies fail, at the relatively low fatigue strain capability of these DB materials with polyester resin. At low fiber contents the multidirectional laminates are able to withstand failure of the DB plies, eventually failing at the independent

unidirectional ply strain condition. Results for epoxy resin with higher density fabrics tend to show that the UD and DB plies fail almost simultaneously in DB laminates, while the behavior with polyester resin is consistent with Figure 5 [21].
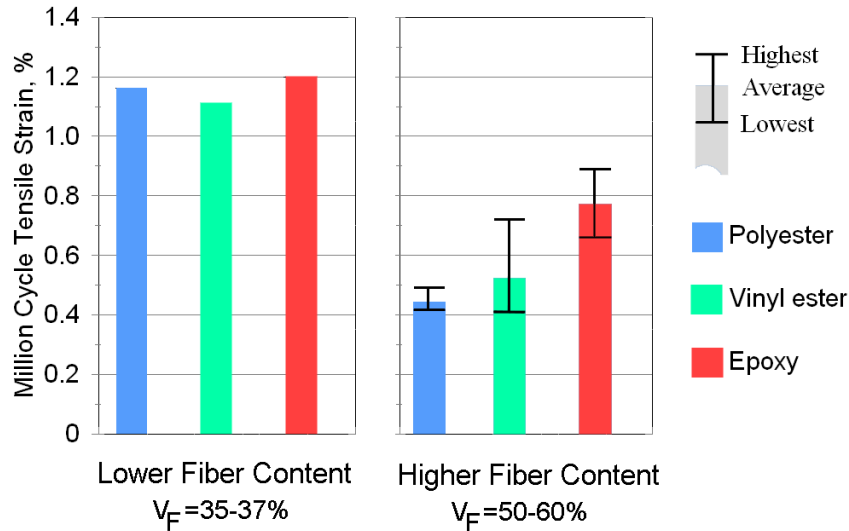
Figure 4. Comparison of polyester, vinyl ester and epoxy resin laminates at low (fabric A) and higher (fabrics D, G and H) fiber contents.
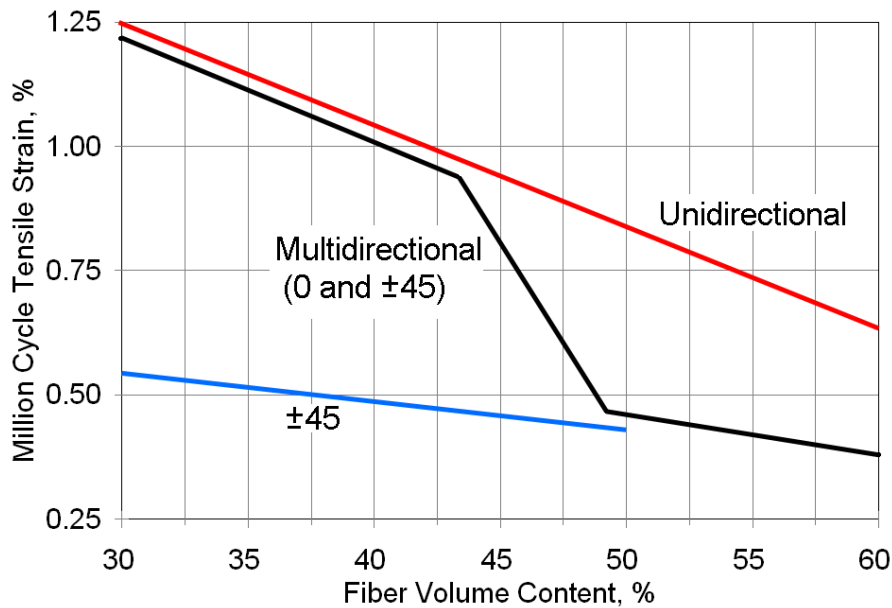
Figure 5. Fatigue trends vs. fiber content for unidirectional, multidirectional and biax laminates based on early [6, 9] low density weft unidirectional Owens Corning/Knytex fabrics D155 and D092, DB fabrics DB120 and DB240, with Interplastic Corp. Corezyn 63-AX-051 polyester resin (UP-2).

When a broad range of laminates, fabricated to different fiber contents in vacuum assisted resin transfer molding (VARTM) were compared in terms of million cycle strain and fiber volume fraction, the results in Figure 3 have been reported [2]. The early results for fabric A laminates,

series DD, used polyester resin; the low density fabric A was compressed to high fiber content in the VARTM mold. The other data represent higher density fabrics currently used in resin infused blades, with epoxy resins. The data in Figure 6 show a marked transition in fatigue strain as the fiber content increases, similar to the MD trend in Figure 5. Data for particular laminate groups with different fabrics show a range of transition fiber contents from around 45% to around 60% depending on the particular fabric and resin. Fabrics with very similar weight and construction showed significant differences in fatigue performance [2].

The results in Figures 4-6 indicate strong effects of glass fabric details and resin on the tensile fatigue resistance. The origins of these effects are explored in Section 5.
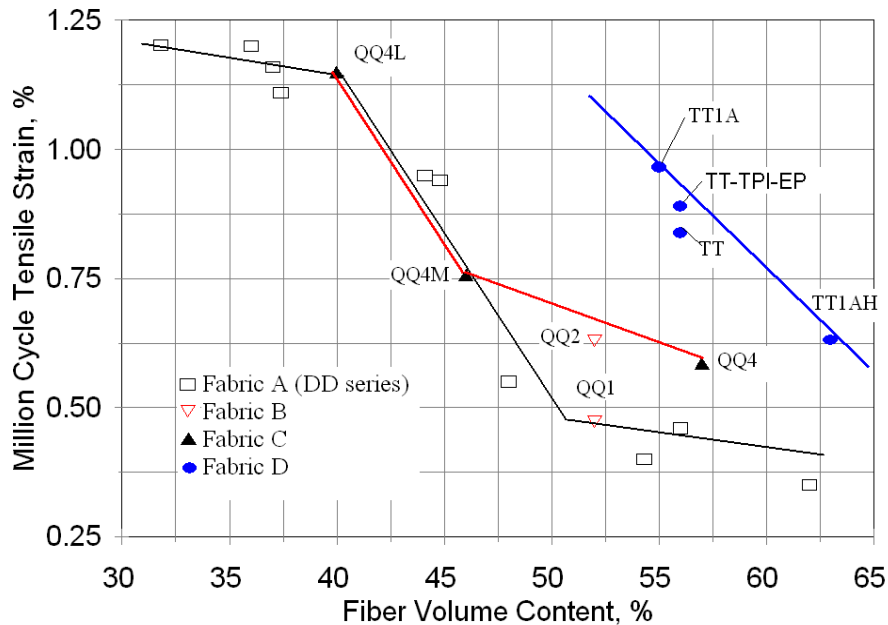
Figure 6. Million cycle strain vs. fiber volume content for various VARTM laminates and one SCRIMP laminate (TT-TPI-EP) showing transitions to reduced fatigue resistance as a function of 0° fabric, R = 0.1 [1,2].

2.2.5 ±45° Laminates
Wind turbine blade structures typically include significant quantities of ±45° laminates in the shells and webs, to resist torsion and buckling, and in the root, to build up the thickness. While not considered the primary structure, represented by unidirectional (UD) plies oriented along the blade axis (0°) in spars, the biaxial laminates and plies must perform without significant damage or failure at the strain levels and environments experienced by the blade in service. Edgewise, reversed loading in large blades is carried substantially by the shell, which may contain some fraction of unidirectional plies for this purpose; often, additional unidirectional fabric reinforcement is added at the trailing edge.

The off-axis orientation of the ±45° fibers as in double bias (DB) fabrics introduces strong material nonlinearity to the static response [2, 21], as well as significant damage accumulation, creep and strength and stiffness loss prior to total failure in fatigue [2,21,23-26]. Bending loads produce the highest strains at the outermost fibers, which are usually biaxial fabric in the shell. Thus, the DB materials must resist the maximum blade strains under static and fatigue loads

25

without failure or softening enough to reduce the blade stiffness or overload adjacent UD material. DB laminates have received relatively little attention in studies compared with UD and multidirectional (MD) laminates, and creep effects in blade laminates have not been well characterized despite their obvious relevance.

2.2.6 Cumulative Time vs. Cyclic Effects.

Blade laminates may be subjected to various combinations of cyclic fatigue loading and static or cyclic creep loading. Most studies have been concerned with cyclic fatigue loading to total failure, primarily with fiber dominated laminates having more than 25% 0° (load direction) fibers. A number of studies have considered creep, creep rupture (sometimes termed static fatigue) and creep/fatigue interactions. Basic treatment of the viscoelastic response can be found in refs. 22-25. Tamuzh, et al. [27] have considered the combined off-axis creep and cyclic fatigue response of glass/polyester laminates. Their findings suggest that cyclic loading results only in a reduction in stiffness as damage accumulates, but does not affect the viscoelastic response. Mandell and Meier [28] systematically varied the waveform, R-value and frequency (over several decades) to explore creep/fatigue interactions for a fiber dominated 0/90 prepreg glass/epoxy laminate under tensile loading. The results re-plotted as trend lines in Figure 7 indicate the typical scenario for fiber dominated glass laminates: the fatigue lifetime was cycle dominated at longer lifetime, with creep effects playing a significant role at higher loads/shorter lifetimes, and low frequencies. In the high cycle/low stress range of interest for wind blades, creep effects are not expected to play a significant role for fiber dominated laminates.

Creep rupture and cyclic data under both tensile and compressive loading for multidirectional infused fiber dominated glass/epoxy blade-type laminates reported by Nijssen, et al. [29], shows much lower failure stresses at the same approximate loading time for cyclic loading at R = 0.1 and 10, compared with creep rupture, consistent with Figure 7. Frequency effects at higher frequencies with sine wave loading have been reported to be consistent with Figure 7 for infused fiber dominated blade laminates [30]. Epaarachchi [31] describes fatigue and creep rupture data for a multidirectional glass/polyester laminate for tensile fatigue loading between R = 0.5 and 1.0. Models incorporating both creep rupture and cyclic parameters provided the best fit to the data.

2.2.7 Double-bias Fabric Laminate Fatigue Behavior.

Tensile fatigue stress (or strain) versus cycles to failure (SN) curves have been reported for a variety of blade materials with $\pm45^O$ construction and epoxy resins, either prepreg or infusion processed. A selection of results from the SNL/MSU/DOE [1] and European OPTIdat [22] databases are compared in Figure 8. Differences are not great considering the range of materials systems. The backing strands in fabric L result in slightly directional behavior [4], and the mat backing on fabric M increases the strength and stiffness but reduces the failure strain significantly [2]. (Fabrics L and M are included in the present study.) Much of the reported study of $\pm45^O$ blade laminates has involved materials composed of UD fabrics or prepreg plies stacked at $\pm45^O$, rather than commercial biaxial fabrics. While most studies have been limited to uniaxial loading of simple test coupons, multi-axial tension/compression/torsion results have been reported by Kensche [32] for a $\pm45^O$ UD fabric laminate.

Philippidis and Eliopoulos [25] provide detailed characterization of both fiber and resin dominated static and fatigue behavior of infused glass/epoxy blade laminates, including stiffness degradation, residual strength and creep effects, and their implementation into a damage progression based code (FADAS). Their treatment is based on individual ply axial, transverse and shear characterization, with the shear response derived from tests of $\pm 45^{O}$ laminates composed of oriented unidirectional fabric plies, similar to the Optimat material MD3, Figure 8.
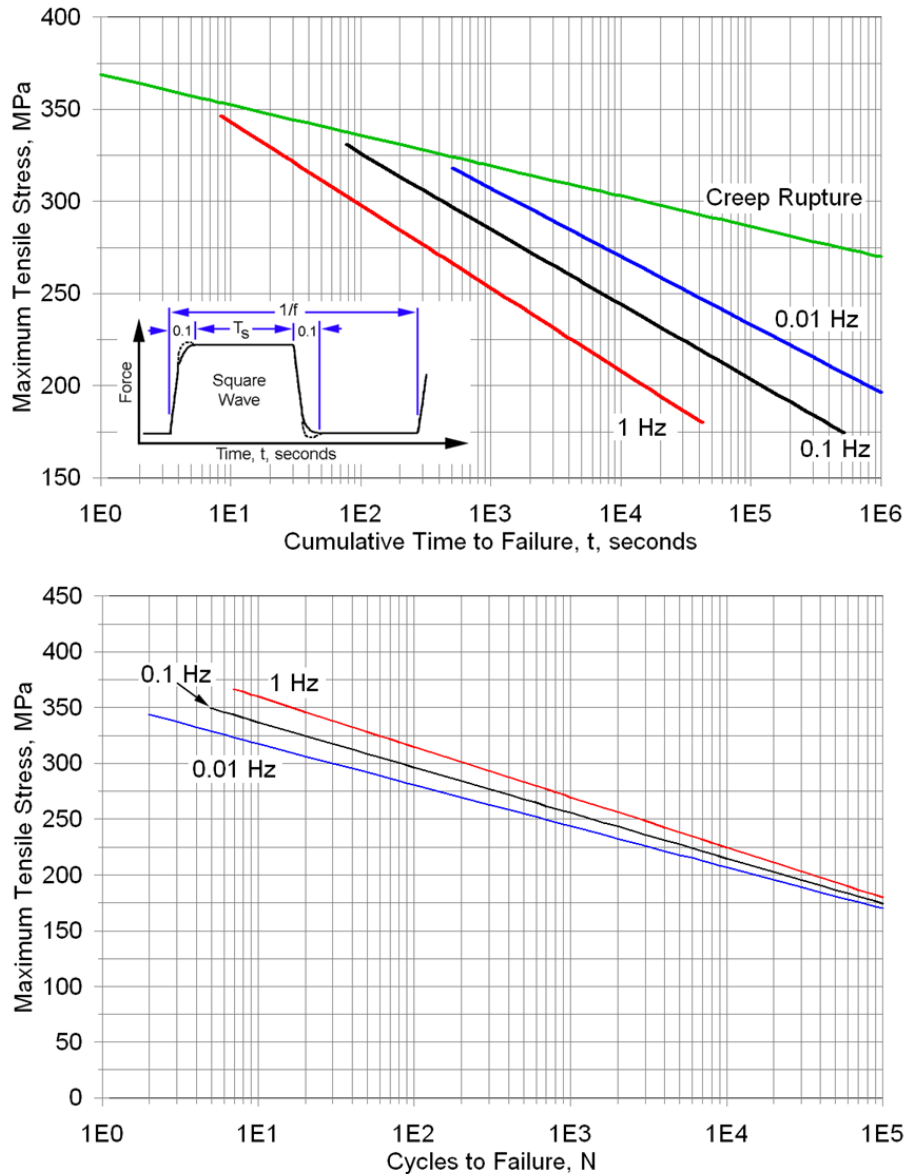
Figure 7. Creep rupture and tensile fatigue trends plotted in terms of cumulative time under load (top) and fatigue cycles (bottom); square wave loading at three frequencies, 0/90 glass/epoxy prepreg laminate (replotted from ref. [28]).

27
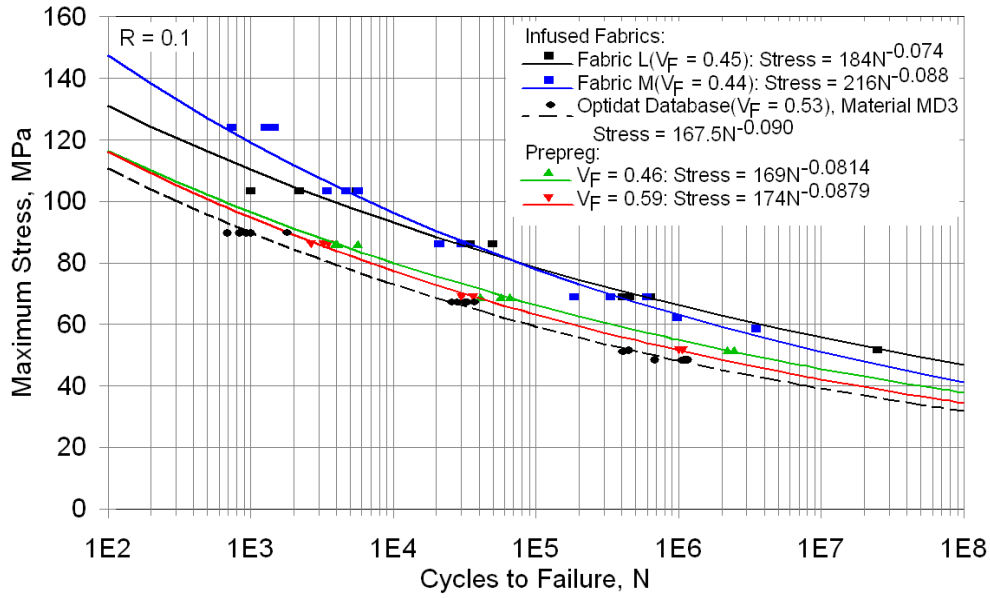
Figure 8. Comparison of literature data [1, 22] for DB glass/epoxy infused and prepreg blade laminates in tensile fatigue, R = 0.1.

The effect of resin on DB fabric laminates has been explored by Mandell, et al. [1, 5, 14]. Fabric M laminates (Table 2) infused with three different epoxies, two vinyl esters and one polyester showed only moderate effects of resin type on tensile stress-strain and tensile fatigue performance [2]. This fabric contains about 27% mat, and behaves in a more fiber dominated or mixed fashion. A similar range of resins with a DB120 biax fabric, which contains no backing strands, showed significantly more variation in strength with resin type [6]. Differences were particularly strong at elevated temperatures and with moisture saturation. Creep rupture data for a wide range of early, low fiber content, fiber dominated and biaxial fabric laminates are available in ref. [6].

2.2.8 Adhesives and Core materials

Wind turbine blades are large composite structures which are typically resin infusion molded in sections, then adhesively bonded together. The large size coupled with cost constraints result in bond lines at least several millimeter thick. Blades are subjected to high cycle fatigue conditions under complex loading in service, and many field failures involving bond lines have been reported. While directly applicable test methodologies and data for appropriate adhesives, loadings and geometries have been lacking in the literature, recent studies by the authors have reported test data for strength and fatigue life using simulated blade joint geometries and lap shear type tests [2, 15]. The study reported here is an extension crack growth testing, which targets the propagation of existing flaws, and can have the advantage of providing properties which are not limited to a specific geometry. Fracture mechanics based studies of adhesive static and fatigue performance have been reported in the literature, primarily directed toward applications with relatively thin adhesive layers [33].

The challenge is to develop test and analysis methods capable of providing a database of static and fatigue crack growth resistance for thick adhesive joints with a broad range of mechanical properties such as toughness, and which can be applied to structures like blades to predict failure

28

from characteristic flaw types. Most adhesive joints are subjected to mixed mode loading, typically a range of opening (mode I) and shear (mode II) combinations. The potential progression of failure from adhesive flaws into typical types of laminate adherends must also be addressed. Finally, joint performance must be predictable under the broad range of static and fatigue loading conditions experienced by blades in service. The latter requirement means that test methods should be capable of reversed and compressive loading without elastic buckling, a need that is not realized by most adhesives test methods. Test methods which are capable of a full range of mode mixity and, potentially, compressive loading, include the ARCAN [34] and scarf joint [35] geometries, and sub-structural elements like beams [36].

The results of testing must be capable of representation in terms of parameters which can be transferred to geometries like blades. Many representations developed for interlaminar fracture in composite laminates have been adapted to adhesive joints, most notably strain energy release rates (SERR) G_{Ic} (mode I), G_{IIc} (mode II) and combinations of them [34], and the total SERR, G_T (= $G_I + G_{II}$), usually calculated by the VCCT method [37] in conjunction with finite element analysis [38]. In the case of extensive yielding or damage other methods may be required [39]. Cohesive zone modeling is increasingly applied [40, 41] and global parameters like adhesive/adherend boundary displacements have been used for ductile adhesives [42].

2.2.9 Environmental Effects
Wind turbine blades are exposed to harsh environments that may deteriorate the mechanical strength of the blade materials. As blade systems see increased deployment in off-shore locations, materials are exposed to an environment with increased moisture content. The mechanical properties of polymer based materials are generally degraded by exposure to moisture or elevated temperatures, particularly over extended time periods. The work reported here relates directly to environmental effects on the materials and properties discussed in other sections of the report. A more extended treatment of the subject is available from an associated on-going study [3].

Early investigation of hygro-thermal effects on composites established the essential technology which guides the current approach and anticipated results. These include the works by Browning, et al. [43] and the three volume series edited by Springer [44]. A recent overview of this general area is provided by Weitsman [45]. Frequency and temperature effects on large blade laminates have been reported by Mishnaevsky, *et al.* [23] and by Cormier, *et al.*[46]. A variety of literature exists for seawater tests of more complex composite structures such as sandwich panels [47].

Intentionally Left Blank

3. Experimental Methods

3.1 Materials and Processing

Processing details are presented in the order appearance of the major sections.

3.1.1 Thick laminates for static testing

The unidirectional glass fabric/epoxy laminates were composed of Vectorply E-LT-5500 infused with Epikote MGS RIMR 135/Epicure MGS RIMH 1366 (100 to 30 mass ratio) epoxy resin. While the primary (warp) reinforcing strands are in the longitudinal direction, the fabric also contains about 6% transverse (weft) backing glass strands to which the warp strands are stitched (but no mat as in fabric H, Figure 1); the backing strands are irregularly spaced, as shown in the transmitted light photographs in Figure 9. Warp strands are PPG 4400 Tex with Hybon 2026 sizing. There is sufficient backing strand content to significantly influence the properties in some directions. The areal weights of the fabric construction are detailed in Table 2; since the fabric is not strictly unidirectional, it is designated 0_b. The stacking of fabric and strands in the 80 ply laminate is shown in Figure 10 for a transverse slice. The internal structure is very heterogeneous on the scale of many 12.7 mm wide coupons, and transverse strands vary as to the number present in the coupon cross-section.
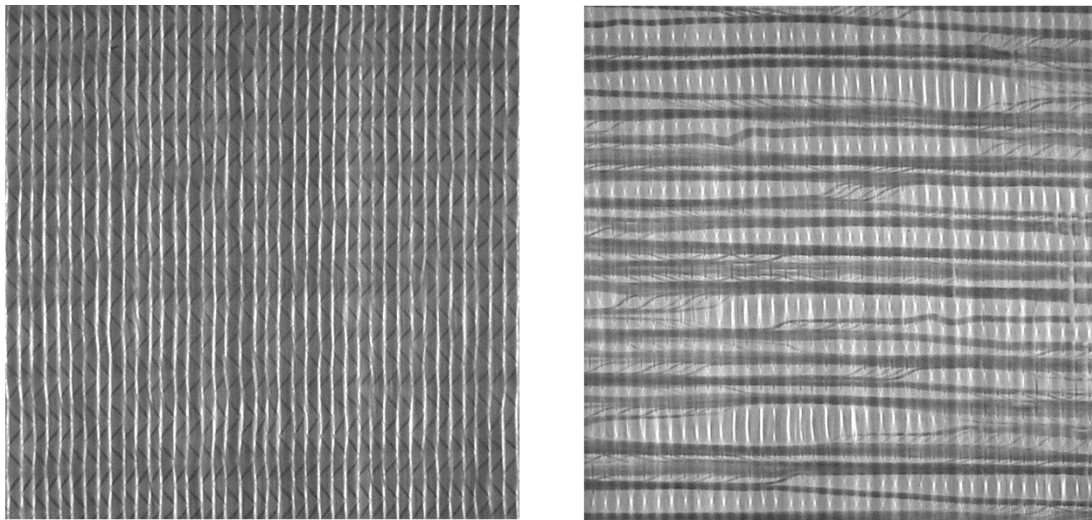
Figure 9. Transmitted light photographs of Vectorply E-LT-5500 (Front and Back)

Properties were determined from 6-ply laminates for in-plane (L, T, LT, TL) properties to reduce possible effects of machining. Properties with a thickness (Z) direction stress were determined from an 80-ply thick laminate, with test coupons removed by wet machining with a diamond edge saw.
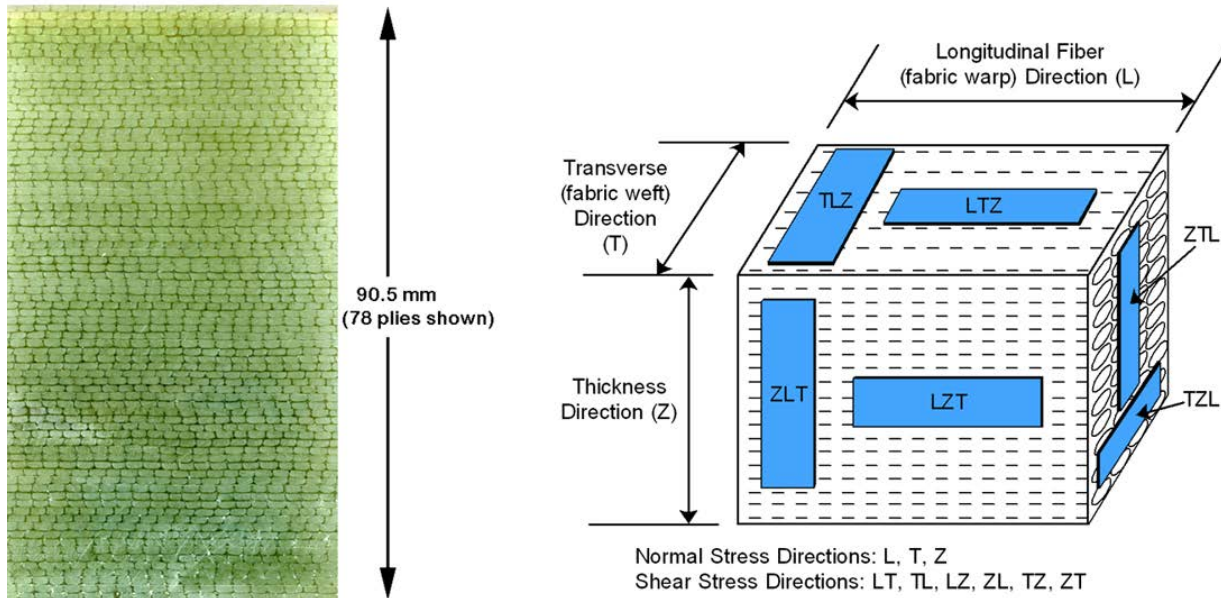
Figure 10. Through-thickness fabric strand stacking for infused 80 ply laminate (50 mm wide x 90.5 mm high slice) and laminate direction nomenclature.

The 80-ply thick laminate, $(0_b)_{80}$, 79 cm long by 27 cm wide by 9.3 cm in thickness, was carefully monitored during cure to reduce cure errors related to the curing exotherm. After the room-temperature infusion was completed, the laminate was initially cured on a room temperature aluminum mold plate until the exotherm subsided (about 12 hrs), then the mold plate temperature was raised to 70°C (mold surface temperature) for 12 hours, de-molded and placed in a post curing oven at 70°C for another 12 hours. Four thermocouples were placed in the laminate for temperature monitoring, detailed in Figure 11. The 6-ply laminate, $(0_b)_6$, used for in-plane properties was cured at room temperature for 24 hours, followed by a 12 hour post-cure at 70°C. Table 1 gives fiber content and ply-thickness data for the two laminates.

Table 1. Fiber Volume Fraction, Standard and Thick laminates (ASTM D2584)

Number of Layers	Fiber Volume Fraction, V_F			Average Ply Thickness, mm
	Average,%	STD	COV	
6-ply laminate	56.8	0.34	0.6	1.19
80-ply laminate	58.2	0.52	0.9	1.16

32
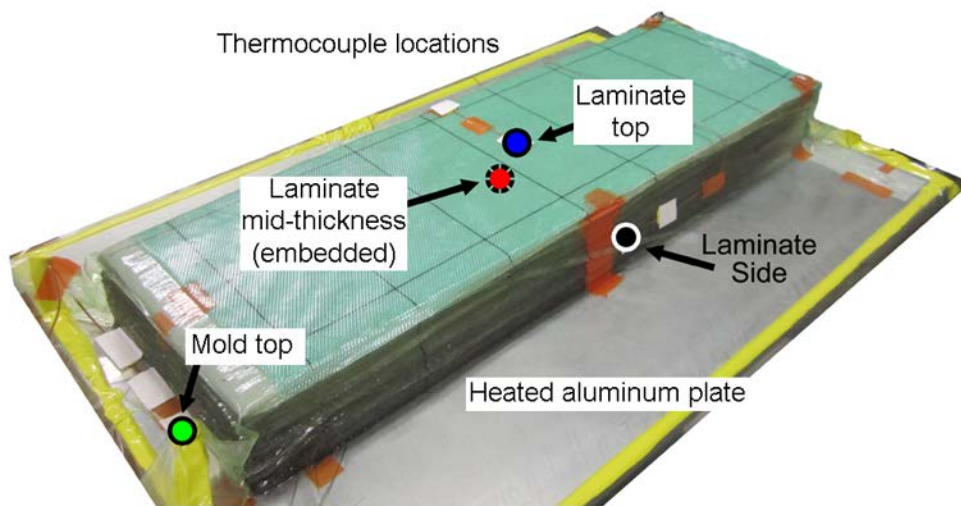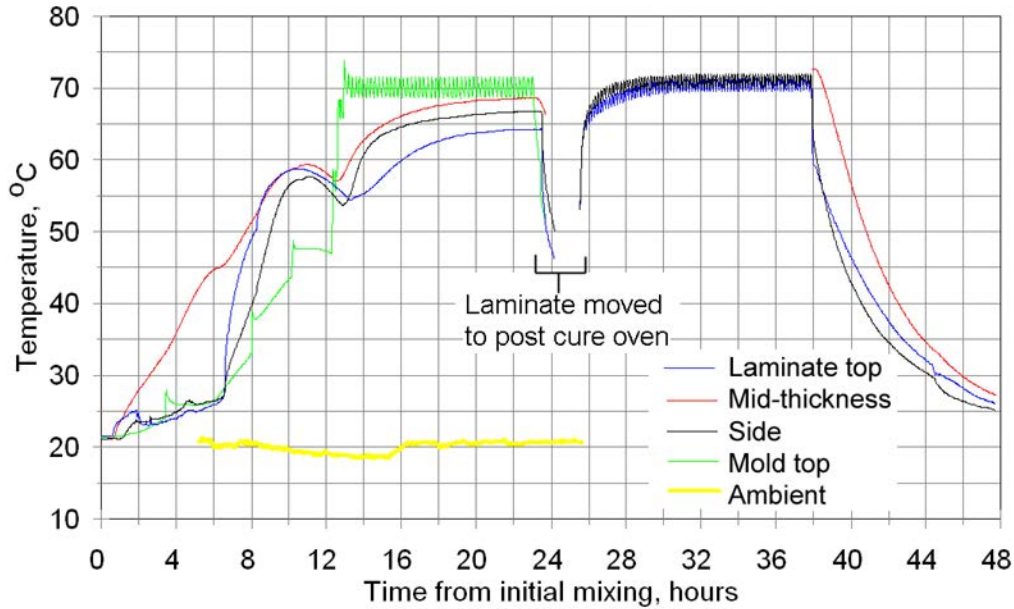
Figure 11. Laminate infusion photograph and temperature traces during cure and post-cure from thermocouples at the indicated positions for the 80-ply laminate.

3.1.2 Typical Blade Laminates

This study has been focused primarily on infused glass fabric/epoxy resin laminates. The baseline materials are given in Tables 2 and 3; other materials are described as they arise. The fabrics are listed in Table 2, resin systems in Table 3. Strand information and laminate designations can be found in [2]. Fabric details given indicate the content of stitching and transverse strands or mat to which the primary strands are stitched. The laminate nomenclature corresponds to the Sandia/MSU/DOE Database. Laminates were processed by resin transfer molding (RTM), vacuum assisted RTM (VARTM), infusion through resin distribution layers, SCRIMP^{TM} infusion, and vacuum bag prepreg molding. VARTM and infusion processes are described in Figures 11 and 12. The materials list covers most materials and process details. Other materials will be described in the results sections.

Most of the materials are in the form of multidirectional laminates containing 0° and ±45° plies, with fiber volume fractions in the range of current infused or prepreg blades. Laminates used in blades typically vary in extreme cases from all unidirectional, Figure 13, in some spars to all ±45° in some skins and webs. Testing experience, both in this program [1] and European OPTIMAT program [22] has found that it is increasingly difficult, often impossible, to obtain gage-section fatigue failures under many testing conditions for laminates with strong fibers, high fiber contents and high fractions of 0° plies. One outcome of this problem is a focus of the databases on laminates with significant ±45° ply content. The testing philosophy is then to represent fatigue results in terms of strain rather than stress. Since all plies experience the same strains, other laminate configurations with a significant fraction of 0° (main load direction) plies, including unidirectional, are assumed to fail at consistent strain-cycle conditions; this assumption is supported by test data in this study.
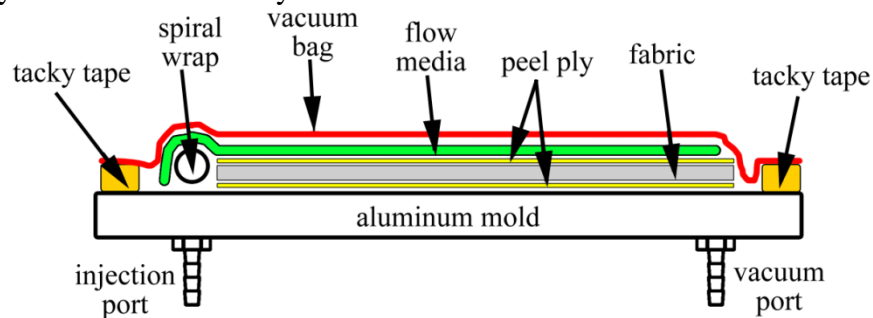
Figure 12. Schematic of the resin infusion process

Figure 13. Aligned strand structure

Table 2. E-Glass Fabric Construction

Fabric[1]	Fabric Type	Manufacturer and Product Designation	Fiber Areal Weight, g/m²					
			Total	0°	90°	±45	mat	stitch
A	UD	Knytex D155	527	0	522	0	0	5
D	UD	Vectorply E-LT-5500	1875	1728	114	0	0	33
G	UD	Knytex A260	868	851	0	0	0	17
H	UD	PPG-Devold L1200/G30-E07	1261	1152	52	0	50	7
L	DB	Saertex -90079-00830-01270	831	0	17	806	0	8
M	DBM	Fiber Glass Ind. SX-1708	857	0	0	583	257	17
P	DB	PPG-Devold 810-E05-A	808	0	0	800	0	8

[1]As listed in the database [1]; for UD fabrics, 0° strands are Hybon® 2026, 2400 Tex (fabric H) and 4400 Tex (fabric D).

Table 3. Infusion Resins (cure conditions listed in Ref. [1])

Resin[1]	Type	Resin
EP1	Epoxy	Momentive Epicote^{TM} RIMR 135/ Epicure^{TM} RIMH 1366
EP5	Epoxy	Momentive Epicote^{TM} RIMR 135/ Epicure^{TM} RIMH 137
UP1	Polyester	U-Pica/Hexion TR-1
UP5	Polyester	Reichhold Polylite^{TM} X4626-31
VE4	Vinyl ester	Reichhold Dion^{TM} 4486-14
VE5	Vinyl ester	Reichhold Dion^{TM} X4235-91
VE6	Vinyl ester	Reichhold Dion^{TM} X4627-39
VE7	Vinyl ester	Ashland 601

[1]As listed in the database [1].

3.1.3 Adhesives and Core Materials

The baseline adhesive is epoxy based Momentive EP135G3/EKH137G (ADH-1), a relatively brittle system which contains short glass fibers. Limited results are also presented for two tougher epoxy based systems: 3M W1100 (ADH-6) and Rhino 405 (ADH-5); the ADH designations are referenced to the SNL/MSU/DOE Fatigue Database where a complete dataset is given [1]. The adhesives as applied in this study are highly viscous for compatibility with the challenging requirements of bonding large blades; when mixed and applied, they contained significant levels of widely distributed small pores, as well as occasional larger pores up to a cm in length. The laminate adherends are infused UD glass fabric Vectorply ELT-5500, which contains a low content of transverse strand backing, with epoxy resin Momentive RIMR135/RIMH1366, 58% fiber by volume. Laminates were four plies thick except for several flexural geometries which used three plies; ply thickness is approximately 1.3 mm. The bonded laminate surfaces were the 0° side of the fabric (as opposed to the backing side) with direct peel-ply (no abrasion). The peel ply used in most cases was Airtech Super Ply F, with comparison data presented for Econo Ply E and Econo Ply J.

Sandwich panels with a 25 mm thick core and 1.6 mm thick glass triax fabric face sheets were infused similar to laminates (Figure 12) with epoxy EP1 resin; flexural fatigue testing followed ASTM C393.

3.2 Test Methods

3.2.1 Thick Laminate Static Tests, Three Directions

Tests were conducted on an Instron 8562 servo-electric test system at a displacement ramp rate of 0.025 mm/s. Axial strains were determined with Micro-measurements Group C2A-06-125LW-120 strain gages for tensile and compressive strains, and C2A-06-062LT-120 strain gages for transverse (Poisson's ratio) and shear strains. For the compression coupons, strains were calculated as the average of gages on both (width) faces.

A variety of test coupon geometries were used following the indicated test standards, with deviations from standard geometries such as added tabs or thickness tapering to obtain gage section failures. Figure 14 gives coupon geometries used for neat resin tests; Figure 15 gives the coupon geometries used for laminates in various orientations.

FaceView

76 mm

1.58 mm thick G10

12.6 mm

76 mm

25.4 mm

1.58 mm thick G10

305 mm radius

SideView

3.15 mm

89 mm
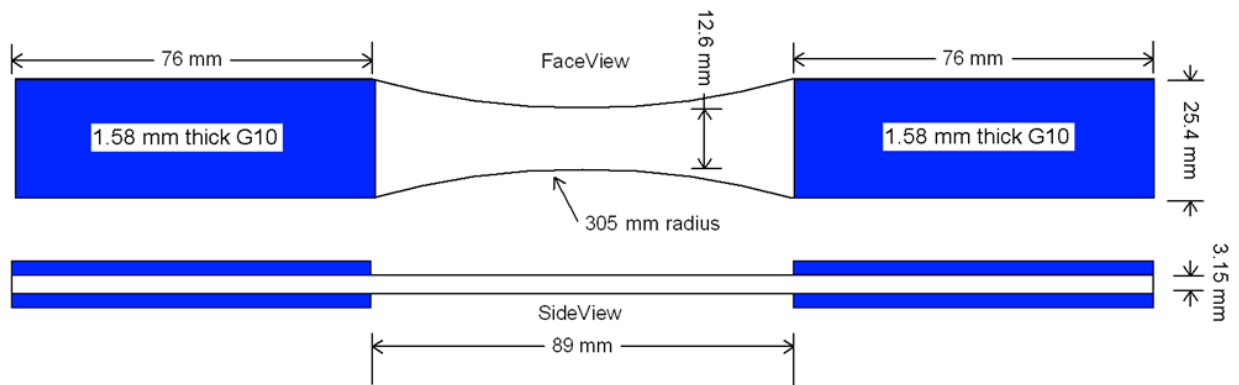
ASTM D638 Tensile test geometry (variation)

12.6 mm

50.8 mm

12.6 mm

12.6 mm

25.4 mm

12.6 mm
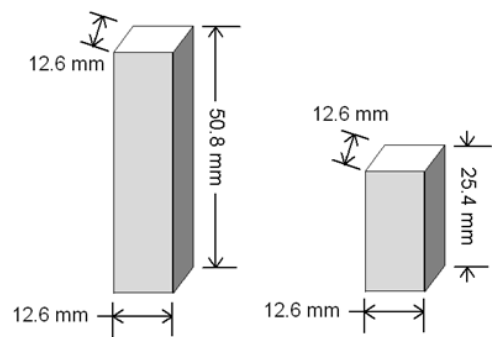
ASTM D695 Compression test geometries

90°

45°

12 mm

20 mm

1.3 mm radius

38 mm

76 mm

Thickness = 8.5 mm
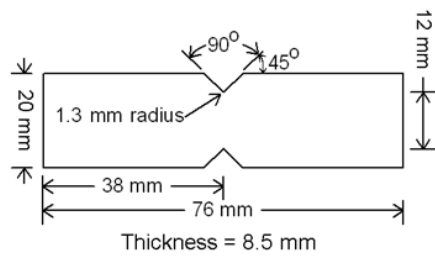
ASTM D5379 Shear test geometry

Figure 14. Neat Resin Coupon Geometries

36

LTZ, LZT thickness tapered, tension (25 mm wide)

100 mm radius

7.2 mm

72 mm

72 mm

3 mm

10 mm
Gage Section

200 mm

TLZ and TZL (straight) tension (25 mm wide)

7.2 mm

200 mm

TZL thickness tapered tension (25 mm wide)

100 mm radius

6.4 mm

36 mm

36 mm

4 mm

10 mm
Gage Section

120 mm

ZTL, ZLT thickness tapered, tension (25 mm wide)

100 mm radius

6.4 mm

21 mm

21 mm

4 mm

10 mm
Gage Section

90 mm

Shear coupon geometry (ASTM D5379):

90°

45°

12 mm

20 mm

1.3 mm radius

38 mm

76 mm

Thickness = 5.5 mm

Figure 15(a). Tensile coupon geometries (ASTM D3039 and D638 with variations):
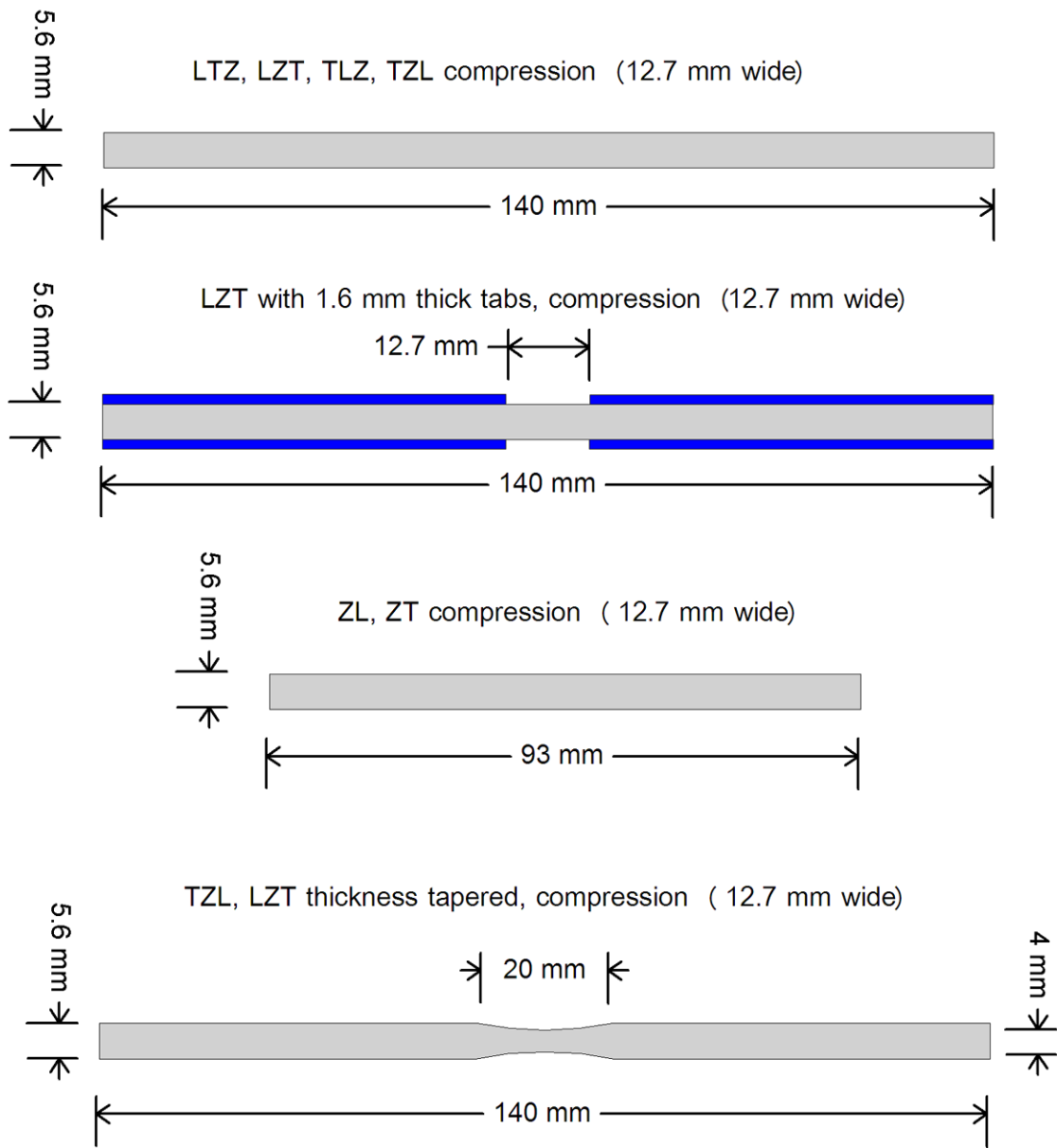
Figure 15(b). Compression coupon geometries (ASTM D6641)

Figure 15. Test coupon geometries for thick laminate static testing in the indicated orientations.

3.2.2 LUR Testing

Loading-Unloading-Reloading (LUR) testing of $\pm45^O$ laminates (which have strongly nonlinear stress-strain curves) followed Philippidis and Eliopoulos [25]. The LUR tests in this program were conducted in compression and reversed loading, in addition to the tensile case reported in ref. [25]. The general loading scheme follows Figure 16, with a fixed ratio of loading and unloading to successively higher loads, and with delay times between loadings established in ref.

[25]. The data are represented in both tension in coupon (x, y) global coordinates and local material coordinates, where the shear deformation is clearly dominant. The tensile performance of DB fabric laminates loaded in the axial (0°) direction is of interest since they must perform adequately in skin areas which see maximum axial blade strains, while the shear properties are critical in resisting blade torsion. The separate $+45^O$ and -45° plies of biaxial fabrics are stitched together, so the individual ply elastic constants are not generally available. Here, the shear properties are calculated following the ASTM D3518 test standard using UD fabric elastic constants for similar fiber contents, available in ref. [1]. The coupon layup and geometry followed the $\pm45^O$ compression and reversed loading case in Section 3.2.4. Shear stress and strain in the material coordinates (1-2) are calculated from the axial stress, σ_x, and the axial and transverse strains, ε_x and ε_y as $\tau_{12} = \sigma_x/2$ and $\gamma_{12} = \varepsilon_x - \varepsilon_y$.

Coupons instrumented with strain gages at 0° and 90° for ASTM D3518 are subjected to a sequence of loads starting at 10% of the strength, and increasing by 10% of the strength on each step, following a triangular waveform, under load control at a load rate of 10 kN/min. There is a delay between loadings of 5x the previous loading time. In reversed loading two cases were tested, with tension followed by compression, and compression followed by tension, for each individual loading.
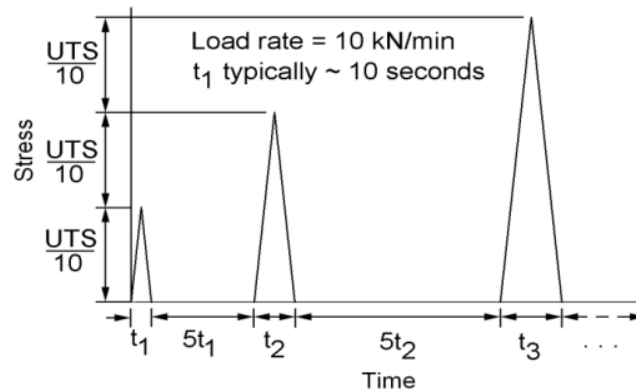
Figure 16. LUR tension test sequence with loading to successively higher loads.

3.2.3 Standard Laminate Fatigue Test Methods
Laminate fatigue test coupons for UD geometries are shown in Figure 17. Most UD fatigue coupons followed ASTM D3039, while thickness tapering was added to avoid grip failures for some aligned strand laminates, as indicated in the results. MD laminate tests used a dog-bone geometry given in Reference 2. Static tests were conducted at a constant displacement rate of 0.025 mm/s, while fatigue tests were conducted under load control at 1-4 Hz, given for each test in the database [1]. Surface cooling with forced air was used for fatigue tests. Detailed test conditions and results can be found in the current or subsequent versions of the database.

Fatigue stress or strain (S) vs. cycles (N) data are used to establish mean lifetime S-N curves, which represent the applied maximum stress or maximum (measured) initial strain in the fatigue test vs. log cycles to failure, fit with a power law model (Eq. 1) and plotted in a linear stress or strain - log cycles format:

$$S = A\,N^B \tag{1}$$

39

where S is the maximum stress or strain in each fatigue cycle, N is the cycles to failure (complete separation), A is the one cycle intercept, and B is the power law exponent, giving the slope of the S-N curve. The exponent can also be represented by n, where n = -1/B. The power law is fit to the fatigue data only, unless noted, and the intercept A often differs significantly from the static ultimate tensile strength (UTS). While the strain is the more general parameter for materials comparisons and many blade design procedures, only the initial strain on the first few cycles is recorded for most UD coupons. Stress plots are sensitive to laminate construction (% 0-degree plies) and fiber content differences when comparing materials.
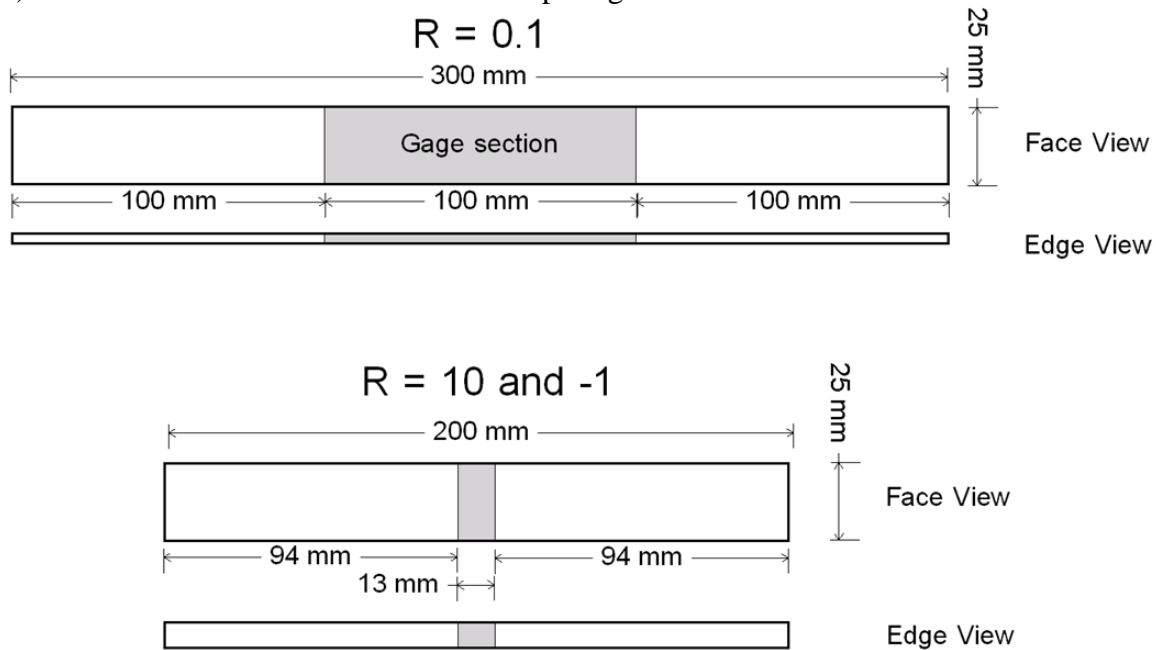
Figure 17. Standard tension static and fatigue (top, 1.7-mm thickness) and static compression and R = 10 and -1 fatigue coupons ($[0]_6$, 5.2-mm thickness) for UD laminates (fabric H/epoxy EP-1).

3.2.4 ±45° Laminates

Double bias (±45°) laminates were resin infusion molded as described in Section 3.1.2. Laminates included several thicknesses given later, all symmetrical layups of DB glass fabric H (Table 2), with epoxy resin EP-1 (Table 3).Cure conditions were 24 hr. at 20°C followed by 24 hr. at 70°C. Test coupons were rectangular in shape without extra loading tabs, which were unnecessary to prevent grip failures in this configuration. Reversed loading and compression tests were run with (±45)$_{8S}$ laminates 8.6 mm thick, with a fiber volume fraction of 0.58 unless noted otherwise. The gage length between grips was approximately 50 mm unless noted, sufficiently short to preclude elastic buckling prior to compressive failure.

During testing, coupons were clamped in laterally-constrained hydraulic wedge grips as described in reference [2]; test frequencies were kept low to reduce heating: 1 to 4 Hz at R = 0.1; 0.5 to 2 Hz for reversed loading and compression, for sine-waveform loading. Unless noted, a sine waveform was used. Creep tests were run at constant load. Strains were recorded with extensometers and with foil strain gages in selected cases (where data were reduced to shear

40

strains). A series of tests was run with a square waveform at frequencies from 1.0 to 0.001 Hz to explore creep and cyclic effects where the time under load can be explicitly defined.

Coupons were conditioned and tests conducted in ambient laboratory air, approximately $20^{O}C$ and 20 to 30% RH. Surfaces were fan cooled [2] and surface temperatures rose by less than 10-$15^{O}C$ up to 95% of the lifetime, but in some cases rose more significantly in the final cycles in the failure zone under reversed loading and compression. The failure zone characteristic of R = -1 failures may indicate that the temperature approached the glass transition temperature in that local area; temperatures as high as $70^{O}C$ were measured. Failure appeared imminent just prior to the rapid temperature rise, so lifetime data may be slightly conservative relative to tests with less temperature rise. Frequency was approximately linearly compensated relative to maximum load. Additional fatigue tests were run using square waveforms at varying frequency to control the relative time on and off load, and cycle numbers relative to cumulative time under tensile or compressive load, during reversed loading at R = -1. Individual test conditions and results can be found in the current or next annual update of the database [1].

3.2.5 Adhesives
Previous studies of thick adhesive joint fatigue have involved strength-type fatigue testing at a full range of R-values with a double notched lap shear coupon [2, 15]. A major focus of the current study has involved the development of a crack growth based test with relatively stiff, thick adhesive cracked lap shear (CLS) specimen geometries capable of fatigue testing under a range of loading conditions from tension-tension (R = 0.1), reversed loading (R = -1) and compression-compression (R = 10), where R is the ratio of minimum to maximum applied load. CLS geometries of this type have been used in earlier adhesives and delamination studies, usually with less thick adherends [39]. Specimen geometries including reinforcement by steel strips (Figure 18a) were selected to provide a range of mode mixity dominated by mode II (shear), with a lesser mode I (opening) component, as well as differences in crack stability and local crack path. Initial data from early versions of these tests were presented in ref. [15]. The CLS geometry pictured in Figure 18 is both stiff and nonsymmetrical, and gripping conditions are not precisely defined. The massive hydraulic grips and lateral constraints on grip movement, Figure 18b [2], resulted in minimal lateral movement of the grips under load; video imaging showed less than 0.2 mm lateral movement where the specimen leaves the grip, at maximum load. Static CLS tests were conducted at a displacement rate of 1.5 mm/min, while fatigue tests were conducted under load control at 1-4 Hz.

Additional static tests were conducted using more standard flexure based geometries including double cantilever beam (DCB, ASTM D5528) for pure opening mode, mixed mode bending (MMB) for combined modes I and II [53] and end notched flexure (ENF) for pure mode II [2]. Figure 19 gives the flexure based geometries; the static flexure based tests were conducted with displacement rates of 0.5 mm/min (DCB) and 2.54 mm/min (ENF, MMB). While the flexure based geometries can be loaded in fatigue [33], a full range of loading conditions is difficult to achieve in practice. As discussed later, the flexure based geometries have deformation patterns and far-field stresses which are different from thick composite structures like wind blades, despite similar conditions very close to the crack tip. Adhesives may develop damage zones (yielding and/or micro-cracking) well ahead of the crack tip, where the far-field stress patterns are important [38, 42].

Bonded joint specimens were machined from a sandwich construction [2, 15]. The two part adhesives were either hand mixed with a trowel or machine mixed using a Dac150.1FVZ Speed Mixer for 4 minutes at 1500 RPM. The mixed adhesive was applied to each surface with a trowel, and the two laminate sides were then assembled into a sandwich. Curing was at room temperature for 24 hours followed by 8 hours at 70$^{\text{O}}$C. Test coupon strips were then machined from the sandwiches and notches for the CLS geometries were also machined, with care to not penetrate the opposite laminate surface.
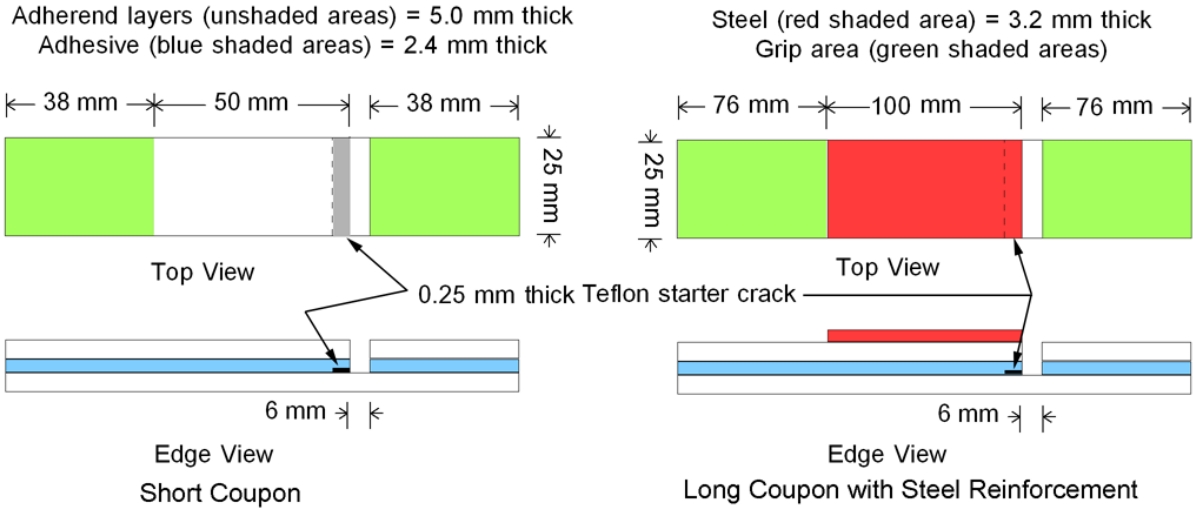
Figure 18(a). Coupon dimensions: left, short coupon with 50 mm gage length; right, 100 mm length specimen showing added steel reinforcement.
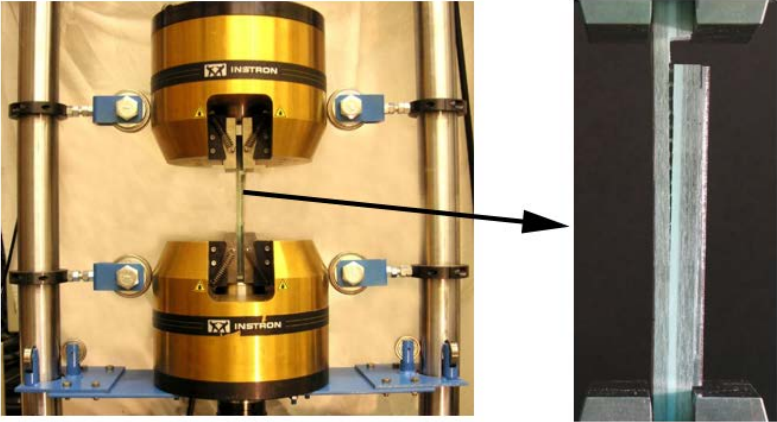
Figure 18(b). Test set-up with long specimen shown under load.

Figure 18. Cracked lap shear (CLS) Specimen (a) schematics and (b) photos of test set-up.
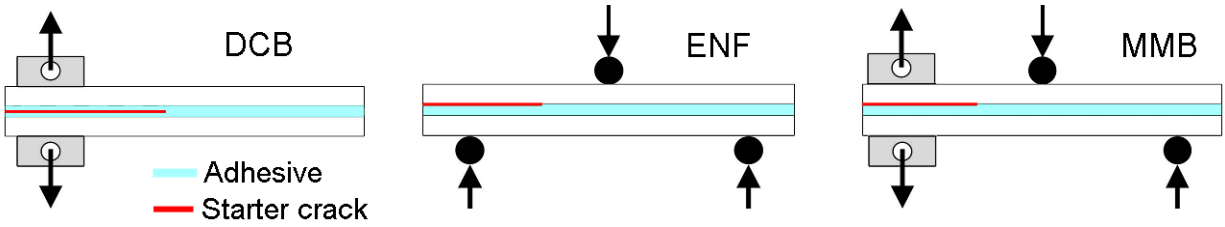
Figure 19. Flexural test geometries showing starter crack positions in adhesive: DCB, center or top; ENF, top; MMB, top.
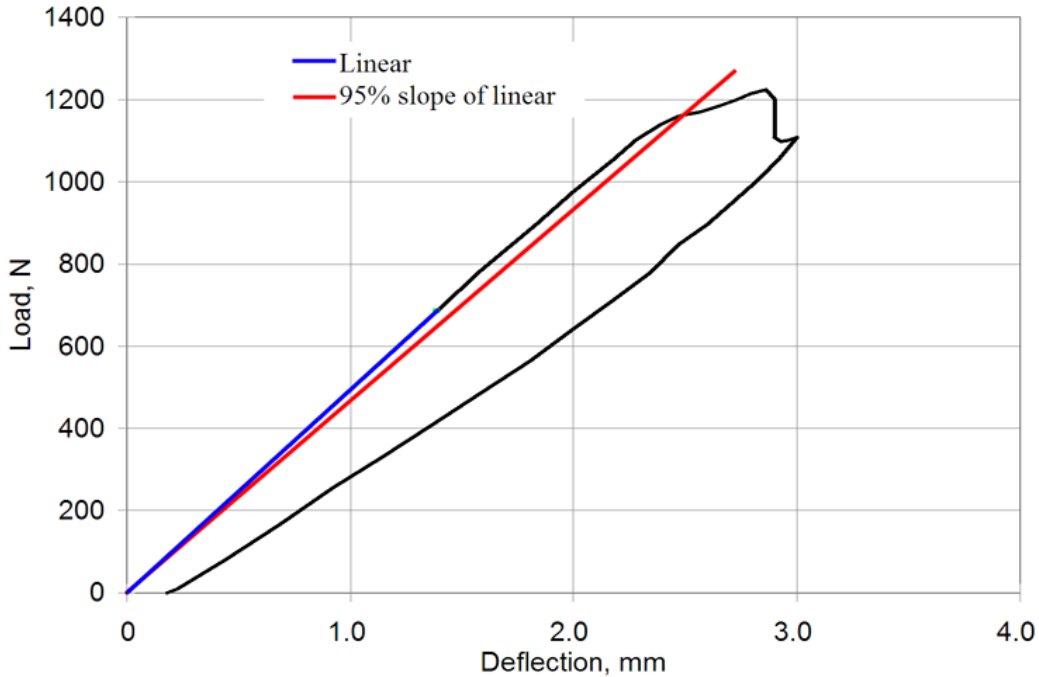
Figure 20. Typical load versus actuator displacement curve and critical load determination for an MMB specimen.

Calculation of strain energy release rates (SERR's) for the flexural-type specimens (Figure 19) followed the description in ref. [2] for ply delamination tests, ignoring the contribution of the adhesive to the stiffness or dimensions; results are compared to more detailed FEA analysis. Measured laminate properties used for these calculations are given for the laminates below; the adhesive properties for FEA analysis were taken from reference [1] as E = 2.76 GPa and ν = 0.35. Critical loads were determined by the offset method illustrated in Figure 20. The critical strain energy release rate to grow a crack in the material can be obtained by the use of the load versus displacement curve of the test (Figure 20) and the modified beam theory (MBT) method [2]. For mode I, DCB:

$$G_{IC} = \frac{3P\delta}{2ba} \tag{2}$$

where: P = critical load at crack propagation

δ = displacement between DCB cantilever arms at critical load

b = specimen width (25 mm nominal)

a = crack length measured from the center of the load pins

For Mode II, ENF [48]:

$$G_{IIC} = \frac{9P^2 a^2 C}{2b(2L^3 + 3a^3)}$$

(3)

where: P = critical load at propagation
a = initial crack length measured from support point
b = specimen width (25 mm nominal)
C = specimen compliance (= center point deflection/P)
L = one-half support spacing distance

For the mixed mode bending (MMB) test (Figure 21) [2, 49]:

$$G_I = \frac{12P_I^2}{b^2 h^3 E_{11}} \left(a_o^2 + \frac{2a_o}{\lambda} + \frac{1}{\lambda^2} + \frac{h^2 E_{11}}{10G_{13}} \right)$$

(4)

$$G_{II} = \frac{9P_{II}^2}{16b^2 h^3 E_{11}} \left(a_o^2 + \frac{h^2 E_{11}}{5G_{13}} \right)$$

(5)

$$\lambda = \frac{1}{h} \sqrt[4]{\frac{6E_{22}}{E_{11}}}$$

(6)

$$P_I = P_C \left(\frac{3c - L}{4L} \right)$$

(7)

$$P_{II} = P_C \left(\frac{c + L}{L} \right)$$

(8)

where,
a_o = initial crack length
b = width of specimen (25 mm nominal)
c = geometric variable that changes the G_I/G_{II} ratio
E_{11}, E_{22} = longitudinal and transverse moduli, taken as 45.8 MPa and 8.33 GPa, respectively
G_{13} = in-plane shear modulus, taken as 8.55 GPa
G_I, G_{II} = strain energy release rate in mode I and II, respectively
h = laminate thickness (5.0 mm nominal, does not include the adhesive thickness)
L = half-length of the bottom support
P_C = critical loading determined from load-deflection curve
P_I, P_{II} = mode I and II loadings, respectively
λ = elastic foundation correction (function of h, E_{11} and E_{22})
See the illustration of the apparatus in Figure 21 for the geometric variables a_o, c, h and L.
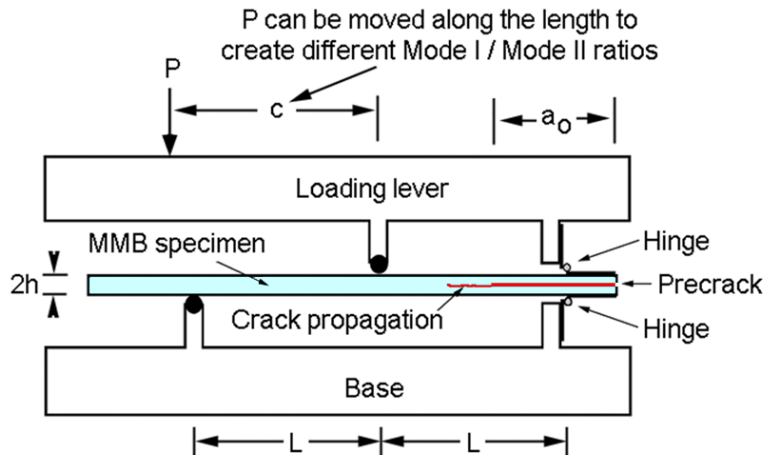
Figure 21. Mixed mode bending apparatus (MMB).

3.2.6. Environmental Effects

Material preparation for resin infused laminates followed the same methods covered in Section 3.1.2. The baseline laminate consisted of EP-1 epoxy resin (Table 3) and the unidirectional glass fiber was fabric H (Table 2). The second laminate consisted of Ashland 601 vinyl-ester resin (VE7) and the unidirectional glass fiber was fabric H. After the infusion process the composite was cured at 20°C for 24 hrs followed by a post-cure of 70°C for 12 hours. The resulting fiber volume content was 56-57% calculated from density measurements. From the unidirectional composite plates, samples were cut to produce $[0]_2$, $[0]_6$ and $[90]_6$ samples with the standard tensile geometry shown in Figure 17.

After fabrication, initial sample weights were recorded and a portion of the samples were submerged in ASTM D1141 synthetic sea water (SSW) at 50°C, while the remainder were retained as controls. Samples to be conditioned were placed in a sealed bath of SSW and stored in a temperature controlled oven at 50°C. Periodically, witness samples were removed from the SSW, patted dry, weighed and recorded until saturation was achieved. Initial moisture content was checked by oven drying control material to equilibrium weight; control weight loss by drying was low, less than 0.1% weight loss depending on thickness. The drying weight loss is added to the saturation weight gain values measured for conditioned materials, so that the moisture content (weight gain values) given for each case are, approximately, total moisture content by weight.

Carbon/epoxy prepreg samples (SparPreg UC600) fabricated and supplied by Gurit were similarly conditioned in SSW at 50°C to saturation. Coupons included $(0)_2$ for longitudinal tension, $(0)_8$ for transverse tension and $(90/0/90/0)s$ for compression. Additionally, a $(\pm45/(0)_2/\pm45)$ hybrid carbon UD/glass DB laminate was conditioned and tested in tensile fatigue ($\pm45°$ plies are Sprint XE600 glass/epoxy). Test coupon geometries for the carbon/epoxy are shown in Figure 22.

Most UD tensile glass coupons followed ASTM D3039, while thickness tapering (Figure 15) was added to preclude grip failures for some laminates. Compression tests followed ASTM

D6641 (Figure 15). Compression testing of carbon coupons followed ASTM D6641, but with (90/0/90/0)s laminates, with the 0° properties backed-out following reference [50]. Addition of the 90° plies avoids kink banding at the grip edge. Static tests were conducted at a constant displacement rate of 0.025 mm/s, while fatigue tests were conducted under load control at 1-4 Hz, given for each test in the database [1]. Detailed test conditions and results can be found in the database [1]. All environmentally conditioned samples were tested in a salt water immersion environment (Figure 23).

Additional SSW saturated tests were run on thick notched lap shear adhesive joint coupons [2] (Figure 24) with UD fiberglass laminate adherends (fabric D/epoxy EP-1). Neat samples of adhesive ADH-1 and epoxy resin EP-1 (all cured at 70^OC) were tested using the tensile fatigue coupons in Figure 14.
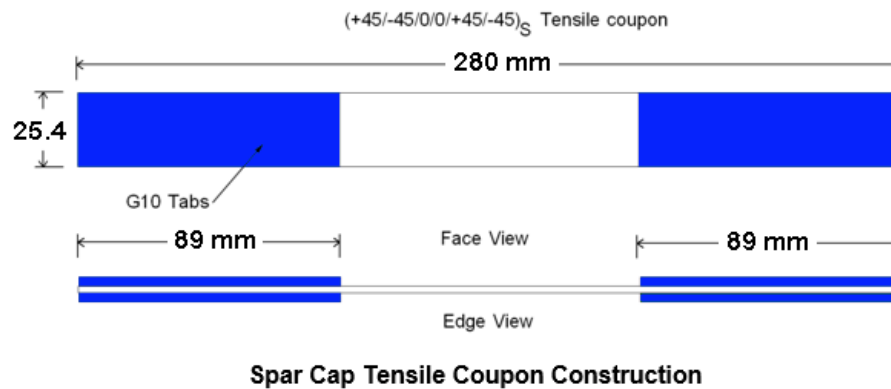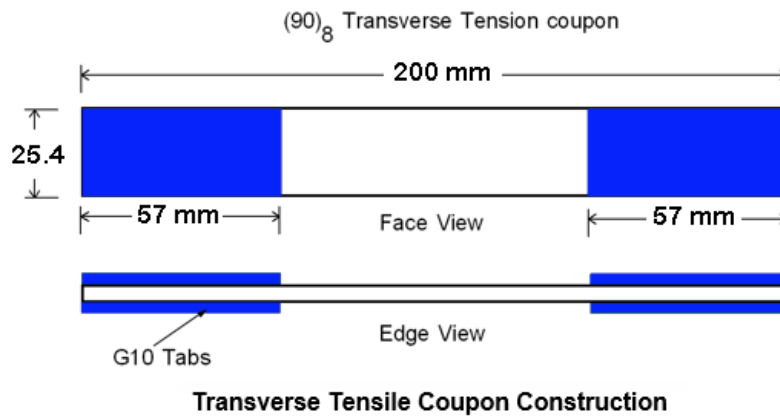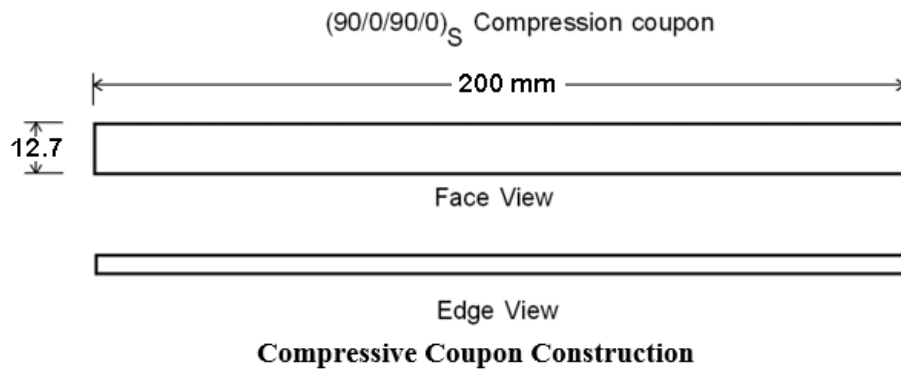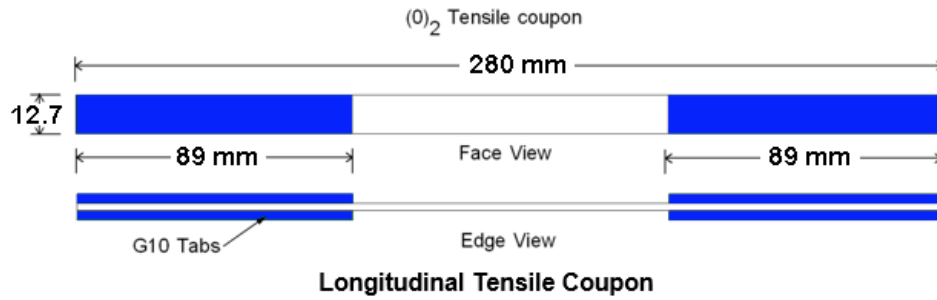
Figure 22. Test coupons for SparPreg UC600 carbon/epoxy environmental tests.
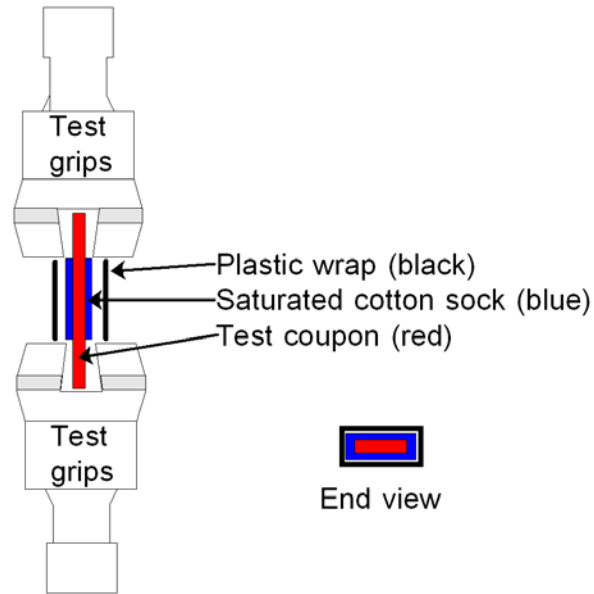
Figure 23. Schematic of seawater immersion test set-up (seawater added as needed).
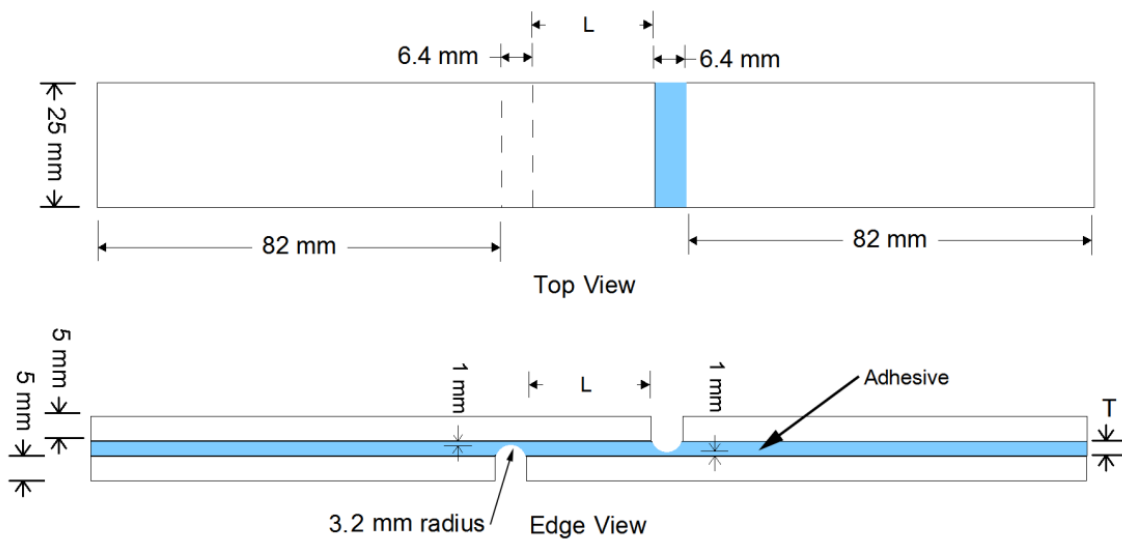
Figure 24. Notched lap shear adhesives test coupon [2].

4. Static Properties: Thick Laminates and LUR Tests

4.1 Static Properties in Three Directions

4.1.1 Overview

Full 3-D elastic constants and in-plane and through-thickness stress-strain response have been obtained for an infused fabric laminate typical of blade spar structure, for use in finite element modeling. The complex architecture of blade reinforcing fabrics raises uncertainty about typical assumptions as to properties in directions which are usually not tested. Multi-axial failure criteria for this class of laminates have also not been adequately tested. In this study, infused unidirectional (UD) 93 mm thick fabric laminates have been carefully prepared, with shear and normal test coupons machined in various directions (Figure 25); in-plane properties were determined from conventional thickness specimens.

Table 4 gives a schematic of test coupon orientation and elastic constants. Table 5 gives strength values; best fit nonlinear shear stress-strain curves and failed coupon photographs are shown in Figures 26 and 27. The fabric stacking and internal structure are evident in the photographs. The relationships between elastic constants are approximately as expected [58]. All six shear moduli are in the same range; shear stress-strain curves are strongly nonlinear over the entire strain range, as expected (Figure 26). The z-component strength properties are significantly weaker than in-plane properties, the latter reflecting the transverse fabric backing strands (Table 5). The z-direction tensile strength is lower than the in-plane transverse tension strength for the same reason; the latter strength is listed as the "knee" value where most of the cross-section cracks, leaving in-tact transverse strands. Z-direction compression strength is similar to the in-plane transverse compression strength.

4.1.2 Property Summary

The material directions and coupon orientations are described in Figure 25. Average elastic constants and strengths are given in Table 4 in the material principal directions; resin properties are added at the end. Properties are averages for coupons with the same stress direction, but orthogonal coupon orientations, such as LTZ and ZLT, which are given separately in the following sections.

4.1.3 Detailed Results and Discussion

Table 5 gives detailed results for each coupon orientation and stress direction. Normal stress tests used the two orthogonal coupon orientations each for L, T, and Z direction stresses, indicated in Figure 25. These results are averaged for the property listings in Table 4, but are listed separately in Table 5. Major nonlinearities occur in the transverse tension and shear tests. In transverse tension, a knee in the stress-strain curves is observed at the stress where resin cracking occurs parallel to the warp direction strands, if the weft direction backing strands remain in-tact; separate results are given for the first cracking stress and strain. Stress-strain curves are nonlinear over most of the stress range in shear, so 0.2% offset data are given where values could be determined. Shear results are limited to 5% shear strain or less by ASTM D5379, so the stress at 5% strain is listed instead of ultimate values.
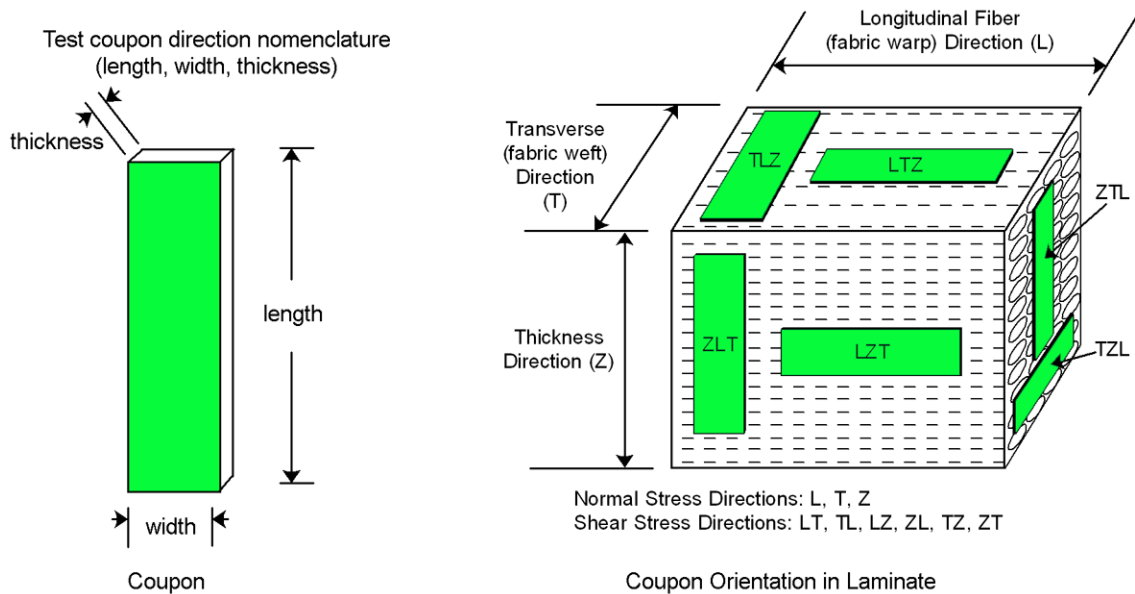
Figure 25. Coupon orientation indices and location in thick laminate.

Table 4. Average 3-D elastic and strength properties for thick unidirectional glass fabric/epoxy laminate and for neat resin.

LAMINATE ELASTIC CONSTANTS[1]	$V_F = 56.8 – 58.2\%$
Tensile Modulus E_L (GPa)	44.6
Tensile Modulus E_T (GPa)	17.0
Tensile Modulus E_Z (GPa)	16.7
Compressive Modulus E_L (GPa)	42.8
Compressive Modulus E_T (GPa)	16.0
Compressive Modulus E_Z (GPa)	14.2
Poisson Ratio v_{LT}	0.262
Poisson Ratio v_{LZ}	0.264
Poisson Ratio v_{TL}	0.079
Poisson Ratio v_{TZ}	0.350
Poisson Ratio v_{ZL}	0.090
Poisson Ratio v_{ZT}	0.353
Shear Modulus G_{LT} (GPa)	3.49
Shear Modulus G_{LZ} (GPa)	3.77
Shear Modulus G_{TL} (GPa)	3.04
Shear Modulus G_{TZ} (GPa)	3.46
Shear Modulus G_{ZL} (GPa)	3.22
Shear Modulus G_{ZT} (GPa)	3.50

[1]Tensile and compressive moduli and Poisson's ratios determined from best fit line between 0.1% and 0.3% strain; shear moduli calculated from best fit line between 0.2% and 0.6% shear strain.

Table 4. Average 3-D elastic and strength properties for thick unidirectional glass fabric/epoxy laminate and for neat resin. (cont)

LAMINATE STRENGTH PROPERTIES	STRESS DIRECTION	STRENGTH (MPa)	ULTIMATE STRAIN (%)
Tension	L	1240	3.00
Tension[1]	T	43.9	0.28
Tension	Z	31.3	0.21
Compression	L	-774	-1.83
Compression	T	-179	-1.16
Compression	Z	-185	-1.44
Shear[2]	LT	55.8	5.00
Shear[2]	LZ	54.4	5.00
Shear	TL	52.0	4.60
Shear[2]	TZ	45.6	5.00
Shear	ZL	33.9	1.10
Shear	ZT	28.4	0.81

[1]Transverse tension properties given for first cracking (knee) stress
[2]Shear values given for 5% strain following ASTM D5379

Neat Resin Properties	
Tensile Modulus (GPa)	3.53
Poisson's Ratio	0.347
Compression Modulus (GPa)	2.98
Shear Modulus (GPa)	0.990
0.2% Offset Tensile Yield Stress (MPa)	41.0
Ultimate Tensile Strength (MPa)	76.3
Ultimate Tensile Strain (%)	4.20
0.2% Offset Compressive Yield Stress (MPa)	-64.7
Ultimate Compressive Strength (MPa)	-91.0
Ultimate Compressive Strain (%)	-5.38
0.2% Offset Shear Stress (MPa)	26.1
Shear Stress at 5% Strain (MPa)	37.7

Individual test stress-strain data and best fit stress-strain curves are given in Figure 28, and tabular individual test data are given in the database [1]. Figure 26 compares the best fit stress-strain curves for various cases, with fit equations given in Table 6. Figure 27 gives photographs of failed coupons for each case. Cases with greater scatter evident in individual test data in Figure 28 such as transverse and thickness direction tension (Figures 28 (c-f)) and ZL and ZT shear (Figures 28 (q and r)) reflect differences in the number of transverse strands in the gage section, local strand packing features (Figures 9 and 10) or the location of the V-notch in the shear coupon relative to the transverse strand position (Figure 15, shear coupon).

<h2 style="text-align:center">Table 5. Detailed Test Results</h2>

Tensile Properties

Stress Direction	Coupon Orientation		$E_{Tension}$, GPa				Poisson's Ratio				Ultimate Tensile Stress, MPa			Failure strain, %		
			Avg	SD	COV		Avg	SD	COV	Avg	SD	COV	Avg	SD	COV
L	LTZ	E_L	43.2	2.1	4.9	ν_{LT}	0.262	0.01	3.2	1180	66	5.6	2.92	0.13	4.4
L	LZT		45.9	2.0	4.4	ν_{LZ}	0.264	0.02	7.3	1293	20	1.6	3.08	0.13	4.2
T	TLZ	E_T	17.2	2.0	12	ν_{TL}	0.079	0.01	17	73.0	3.7	5.0	0.45	0.03	6.5
T	TZL		16.7	0.73	4.4	ν_{TZ}	0.350	0.02	6.5	65.5	9.6	15	1.09	0.57	53
Z	ZLT	E_Z	16.3	2.1	13	ν_{ZL}	0.090	0.02	20	32.6	1.6	4.8	0.23	0.02	8.7
Z	ZTL		17.0	2.3	14	ν_{ZL}	0.353	0.06	16	29.9	3.5	12	0.19	0.05	28
----	Neat Resin	E	3.53	0.08	2.2	ν	0.347	0.01	1.7	76.3	0.63	0.83	4.2	0.50	12

First cracking (knee) tensile stress and strain

Stress Direction	Coupon Orientation	First cracking stress, MPa			Strain at First cracking, %		
		Avg	SD	COV	Avg	SD	COV
L	LTZ	--	--	--	--	--	--
L	LZT	--	--	--	--	--	--
T	TLZ	44.0	3.2	7.3	0.27	0.04	16
T	TZL	43.8	6.2	14	0.29	0.06	22
Z	ZLT	--	--	--	--	--	--
Z	ZTL	--	--	--	--	--	--

Compression Properties

Stress Direction	Coupon Orientation	$E_{Compression}$, GPa			Ultimate Compressive Stress, MPa			Failure Strain, %		
		Avg	SD	COV	Avg	SD	COV	Avg	SD	COV
L	LTZ	42.5	2.3	5.4	-750	42	5.5	-1.78	0.17	9.5
L	LZT	43.1	1.8	4.1	-797	66	8.3	-1.87	0.25	13
T	TLZ	16.4	1.8	11	-189	3.7	2.0	-1.18	0.15	13
T	TZL	15.6	1.3	8.6	-168	24	14	-1.13	0.13	12
Z	ZLT	13.8	0.79	5.7	-180	6.3	3.5	-1.44	0.10	6.6
Z	ZTL	14.6	1.2	8.0	-189	7.2	3.8	-1.44	0.10	6.8
----	Neat Resin	2.98	0.02	0.70	-91.0	1.3	1.4	-5.38	0.37	6.9

Shear Properties

Stress Direction	Coupon Orientation		Shear Modulus[1], G, GPa			0.2% Offset Stress, MPa			Maximum Shear Stress, MPa			Maximum[2] Shear Strain at Maximum Stress, %		
			Avg	SD	COV	Avg	SD	COV	Avg	SD	COV	Avg	SD	COV
LT	LTZ	G_{LT}	3.49	0.39	11	38.7	3.8	9.7	55.8	0.79	1.4	5	--	--
LZ	LZT	G_{LZ}	3.77	0.25	6.6	39.1	2.8	7.1	54.4	2.4	4.4	5	--	--
TL	TLZ	G_{TL}	3.04	0.37	12	38.0	4.3	11	52.0	1.7	3.3	4.6	0.30	6.5
TZ	TZL	G_{TZ}	3.46	0.51	15	36.3	3.6	9.9	45.6	3.0	6.6	5	--	--
ZL	ZLT	G_{ZL}	3.22	0.38	12	--	--	--	33.9	5.5	16	1.1	0.28	25
ZT	ZTL	G_{ZT}	3.50	0.44	13	--	--	--	28.4	3.6	13	0.81	0.25	31
----	Neat Resin	G	0.99	0.19	19	26.1	4.1	16	37.7	2.0	5.3	5	--	--

[1]Shear modulus calculated from best fit line between 0.2% and 0.6% shear strains.
[2]ASTM D5379 limits the maximum shear strain to 5%.
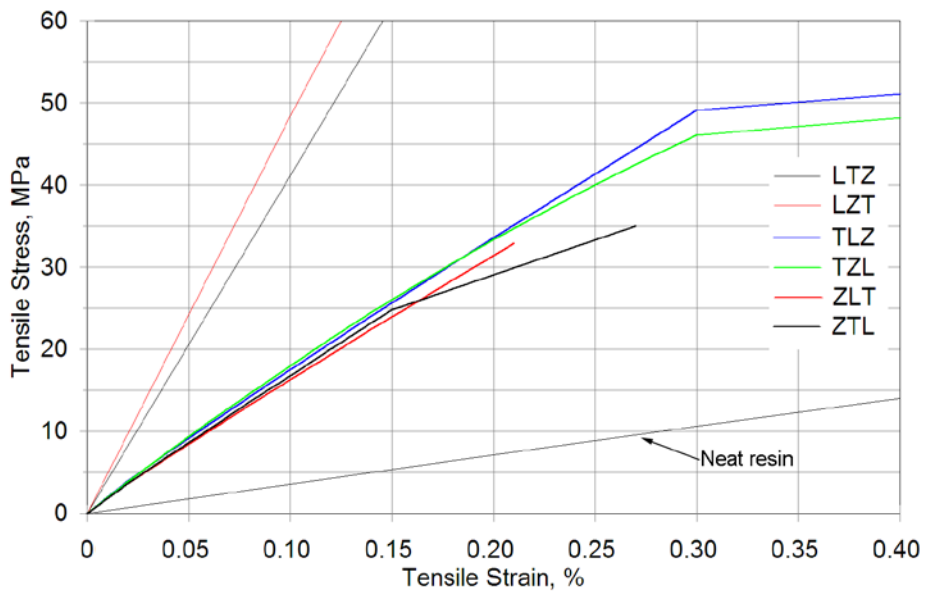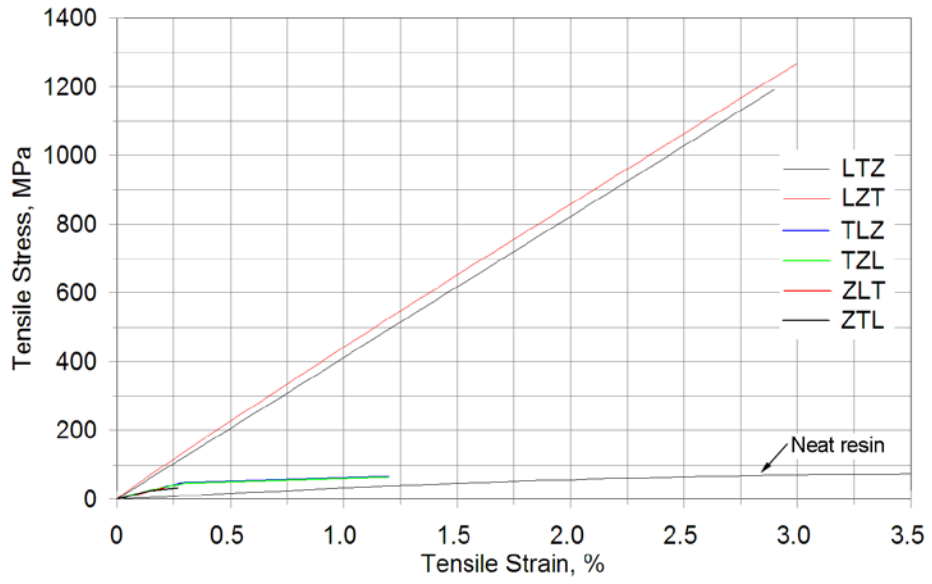
Figure 26a. Tensile Best Fit Stress-Strain Curves (Two Scales)

53
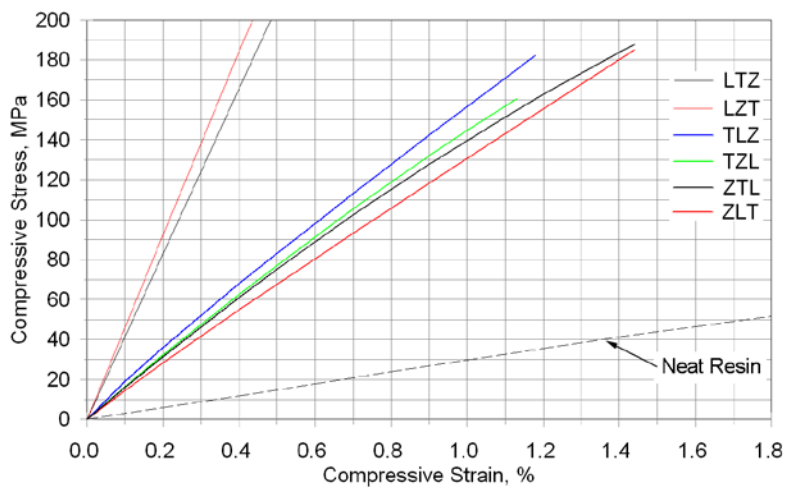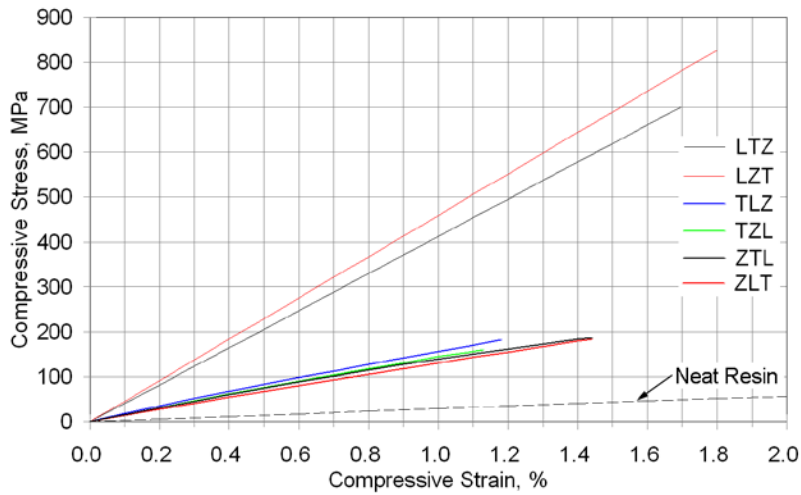
Figure 26b. Compression Best Fit Stress-Strain Curves (Two Scales)
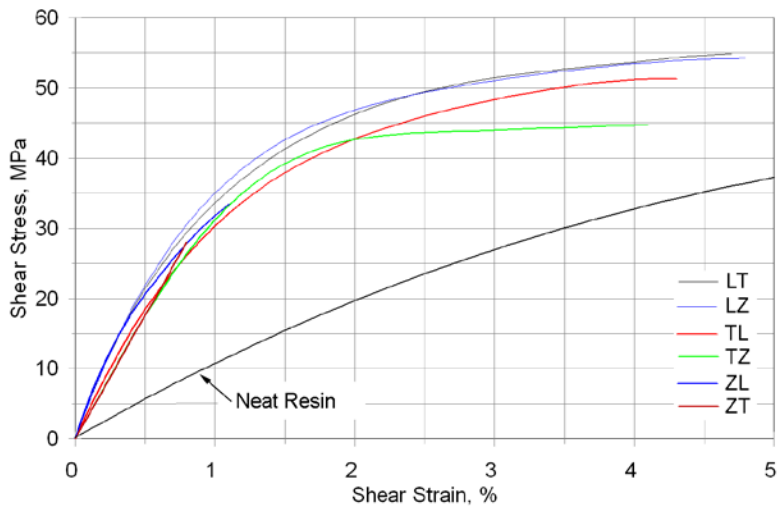
Figure 26c. Shear Best Fit Stress-Strain Curves

Figure 26 (a, b, c). Best fit stress-strain curves, curve fits in Table 6.

Table 6. Best fit stress-strain curve fits.

Tensile Stress-Strain Curve Best Fit Equations

Stress Direction	Coupon Orientation	Tensile Stress Best Fit Equations
L	LTZ	Stress (MPa) = 411.36(%strain)
L	LZT	Stress (MPa)= 441.67(%strain)$^{0.96}$
T	TLZ	Stress (MPa)=152.32(%strain)$^{0.94}$ for 0 – 0.3% strain Stress (MPa) = 19.53(%strain)+43.26 for 0.3 – 1.2% strain
T	TZL	Stress (MPa)= -130.83(%strain)^2 + 192.87(%strain) for 0-0.3% strain Stress (MPa) = 21.01(%strain)+39.79 for 0.3 – 1.2% strain
Z	ZLT	Stress (MPa)= 144.9(%strain)$^{0.95}$
Z	ZTL	Stress (MPa)= 153.06(%strain)$^{0.96}$ for 0-0.15% strain Stress (MPa) = 85.33(%strain)+11.96 for 0.15 – 0.27% strain
	Neat Resin	Stress (MPa)= 0.1448(%strain)^4 - 1.1038(%strain)^3 - 2.1641(%strain)^2 + 36.005(%strain)

Compression Stress-Strain Curve Best Fit Equations

Stress Direction	Coupon Orientation	Compressive Stress Best Fit Equations
L	LTZ	Stress (MPa) = 412.95(%strain)
L	LZT	Stress (MPa) = -23.901(%strain)^2 + 469.19(%strain)
T	TLZ	Stress (MPa) = 156.67(%strain)$^{0.9135}$
T	TZL	Stress (MPa) = -19.415(%strain)^2+164.07(%strain)
Z	ZLT	Stress (MPa) = 130.8(%strain)$^{0.951}$
Z	ZTL	Stress (MPa) = -20.956(%strain)^2+160.7(%strain)
	Neat Resin	Stress (MPa) = 0.1438(%strain)^4 - 1.6118(%strain)^3 + 2.1803(%strain)^2 + 29.189(%strain)

Shear Stress-Strain Curve Best Fit Equations

Stress Direction	Coupon Orientation	Shear Stress Best Fit Equations
LT	LTZ	Shear Stress (MPa) = -0.034(%strain)^6 + 0.5624(%strain)^5 – 3.7974(%strain)^4 + 14.06(%strain)^3 – 33.504(%strain)^2 + 56.362(%strain)
LZ	LZT	Shear Stress (MPa) = 0.0328(%strain)^5 - 0.7284(%strain)^4 + 6.1254(%strain)^3 - 25.332(%strain)^2 + 54.909(%strain)
TL	TLZ	Shear Stress (MPa) = -0.2925(%strain)^4 + 3.6075(%strain)^3 – 17.746(%strain)^2 + 44.791(%strain)
TZ	TZL	Shear Stress (MPa) = 0.0634(%strain)^6 -1.0294(%strain)^5 + 6.1689(%strain)^4 -15.38(%strain)^3 + 6.5506(%strain)^2 + 34.848(%strain)
ZL	ZLT	Shear Stress (MPa) = -19.231(%strain)^4 +56.534(%strain)^3 – 69.789(%strain)^2 + 64.356(%strain)
ZT	ZTL	Shear Stress (MPa) = 35.097(%strain)
	Neat Resin	Shear Stress (MPa) = 0.0023(%strain)^4 – 0.03(%strain)^3 – 0.5587(%strain)^2 + 10.608(%strain)

There do not appear to be significant differences between coupons taken from the 6-ply laminate (LTZ and TLZ) compared to those sectioned from the 80-ply laminate (LZT and TZL). The longitudinal tension coupons were each machined with a radius (Figure 15), while the other LTZ and TLZ coupons used as-molded surfaces. The fiber content was slightly higher for the 80-ply laminate (Table 4).
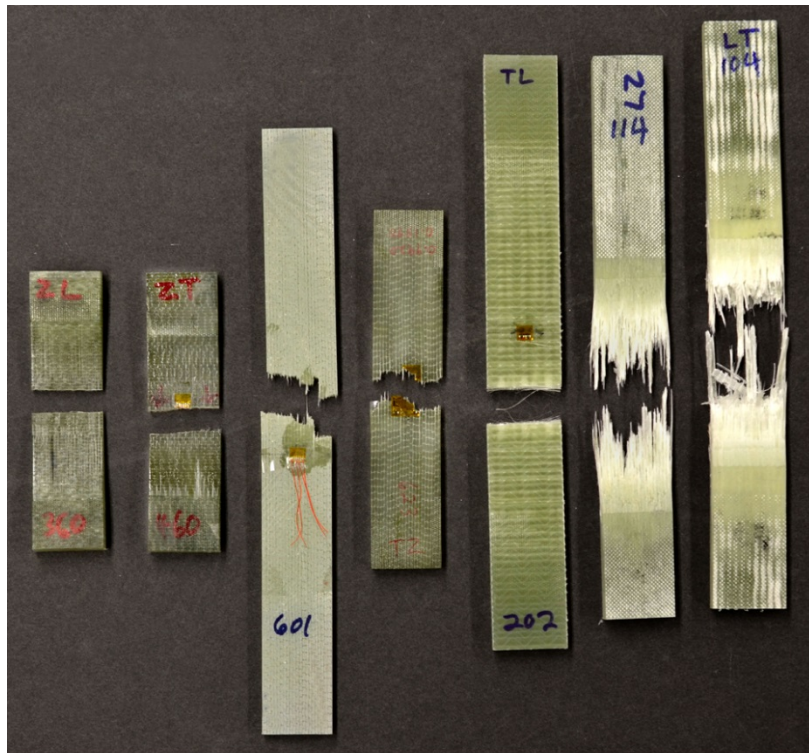
ZLT ZTL TZL TZL TLZ LZT LTZ
tapered

Figure 27a. Tensile Coupon Failure Photos
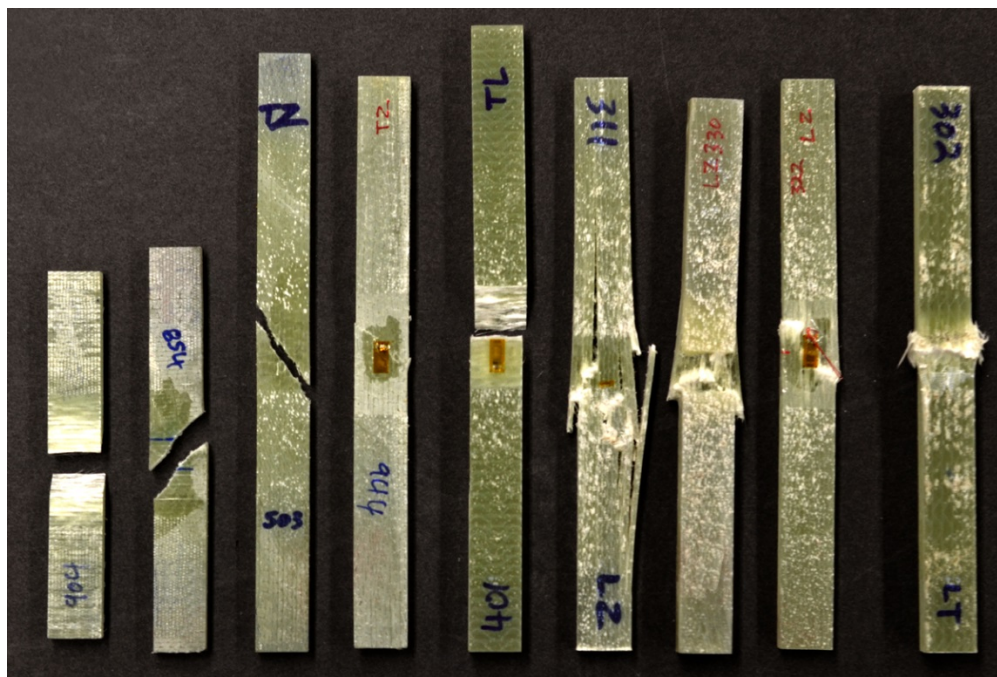
ZLT ZTL TZL TZL TLZ LZT LZT LZT LTZ
tapered   tabs tapered

Figure 27b. Compression Coupon Failure Photos
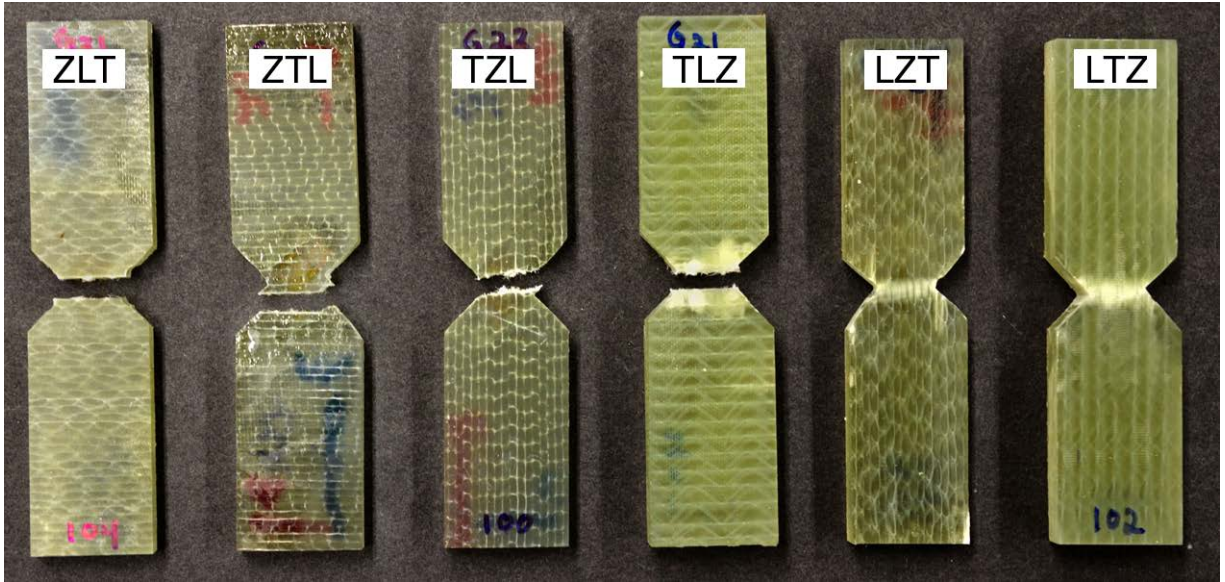
Figure 27c. Shear Coupon Failure Photos

Figure 27 (a, b, c). Failed Tension, Compression and Shear Coupon Photographs

$$\text{Stress (MPa)} = 411.36 \, (\% \text{ strain})$$
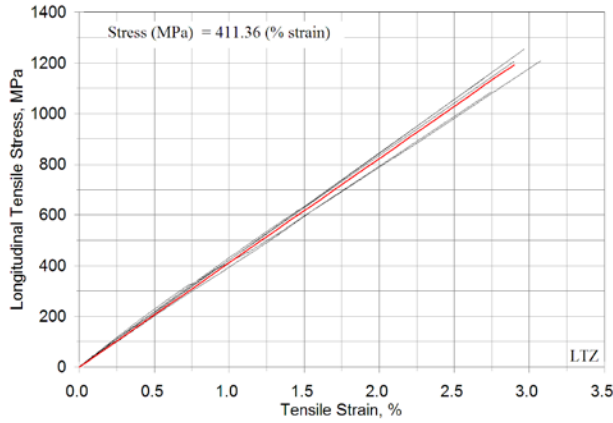
(28a) Longitudinal tension, LTZ orientation

$$\text{Stress (MPa)} = 441.67 \, (\% \text{ strain}^{0.96})$$
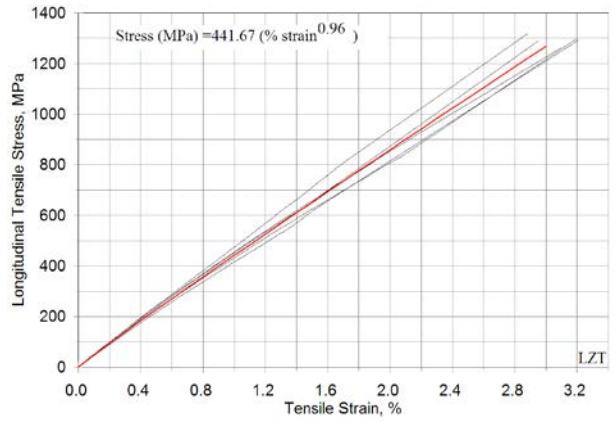
(28b) Longitudinal tension, LZT orientation

Fabric weft glass tow

$$0 - 0.3\% \text{ strain: Stress (MPa)} = 152.32 \, (\% \text{ strain}^{0.94})$$
$$0.3 - 1.2\% \text{ strain: Stress (MPa)} = 43.26 + 19.53 \, (\% \text{strain})$$
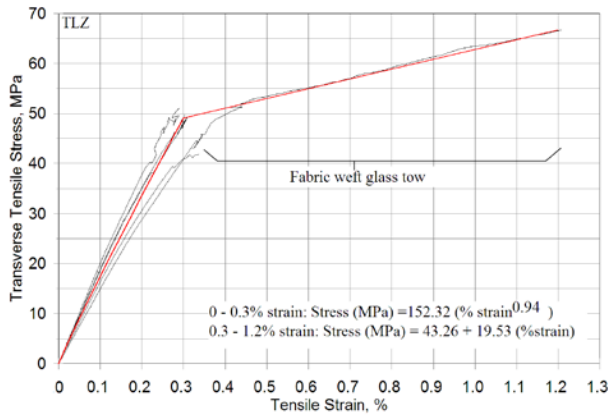
(28c) Transverse tension, TLZ orientation

Rectangular geometry
Thickness tapered
Best fit

Fabric weft glass tow

$$0 - 0.3\% \text{ strain: Stress (MPa)} = -130.83(\% \text{strain}^2) + 192.87 \, (\% \text{strain})$$
$$0.3 - 1.2\% \text{ strain: Stress (MPa)} = 21.01(\% \text{strain}) + 39.79$$
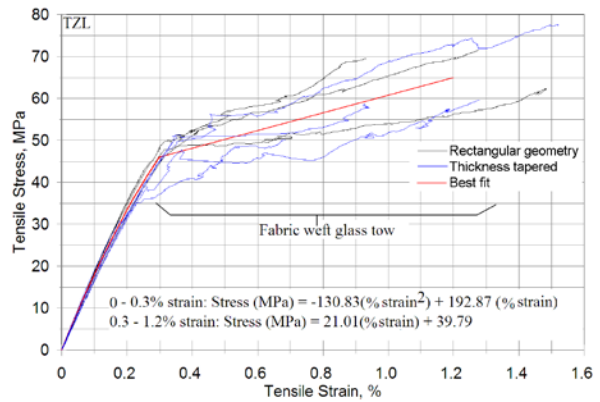
(28d) Transverse tension, TZL orientation

$$\text{Stress (MPa)} = 144.9(\% \text{ strain}^{0.95})$$
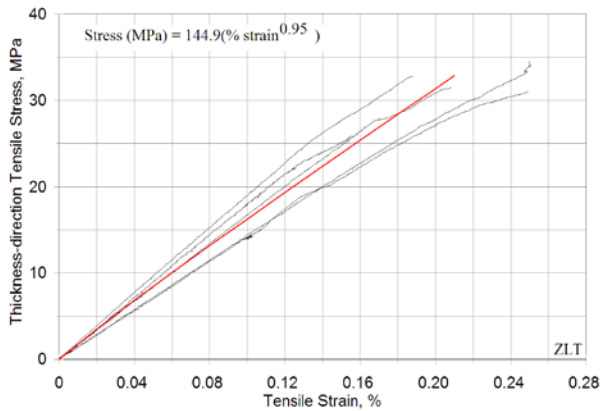
(28e) Thick dir. tension, ZLT orientation

$$0-0.15\% \text{ Strain: Stress (MPa)} = 153.06 \, (\% \text{ strain}^{0.96})$$
$$0.15-0.27\% \text{ Strain: Stress (MPa)} = 85.33(\% \text{strain})+11.96$$
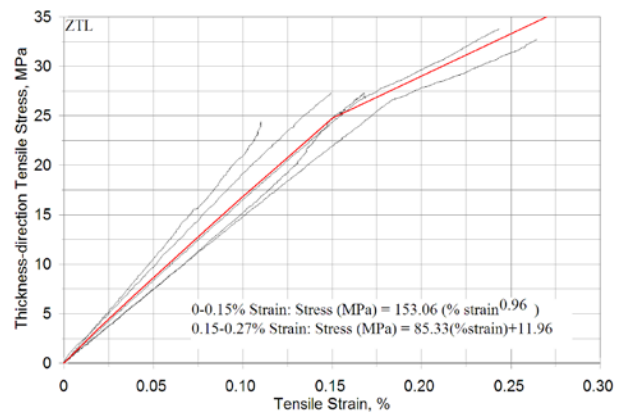
(28f) Thick dir. tension, ZTL orientation
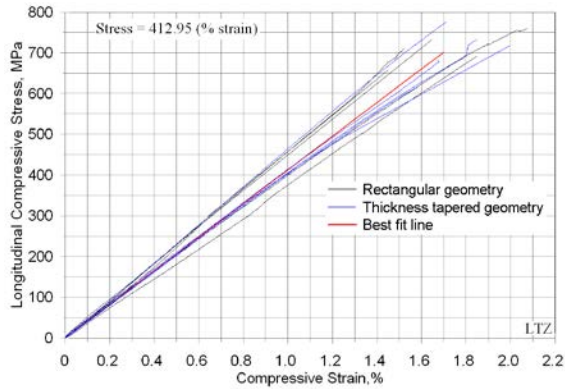
(28g) Long. compression, LTZ orientation
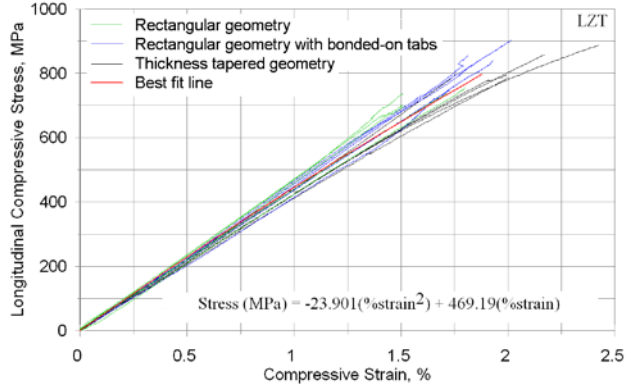
(28h) Long. compression, LZT orientation
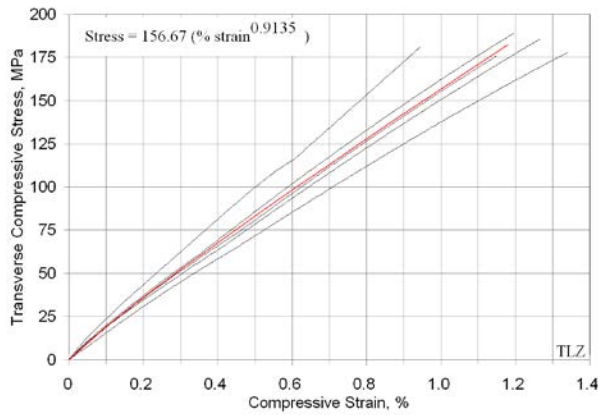
(28i) Transverse compression, TLZ orientation
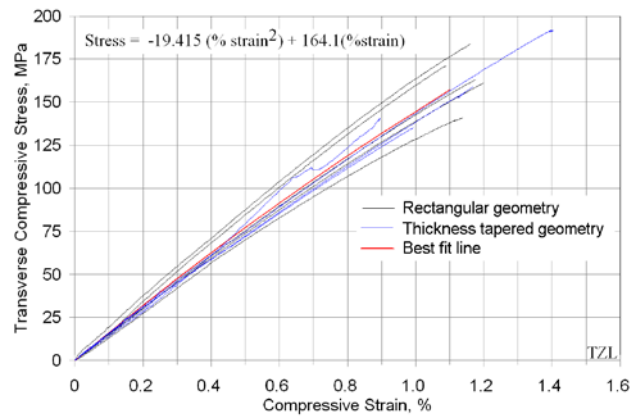
(28j) Transverse compression, TZL orientation
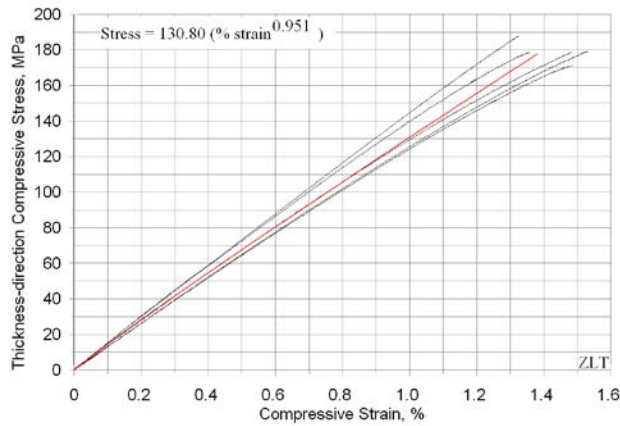
(28k) Thick dir. compression, ZLT orientation
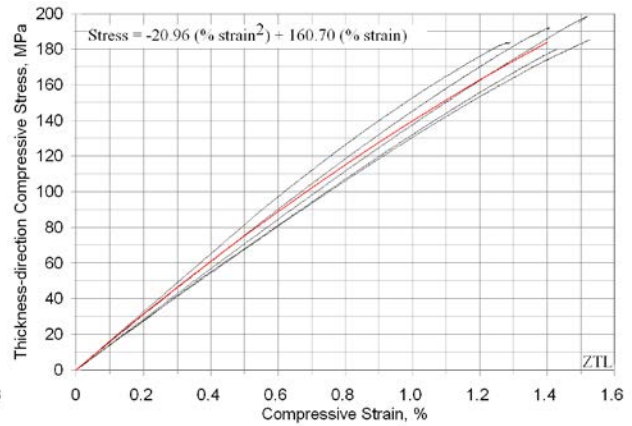
(28l) Thick dir. compression, ZTL orientation
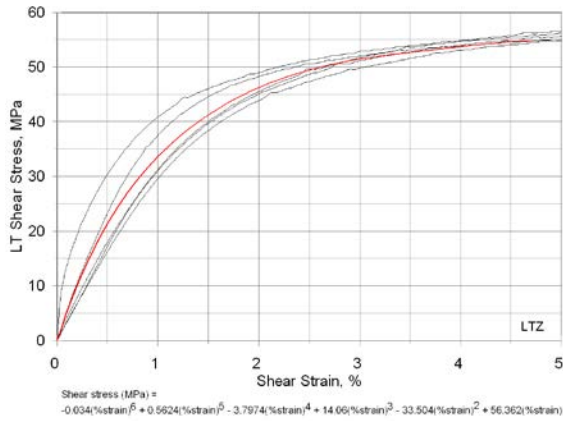
(28m) LT shear direction, LTZ orientation (28n) LZ shear direction, LZT orientation
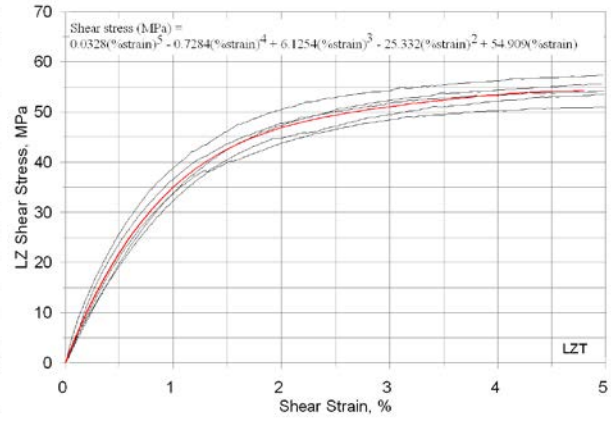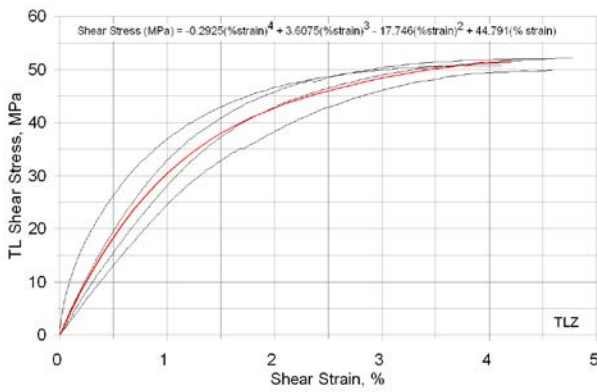
(28o) TL shear direction, TLZ orientation (28p) TZ shear direction, TZL orientation
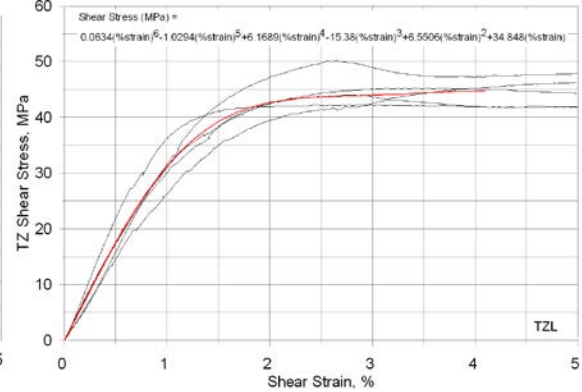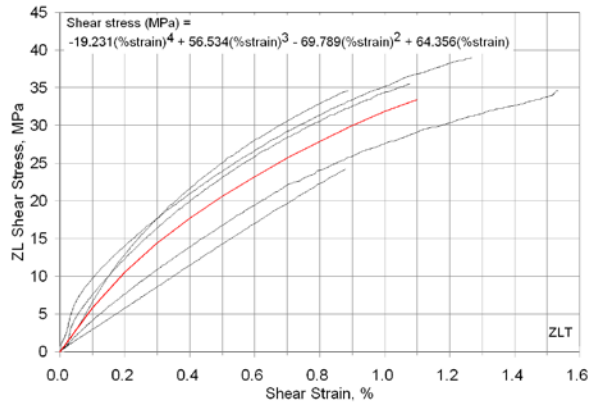
(28q) ZL shear direction, ZLT orientation   (28r) ZT shear direction, ZTL orientation
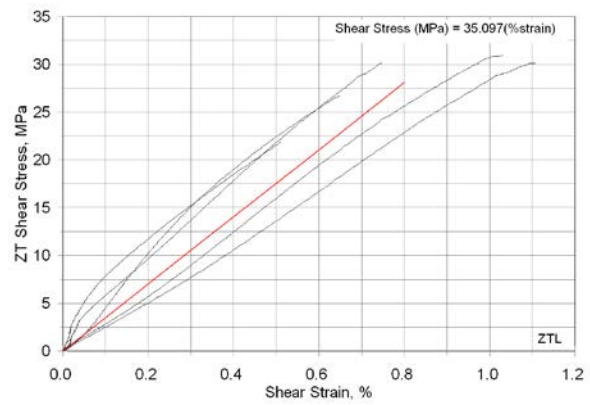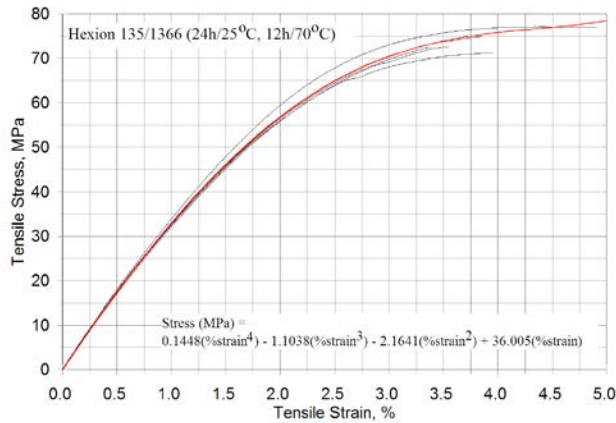
(28s) Neat resin tension
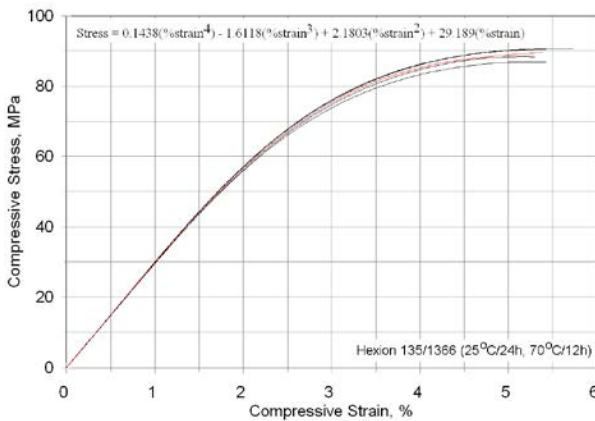
(28t) Neat resin compression
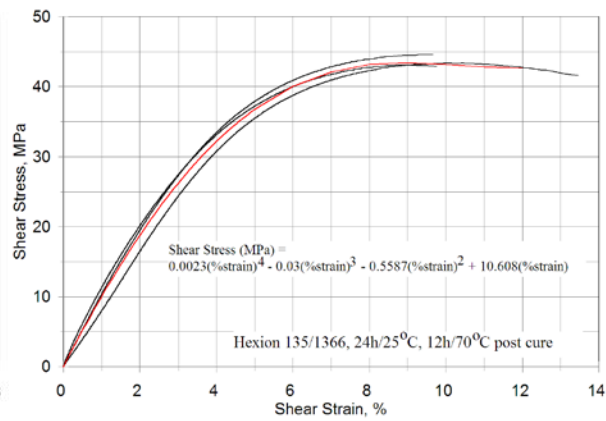
(28u) Neat resin shear

Figure 28 (a)-(u). Individual test stress-strain curves for various stresses and coupon orientations and neat resin loading cases, shown with best-fit curves (red).

4.2 LUR Tests

Figures 30-32 give Loading-Unloading-Reloading (LUR) data following Philippidis and Eliopoulos [25], using the loading sequence in Figure 16. The LUR data, with loading and unloading to successively higher loads, indicate that the unloading response is at a similar modulus to the initial loading curve, but with an associated permanent strain. These results are applicable in various materials models which require unloading. The data are represented in both tension in coupon (x, y) global coordinates (top of Fig. 30) and shear in local material coordinates. The tensile performance of DB fabric laminates loaded in the axial (0°) direction is of interest since it must perform adequately in skin areas which see maximum axial blade strains, while the shear properties are critical in resisting blade web shear and torsion. The separate $+45^O$ and -45° plies of biaxial fabrics are stitched together, so the individual ply elastic constants are not generally available. Here, the shear properties are calculated following the ASTM D3518 test standard using UD fabric elastic constants for similar fiber contents, Table 5.

61

A comparison of typical tensile and compressive stress-strain curves for $\pm 45^O$ laminates in this study is given in Figure 31 (left), and LUR diagrams for compression are given in Figure 31 (right). The shear diagram based on compression tests showed slightly higher stiffness, consistent with the higher compressive stress-strain curve which appears to result from the small transverse compression stress under compressive loading (at 0°). The results in Table 7 show reduced stiffness in the low strain range for increasing load steps for each loading scheme. Thus, the prior loading history steadily reduces the slope of the subsequent load-strain loop.

Reversed loading LUR sequences were carried out in two orders: tension then compression (reverse1) and compression then tension (reverse2). Figure 32 gives the response for the reverse1 sequence in terms of strain-time (left) and stress-strain for typical loops (right).
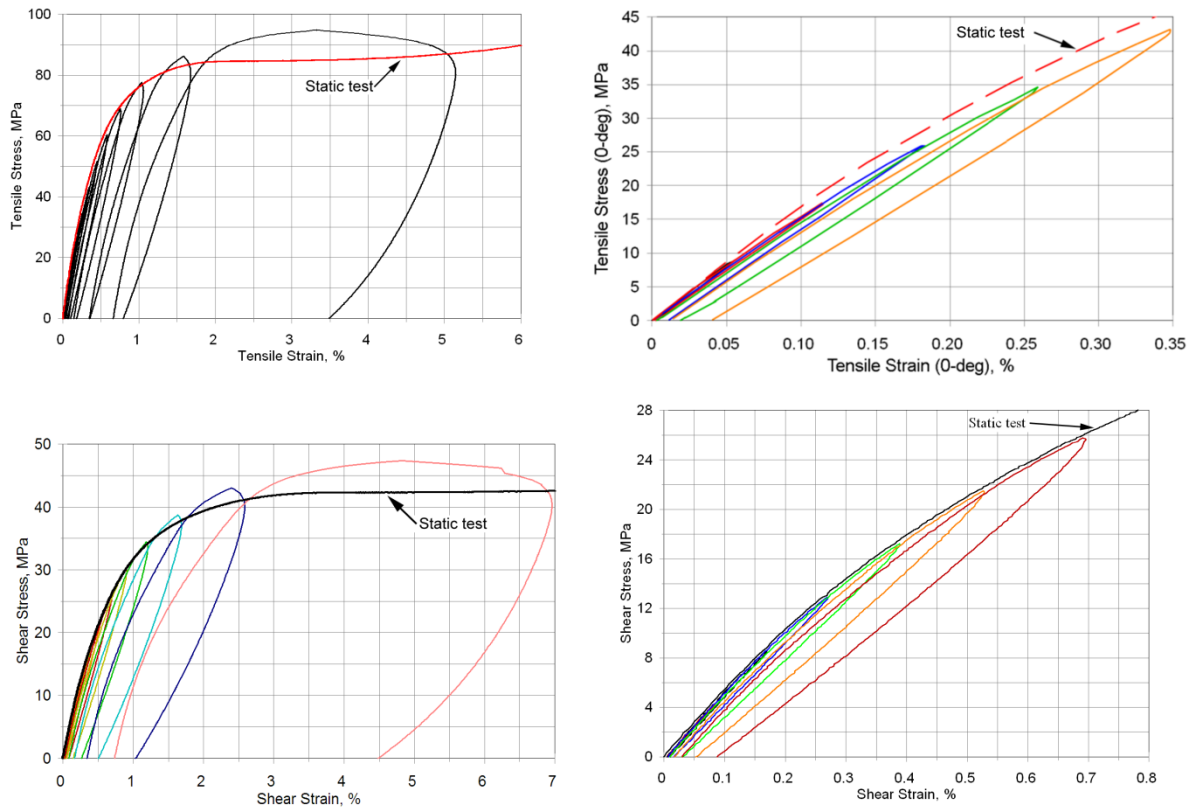
Figure 29. Tensile loading LUR results in terms of tensile stress and strain in the 0° direction (top left: full scale; top right: first few cycles magnified) and the corresponding calculated shear LUR curves in 1-2 coordinates (bottom).
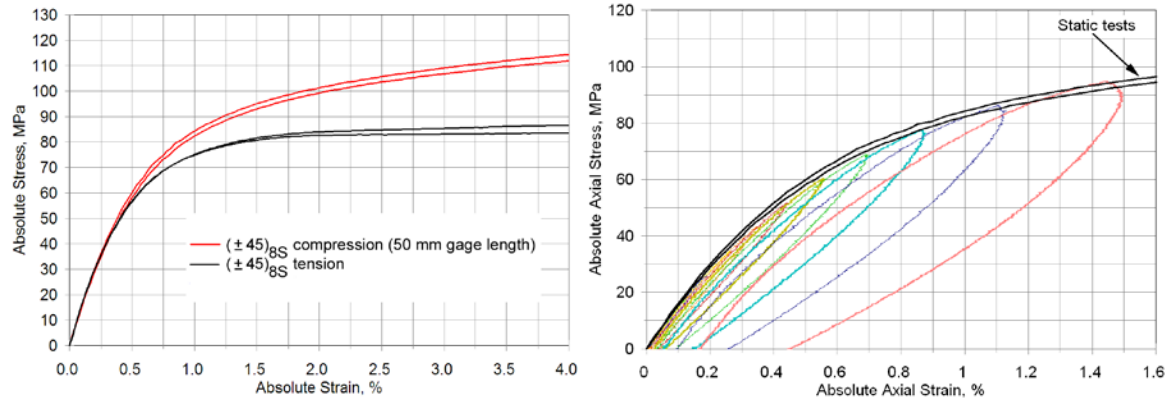
Figure 30. Comparison of typical ±45° stress-strain curves in tension and compression (left); compression LUR results (right).
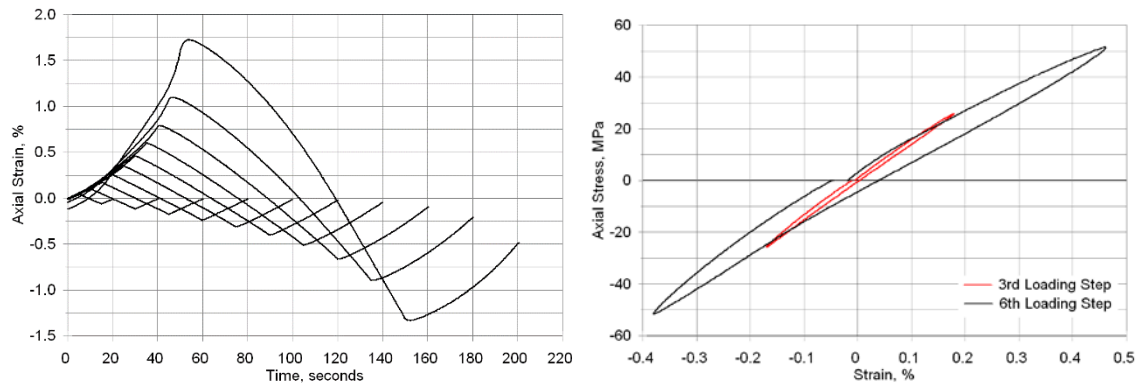
Figure 31. Reversed loading LUR results; left: strain vs. time at each loading step; right: stress-strain loops at the third (±25.8 MPa) and sixth (±51.6 MPa) steps.

Table 7. Low strain (0 to 0.2% strain) elastic modulus of loading and unloading steps for each LUR load case.

Max. Stress, MPa	Modulus (0 – 0.2%) of LUR steps, GPa						
	Tension		Compression		Reversed		
	up ramp	down ramp	up ramp	down ramp	up ramp	down ramp	up ramp
8.62	15.60	15.30	15.28	15.27	18.83	15.70	16.20
17.2	15.24	15.26	14.93	14.97	15.09	15.40	15.98
25.9	14.58	14.66	14.22	14.47	14.16	14.65	16.04
34.5	14.26	13.66	14.26	13.67	13.46	13.76	15.40
43.1	14.05	12.73	14.14	12.85	12.78	12.71	14.28
51.7	14.08	12.73	14.15	12.85	12.78	12.69	14.30

Reversed loading data are given in more detail in Figures 33 and 34. Data from face-mounted extensometer and bonded strain gages are compared in Figure 33 for the reverse1 sequence, full data (top) and expanded lower strain data (bottom). The results are similar for both types of

instrumentation. Other reverse1 test coupons used strain gages on both faces (averaged) with no extensometer. No elastic buckling response was found. Reverse2 results are given in Figure 33 for the strain gage and extensometer combination, as well as a comparison of actuator position from the actuator LVDT. Some variance of the strain gage data relative to the extensometer/stroke results is evident in compression at higher loads. This may reflect local response near the smaller (8 mm long) strain gages or some curvature of the coupons. The relative softening and strain increase on the tensile side (load control, see Section 3) is evident in the individual loadings at higher strains in Figure 34. Figure 35 (a)-(j) give measured axial strain-time curves and stress-strain loops, and calculated shear stress-strain loops for all four loading schemes: tension, compression, reverse1 and reverse2. The most notable trend outside of increasing nonlinearity at higher stresses is that the reverse2 scheme (compression followed by tension) is stiffer than the others on the compression side.
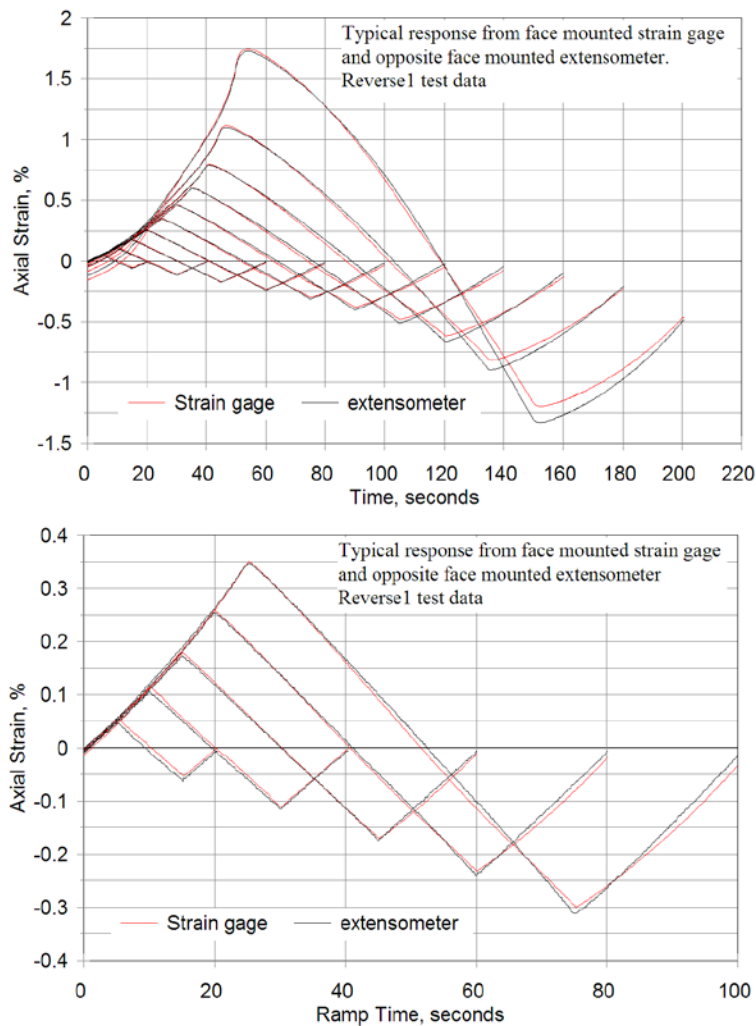
Figure 32. Strain-time traces for the reverse1 loading sequence comparing extensometer and strain gage readings for the same test; full loading range (top) and magnified range (bottom).

64
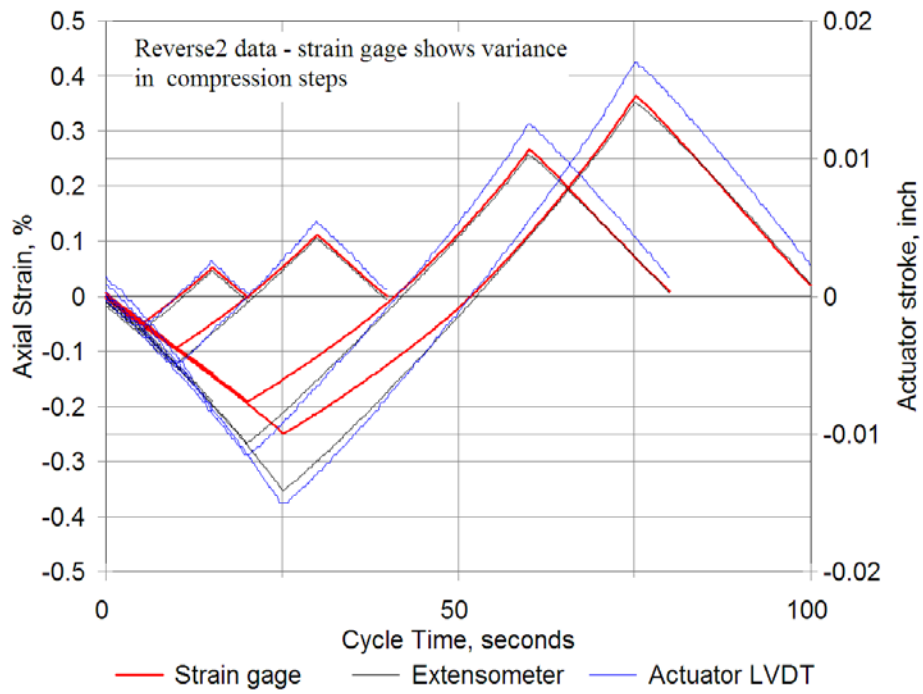
Figure 33. Reverse2 LUR results .
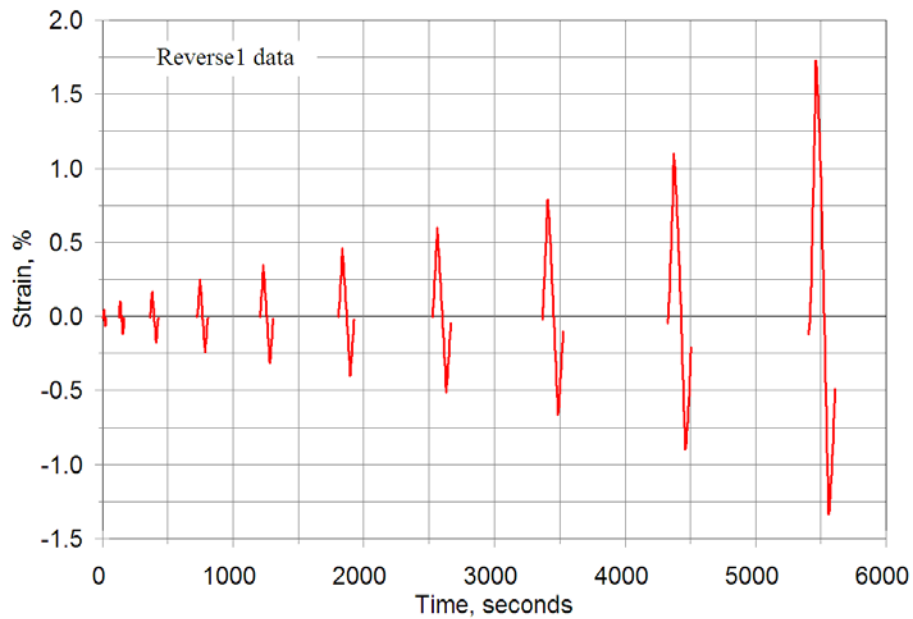
Figure 34. LUR strain-time response for each loading step for four reverse1 coupons.

65
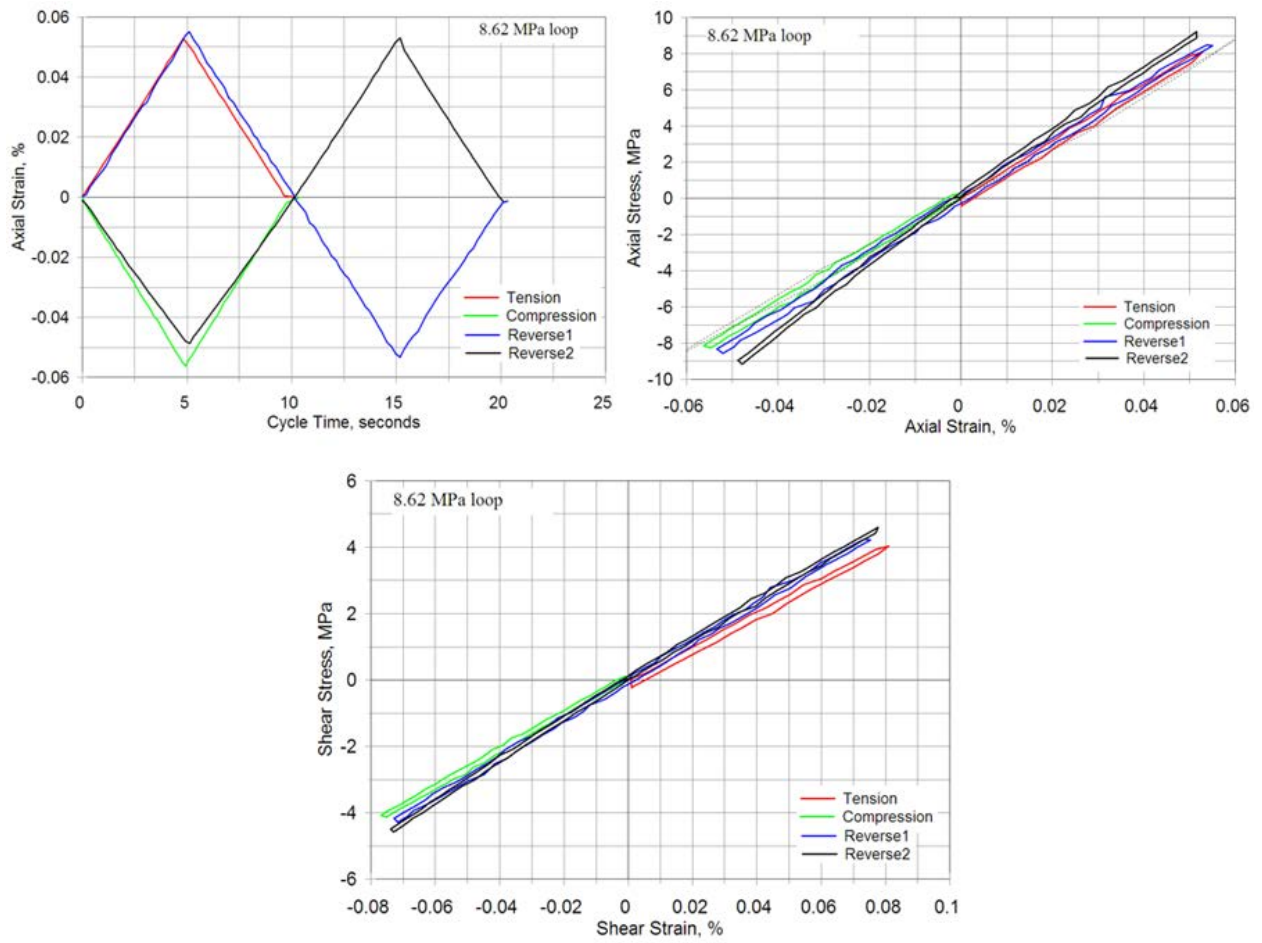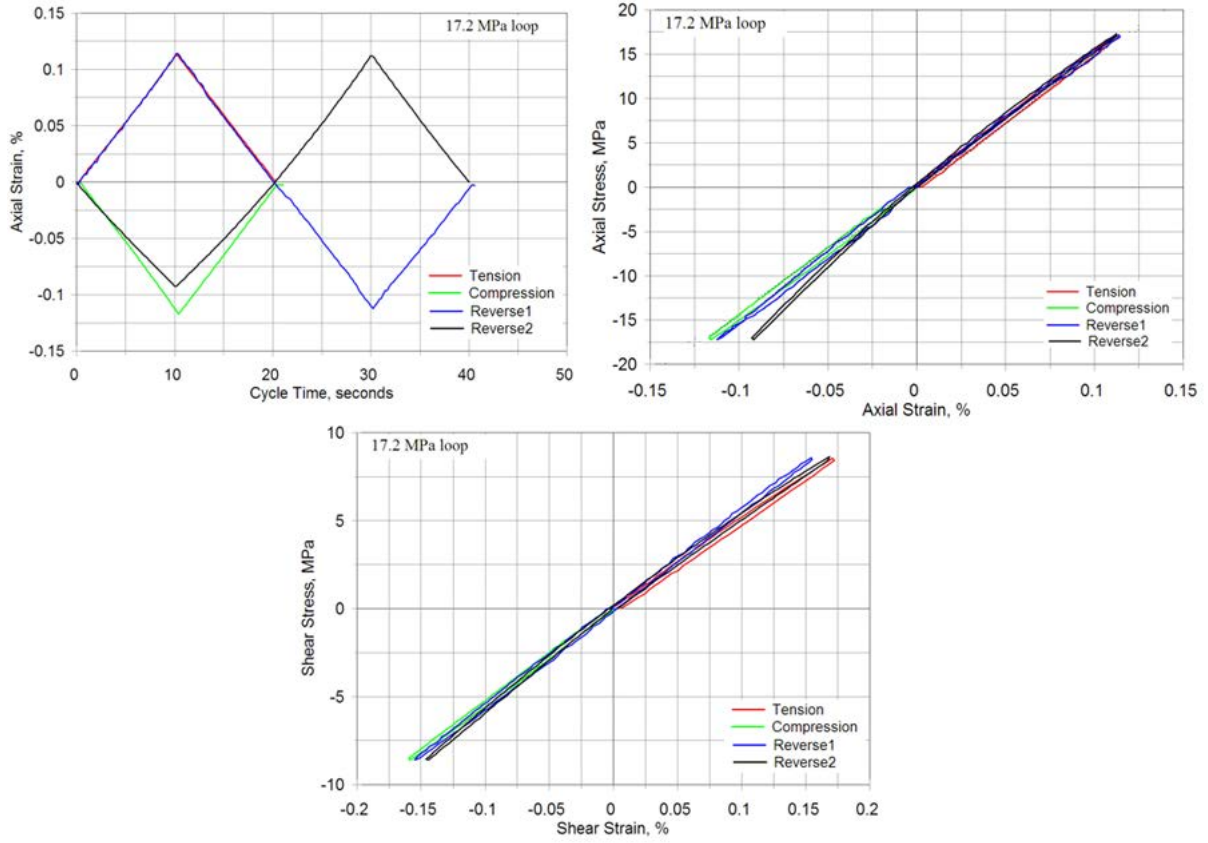
Figure 35(a). 8.62 MPa

Figure 35(b). 17.2 MPa
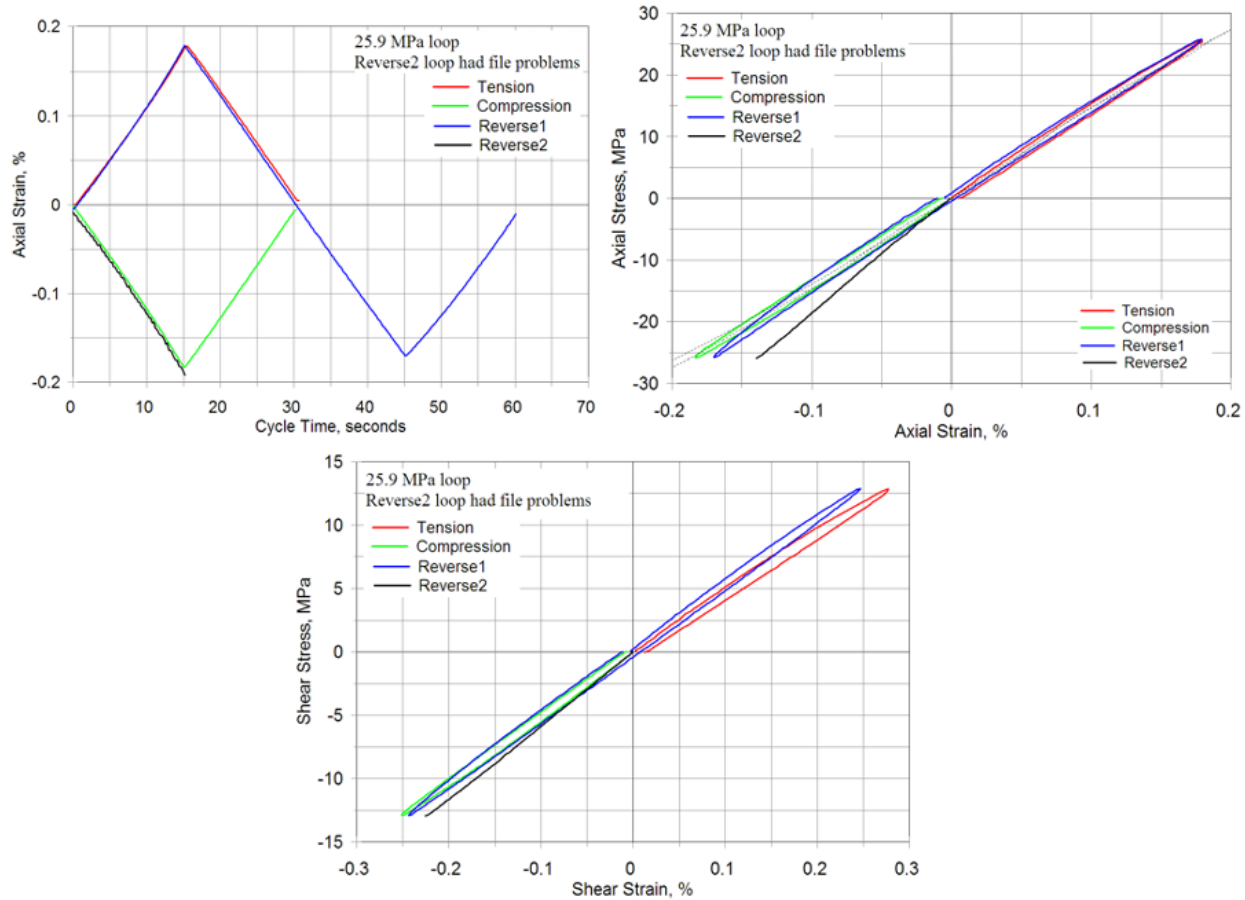
Figure35(c). 25.9 MPa
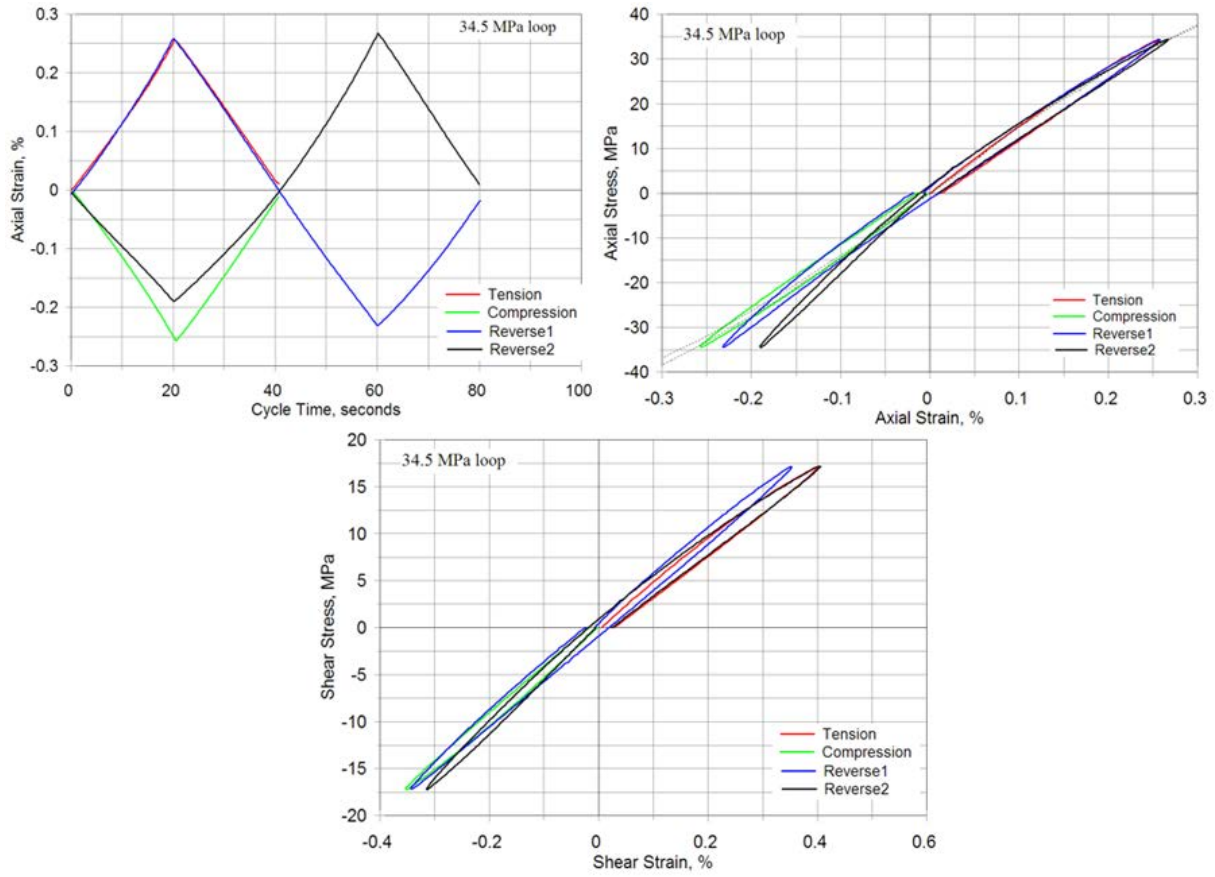
Figure35(d). 34.5 MPa
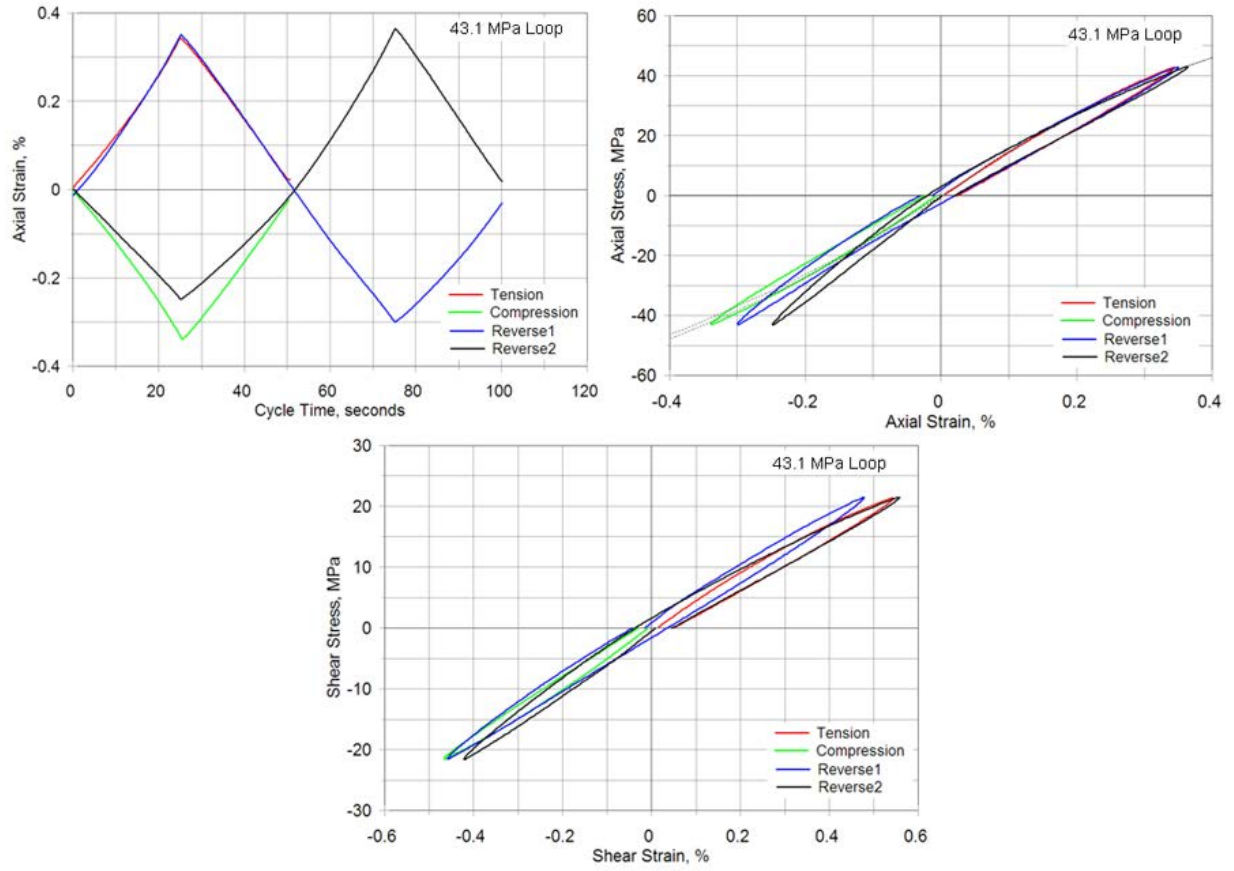
Figure 35 (e). 43.1 MPa
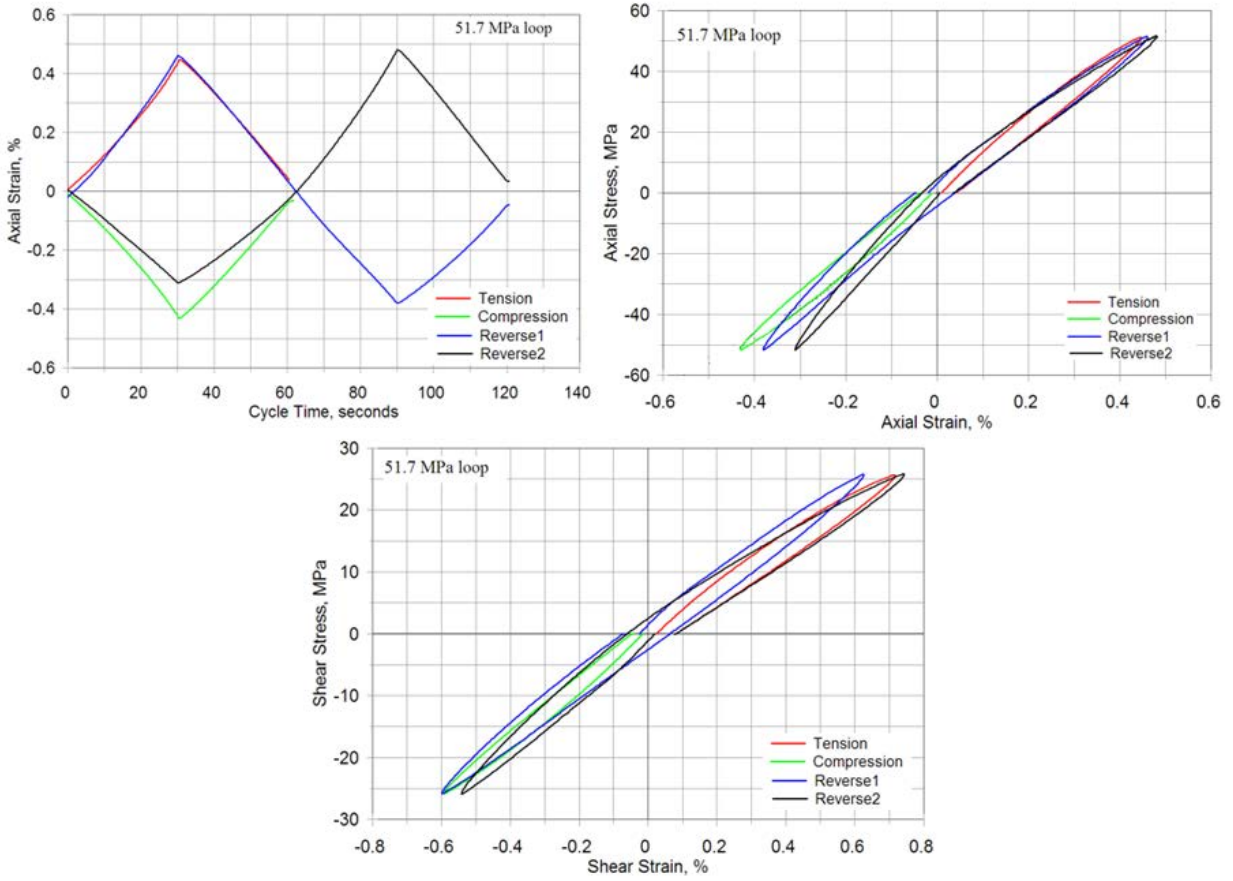
Figure 35(f). 51.7 MPa
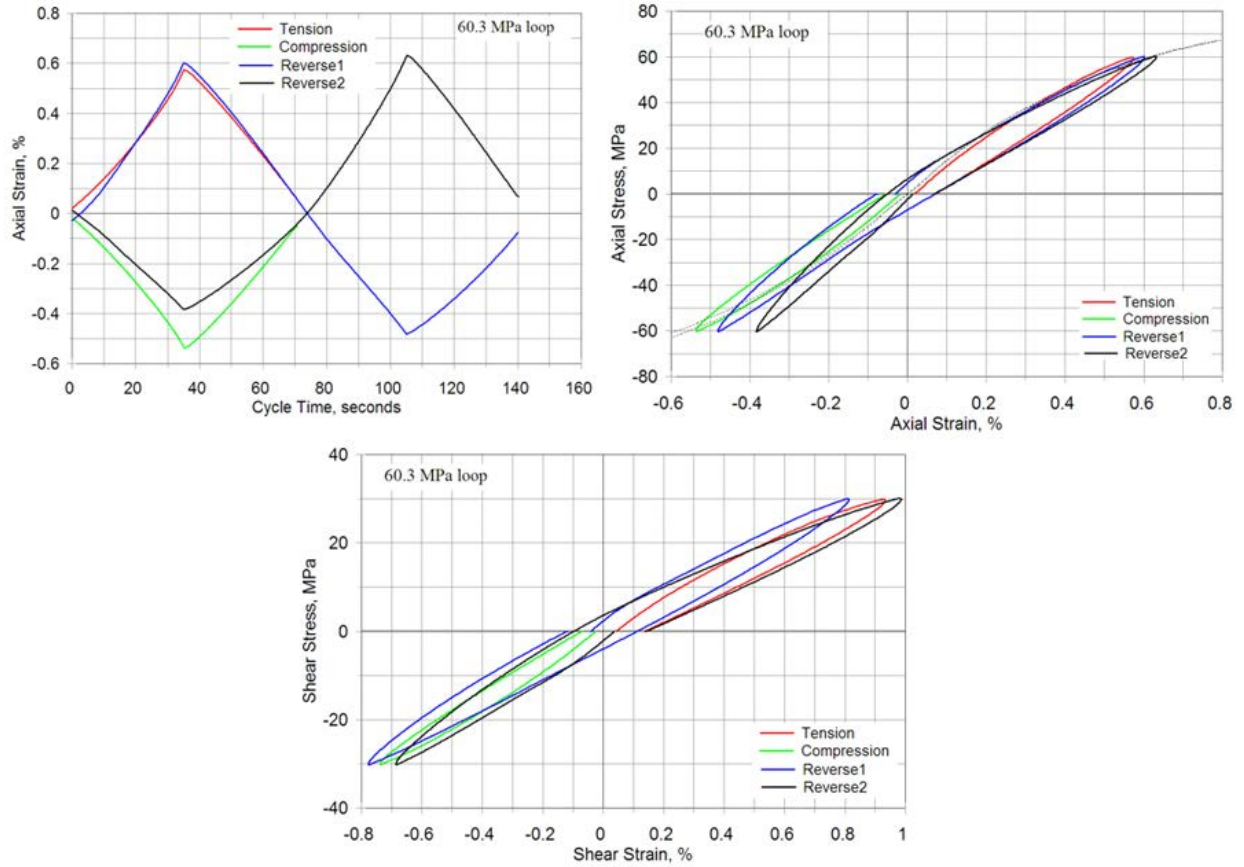
Figure 35(g). 60.3 MPa
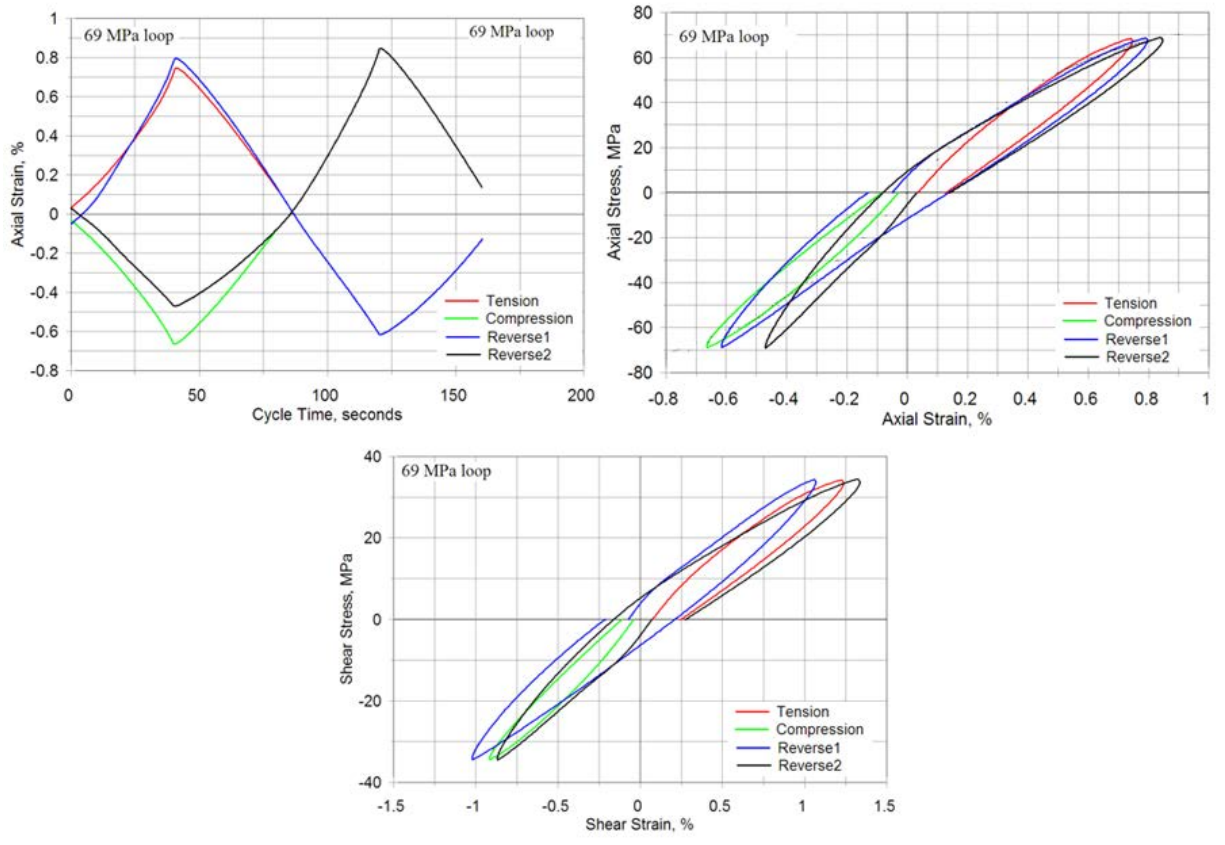
Figure 35(h). 69 MPa
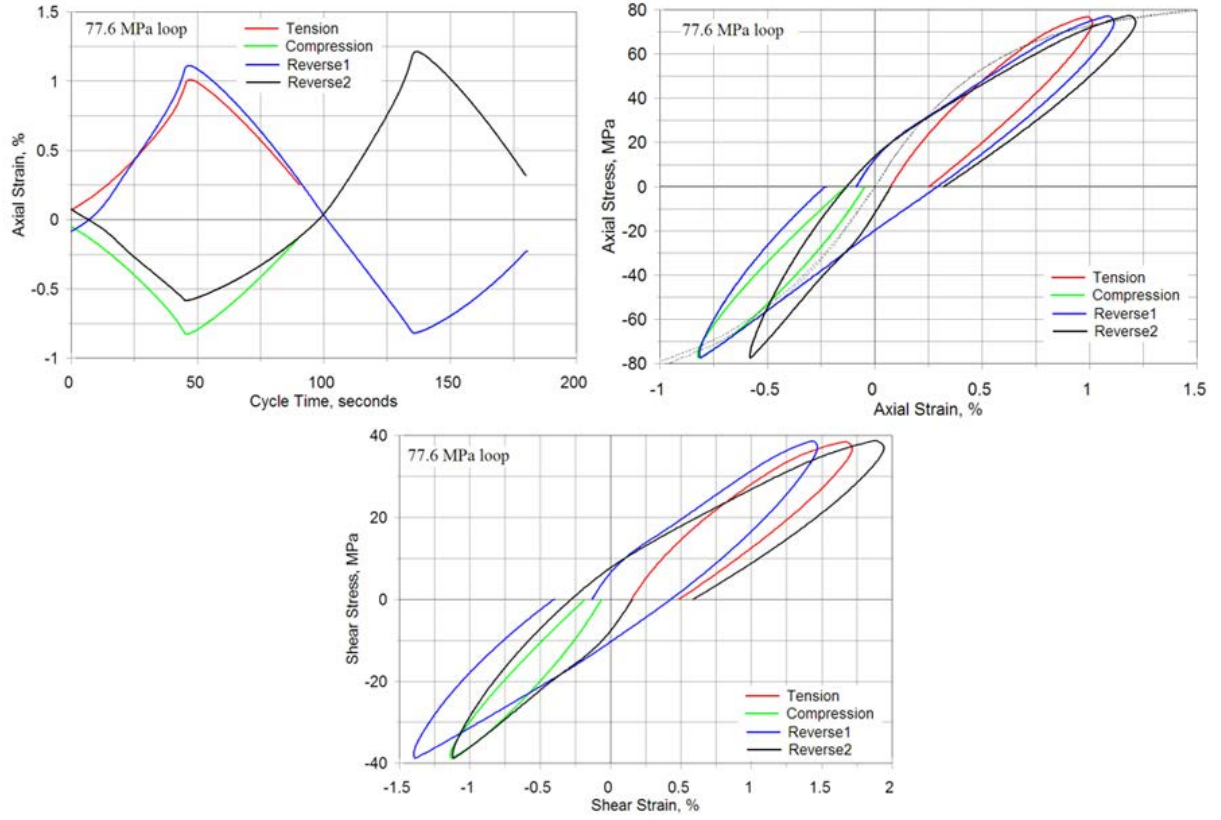
Figure 35(i). 77.6 MPa
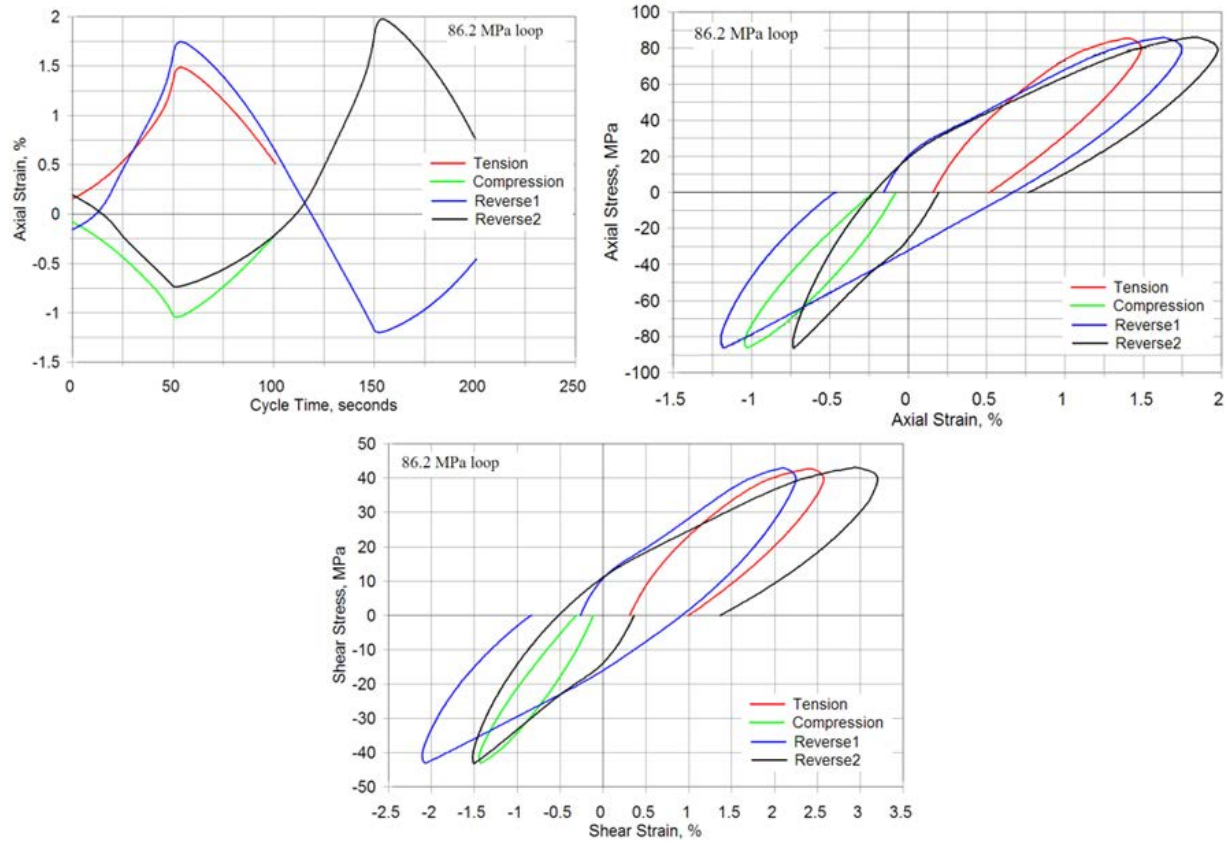
Figure 35(j). 86.2 MPa

Figure 35 (a)-(j). Axial strain-time, axial stress-strain and shear stress-strain data for maximum stresses 8.6 MPa to 86.2 MPa, four LUR loading schemes.

Intentionally Left Blank

5. Laminate Tensile Fatigue: Fabric Architecture, Aligned Strands and Resin Effects

5.1 Overview

Section 2.2.4 and Figures 4-6 summarize earlier studies of the effects of laminate construction, loading conditions and resin type on fatigue performance [1,2]. This chapter explores unidirectional ply tensile fatigue resistance in greater detail, including the effects of UD glass fabric structure, fiber alignment and resin.

5.2 Effects of Fabric Construction and Resin on Blade Laminates

The tensile fatigue resistance for laminates with a range of typical wind blade reinforcing fabrics and resins has been reported in recent years [2,16]. The tensile segment of fatigue cycles for various R-values (R = minimum load/maximum load) represents the most critical fatigue response for glass fiber laminates. Infused laminates with stitched fabrics and epoxy or polyester resins have shown significantly better performance for epoxies in terms of fatigue strains and fatigue exponents. Particular resins show consistent fatigue resistance for a range of generally similar UD reinforcing fabrics in UD and multidirectional (MD) laminates.

A pronounced effect of the type of resin on the fatigue resistance has been evident for epoxy, vinyl ester and polyester resins [2,14,16,21]. Figure 36 gives a comparison of the maximum tensile strain which can be withstood for one million cycles for typical epoxy (EP) and unsaturated polyester (UP) resins in the database, under tensile fatigue loading, R = 0.1. Various vinyl ester resin results are intermediate between epoxy and polyester. These trends are for UD fabric laminates, MD laminates containing UD and biax fabrics (±45° strands plus mat and/or transverse strand backing), triax fabrics containing UD and biax layers stitched together (about 50% UD) and biax fabrics only. Earlier study of lower fiber content laminates typical of hand layup fabrication, with weft UD fabric having no backing, showed very little effect of resin type on fatigue resistance [16].
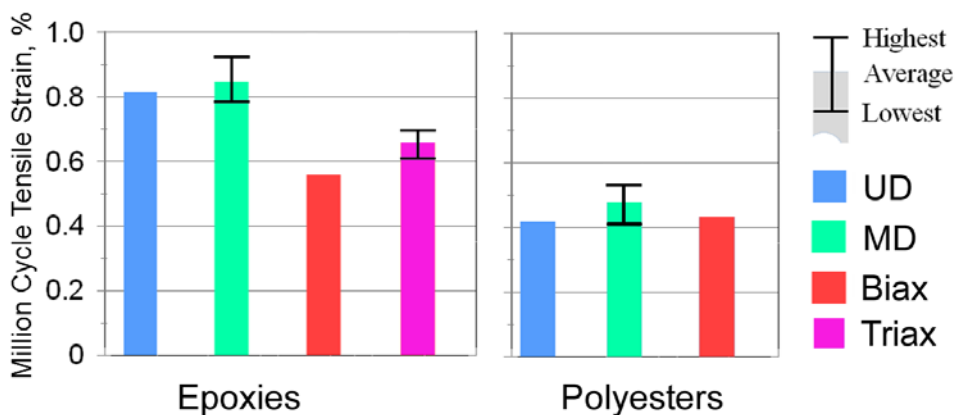
Figure 36. Comparison of million cycle fatigue strains for typical EP and UP resin laminates.

5.3 Aligned Strand vs Fabric Laminates

The sensitivity to fabric structure of the UP and VE resin infused UD laminates is evidenced in Figure 37 by coupon fatigue failures associated with the transverse backing strands, and by microscopy observation of cracking along these strands, apparently initiating at the stitching, and then failing the primary 0° strands. In a series of specialized experiments, the transverse backing strands in fabric H were removed prior to infusion. Laminates fabricated and tested with transverse strands removed were tested [14,21], and demonstrated that the epoxy UD laminates, which typically do not fail at the transverse backing strands (but do show cracking there), show no improvement when the strands are removed. However, the UP laminates improve significantly in fatigue resistance when the transverse strands are removed.

The aligned strand (AS) reinforced (Figure 13) laminate structure serves as a baseline for fatigue resistance in the absence of complications from fabric structure. Stress and strain vs. cycles to failure tensile fatigue results are compared in Figure 38 for AS and fabric H reinforced laminates for three resin types (Table 3). Both laminate types contain the same UD strands, PPG 2400 Tex with Hybon 2026 finish. The fabric data are typical of data for other fabrics of similar construction for the epoxy resin. (Note that epoxies EP1 and EP5 differ only slightly; both have RIMR 135 resin, but the EP1 hardener is RIMH 1366 while the EP5 hardener is very similar, RIMH137.)

The data in Figure 38 establish the following [14,16,17]:
1. Infused laminates with only aligned strand for reinforcement significantly out-perform laminates containing typical fabric (Figure 1) in terms of both stress and strain over the entire cycle range.
2. The epoxy resin significantly out-performs the other two resins with fabric reinforcement, but the vinyl ester is similar to epoxy for AS reinforcement.

Fiber contents are about 64-68% by volume for the AS laminates, 54-58% for the fabric laminates. Additionally, fabric H is only 92% 0° strand, the remainder being backing and stitching (Table 2). These factors contribute to an approximately 27% higher axial fiber content for the AS structure than for the fabric. Higher axial fiber volume fractions are possible for the AS laminate structures, raising the modulus and tensile strength proportionally.
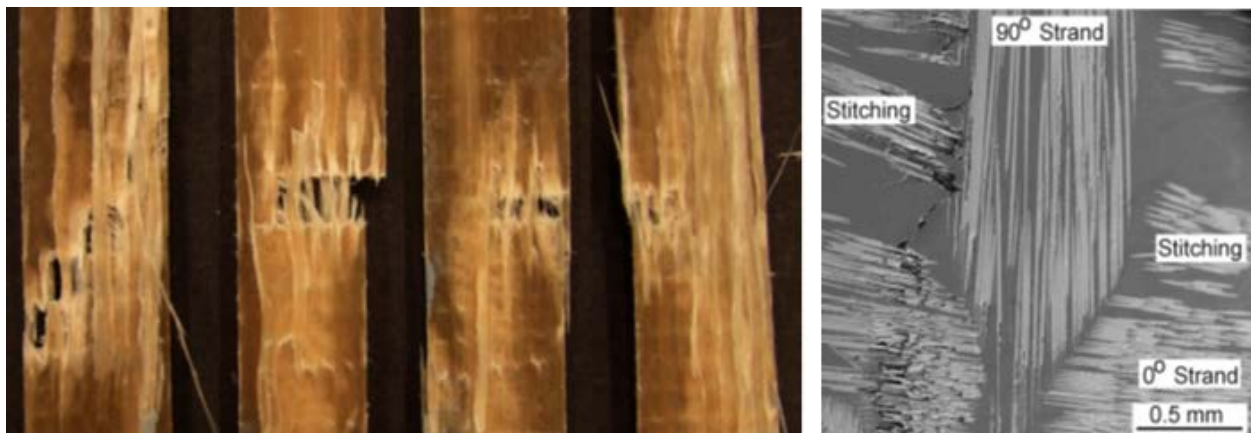
Figure 37. Cracking along transverse (90°) backing strands of UP5/fabric laminate; left: failed coupons; right: micrograph of crack following the backing strand, and failing the 0° strand.

Symbol	Resin	Lay-up	Best Fit Equations	
			Stress	Strain
■	EP5	AS	$1573(N)^{-0.0716}$	$3.58(N)^{-0.079}$
■	VE4	AS	$1952(N)^{-0.088}$	$4.03(N)^{-0.086}$
■	UP5	AS	$2153(N)^{-0.123}$	$6.33(N)^{-0.151}$
□	EP1	$(0)_2$	$1259(N)^{-0.088}$	$4.33(N)^{-0.115}$
□	VE4	$(0)_2$	$2266(N)^{-0.170}$	$5.67(N)^{-0.172}$
□	UP5	$(0)_2$	$1715(N)^{-0.173}$	$4.22(N)^{-0.173}$
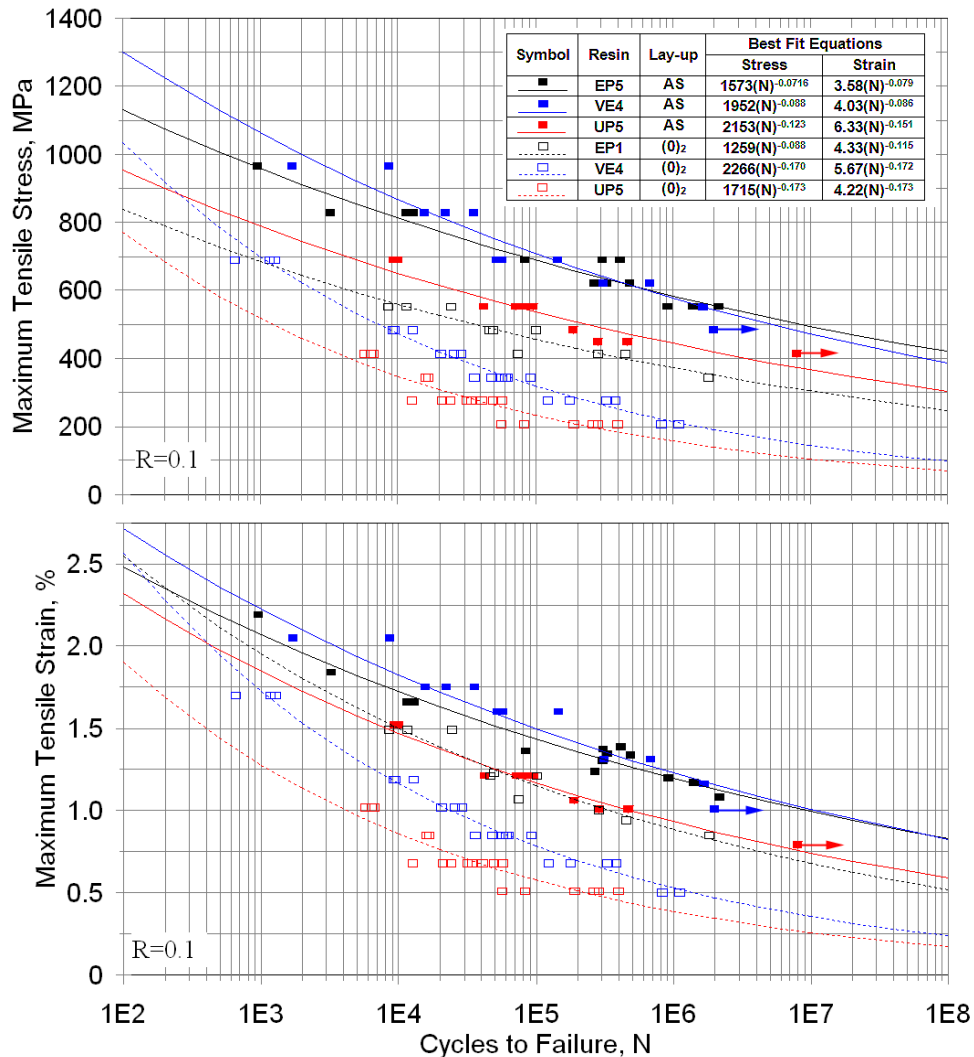
Figure 38. Comparison of stress and strain fatigue trends for aligned strand and $(0)_2$ fabric H based laminates for epoxy (EP1 and EP5), vinyl ester (VE4) and polyester (UP5) resins.

5.4 Resin Effects on UD Fabric Efficiency

The results in Figure 38 demonstrate the superiority of aligned strand reinforcement relative to fabric reinforcement. Fatigue stresses are more than double at the same lifetime for AS vs. fabric for the UP and VE resins; for the EP resin, stresses are increased on the order of 40 to 50%. These differences are due in part to overall fiber content differences, as fiber packing is improved for AS laminates. A second factor is the difference in fiber content in the axial, 0° direction, as the transverse and mat backing strands do not contribute significantly to strength properties in the axial (load) direction. Table 8 gives the overall and 0°-direction fiber contents. The substantial differences between 0° fabric V_f and AS V_f help to explain the observed property differences.

A simple definition of fabric efficiency which reflects the actual laminate properties obtained is the ratio P_F/P_{AS}, where P_F is the property of the fabric laminate and P_{AS} is the property of the AS laminates without the fabric structure. The ratio for the 0° V_f ranges from 0.76 to 0.83. The modulus ratios are slightly higher, reflecting the backing contribution to increasing the modulus relative to pure resin. The UTS and fatigue parameters fall below the ratio for 0° V_f, indicating more than proportional decrease for these fabric properties with fiber content, particularly for the UP and VE resins.

Table 8. Fabric Efficiency Relative to Aligned Strands

Resin	EP1 /EP5[1]	VE4	UP5
Fiber Volume Fraction, V_f			
AS Laminates	0.64	0.66	0.68
Fabric Laminates	0.58	0.55	0.58
0° V_f, Fabric Laminates	0.53	0.50	0.53
0° Direction Fabric Efficiency: P_F/P_{AS}			
0° V_f	0.83	0.76	0.78
Modulus, E	0.88	0.85	0.81
UTS	0.73	0.68	0.62
10^6 cycle stress	0.64	0.37	0.40
10^6 cycle strain	0.73	0.43	0.49
P_F/P_{AS} Adjusted for 0° V_f : (P_F/P_{AS}) (AS V_f /Fabric 0° V_f)			
Modulus, E	1.06	1.12	1.04
UTS	0.88	0.89	0.79
10^6 cycle stress	0.77	0.49	0.51
10^6 cycle strain	0.88	0.49	0.63

[1]EP1 for fabric laminates, EP5 for AS laminates

Clearer relationships emerge if the fabric efficiency is adjusted for the 0° V_f difference by considering the parameter (P_F/P_{AS}) (AS V_f/Fabric 0° V_f) in the bottom section of Table 8. The fully adjusted efficiency indicates fabric properties relative to expectations from AS laminates assuming proportional changes with 0° V_f. The fabric laminate modulus now shows a value greater than 1.0 due to the small contribution of the backing strands. The UTS is 79 to 89% of the expected proportional change, probably due to relatively poor strand alignment in the fabric as can be seen in Figure 1. The fatigue ratios for the epoxy are close to the UTS ratio, about as good as could be expected. However, the fatigue ratios for the UP and VE resins fall well below the UTS ratio, showing the particular sensitivity to fabric structure for these resins, apparently related to the transverse strands.

Additional UD results with fabric H have been obtained using a tough urethane resin following identical procedures. Laminates were infused and supplied by an industry partner; additional discussion can be found in Section 6.5. Table 10 gives UD tensile and compressive static properties and other characterization data, which are similar for the urethane and the baseline EP-1 epoxy. The urethane resin UD laminates are compared with Epoxy EP-1 and Polyester UP-5 resin laminates (Figure 38) in Figure 39. The tough urethane resin performs on a par with the epoxy, perhaps better at high cycles, the first non-epoxy resin in this program [1] to do so with

this fabric. Data for the urethane resin with aligned strands are not available. Urethane performance vs epoxy is less advantageous for $\pm 45^O$ laminates due to increased resin creep, Section 6.5).

Table 9. Comparison of static strength and stiffness properties for unidirectional laminates with epoxy and urethane resins

Resin	Elastic Modulus, GPa	Tensile Strength, MPa	Maximum Tensile Strain, %	Compressive Strength, MPa	Maximum Compressive Strain, %
Epoxy EP-1	41.4	1040	2.6	723	1.6
Urethane	40.6	1060	2.9	745	1.8
*Fiber volume fractions: epoxy, 0.58, urethane, 0.59 ; fabric PPG-Devold L1200/G-50-E07, layup $(0)_2$ for tension, $(0)_6$ for compression; the modulus is calculated from the best line fit between 0.1% and 0.25% strain					
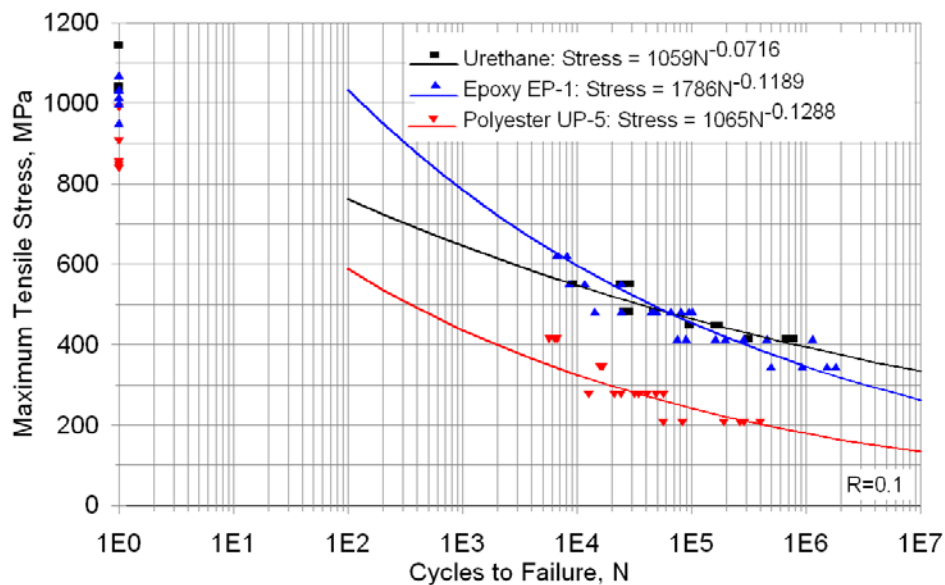
Figure 39. Comparison of tensile fatigue (R = 0.1) S-N trends for fiber dominated unidirectional (0°) urethane, epoxy (EP-1) and polyester (UP-5) resin laminates.

The results in Table 8 and Figure 39 relate specifically to fabric H. UD laminate fatigue data have also been obtained for the heavier fabric D, which only contains transverse strands in the backing (no mat), and also has 4400 Tex warp strands (AS laminate data are not yet available with these strands). Figure 40 indicates similar fatigue trends for both fabrics for EP and UP resins, with the previously observed higher performance for the epoxy. However, the VE resin approaches the epoxy performance at higher cycles only for the fabric D laminates, as it did for AS laminates in Figure 38. Thus, the VE resin may perform on par with epoxy for some fabric structures or strands, but not others.
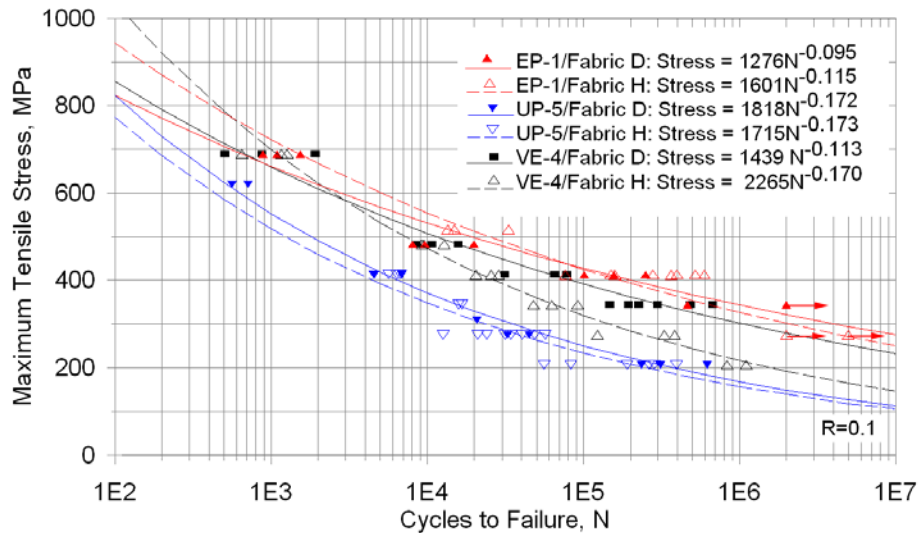
Figure 40. Effect of UD fabric D vs. fabric H, for EP, VE and UP resins, $(0)_2$ laminates.

5.5 Effects of Fabric Weight and Structure with Epoxy Resin Laminates

The foregoing suggests that epoxy resins like EP1 are not strongly sensitive to the fabric structures beyond changes in fiber content in the axial direction. Three series of laminate studies have been carried out to explore the influence of fabric details on fatigue sensitivity with the EP1 and EP5 epoxies described earlier. The most extensive test series was on laminates supplied by Roman Hillermeier of Devold AMT AS. Ten stitched fabrics with differences in weight, backing structure and stitching (with other parameters like yarn tension controlled) were specially prepared (Table 10). Most were tested in fatigue at a single maximum stress level, while four were tested at several stress levels. All laminates were MD structure with the UD fabrics listed, combined with a Devold 800 gsm biax fabric. All laminate configurations were $(\pm 45/0_2)s$ except for the heaviest, L2400, which used single 0° layers due to its doubled areal mass relative to the standard L1200.

The first three fabrics, L1200, L1400 and L2400 vary only in fabric weight. L1400 has more closely spaced yarns while 2400 has larger yarns. More complete data for different stress levels are given in Figure 41. The effect of fabric weight is not great, with only a suggestion of slightly lower cycles for the heaviest fabric at the lowest stress. The next three fabrics in Table 10 varied in backing structure: weft yarn on lower side (LT), weft yarn top and bottom (TLT), and weft yarn plus chopped strand (LT1200_G50). The bottom four fabrics in Table 10 varied in stitching details: tricot (T), un-symmetric tricot chain (UTC), symmetric tricot chain (STC), and stitch in-between roving (BTW). The log cycles to failure were not significantly affected by any of these variations for this epoxy resin.

82

A study of OCV^{TM} UD fabrics in UD laminates with epoxy EP1 is represented in Figure 42, and a similar study of three different weight triax fabrics is represented in Figure 43. Only the strain is given to reduce inconsistencies due to variations in laminate fiber content. The OCV UD fabrics contain Advantex$^®$ glass fibers with an OCV^{TM} sizing. These figures show little effect of fabric weight using the EP1 epoxy system, and fatigue resistance is similar to that for laminates based on fabrics D and H.

The sixteen different fabrics reported in this section demonstrate that tensile fatigue resistance with epoxy resin EP1 is not significantly affected by fabric details for a broad range of fabric weights, backing, stitching, orientation and strands/fibers/finishes. Strain levels are slightly lower for the triax fabrics compared with the UD fabric laminates, discussed later (Section 8).

Table 10. Fatigue results for ten MD laminates supplied by Devold with varied UD fabrics, epoxy EP5, R = 0.1

Material	V_F, %	Tensile Modulus, E_T, GPa	Ult. Strain, %	Ultimate Tensile Stress (UTS), MPa	Normalized Maximum. Stress, 414 / UTS	Log Cycles to Failure at a Maximum Stress of 414 MPa	COV %
L1200	57	35.7	2.8	891	0.465	4.77	2.7
L1400	60	38.6	2.8	896	0.462	4.91	4.3
L2400	61	35.8	2.9	920	0.450	4.80	3.2
LT1200	58	35.2	2.8	818	0.506	4.36	0.80
TLT1200	60	36.3	2.5	857	0.483	4.74	0.74
LT1200_G50	59	36.8	2.8	809	0.512	4.35	3.9
L1400_T	54	36.8	2.8	770	0.538	4.88	5.9
L1400_TCU	59	40.9	2.8	779	0.531	4.53	4.0
L1400_TCS	54	37.4	2.7	760	0.545	4.74	2.7
L1400_btw	59	38.3	3.1	946	0.437	4.89	2.5
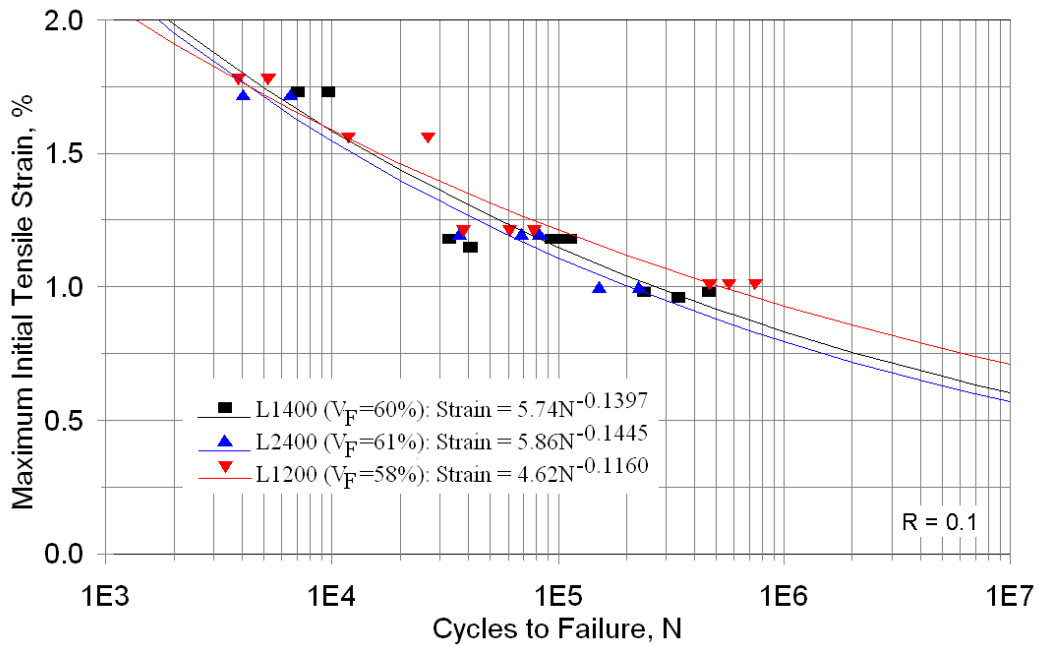
Figure 41. Strain vs. cycles for MD laminates fabricated with three different weight UD fabrics from Table 10, epoxy EP5, R = 0.1.
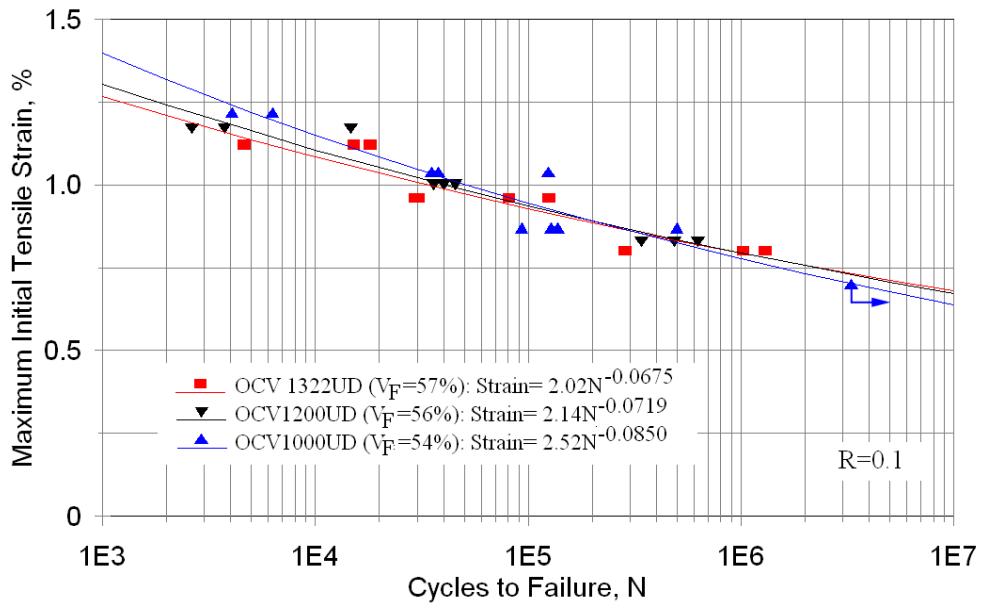
Figure 42. Strain vs. cycles for UD laminates with three different weight OCV^{TM} fabrics, EP1 epoxy, R = 0.1.
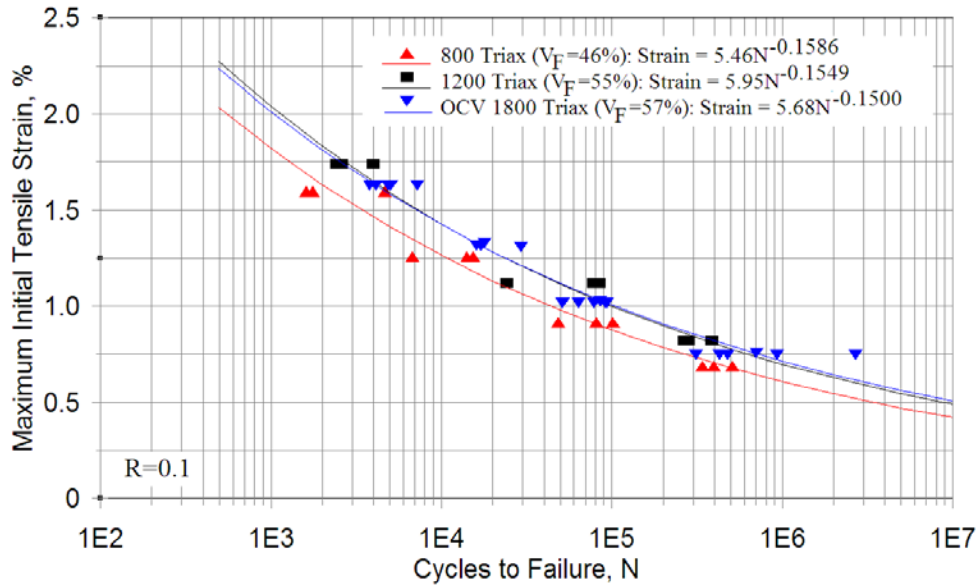
Figure 43. Strain vs. cycles to fail for triax fabric laminates with two Saertex fabrics (800 and 1200 gsm) and a heavier OCV^{TM} fabric (1800 gsm), epoxy EP1, R = 0.1.

5.6 Epoxy Resin Curing Effects

Curing effects have been observed in several UD and MD laminate systems in tensile fatigue. While some are for individual batches, Figure 44 gives data showing a consistent decrease in UD tensile fatigue resistance for laminates of the baseline Momentive RIMR 135 epoxy with very similar RIMH 1366 and 137 hardeners when the cure is a 40-70°C ramp over 1.5 hrs and the postcure temperature is 70°C. The fatigue life is reduced by more than a factor of ten at most stress levels, relative to longer cures and post cures.
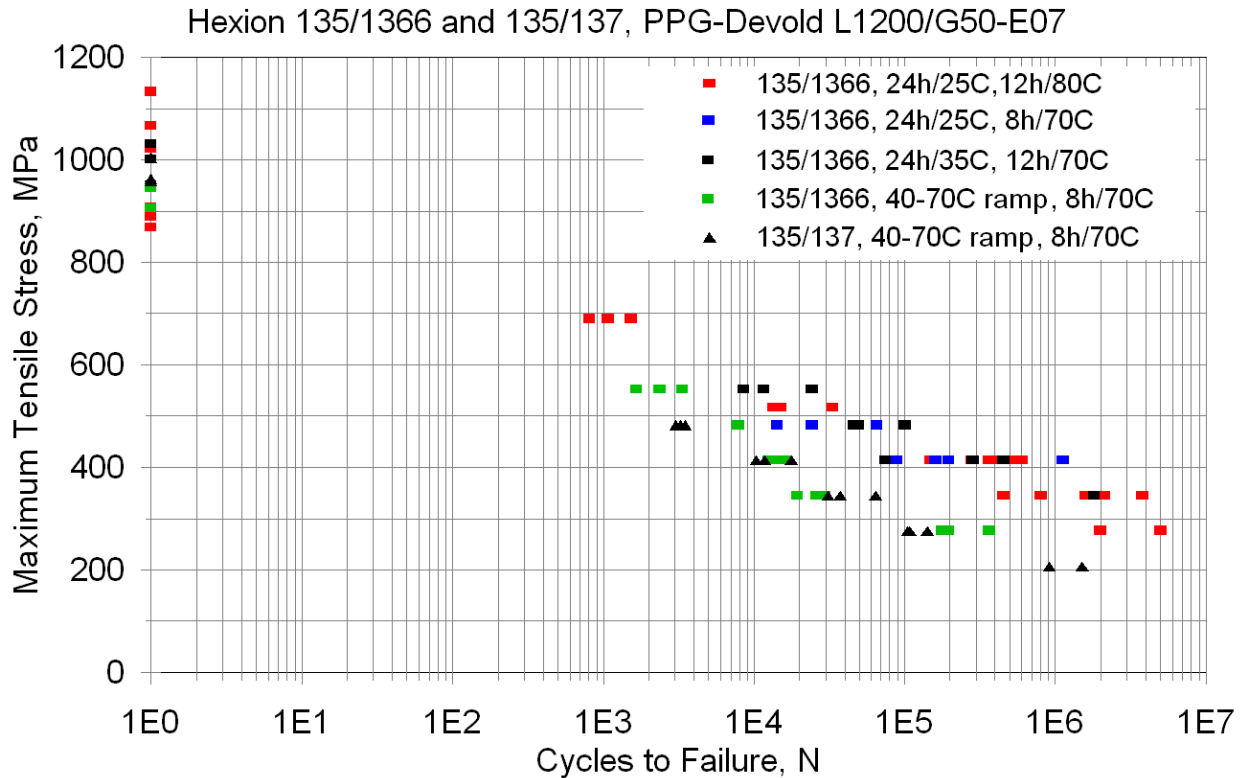
Figure 44. Tensile fatigue data for UD laminates, fabric H with 135/1366 or 135/137 epoxies with different cure and post-cure conditions shown, R = 0.1

5.7 Fatigue of Precured Aligned Strand Rod (RodPack) Reinforced Laminates

The baseline unidirectional laminate for comparison, from the SNL/MSU/DOE Composite Materials Database, uses the PPG-Devold LLC, L1200/G50-E07, 1261 g/m^2 (Fabric H) glass fiber unidirectional fabric infused with Hexion MGS RIMR 135/MGS RIMH 1366 epoxy resin (resin EP1), cured at 24h/25°C and 12h/70°C. Table 11 compares static modulus, strength and ultimate strain values: RodPack modulus values are higher in the principle directions, and in longitudinal compression; baseline transverse strengths and strains are higher than for RodPack. Fiber volume fraction is slightly higher overall (0.60 vs. 0.57) for RodPack, and not all of the baseline material fiber is in the longitudinal direction. Figures 45 and 46 give a comparison of the RodPack data with the baseline system trends. Fatigue stresses are consistently higher for the RodPack laminates under all loading conditions for the same cycles; fatigue exponents are also somewhat higher. Maximum absolute initial strain values were higher for the RodPack laminates at R = 0.1 and 10, similar at R = -1.

Table 11. Summary of average static values, RodPack vs control UD fabric.

	RodPack		Baseline Laminate	
Direction	L	T	L	T
E, GPa	48.4	18.7	40.5	12.8

UTS, MPa	1174	32.2	974	56.6
Ultimate tensile strain, %	2.5	0.17	2.5	0.36 / 1.6*
UCS, MPa	-986	-141	-706	-161
Ultimate compressive strain, %	-1.9	-1.0	-1.7	-1.3
*Transverse strain to first cracking / strain at failure; due to fabric 0's presence.				
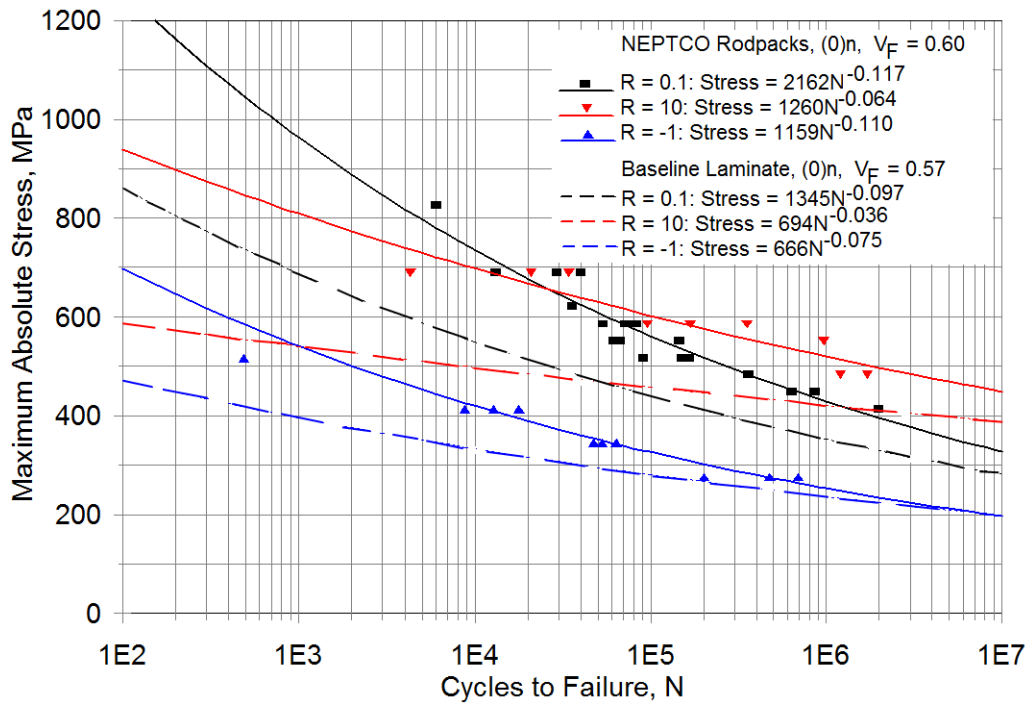
Figure 45. Maximum absolute stress versus cycles to failure, RodPack versus baseline laminates.

87
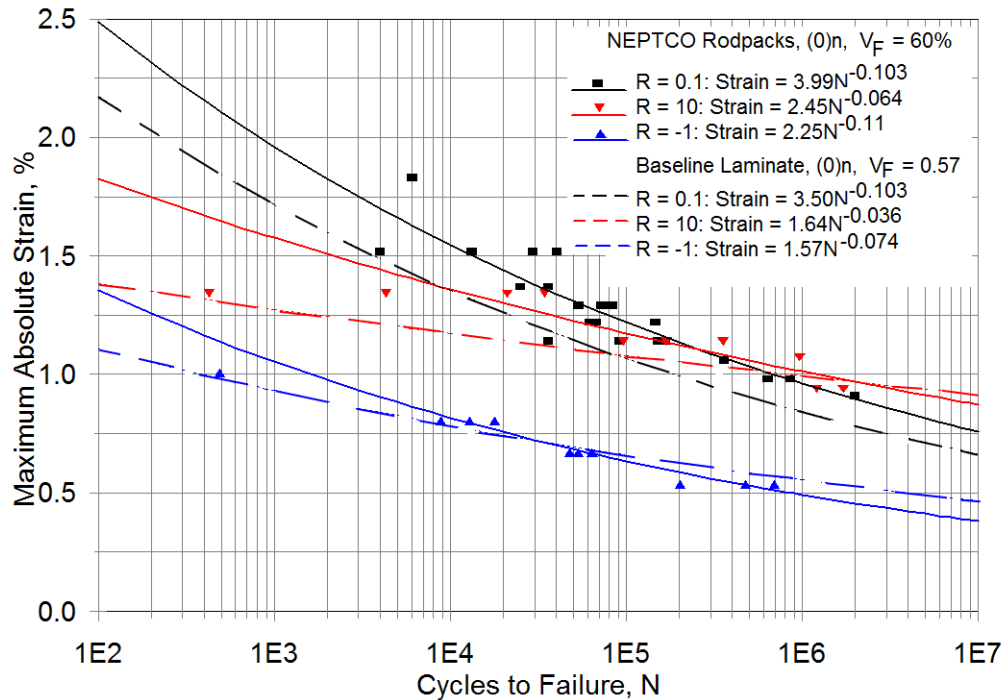
Figure 46. Maximum absolute strain versus cycles to failure, RodPack versus the baseline laminate.

5.8 Testing Issue with Reversed Loading R-values

Figure 47 Gives fatigue data for the baseline UD glass/epoxy (EP-1/Fabric H, Tables 2 and 3) at three R-values. Testing in reversed loading, R = -1, has been an issue over many years, as have the data, which show relatively short lifetimes at the same maximum absolute stress levels as typical R = 0.1 (tensile) and 10 (compressive) fatigue tests. Different test coupon geometries are typically used for R = 0.1 (100 mm long gage section, Fig. 17, top), with short gage sections and increased laminate thickness for compression and reversed loading, to avoid buckling [2]. Typical gage lengths for compressive and reversed R-values have been 13mm in most studies unless lateral supports or extreme thickness tapering is used [2]. Test geometries for DB or MD laminates have been less problematical if the content of UD plies is low. Failure modes for UD laminates with short gage lengths typically involve the tabs except for very thin sections.

In Figure 47 the main dataset for R = 0.1 was for two ply laminates with a thickness of approximately 1.7 mm (solid squares) while other data are for six ply laminates with a thickness of approximately 5 mm. The open square symbols near the R = -1 dataset are for tensile fatigue (R = 0.1) of the short gage length coupons. These data suggest that the poor performance of the laminate tested in reversed loading may derive from grip associated stress concentrations which produce premature failure in the tensile part of the cycle. This issue is difficult to avoid, and may affect many large datasets such as [1-3]. Representations of the reversed loading fatigue resistance may be systematically conservative and distort UD and some MD constant life diagrams, particularly at shorter lifetimes.
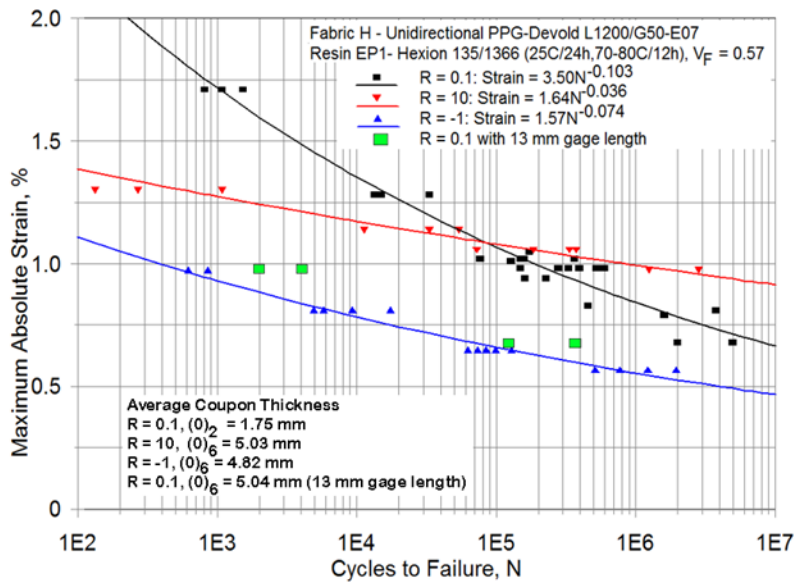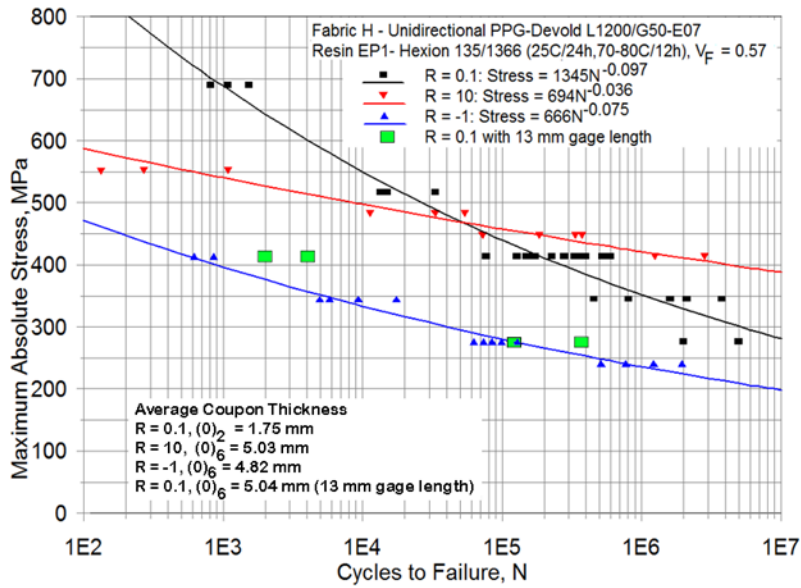
Figure 47. Fatigue S-N data for baseline UD laminates tested at three R-values, showing the influence of thickness and gage length on tensile fatigue results.

Intentionally Left Blank

6. Creep/Fatigue Interaction of ±45° Laminates

6.1 Summary

The creep and fatigue behavior of double bias (±45°) glass/epoxy laminates have been explored with a variety of tests, including conventional sine-wave fatigue loading at nine loading conditions (R-values), residual property stress-strain tests, square wave fatigue tests and creep tests. The fatigue results are presented as a strain-based constant life diagram (CLD) representing a 50% strain increase failure criterion which correlates with a transition to rapid strain increase and failure. Reversed loading effects are explored in detail, and show a substantial creep response during both the tensile and compressive parts of the wave-form; the creep response relates to the resin viscoelastic shear response. The off-axis laminate cyclic lifetime data can be correlated through a cumulative time under load criterion as opposed to a cumulative cycle criterion which correlates fiber dominated laminate fatigue data. The baseline epoxy resin is compared with a urethane resin, showing the effects of a tougher but more creep sensitive resin on the creep and fatigue resistance for ±45° laminates.

6.2 Effects of Fabric and R-value on Fatigue S-N Results

This section presents fatigue S-N results for coupon failure under constant force amplitude fatigue testing for different resins, fabrics and loading conditions for double bias glass/epoxy laminates.

6.2.1 Damage Development and Failure

Matrix cracking (Figure 48) is observed during much of the fatigue lifetime before failure, with differences in details for each R-value. In tension (left), R = 0.1, matrix cracks tend to start at coupon edges and progress across the coupon; in reversed loading (center) R = -1, cracking tends to initiate over the fabric stitch lines; and in compression (right), R = 10, cracking and small delaminations are observed between the fabric stitch lines. Final coupon failure was separation for tensile R-values, but high strain accumulation for compression R-values. The final cycles of lifetime under reversed loading (at R = -1), after the accumulation of high strains and resin cracking levels, resulted in rapid temperature rise and thermal softening (Figure 49).
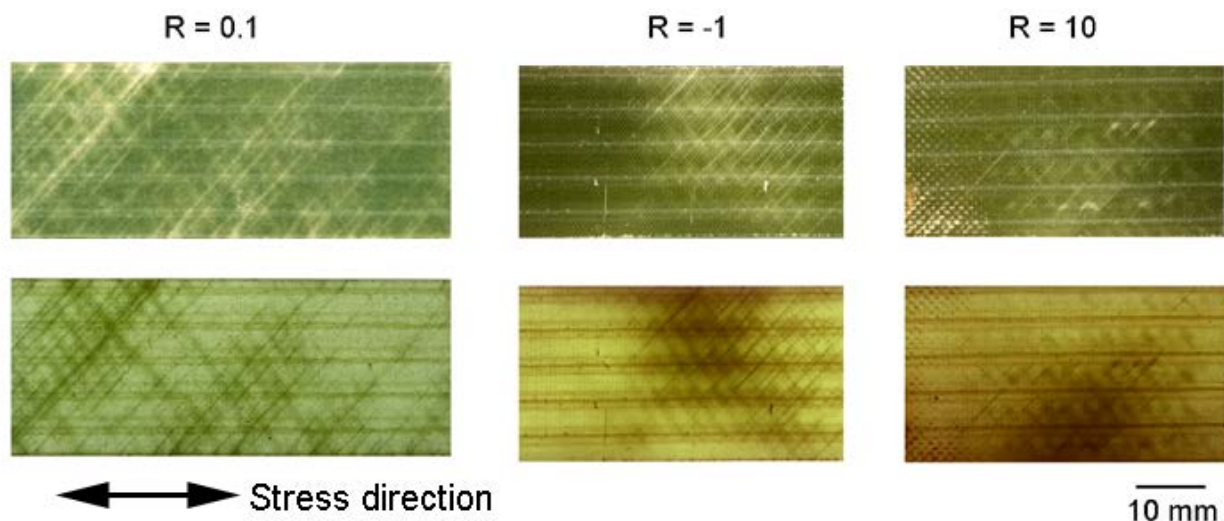
Figure 48. Matrix cracking at three R-values in reflected light (top) and transmitted light, fabric P laminates.
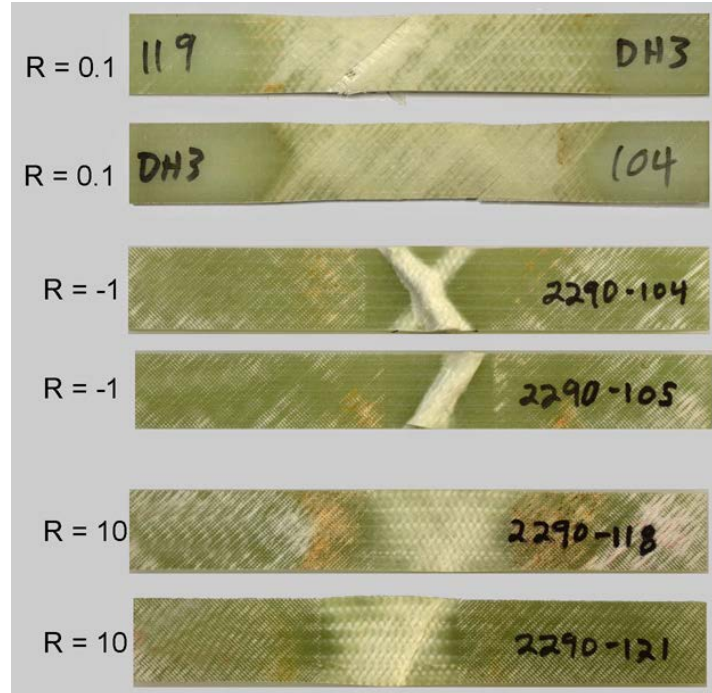
Figure 49. Failed fatigue coupons at indicated R-values, fabric P laminates.

6.2.2 S-N curves for different reinforcing fabrics

A comparison of fatigue S-N curves for laminates based on fabrics L, M and P loaded in the warp direction, and tested at R-values 0.1, -1 and 10 is presented in Figure 50. It was thought that the lower stresses for fabric P may relate to its higher fiber volume content, 56%, compared to the other fabrics, 44-45%. The fabric P data at R = 0.1 fall slightly below the OptiDAT MD3 biaxial laminate (Figure 8) which has a similar fiber content (53%) and resin. Tensile fatigue data for a specially prepared panel using fabric P, but with 46% fiber, showed about the same tensile strength and fatigue lifetimes as for the higher fiber content laminates, so fiber content may not play a major role for fabric P laminates in this range. A second factor with fabric P is the absence of significant backing strands relative to the other fabrics (Table 2). The fabric P laminate data fall slightly below the others in Figure 8 (the fabric L and M data were reported in reference [2], and are shown on Figure 8). Finally, the post cure temperature with fabric P was 20°C lower, as noted earlier.

Comparing results for different R-values in terms of maximum stress (Figure 50, left), the fatigue stresses are significantly higher for compression compared with tension, contrary to some literature assumptions [25] and reversed loading is significantly lower, with the same relative trend observed for each of the fabrics in Figure 50. The performance at R = -1 shows a greater drop relative to 0.1 in terms of max stress, than for typical fiber dominated laminates [2]. Fatigue exponents shown on the curve fits indicate S-N trends which are significantly less steep than for many fiber dominated laminates, particularly for fabric P [2].

The data for different R-values are re-plotted in Figure 51 in terms of stress and the absolute stress amplitude, (max stress – min stress). In these terms, the reversed loading performance is similar to that in compression, and superior to that in tension.

Although DB fabrics are used in blades as a stitched unit, their behavior can be more clearly understood by examining the stress field in each ply separately. Standard elastic ply-by-ply laminate analysis [51] of $\pm45^O$ laminates with glass/epoxy ply properties obtained from UD coupons[1], loaded in the axial (0°) direction by a typical applied average stress, σ_x, of 50 MPa in tension or compression, gives the ply coordinate stresses in Table 12. These stresses provide an approximate idea of the nature of the stress state in typical tests, ignoring nonlinearity. (The shear stresses, σ_6, are identical to those obtained following ASTM test standard D3518, $\sigma_x/2$.) Approximate local stresses at other applied stress levels would change proportionally. Under axial loading in the 0° direction, the results in Table 12 show that a tensile axial load produces transverse tensile (+) stress in each ply, and an in-plane shear stress which is in opposing directions (signs) in the two ply orientations. Transverse compression and opposite shear directions occur under axial compression. In fatigue, resin cracking develops parallel to the fibers (Figure 49). Ultimately, the plies are bonded together by resin as well as stitching, and total separation requires delamination, which is the final mechanism of failure for R = 0.1.

Table 12. Local ply stresses from classical laminate theory for a $(\pm45)_{ns}$ glass/epoxy laminate, resulting from an applied axial tensile or compressive stress.

Ply Direction In ±45 Laminate	Applied Stress, σ_x (MPa)	Longitudinal σ_1 (MPa)	Transverse σ_2 (MPa)	Shear σ_6 (MPa)
+45	+50	+47.7	+2.27	-25
-45	+50	+47.7	+2.27	+25
+45	-50	-47.7	-2.27	+25
-45	-50	-47.7	-2.27	-25

Figure 50. Maximum absolute stress vs. log cycles to failure for R = 0.1 (top left), -1.0 (top right) and 10 (bottom) for fabrics L, M and P, resin EP-1 (Tables 2 and 3).
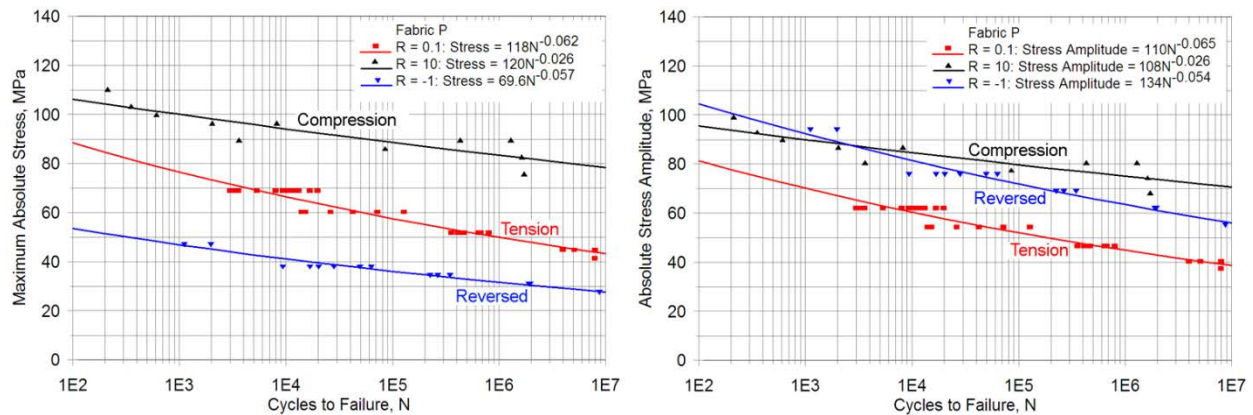
Figure 51. Comparison of maximum stress (left) and stress amplitude (right) S-N plots for fabric P laminates at R = 0.1, -1 and 10.

Under reversed loading the shear and transverse tension stresses reverse in direction as the load changes from tension to compression; the failure mode was discussed earlier as related to local temperature rise resulting from damage and the large strain amplitude and hysteresis (shown

94

later). The magnitude of the transverse stresses is low for this material relative to the shear stresses, but the fatigue response is significantly different under tensile versus compressive loading (Figure 51). Van Paepegem, et al., provides detailed experimental characterization and modeling [26] of the nonlinear stress-strain response of $\pm 45^O$ glass/epoxy laminates.

6.2.3 Stress-Strain Loops and Residual Stress-Strain Curves

The data in Figures 50 and 51 represent total coupon failure, taken as separation for tension, and large strains or crushing in tension and compression [12]. As noted in Section 2.2.4, off-axis laminates show extensive matrix cracking and large cumulative strains prior to complete failure in tension, which may be limiting in service [52]. Reversed loading is generally not expected to produce a mean strain creep response [52,54]. Figure 52 (top) illustrates the typical creep-type shifting (ratcheting) of cyclic stress-strain loops in tension and compression, as well as the tilting of the loops in tension, reflecting the loss in stiffness associated with cyclic damage [12,17,27]. The residual stress-strain curves for this case show little strength reduction relative to virgin material; significant softening is evident in tensile but not compressive residual response. Other studies have reported a steady reduction in residual strength as a function of fractional lifetime in tensile fatigue for $\pm 45^O$ laminates [25]. Stress-strain loops under reversed loading (bottom right) may remain centered close to the origin, tilting as creep occurs in fatigue, whether or not there is a modulus decrease. The contrast between tension and reversed loading responses is consistent with results for $\pm 45^O$ carbon/epoxy reported by Plumltree, *et al* [53].

In Figure 52 bottom left, the higher compression control stress-strain curve vs. tension reflects the change from a tensile transverse stress with a tensile load to a compressive transverse stress for a compressive load; shear stress is numerically the same in each case, but reversed in direction (Table 12). At higher strains the residual curves show higher stresses than the control curves, but the initial stiffness is reduced for the residual curves, similarly for tension and compression, reflecting the similar shear response (Table 13). Ultimately, the residual strength drops steadily prior to total failure, at least in tensile fatigue [24,25].

Table 13. Data for control and residual tensile and compressive stress-strain curves.

Coupon	First cycle max/min fatigue strains, %	110,000 cycle max/min fatigue strains, %	Initial cycle modulus, GPa (T / C)*	110,000 cycle modulus, GPa (T / C)*	Residual strain after 110,000 cycles, %
Residual tension tests					
2361-302	0.24 / -0.24	0.31 / -0.38	14.6 / 14.0	9.12 / 9.29	-0.0113
2361-331	0.25 / -0.25	0.35 / -0.32	15.0 / 14.5	9.71 / 9.70	0.0178
Residual compression tests					
2361-330	0.26 / -0.26	0.36 / -0.33	14.9 / 14.6	9.44 / 9.70	0.0180
2361-310	0.24 / -0.23	0.37 / -0.24	15.8 / 15.7	9.44 / 10.8	0.0842
*The modulus is calculated from the best line fit between 0.1% and 0.23% strains. T = tensile, C = compressive					
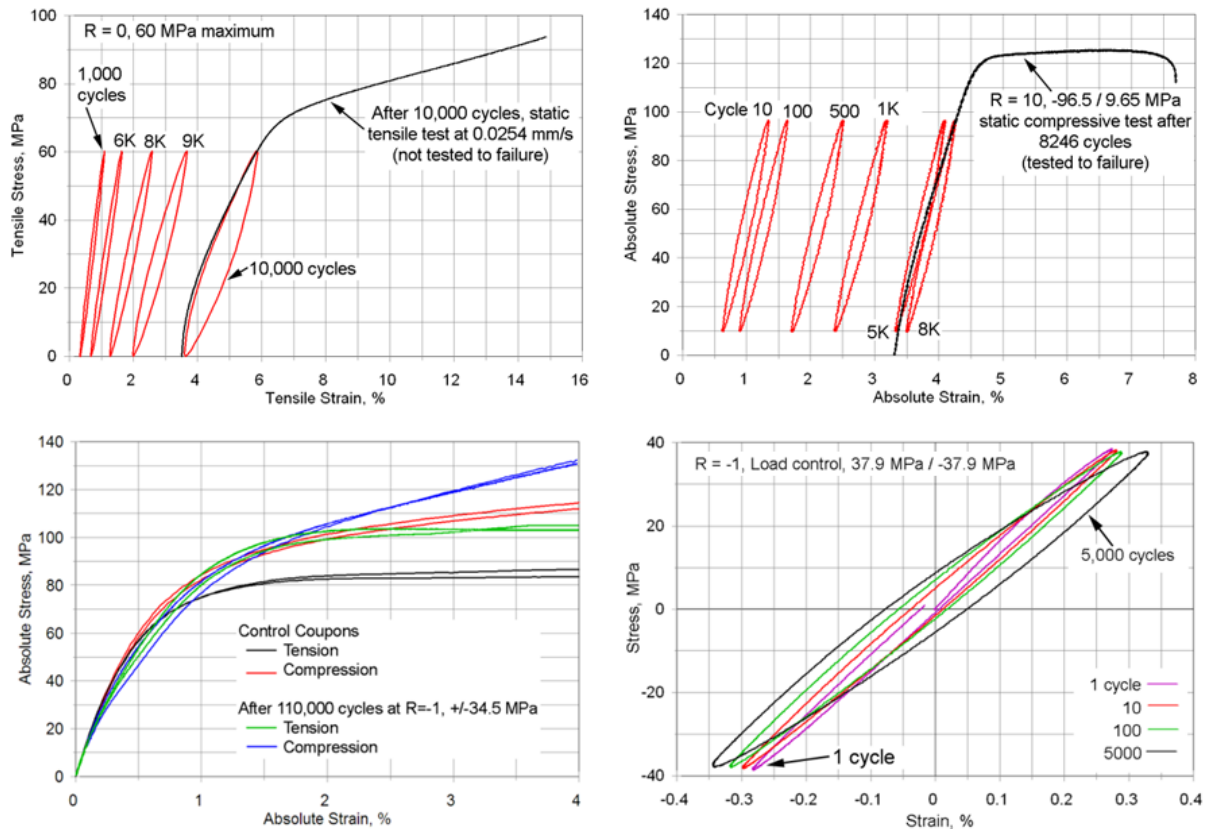
Figure 52. Top left, coupon tested at R = 0 (0-tension), max stress 60 MPa, stress-strain loops with residual tensile stress-strain test immediately after cycle 10,000; top right, compression loops, R = 10, max abs stress 96.5 MPa, with residual compressive stress-strain curve after cycle 8,246 (from ref. [1]); bottom right, typical stress-strain loops under reversed loading at ±37.9 MPa; and bottom left, residual vs. control tensile and compressive stress-strain curves after reversed loading fatigue at ±34.5 MPa to approximately 50% of the mean lifetime.

6.2.4 Cyclic Creep and Stiffness Change

Stress-strain changes during load controlled cycling (Figure 52, top) reflect both a cyclic creep effect, with the coupon lengthening appreciably in tension or shortening in compression as cycles accumulate and both max and min strains increase, and a significant reduction in stiffness, indicated by a tilting to lower slope of the individual loops, most notable for R = 0.1 and -1. The results in Figure 52 generally correspond with the LUR results presented in Section 4.2 as to nonlinearity and creep. The stiffness is calculated as (max-min) absolute stress/(max-min) absolute strain for an individual cycle. Plots of the average strain and the strain range vs. cycles are given in Figure 53 for typical tests of similar lifetime at each R-value. The average strain and strain range for particular cycles can be taken as measures of the creep strain and stiffness change, respectively [26]. The creep strain increases steadily for the R = 0.1 and 10 coupons, more rapidly toward the end for 0.1; much lower creep strain is present for R = -1 over most of the lifetime. The strain range, proportional to the stiffness, does not change significantly for

compression (consistent with the residual stress-strain curve given later), but increases in the last decade for tension and reversed loading. Tamuzh, et al. [26] attribute the stiffness change to cyclic damage effects which are independent of viscoelastic (creep) response, for off-axis laminates. Thus, the R = 10 response appears to be entirely dominated by creep, while the R = 0.1 and -1 responses show significant stiffness change associated with cyclic effects in the last decade, as well as significant creep strain for 0.1. The fatigue exponents (Figure 58) are similar for R = 0.1 and -1, but much lower for 10.

Plots of maximum absolute strain for varied stress levels at each R-value in Figure 54 indicate maximum strains reaching several per cent in most tests before failure, with reduced strains at the lowest stresses and under reversed loading. The max strain typically increases by many times the initial max strain before failure. These figures indicate that very substantial strains accumulate for R = 0.1 and 10 before the stiffness decreases appreciably. Reversed loading also produces significant creep strains, discussed in Section 6.3.4.

It has been the practice in the past to report only the initial strains for the first few cycles for fatigue of $\pm 45^{\circ}$ laminates in the database and reports [1,2], but these values have little meaning in characterizing test conditions, as evident from the results in this paper. However, for fiber dominated laminates, strain and stiffness changes are small, and initial strains, while approximate in terms of cyclic conditions, provide simple and useful information.

Strain controlled fatigue produced markedly different response, Figure 53 (bottom). For tensile fatigue (run with the thicker coupons to withstand compressive stresses), stress-relaxation at the higher strains on the first and subsequent cycles reduces the peak stress; the stiffness is not changed early in the lifetime, so the unloading strain excursion produces a compressive minimum stress. As cycling continues, the loop bottoms stabilize, but the stiffness now steadily decreases, lowering the maximum stress further. Compression loading in strain control produces changes which are the inverse of those for tension, Figure 53, bottom right compared with bottom left, as the loop bottoms relax and the tops progress into tension. Under reversed loading at lower maximum strains, (R = -1, center bottom, Figure 53), the loops drift in a positive (tensile) direction similar to those for compression.
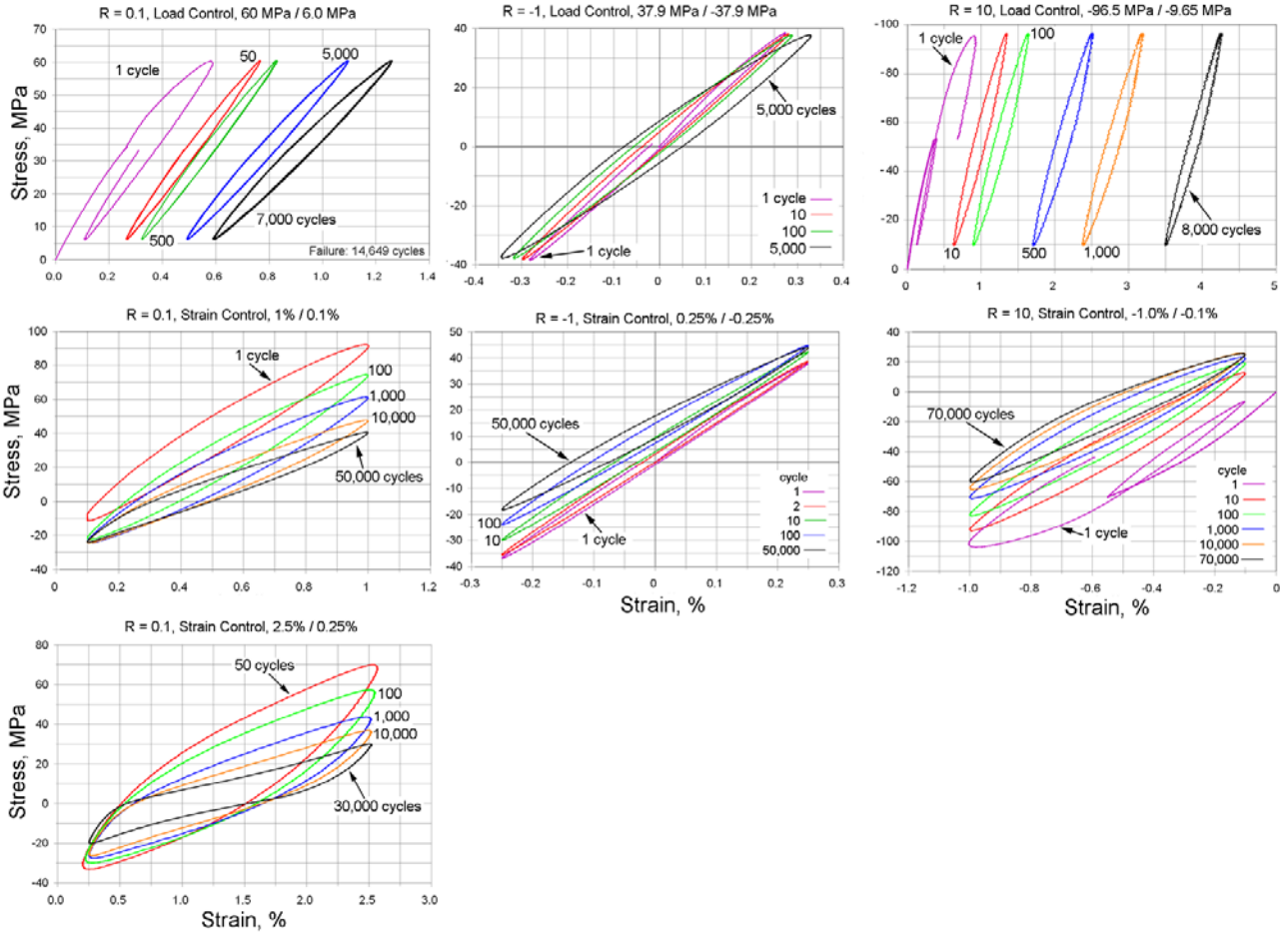
Figure 53. Typical cyclic stress-strain hysteresis loops for load control (top) and strain control (middle and bottom), fabric P, strain based R = 0.1(left), -1 (center) and 10 (right).

6.2.5 Residual Stress-Strain

Cycles to complete failure for the R = 0.1, 60 MPa max load control case ranged from 10,000 to 100,000 cycles (Fig. 53). Selected coupons were cycled at R = 0 (for simplicity) to 4,000 and 10,000 cycles, then immediately tested for residual tensile stress-strain curve. Similarly, in compression fatigue, a coupon was cycled at R = 10, maximum absolute stress of 96.5 MPa, with an expected lifetime around 10,000 cycles; the residual compressive stress-strain curve was determined on cycle 8,642. Stress-strain loops and the residual stress-strain curves are given in Figure 54, top. The residual stress-strain curves are compared with the virgin stress-strain curves, by offsetting the residual curves to zero strain by the amounts shown. The offset residual tensile stress-strain curve at 10,000 cycles is dramatically softened at most strains, but the maximum stress reached is only slightly reduced, relative to the virgin tensile stress-strain curves; less softening is evident for the 4,000 cycle tensile case. The offset residual compression curve shows no modulus change up to moderate stress, consistent with the absence of stiffness change discussed earlier, increased stiffness at high stress, and reduced maximum strain (by about the offset amount) relative to the virgin stress-strain curves. These limited cases show no significant decrease in residual ultimate strength, but more comprehensive testing for residual strength of similar ±45° laminates has shown a steady decrease in tensile residual strength and stiffness after

tensile fatigue loading; compressive residual strength is not found to decrease in a steady manner regardless of the fatigue loading condition [20]. Figure 52 (bottom) shows stress-strain loops and residual stress-strain curves in tension and compression vs control (uncycled) material. The stress-strain curves show softening at low strains but stiffening at higher strains, as a result of reversed load cycling at this condition.
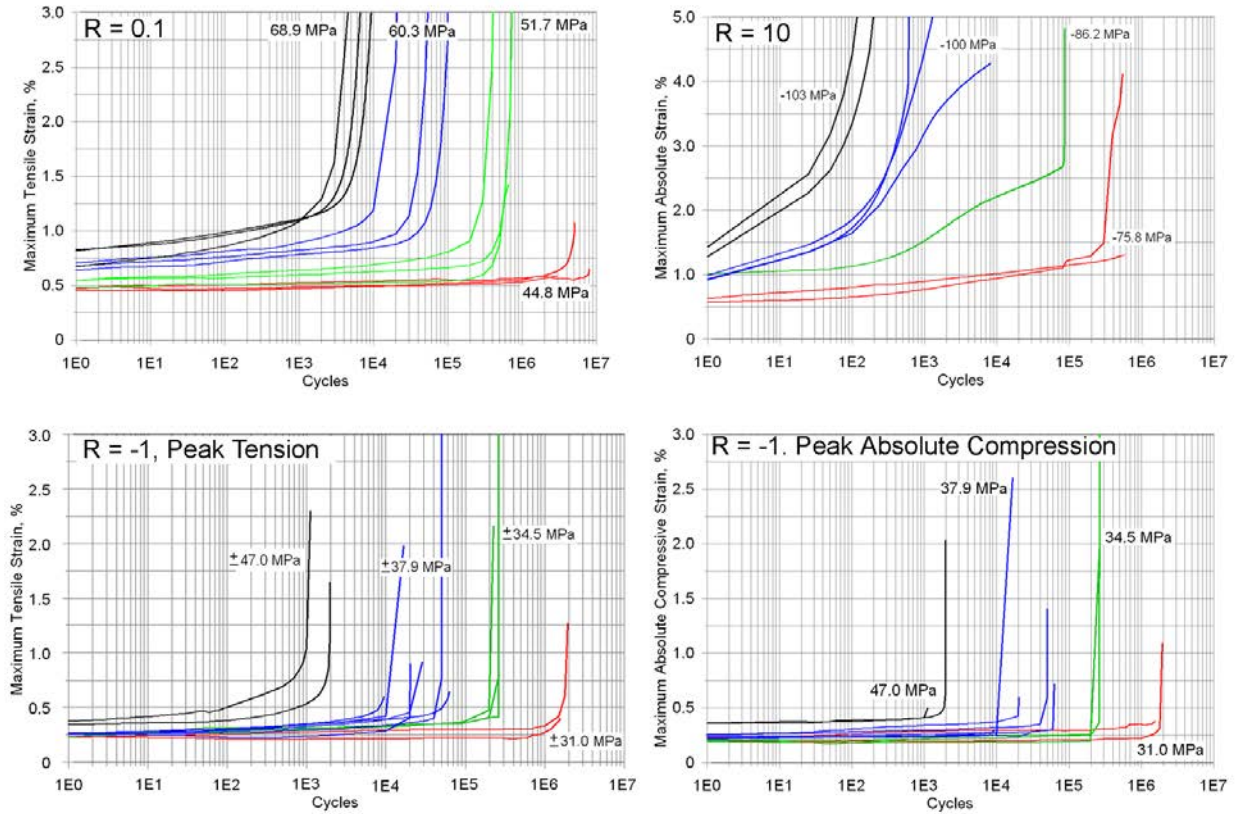
Figure 54. Maximum running strain over lifetime at different max loads: R = 0.1 (top left), 10 (top right) and -1 (bottom: left, tension part of cycle; right, compression part).
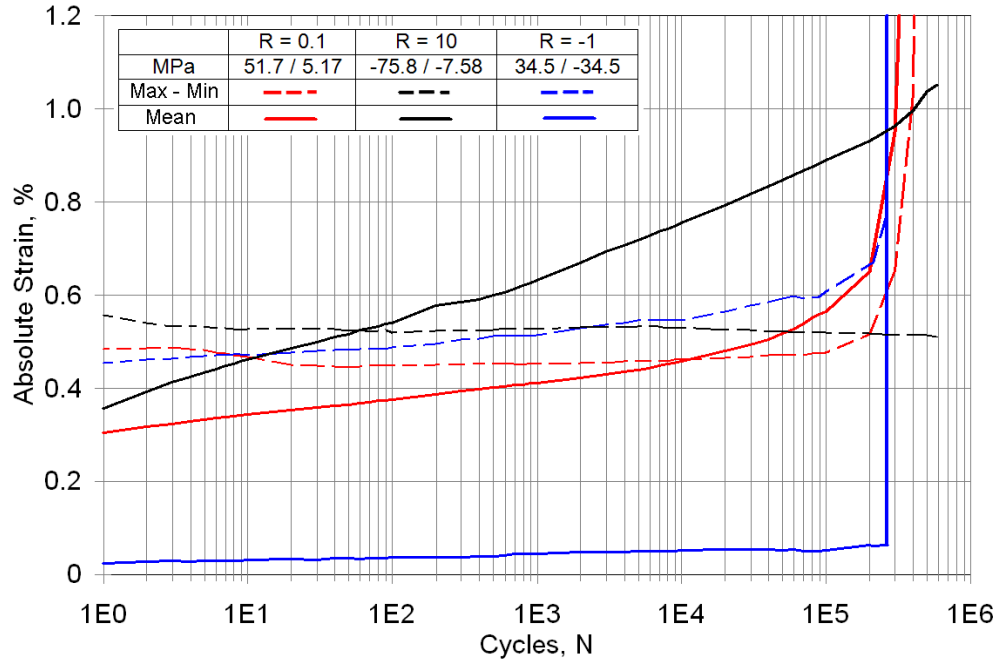
Figure 55. Typical individual test average strain, (max + min)/2, and strain range (max-min) at each R-value.

Plots of maximum absolute strain for varied stress levels at each R-value in Figure 54 indicate strains reaching several per cent in most tests before failure, whether due to creep or a large stiffness decrease. The creep and stiffness changes are separated in Figure 55 following Tamuzh, *et al*. [26], who attribute the stiffness change to cyclic damage effects which are independent of viscoelastic (creep) response, for off-axis laminates. The stiffness is calculated as (max-min) absolute stress/(max-min) absolute strain for an individual cycle, while creep is taken as increases in the mean strain (abs (max + min strain)/2). Thus, the R = 10 response appears to be entirely due to creep, while less creep is measured under reversed loading. Tensile fatigue produces significant creep earlier in the lifetime, followed by large stiffness changes later. Reversed loading produces only slight drift in the mean strain before relatively sudden failure related to progressive stiffness reduction.

6.3 S-N Fatigue Trends and Constant Life Diagram

6.3.1 S-N Trends and Damage Metrics
S-N fatigue lifetime was characterized for tension-tension, compression-compression, and reversed loading fatigue, Figure 50 (R = 0.1, 10 and -1, respectively, where R = min load/max load). Data have also been obtained for additional R-values given in the next section. As noted above, reversed loading performance falls well below tension and compression when compared in terms of maximum stress, but is similar to compression in terms of stress amplitude or range (max-min). Fatigue coupons were instrumented with an extensometer to follow the running strains. Stiffness and strain data allow the use of damage metrics in addition to total failure, as illustrated in Figure 57. Total fatigue failure results are compared to cycles for a 25% decrease in stiffness (slope of the cyclic stress-strain loop) and a 50% increase in cumulative maximum absolute strain. The 50% maximum strain metric is selected since it approximates the point of

rapid upturn on the maximum strain plots (Figure 57). For R = 0.1 and -1, individual tests reach the 50% max strain increase first, followed by the 25% stiffness loss and then total failure over most of the stress range. At the lowest stresses, of greatest significance to blades, the R = -1 data tend to converge to a similar lifetime for the 25% stiffness change and failure, with the 50% strain increase not achieved in some cases. In compression, R = 10, the 25% stiffness reduction is not reached before creep strains accumulate sufficiently (several %) to constitute failure. The 50% strain increase condition is reached much earlier than the failure condition in compression.

Reversed loading is of particular importance for DB fabric laminates because they may play an important role in large blades with significant edge loading from gravity, where cycles are predominantly reversed. Additionally, damage and failure occur at the lowest max loads under reversed loading compared to tension or compression R-values. In addition to reversed loading of ±45° laminates, reversing of the shear direction has also been shown to produce the most rapid fatigue crack growth in pure mode II delamination crack tests [55] and delamination at mode II dominated structural details like ply drops [2].

6.3.2 CLD Diagram

The S-N trends were fit to a power law equation for each of nine R-values. Data and curve fits are shown in Figure 58, with curve fits given in Table 14. The 50% maximum strain increase could be easily determined for the entire dataset, while the 25% stiffness decrease did not occur prior to failure for the more compressive R-values, and total failure was difficult to define for many cases without complete separation. Curve fits for the various R-values were assembled into a CLD for 50% maximum strain increase, Figure 59, following the procedures in ref. [4]. This plot represents the lifetime which would be reached prior to exceeding a 50% strain increase for the repeated application of cycles at a particular stress amplitude (max-min stress) and mean stress, which can be linearly interpolated from the plot. The resulting lines of constant lifetime approach a symmetrical shape at lower stresses and longer lifetimes, reflecting the shear domination which is similar in tension and compression. Figure 59(a) represents the CLD in terms of axial stresses at 0°, while Figure 59(b) represents shear stress in 1-2 material coordinates. The zero amplitude, mean stress creep response may be applied for R-values approaching 1.0 on each side, Figure 60, indicated as tick marks on the abscissa in Figure 59. The creep stresses (tick marks) are shifted towards the origin relative to an extrapolation of the low alternating stress lines to zero amplitude, apparently representing the very short time at max load per sine-wave cycle compared to constant load creep data. Thus, cyclic sine-wave loading is less damaging for the same total cumulative test time than creep loading, contrary to the case with fiber dominated laminates (Figure 7). Design procedures for strain based service time have been reported by [52]. By way of comparison, CLD's for fiber dominated loading tend to show more fatigue resistance for the compression dominated quadrant, as do transverse direction CLD's [2].
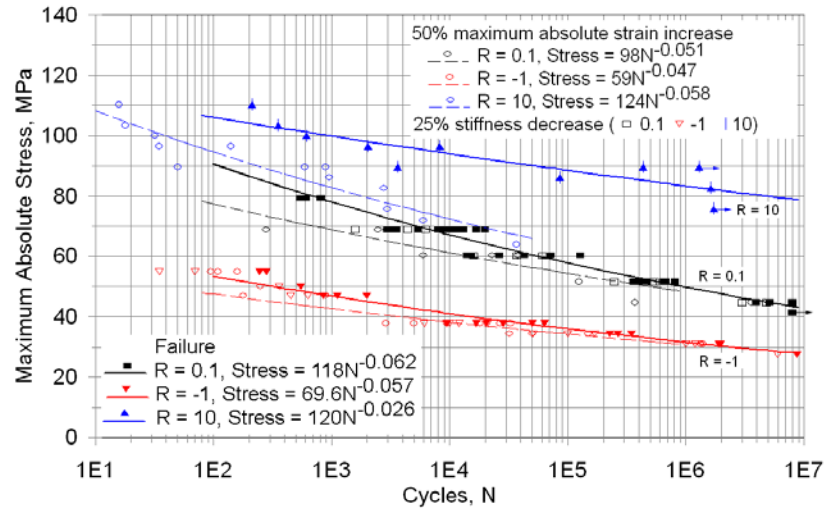
Figure 56. Data for 25% stiffness decrease and 50% max absolute strain increase plotted with failure S-N curves.
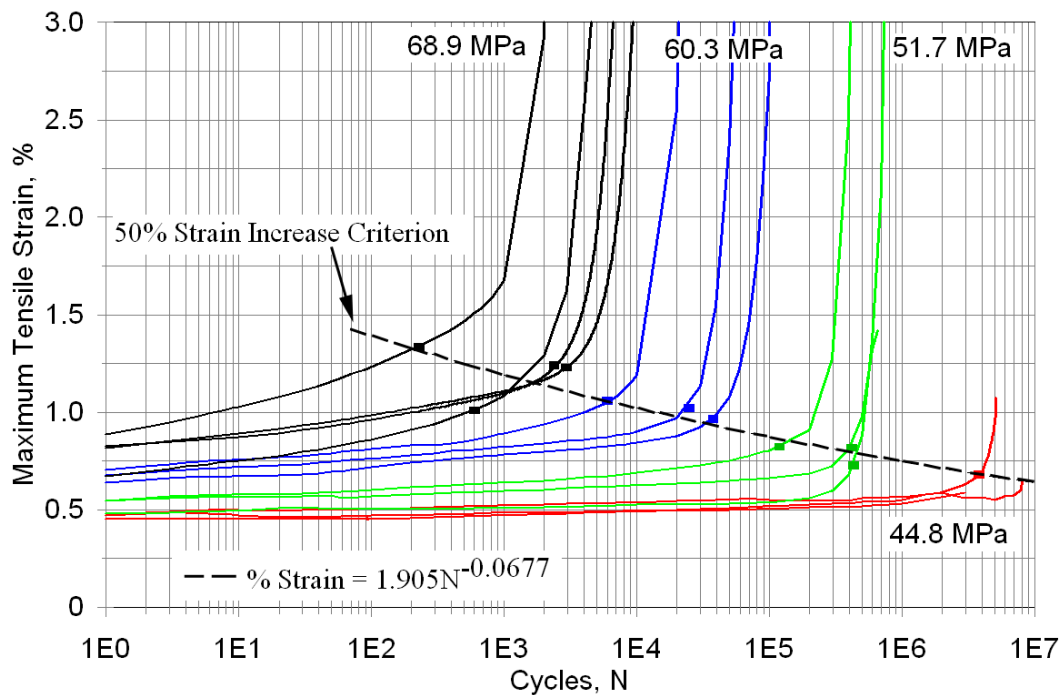
Figure 57. Maximum running strains during R = 0.1 fatigue at various maximum stresses showing 50% cumulative strain failure criterion (dashed line).
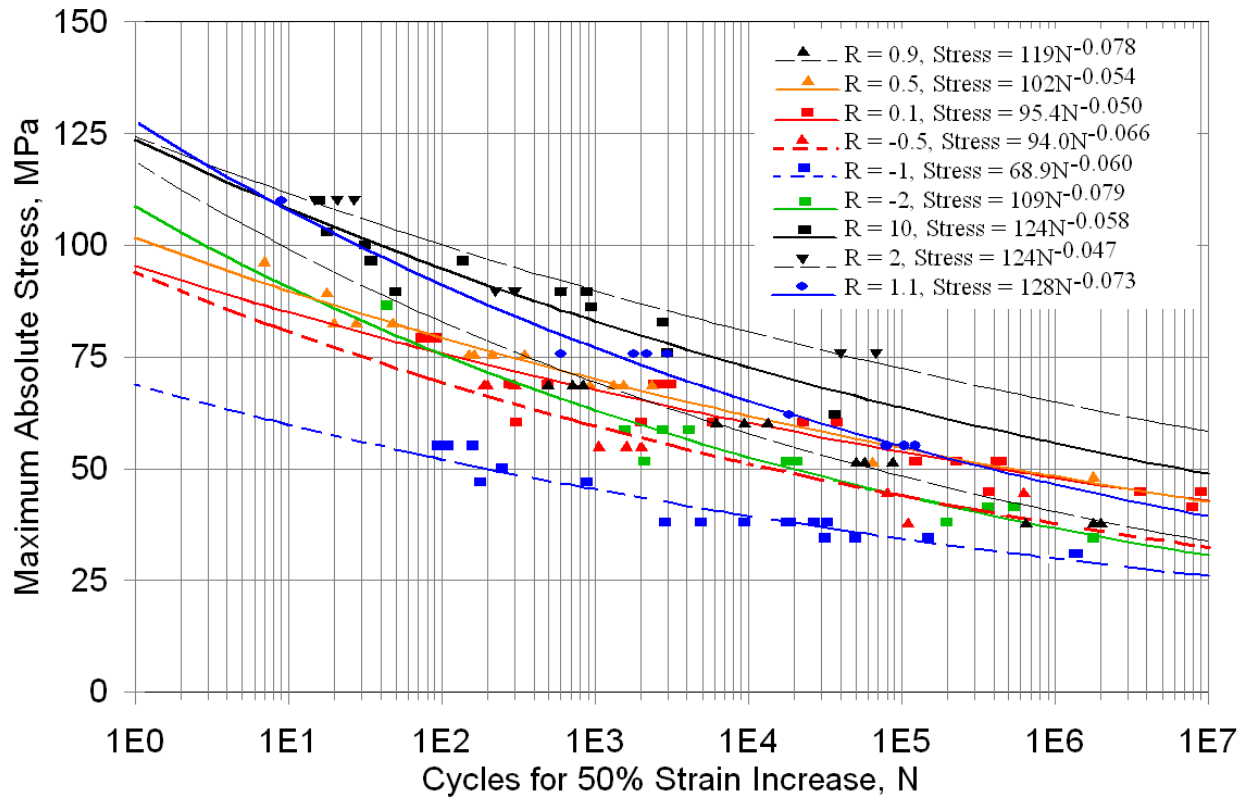
Figure 58. S-N data and trend lines for DB laminates tested at nine R-values.

Table 14. Best fit S-N equations to cycles for 50% maximum strain increase, where S = A N^B.

R-Value	A (MPa)	B
1.1	128	-0.073
2	124	-0.047
10	124	-0.0576
-2	109	-0.0786
-1	68.9	-0.0603
-0.5	89.7	-0.0271
0.1	95.4	-0.0497
0.5	102	-0.0540
0.9	119	-0.078

103
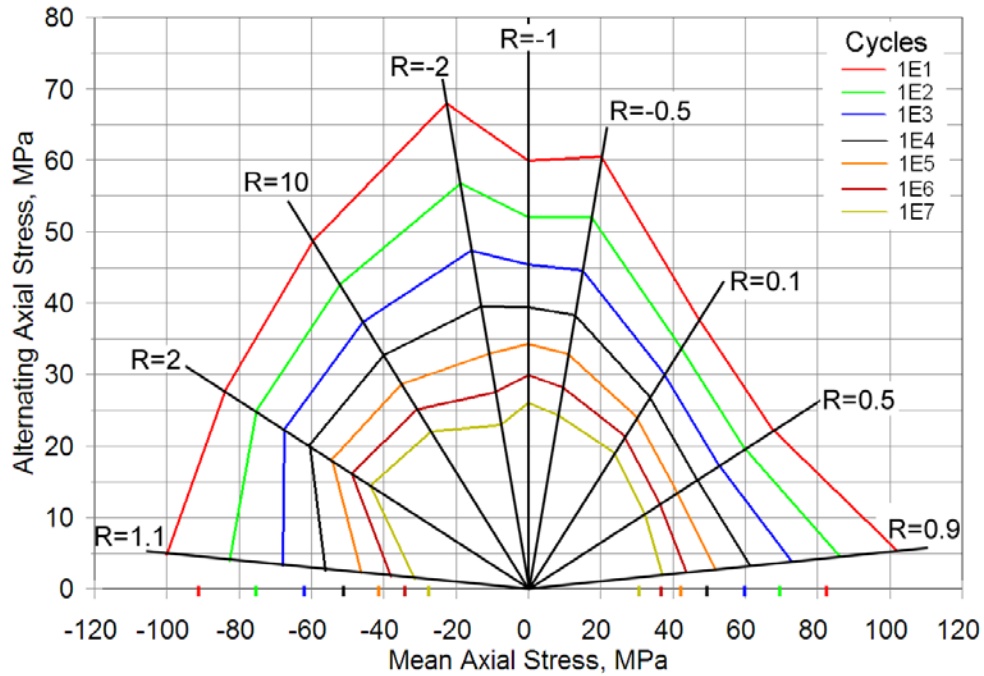
Figure 59(a). Axial Stress
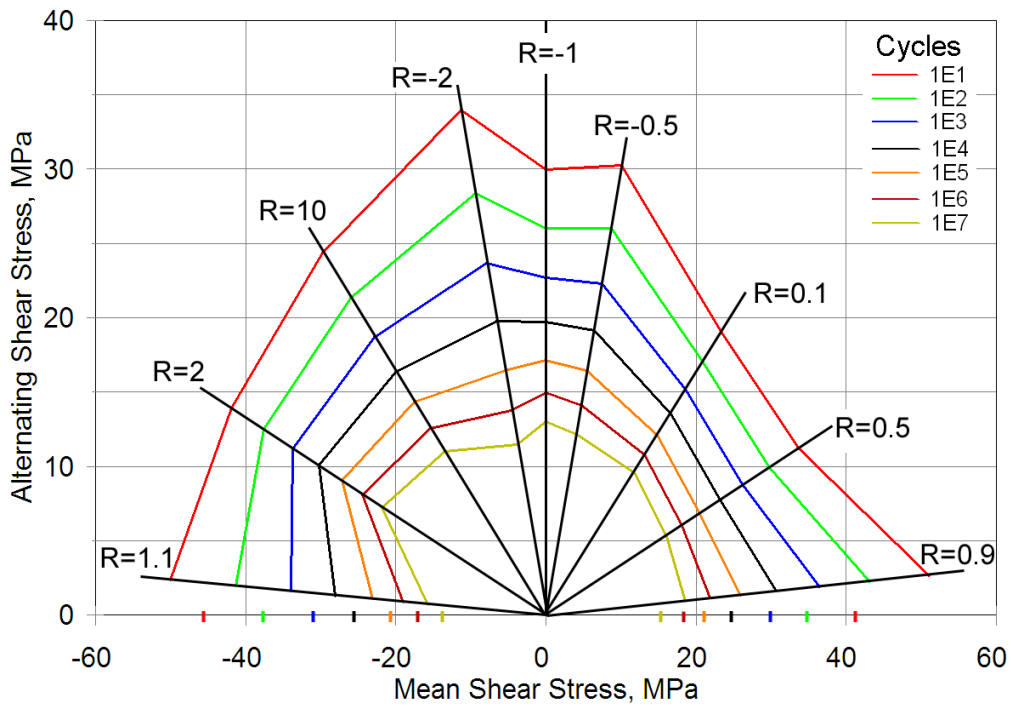
Figure 59(b). Shear Stress

Figure 59. Constant Life Diagrams (CLD) for 50% maximum cyclic strain increase relative to the first cycle: (a) Axial (0°) Stress and (b) Shear Stress (material 1-2 coordinates).
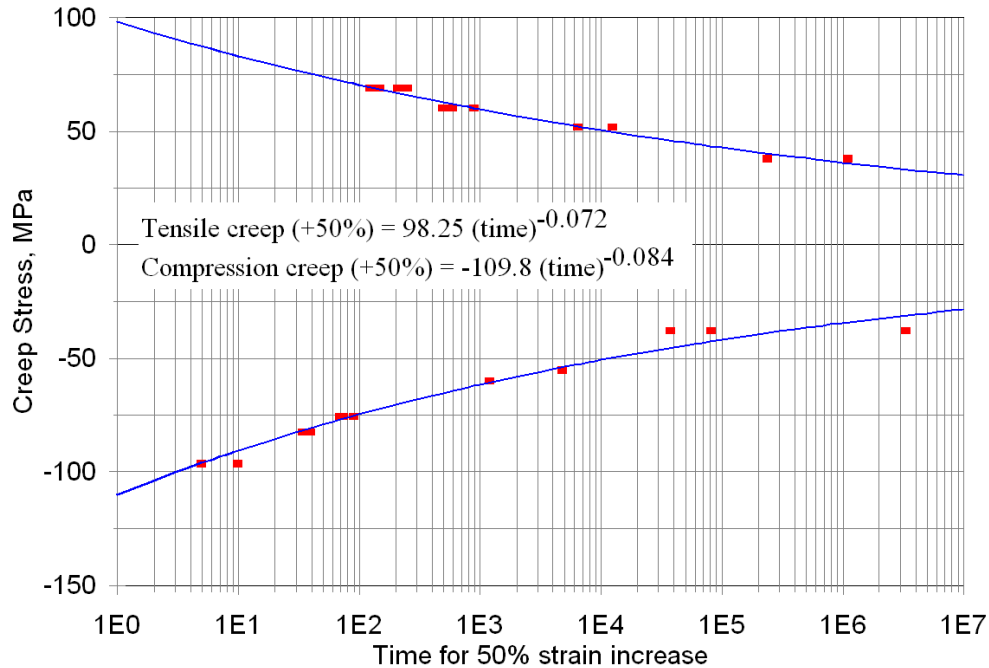
Figure 60. Creep trends from curve fits to tensile and compressive creep data for strain vs. time at various applied constant stress levels (0-stress amplitude), creep stress vs. cumulative time to 50% strain increase.

6.3.3 Square wave and creep comparison in reversed loading

The sine-wave loading fatigue results described in the foregoing have been considered in terms of understanding the effects of creep on reversed loading behavior. As noted earlier, similar creep response during the tensile and compressive parts of the wave-form at R = -1 lead to an apparent decrease in stiffness and low initial creep at mean load. Comparing the max and min strains as cycling progressed indicates that, in the final stages of lifetime, the tensile strain tended to increase more rapidly as matrix cracking accumulated and stiffness decreased. The ratio of max/min strain at various maximum loads is given in Figure 61, which supports this observation.

In terms of the effects of creep on the fatigue lifetime, the overall coupon lifetime in tension was found to be approximately consistent between sine-wave fatigue loading and constant-load creep loading, based on the 50% strain increase metric, Figure 62. However, the time under load is difficult to define for the sine-waveform. Thus, a series of tests was conducted using a square wave-form. This allows a direct calculation of time under load in both tension and compression for reversed loading, which can be directly compared to creep results. Figure 63 gives typical square wave results for a low frequency of 0.01 Hz in terms of extensometer strain and actuator (LVDT) position. Strain gages were also used to confirm other instrumentation, but failed early in the tests. Even the extensometer, with a 12.5 mm gage length, became affected by its positioning relative to matrix cracking bands (Figure 48) as damage developed. The most consistent data were from the actuator LVDT (Figure 63, left), but the LVDT displacement cannot be reliably converted to strain with hydraulic grips. Tests were also run at higher frequencies, but hysteretic heating was severe late in the lifetime, after damage (resin cracking) was observed, for 1 Hz and above at stresses of ±37.9 MPa and above.

Data as in Figure 63 give a clear indication of the creep on various cycles, on the tension and compression sides of the wave-form. Consistent with Figure 61, the tensile side strains generally accumulate faster than on the compressive side, after being similar at low cycles. The modulus during loading for each cycle, shown in Figure 64 as relative modulus, E/E_o, where E_o is the initial modulus, vs. relative lifetime, n/N, where n is the current cycle number and N is the coupon lifetime, steadily decreases as cycles accumulate, consistent with the residual data in Table 14 for sine-wave loading.
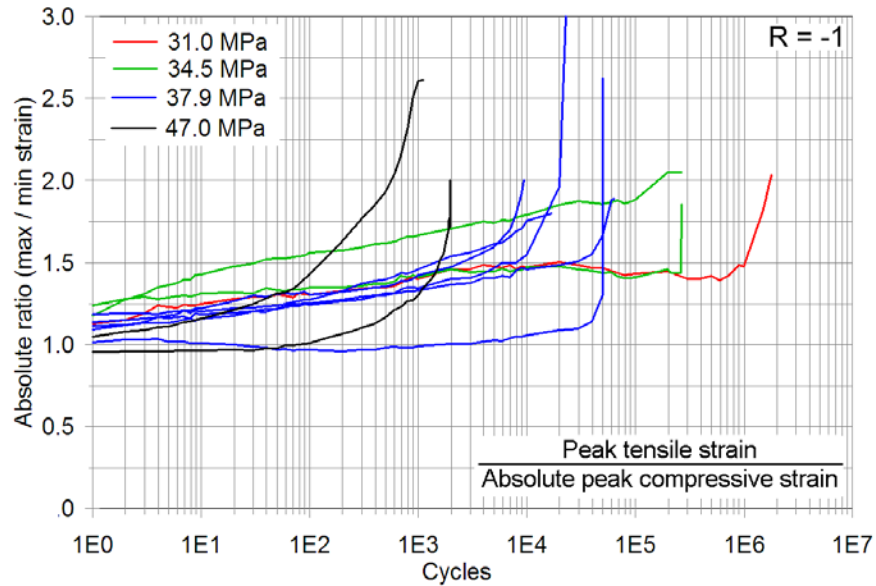
Figure 61. Ratio of peak tension and compression strains for R = -1 cycles at various mamximum applied stresses, sinewave loading.
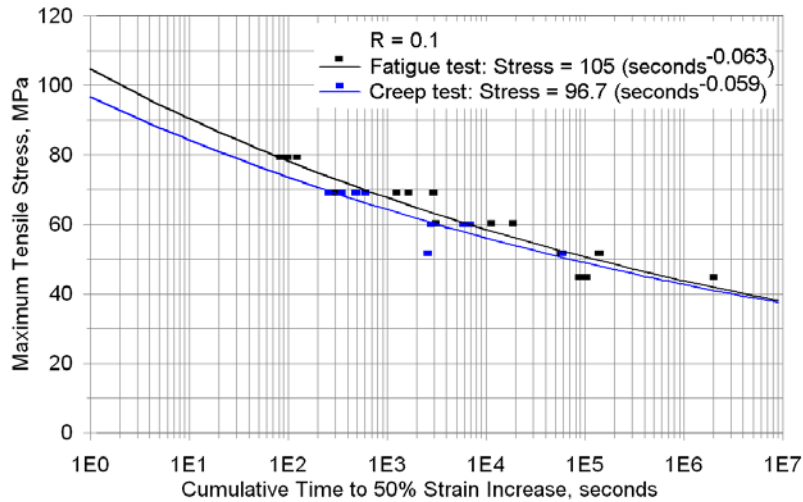
Figure 62. Cumulative test time to reach 50% increase in max strain at different max stresses for tensile creep loading, compared with sine-wave fatigue at R = 0.1.

106
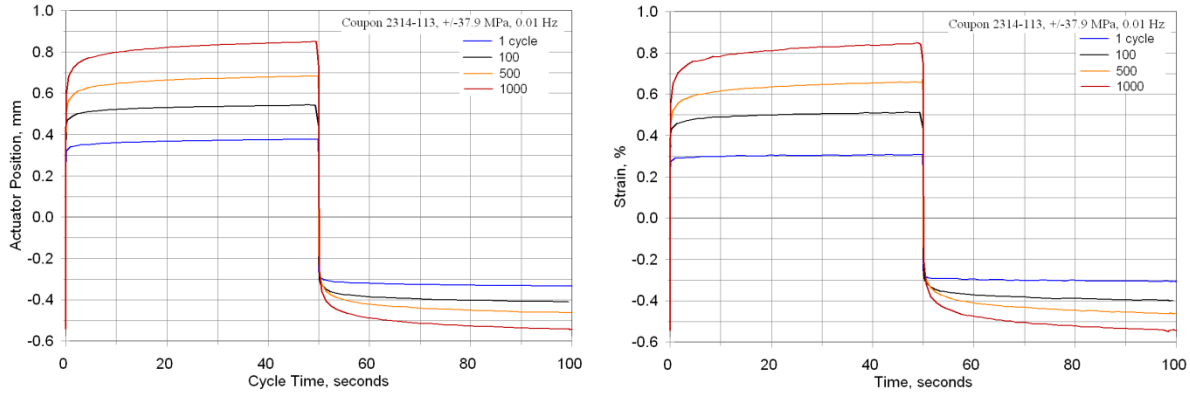
Figure 63. Typical square wave actuator position and extensometer axial strain for selected individual cycles; R = -1, frequency 0.01 Hz.
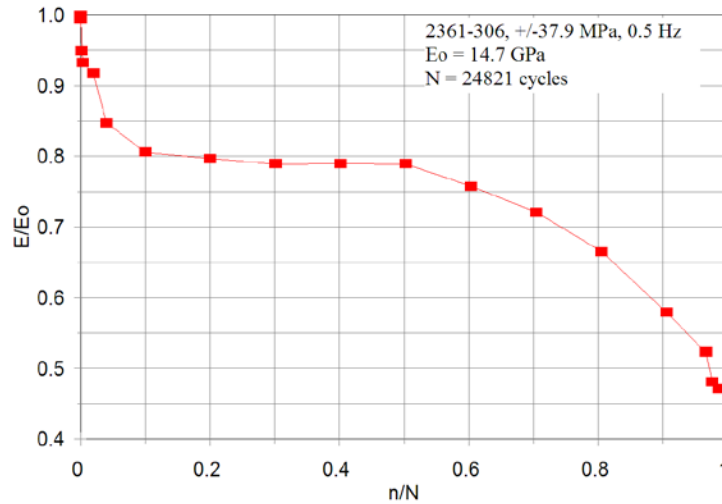
Figure 64. Decrease in modulus (E/E$_o$) of the square wave loading vs. the cycles relative to total coupon lifetime (n/N) at ±37.9 MPa and 0.5 Hz.

6.4 Cycle Based or Cumulative Time under Load Based Fatigue Response

As discussed earlier (Section 2.2.4) the lifetime of fiber dominated fiberglass laminates (such as (0)n, (0/±45)n and (0/90)n) have been found to follow a cumulative cycles to failure criterion like most metals, with cumulative time under load only of importance at very low cycles or R-values with low cyclic amplitude relative to the (tensile) mean stress, where fiber static fatigue response becomes significant [28,31]. However, the cumulative strain based metric applied here to off-axis laminates implies a creep dominated, cumulative time under load rather than total fatigue cycles based criterion.

The sine-wave loaded fatigue tests, when compared to creep tests in terms of gross test duration to failure, show very similar trends for simple tensile-tensile or compression-compression R-values like 0.1 or 10 (Fig. 58), implying a cumulative time criterion. Reversed loading complicates the interpretation of cyclic creep response, although high cumulative strains are still

107

observed (Fig. 54). When plotted with tensile and compressive creep data in Figure 65, the square wave fatigue strains are consistent with the creep strains both for tension and compression, at shorter times. As resin cracking is observed, around 0.75% strain or below, the square wave strains diverge from the respective creep strains, and failure ensues. The timescale where this occurs is in a similar range for all frequencies, considering the decade or so typical scatter at a particular stress level. When the data are plotted in terms of cycles rather than time, they separate according to frequency, Figure 66. As shown in Figure 67, the cycles to approach 0.75% strain, where rapid strain increases ensue, are simply proportional to the frequency, since the damage process is governed by cumulative time under load, not cycle numbers.

Thus, as evidenced by square wave data which allows a clear definition of cumulative time, test results for a broad range of frequencies (below the range which produces significant hysteretic heating), failure of off-axis laminates occurs after a consistent cumulative time under tensile or compressive load, regardless of total cycles endured. This is contrary to the cycle dominated behavior of fiber dominated laminates.
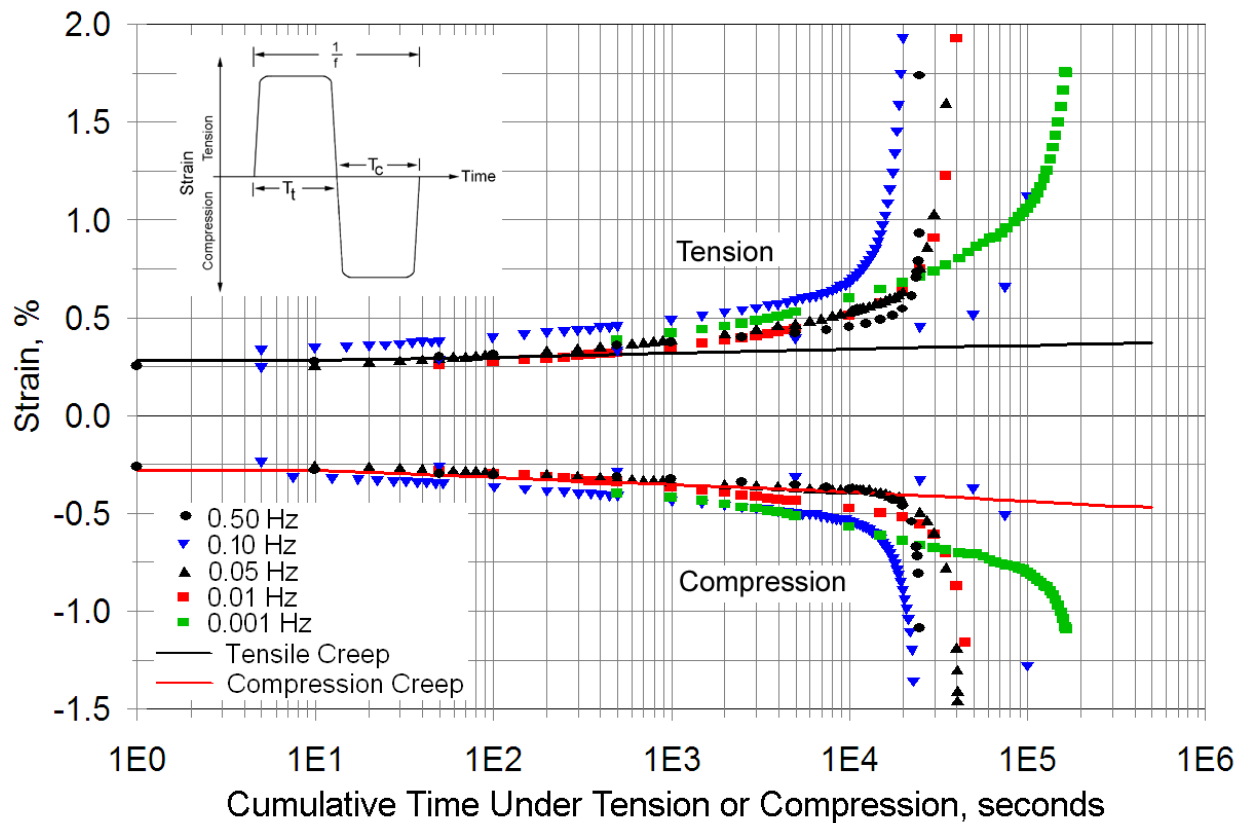
Figure 65 Strain accumulation vs. cumulative time under tension and compression parts of R = -1 square waveforms at different frequencies, compared to simple creep strains at the same stress of ±37.9 MPa, R = -1.
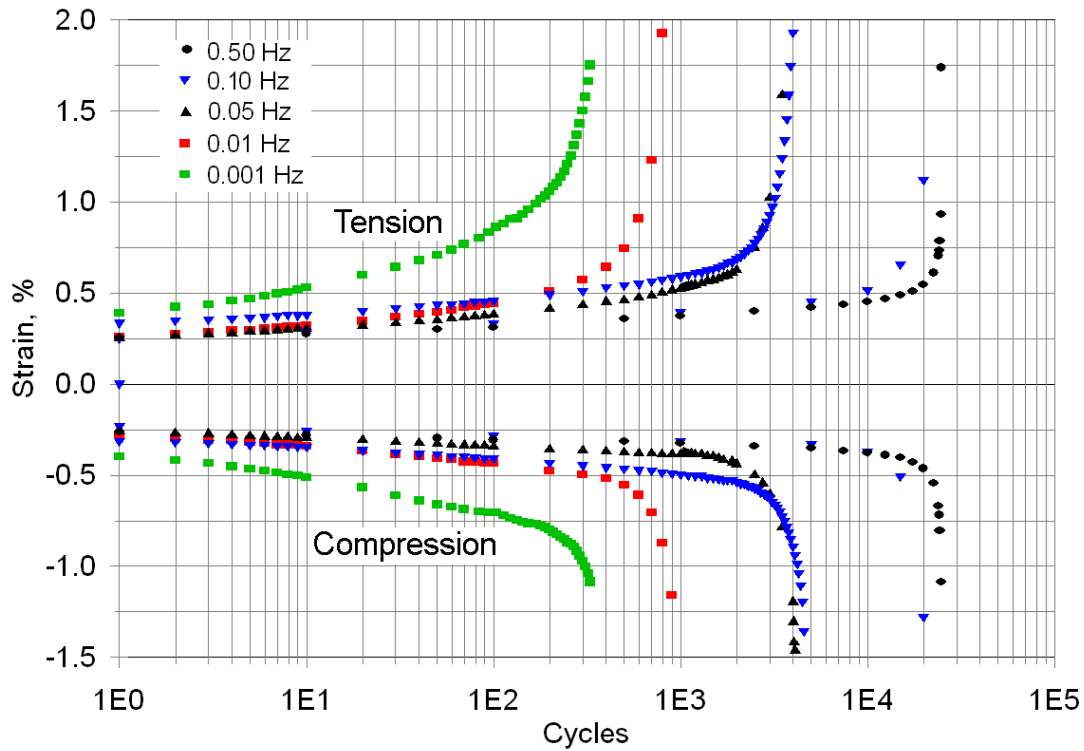
Figure 66. Data from Figure 65 plotted in terms of cycles rather than cumulative time.
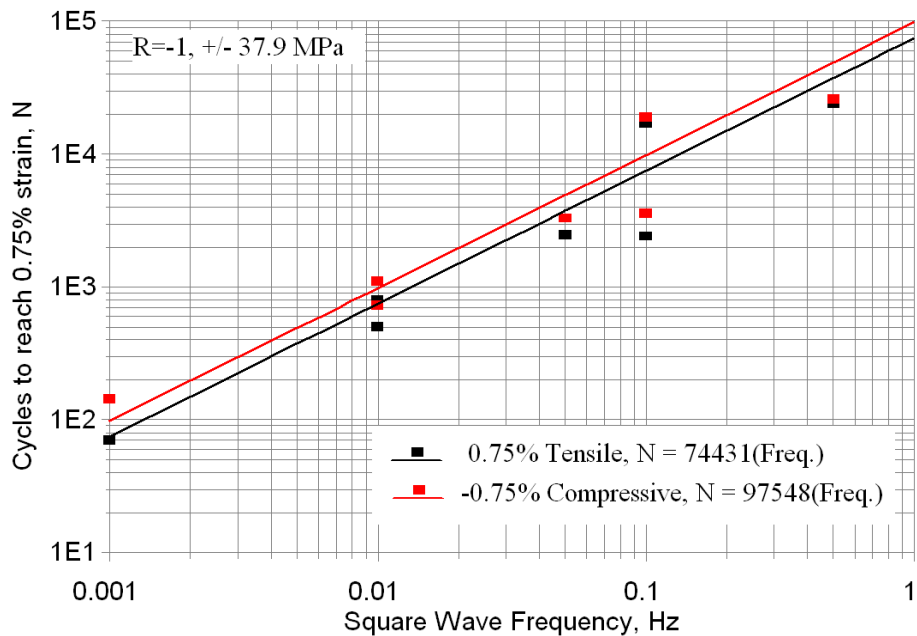
Figure 67. From Figure 66, plot of cycles to reach a strain of 0.75% (where damage becomes prevalent) vs. square wave frequency.

6.5. Resin Effects

A series of tests was also conducted on a tougher but less creep resistant urethane resin, as a comparison to the baseline epoxy system (urethane resin laminates were supplied by an industry partner). Tensile fatigue tests of unidirectional, 0° laminates discussed earlier (Section 5.4, Fig. 40) showed comparable or slightly improved fatigue resistance for the urethane compared to the epoxy; both were much superior to a typical polyester.

Double bias laminates with fabric P were also supplied with the urethane resin. DB laminates are resin dominated in their properties as discussed in the last section, and the basic tensile stress-strain curves (Figure 68) and creep curves (Figure 69) (compression curves are similar) show higher strains and reduced stiffness compared to the baseline epoxy resin laminates. The fatigue S-N curves for the DB laminates (Figure 70) show reduced fatigue resistance in tensile fatigue (R = 0.1) but only slightly reduced resistance in reversed loading (R = -1). Fatigue exponents shown on the curve fits were slightly higher for the urethane, and consistent between the two R-values for each resin.

Thus, the reduced tensile creep resistance (Figure 69) for the urethane resin laminates correlates to reduced DB laminate tensile fatigue resistance (Figure 70). Strains recorded during tensile fatigue show a similar pattern to the epoxy (Figure 71), but the fatigue running strains are again higher for the $\pm 45^O$ urethane resin laminates than for the epoxy at the same stress levels.
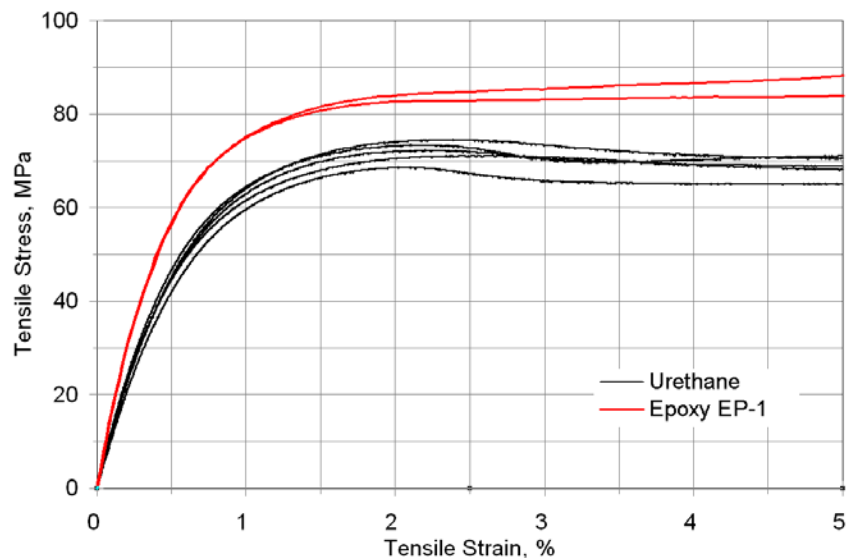
Figure 68. Comparison of tensile stress-strain curves for polyurethane and epoxy resin $\pm 45^O$ laminates loaded at 0°.
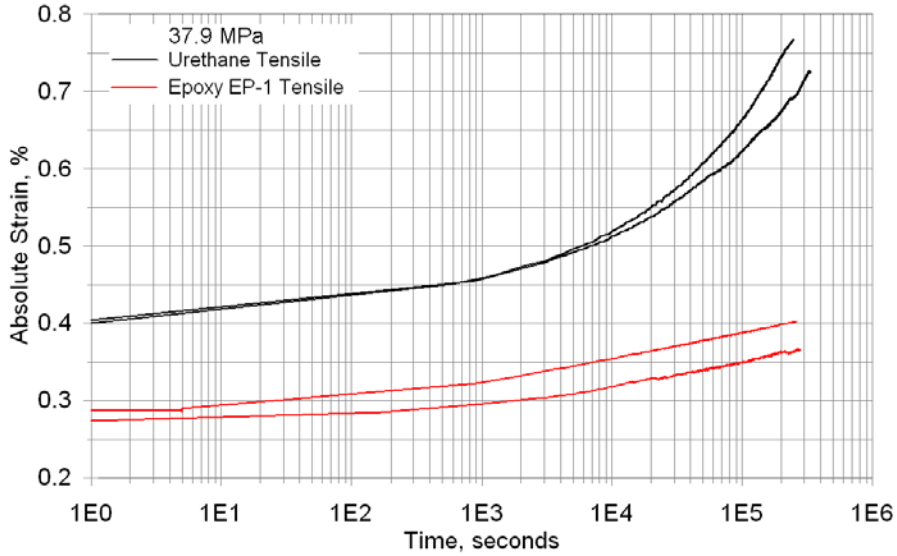
Figure 69. Comparison of creep strain vs. time curves for ±45° laminates with urethane and epoxy EP-1 resins at 37.9 MPa constant applied tensile stress.
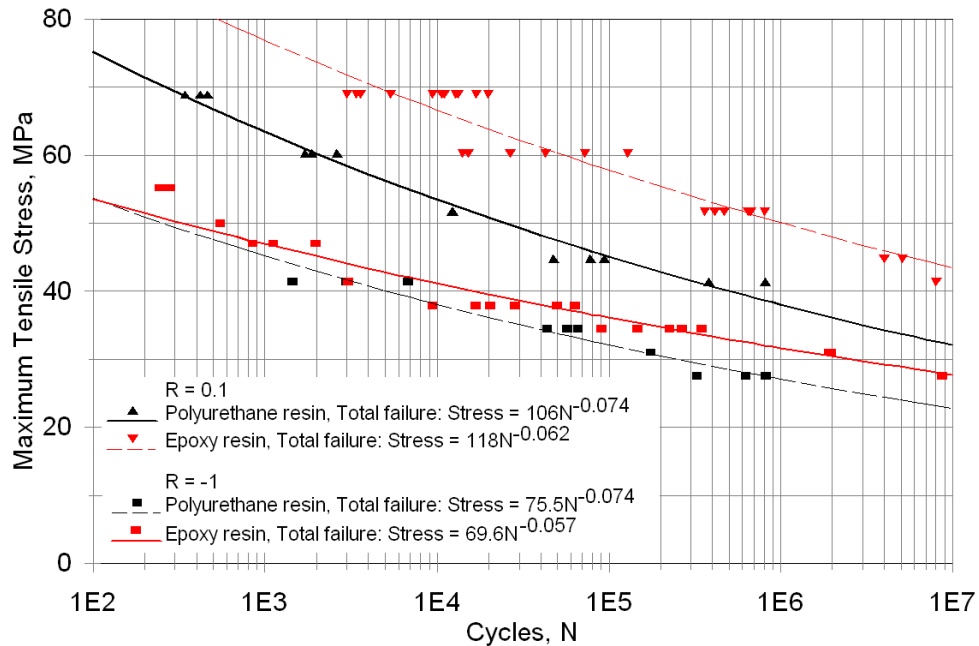
Figure 70. Tensile and reversed loading fatigue S-N results for total failure for urethane and epoxy EP-1 resin ±45° laminates with the same DB glass fabric, R = 0.1.
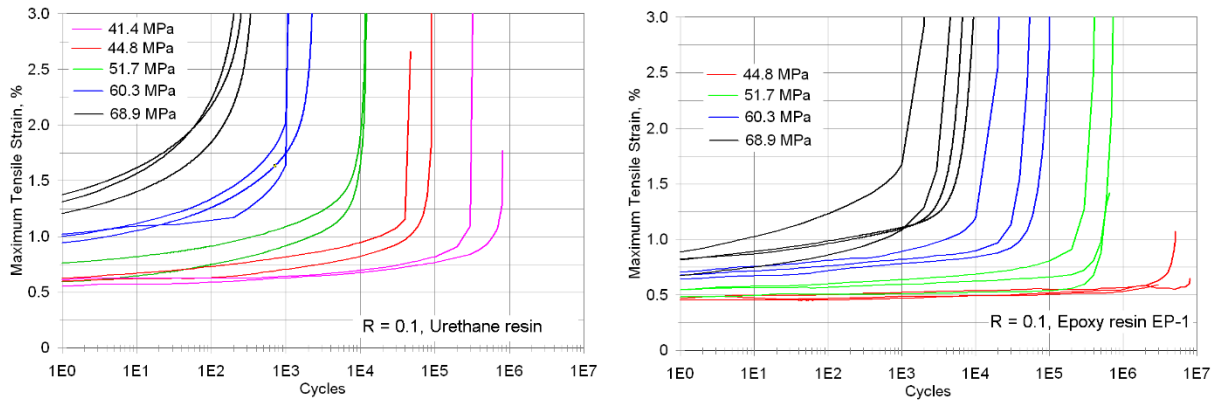
Figure 71. Comparison of maximum strain vs. cycles data at corresponding maximum stresses for urethane (left) and epoxy resin ±45° laminates; R = 0.1, sine wave loading.

7. Adhesive and Core Material Fatigue

7.1 Overview

This section presents recent studies of blade adhesive joint testing and analysis and limited test results for core material tests. Ref. [2] gave extensive results for strength-based testing of adhesive joint coupons including the development of a stiff notched lap shear coupon suitable for thick adhesives and loading at all R-values (Figure 72). Figure 73 gives typical fatigue data for R = 0.1 and -1.0 for a baseline epoxy adhesive and a recent toughened adhesive. Failure for this coupon geometry initiates at the notch root, in the adhesive, as intended. The fatigue failures tend to be initiation dominated, although some stable crack growth is observed [2].

The results presented in this section are directed towards fracture mechanics based testing, where the propagation of cracks in coupons containing starter cracks is studied [58]. Fracture mechanics treatment is more appropriate for large, complex structures like blades which typically contain flaws (see background Section 2.2.5; adhesive and adherend materials are given in Section 3.1.3, and test methods are described in Section 3.4.3).
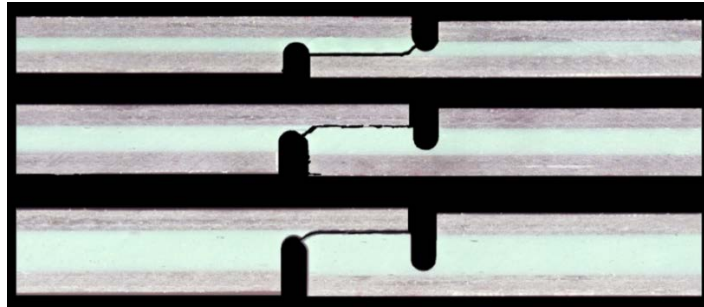
Figure 72. Failed coupons with 3.25, 6.50 and 9.75 mm thick adhesive layers, ADH-1, 25.4 mm overlap length [2].

Legend:
- ADH-1 R=0.1, Stress = $22.6N^{-0.109}$
- ADH-1 R=-1, Stress = $24.6N^{-0.146}$
- ADH-6 R=0.1, Stress = $29.2N^{-0.135}$
- ADH-6 R=-1, Stress = $20.8N^{-0.128}$
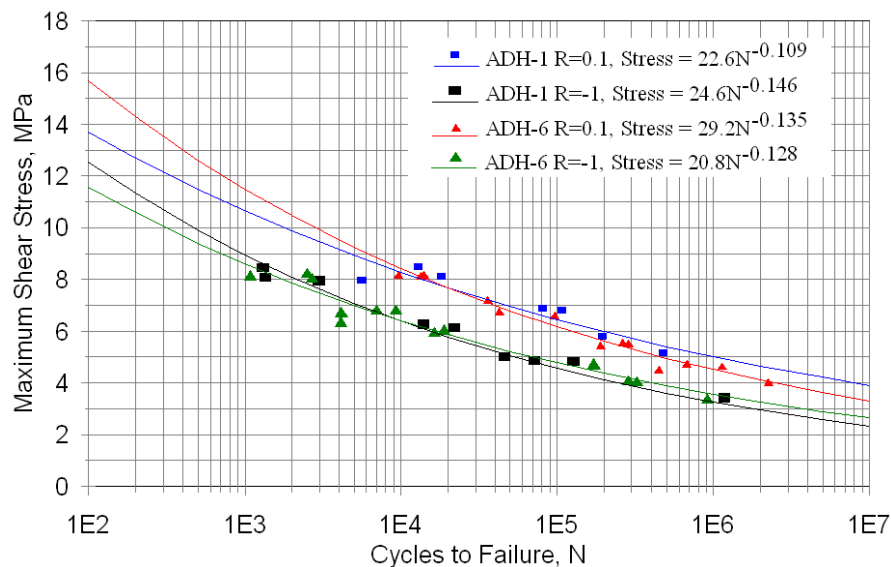
Figure 73. Tensile and Reversed Loading Fatigue S-N data for Two Blade Adhesives, Notched Lap Shear Coupon [2].

7.2 Mixed Mode Static and Fatigue Crack Growth in Wind Blade Paste Adhesives

7.2.1 Crack Propagation Paths and Stability

Crack paths in adhesive joints are recognized [33] to vary depending on overall geometry, far field stresses (T-stresses), and adhesive, adherend and interface properties. Cracks do not necessarily follow the path of least resistance [33], as observed in this study and discussed later. Simulated wind blade joints [2] and actual wind blade failures are typically characterized by cracks starting in the adhesive layer, and then transitioning to interlaminar cracks in adjacent laminates. A transition from the adhesive into the laminate (through the first ply) is shown in Figure 74 for a static crack in a symmetric version of the long CLS specimen with steel reinforcement (Figure 18); this was the only geometry where a transition into the laminate interior was observed for the thick unidirectional fabric used in this study. The laminate adherends selected for this study were intended to reduce the tendency for the crack to transition into the laminate, to allow study of adhesive and interface failure. In particular, thick unidirectional fabric was used as contrasted with less thick off-axis fabrics like DB [2]. Actual wind blades often contain structure bonded to DB layers, so there would be a greater tendency of cracks to transition into the laminate than for the tests reported here. The topic of mixed mode interlaminar cracks with this class of laminate is discussed briefly, later. The major transition from adhesive to interior laminate is in addition to more localized crack path transitions from cohesive in the adhesive to the laminate fabric interface. These crack path transitions were always associated with unstable jumps or arrests of the crack in this study.

Crack paths and crack path transitions observed in this study are illustrated in Figure 75, on sections parallel and transverse to the crack growth direction. Cracks in the baseline adhesive, ADH-1, tended to grow inside the adhesive, but associated with the peel-ply surface of the laminate resin, path B. Shown at several stages of development in Figure 76, the crack tip area gradually formed from micro-cracks initiating at peel ply features, pores, and short adhesive fibers, over a zone about 0.2 to 0.4 mm length, then merging into a continuous crack over 1-2 mm ahead of where complete crack opening and sliding appeared possible. The extensive porosity is evident in the micrographs. ADH-1 cracks in this path were stable, growing slowly in static or fatigue tests for the CLS geometries. Often, the entire 100 mm crack length for CLS specimens with steel reinforcement (Fig. 18), and 50 mm crack length for short CLS specimens without steel, would show this path, although rare transitions to path C were observed (Figure 77, bottom). The crack stability for these CLS geometries satisfied the major requirement for the study of mixed mode crack propagation. Other geometries such as the long CLS specimen without steel reinforcement, and a symmetrical CLS geometry with two adhesive layers, produced frequent unstable crack jumps to path C for adhesive ADH-1 under both static and fatigue loading. Cracks in the DCB, MMB and ENF geometries (Figure 19) also became unstable after a few mm of growth, transitioning from path B to path C (Figure 78), with the ENF geometry showing the greatest extent of stable growth (Figure 77, top), about 10 mm.

Damage along and ahead of the cracks in adhesive ADH-1 (Figs. 76 and 77) is typical of hackle formation commonly observed for mixed mode and mode II delamination cracks in brittle resin laminates [57]. While the thick adhesive allows hackle-like features associated with the crack, which are relatively large (0.1-0.3 mm deep) compared to those possible with thin adhesive

114

layers or interlaminar regions in most composites, the damage was localized to a small fraction of the total adhesive thickness for path B cracks. Occasional larger zones of crack kinking were observed for unstable cracks on path C.
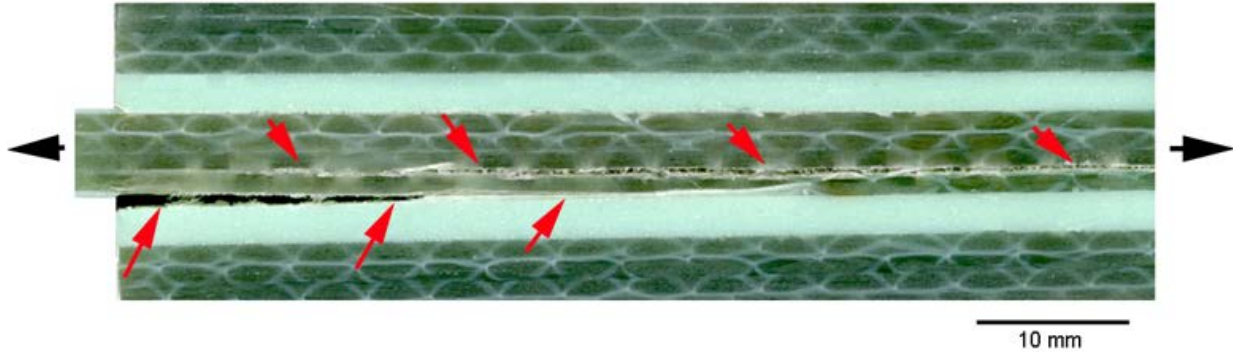
Figure 74. Photograph of crack transition from adhesive into laminate interior, symmetrical CLS geometry, 2.4 mm thick adhesive ADH-1, crack growth left to right.
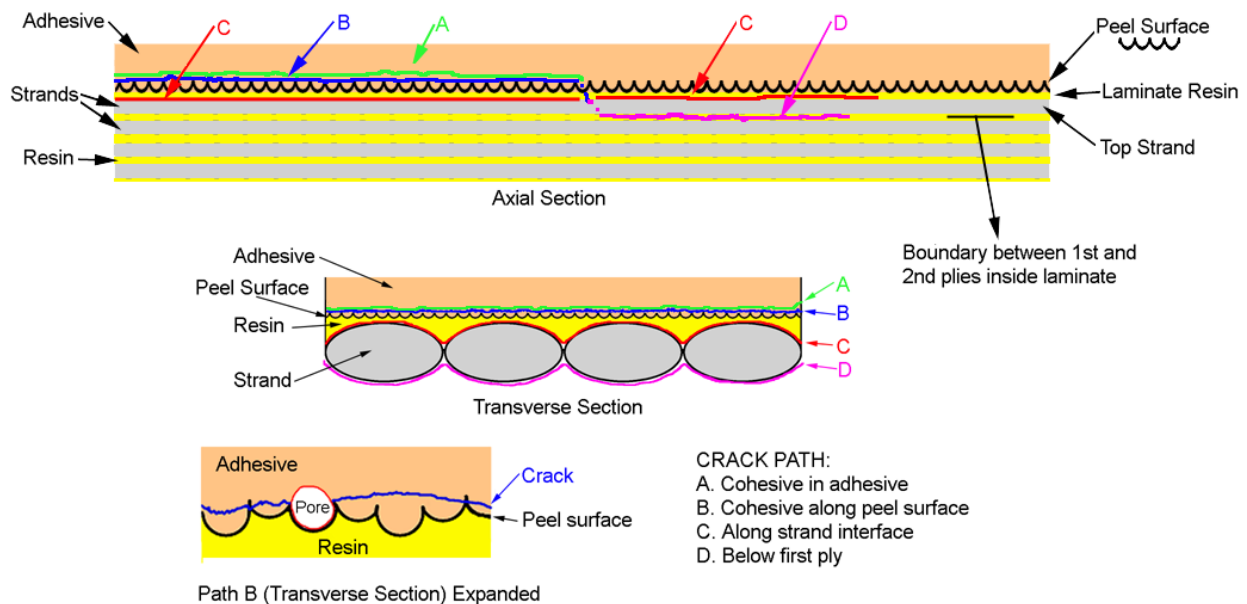
Figure 75. Schematics of local crack growth paths in axial and transverse directions (possible transitions shown on axial section, crack growth left to r): path A, ductile, cohesive within the adhesive, typical of adhesive ADH-6; path B, cohesive within the adhesive, but associated with micro-fracturing along laminate resin peel ply surface, typical of ADH-1; path C, along the laminate strand interface, typical of ADH-5 throughout, and other adhesives after transition; and path D, within the laminate, below ply which is adjacent to adhesive.

Figures 79-84 show SEM micrographs of fracture surfaces. As noted above, cracks in the most brittle adhesive, ADH-1, which also contains short glass fibers, propagated primarily along path B, sometimes transitioning to path C at longer lengths. Fracture surfaces for the as molded peel-ply surface and a path B crack are shown in Figures 79 and 80 at similar scale. The mode II component to the crack forces it to the laminate interface area [34]. The zone along the peel-ply contains many small pores and oriented short fibers from the adhesive, which produce extensive sub-crack initiation, coalescing into the main crack (Figure 76). The complex fracture pattern produces rough, high energy surfaces, so that the ADH-1 adhesive, which has the lowest G_{Ic} in pure mode I, has the highest crack resistance in the CLS test, shown later. The surface roughness is much greater for ADH-1 in mixed mode than pure mode I DCB with the crack in the mid-thickness (compare Figures 80 and 81, taken at the same magnification). The fracture surface features for crack path B, Figure 80, and the corresponding hackle formation in Figure 76, correlate to the spacing of the peel-ply features in Figure 79.

Cracks in mixed mode for the intermediate toughness adhesive, ADH-5, propagated along path C (Figure 82). Occasional chunks of resin and adhesive up to the peel ply surface can be seen where there are local pores on the peel ply surface, as near the center of the micrograph in Figure 82. The toughest adhesive, ADH-1, generally fails along path A, just inside the adhesive, similar to path A, with significant porosity associated with the peel-ply pattern for this hand mixed adhesive case (Figure 83). At longer crack lengths for the CLS specimens, a transition to path C is observed.

Crack growth paths under both fatigue and static loading were similar for each adhesive. A reversed loading fatigue crack surface for adhesive ADH-1 is given in Figure 84. This micrograph indicates a mixture of paths B and C. Mixtures of paths A and C were observed on adhesive ADH-6 fatigue crack surfaces. ADH-5 fatigue cracks remained in path C throughout.
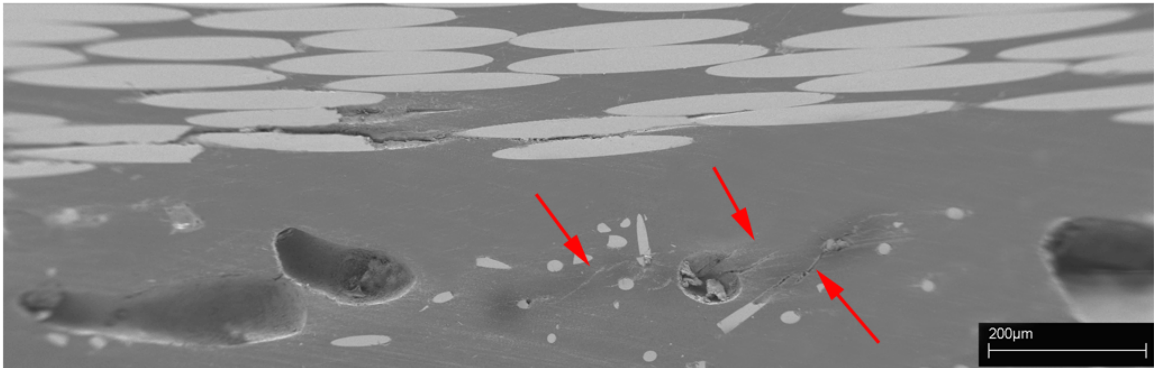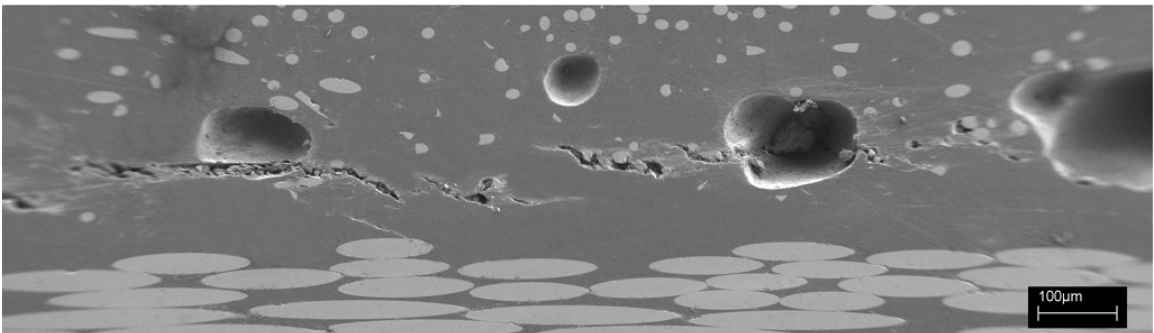
Figure 76. SEM micrographs of crack tip area, static CLS specimens with adhesive ADH-1, crack path B, crack growth left to right: fully cracked, partial shear displacement (top, crack 1a); mostly cracked (middle, crack 1b); and local micro-cracking at arrows ahead of tip at fibers and pores (bottom, crack 1a).
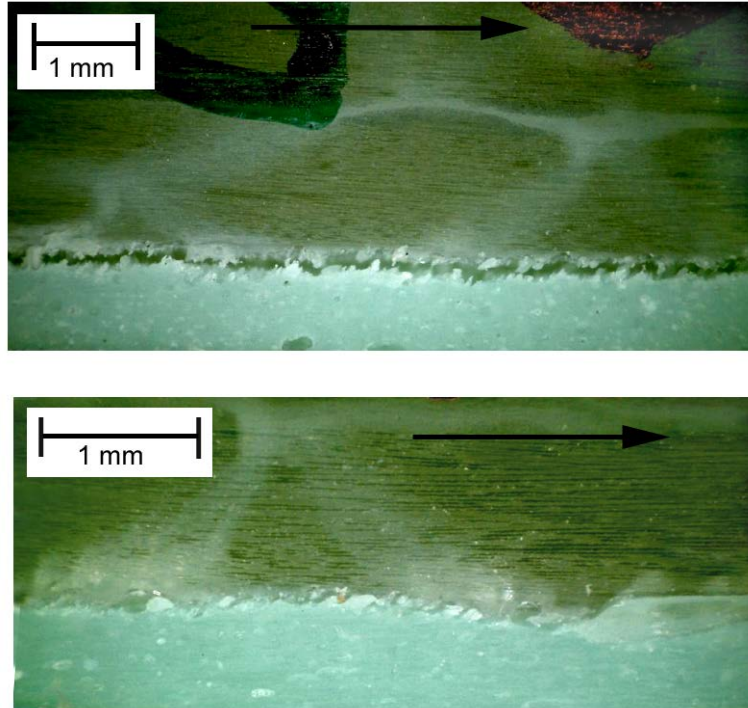
Figure 77. Optical micrographs of static crack paths with laminate strand and stitching visible on top, adhesive on bottom: ENF specimen, path B, crack growth left to right (top) and CLS specimen with steel showing transition from path B to path C on right end, crack growth left to right (bottom); adhesive ADH-1.
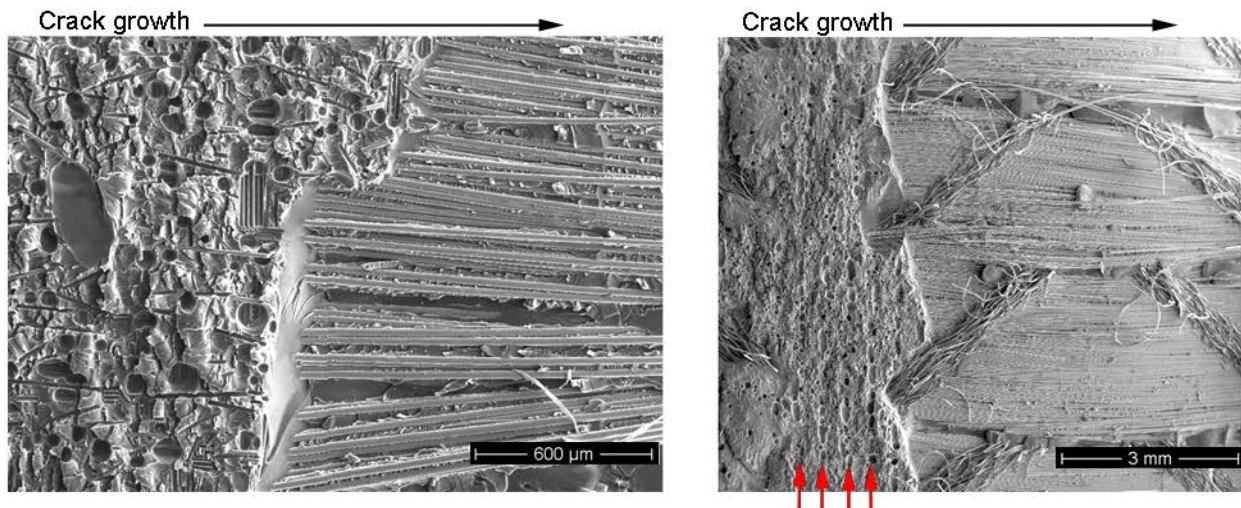
Figure 78. SEM micrographs of typical crack path transitions from path B to C in two MMB specimens, adhesive ADH-1, crack growth left to right. Low magnification fracture surface on right shows rows of pores on left side whose spacing corresponds to the peel-ply pattern dimension, and possible interaction of transition crack with fabric strand stitching (arrow).
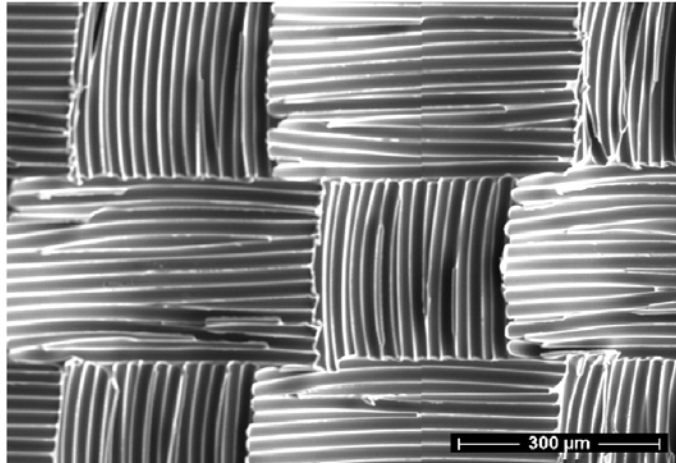
Figure 79. Laminate peel-ply surface as-molded.
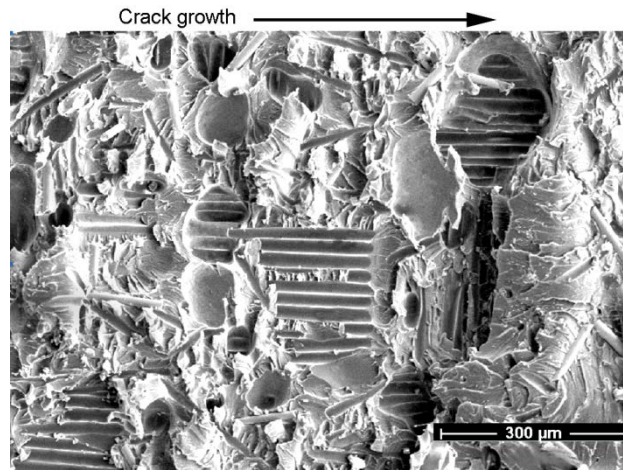
Figure 80. Path B showing fracture through pores over peel ply and through adhesive, ADH-1, static test, looking toward laminate side.
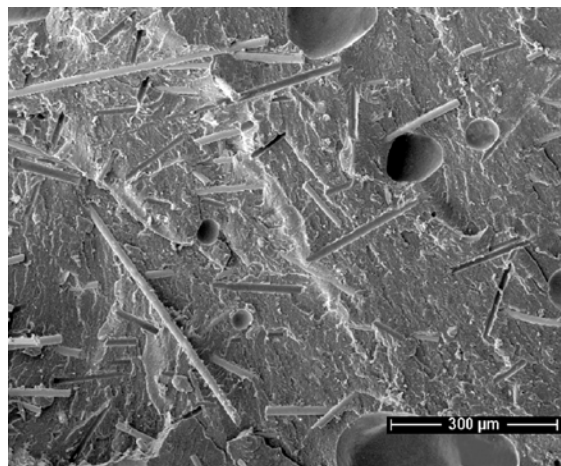
Figure 81. Static fracture surface of ADH-1, DCB test, crack growth at mid-thickness left to right, showing relatively smooth surface compared to Figure 11, with pores and short fibers.
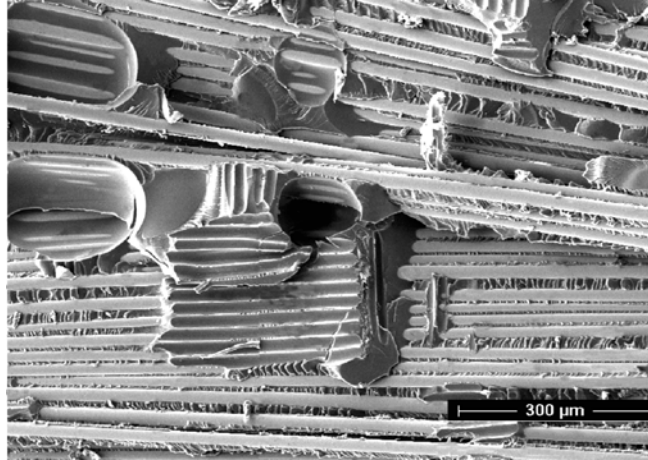
Figure 82. Crack path C, along reinforcement surface, with resin patch showing peel-ply imprint at pore (center), static CLS test, ADH-5, crack growth right to left.
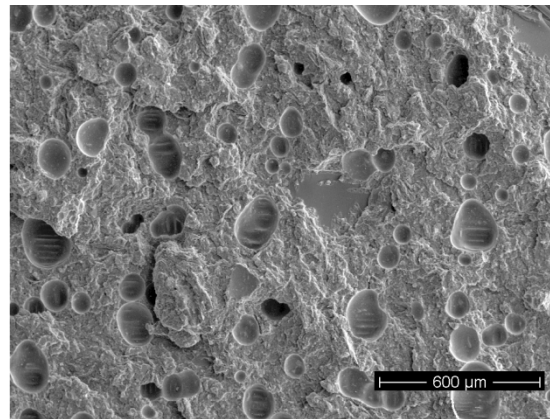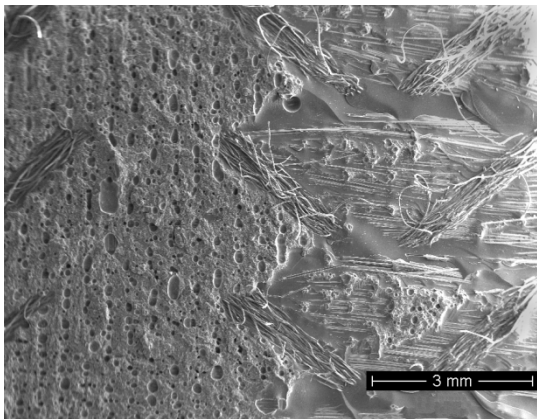
Figure 83. Crack Path A, cohesive near the interface, showing transition to path C (left), crack growth left to right, static CLS test with adhesive ADH-6.
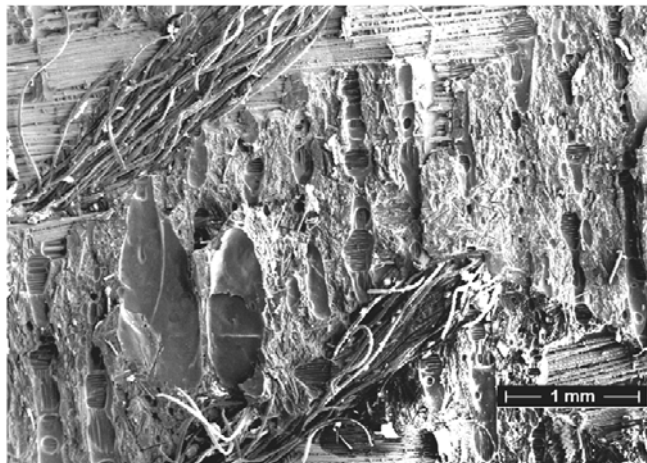
Figure 84. Low magnification reversed loading fracture surface looking toward laminate side, showing transitional characteristics of crack paths B (patches of fractured adhesive) and C (growth along glass strand surface inside laminate, also showing polyester fabric stitching), crack growth left to right, ADH-1, R = 0.1, CLS test.

7.2.2 Mixed Mode Bending Static Tests

As noted above, for many different geometries, cracks tend to transition from the adhesive (paths A and B), into the strand surface (Figure 78) or the laminate interior (Figure 74). Resistance to propagation is then governed by the laminate delamination resistance (interior laminate) or the similar resistance to separation of the laminate surface resin from the strands (laminate surface). The strand structure of most infused laminates creates matrix rich areas between strands which penetrate through the ply, and are separated from the strands as part of the crack growth process (Figure 76, path C). As a comparison to the adhesive fracture resistance, which follows, a typical dataset for mixed mode interlaminar fracture is given in Figure 85. The various SERR values are calculated from MBT, Eq. 2-7, with critical initial crack propagation loads determined as in Figure 20. Figure 85 is a plot of the total calculated SERR at initial crack growth, G_T (= $G_I + G_{II}$) vs. the fraction of G_{II} at the test condition, G_{II}/G_T. G_{II}/G_T equals G_{Ic} for the DCB test ($G_{II} = 0$) and equals G_{IIc} for the ENF test ($G_I = 0$).This laminate is similar to the adherends in the adhesives study except for the resin, which is SP Systems Prime 20LV, a similar infusion epoxy to that in the adhesives study. Tests were the same as those illustrated in Figure 19. The data indicate much higher mode II toughness, G_{IIc}, compared with mode I G_{Ic}; mixed mode cases are significantly tougher in terms of total strain energy release rate than G_{Ic} as the mode II contribution increases. This trend is typical of relatively brittle resin laminates which show the hackled growth pattern discussed previously when a significant mode II contribution is present [57].

Relative to Figure 85, pure G_{Ic} and G_{IIc} values for the adherend laminate system used here are similar [2], 303 J/m^2 and 3446 J/m^2, respectively at $V_f = 0.60$, for the same $0^o/0^o$ interface. If the fabric backing to backing interface is cracked, the G_{IIc} value is reduced to 1887 J/m^2, as the backing creates a more nearly flat crack surface which doesn't follow the strand surfaces. Delamination results for other laminates may vary; biax ($\pm45^O$) interfaces with RTM polyester resin laminates showed higher G_{Ic} and G_{IIc} compared to $0^O/0^O$ interfaces in an early study, apparently related to extensive resin cracking away from the immediate crack interface [37].

MMB static test results for the adhesive joints in Figure 19 are given in Figure 86 (2.4 mm thick adhesive ADH-1). The data are presented for MBT calculations, Eq. 2-7, and finite element analysis (FEA) using the VCCT method [37] of calculation for the strain energy release rates. The two calculation procedures are in general agreement for this series of tests. As noted earlier, crack propagation for these tests became unstable after a few mm of growth, transitioning from path B to path C, Figures 75 and 78. Only the pure mode II, ENF tests showed stable growth for the order of 20-30 mm. All mixed mode and pure mode II cracks remained in the top (compression side) interface as indicated in Figure 19; if the starter crack film was located on the bottom interface, the growing crack would kink to the upper interface.

The trend of the data in Figure 86 for the adhesive joint is generally similar to that for laminate delamination in Figure 85. The adhesive G_{Ic} value (G_T at $G_{II}/G_T = 0$) is higher, but the mixed mode G_T increases less rapidly as the mode II contribution increases, relative to laminate delamination. G_{IIc} values ($G_{II}/G_T = 1$) for both test series fall in a similar range. The several G_{Ic} values shown represent variations of the starter crack for the DCB test. When the Teflon film is positioned near mid-thickness of the adhesive, the lowest G_{Ic} values are obtained. G_{Ic} is increased when the starter film is positioned at the top interface, and is highest when the starter

crack is produced by mixed mode loading at $G_{II}/G_T = 0.55$, again at the top interface. When the starter crack is at the interface, subsequent mode I propagation is away from the interface, into the adhesive mid-thickness. Also shown on the plot are results for different adherend thicknesses, 3.9 (0_3) and 5.0 mm (0_4). The thicker adherends produced somewhat lower G_{Ic} and G_{IIc} values.

FEA analysis includes the adhesive geometry and properties, while the MBT Equations 2-7 do not, as noted earlier. The FEA calculated results generally follow the MBT values in trend; minor differences in mode mixity are not shown on Figure 86. The FEA calculated DCB G_{Ic} is 34% lower than the MBT value, but G_{Ic} values for the crack near the interface are within 10% of the MBT values. The FEA results show a 2% mode II component to the DCB SERR with the crack near the interface. The symmetric CLS specimen is similar to the un-symmetric case in Figure 18, but with additional adhesive layer, laminate adherend, with notch, to create a symmetric sandwich with the single thickness of un-notched laminate adherend in the mid-thickness (100 mm long, no steel). The first crack to form grew unstably after a very short distance of stable growth. SERR values were calculated by FEA.
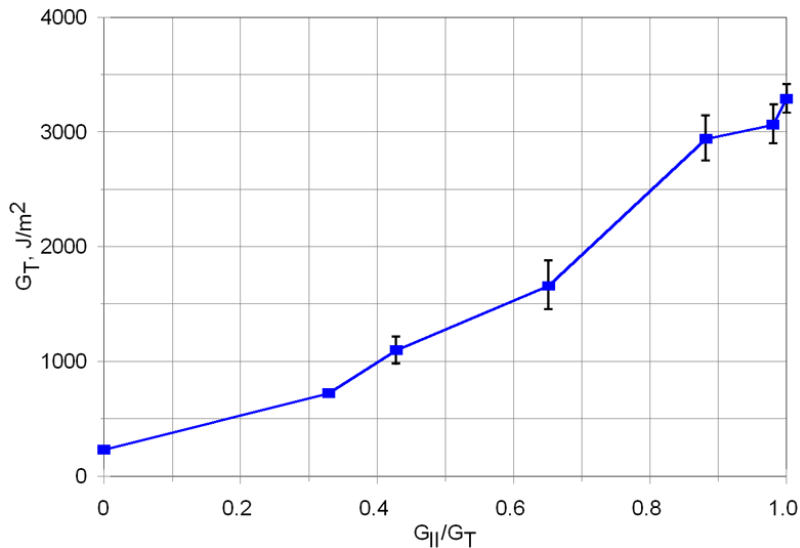
Figure 85. Mixed mode bending static test average results for laminate delamination resistance, unidirectional infused Vectorply ELT-5500 glass fabric with SP Systems Prime 20 LV epoxy, V_f = 0.51 [1].
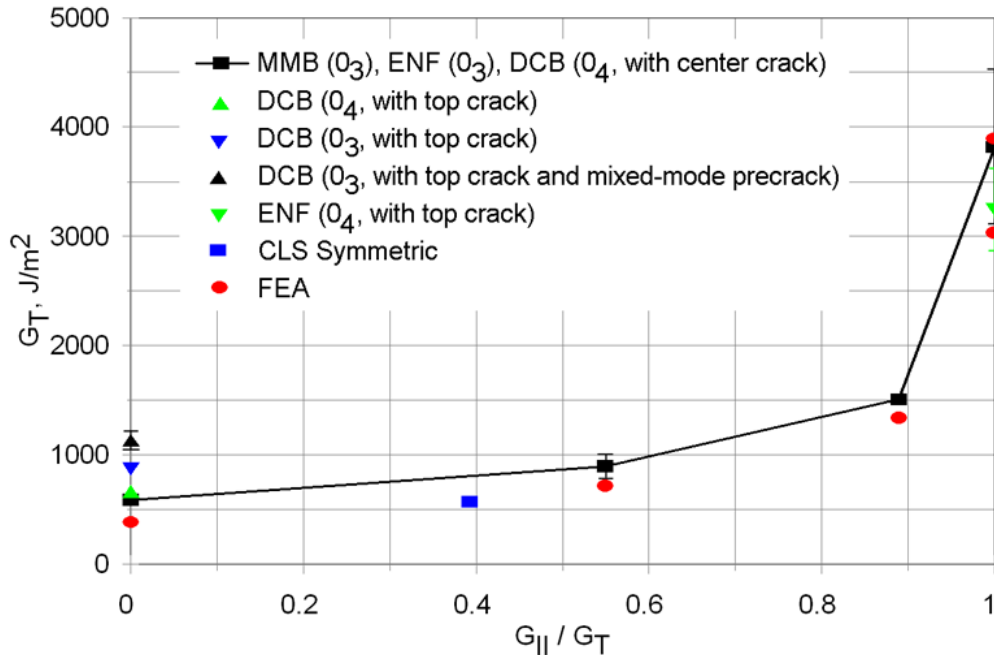
Figure 86. Mixed mode bending static test results for crack growth resistance of 2.4 mm thick ADH-1 adhesive joints: modified beam theory calculations (Eq. 2-7), comparison to FEA calculations from VCCT. Legend indicates laminate adherend thickness: $(0)_3$, three plies, $(0)_4$, four plies, starter crack at the top interface in Fig. 1, or center of adhesive (DCB); or MMB starter crack for DCB case.

7.2.3 Cracked Lap Shear Static Tests

Static crack growth results for the CLS specimens with the baseline adhesive are given in Figure 87 as the critical load for propagation, Pc, vs. crack length, a. Cracks were grown from the notch with no starter crack. All of the cracks propagated in a stable manner along path B. When Teflon film starter cracks of differing length or a fatigue starter crack were used (Figure 88), the results were similar, with the propagation load rising rapidly, approximately along the trend line from Figure 87. The fatigue crack tip was grown at Pmax/Pc = 0.40. The method of crack formation does not appear critical, and severe R-curve effects (increasing crack resistance with crack extension [58]) are not evident. The effects of type of peel-ply used to form the laminate surface, and the mixing method are shown in Figure 89. Little effect of peel ply type is evident; all cracks followed path B. Hand mixing appeared to result in more unstable crack jumps (dashed line), possibly associated with larger pores.
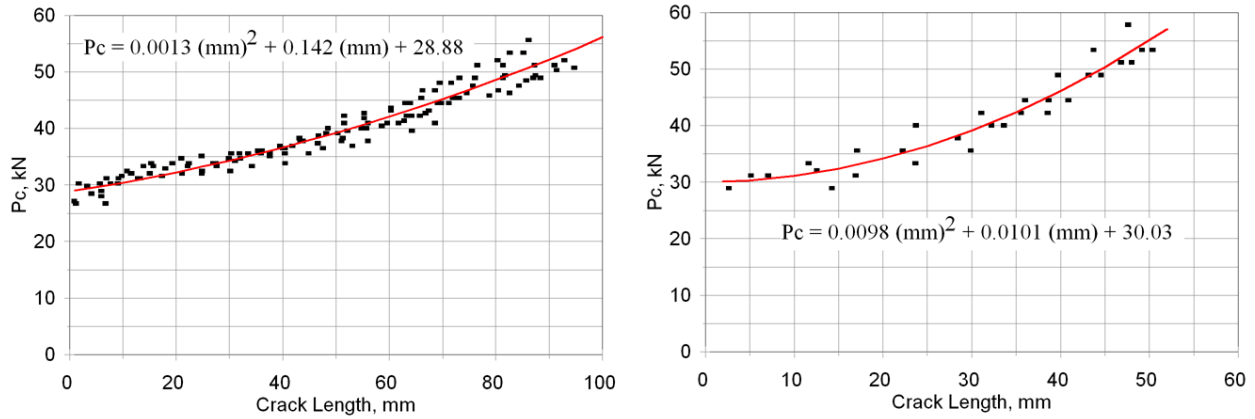
Figure 87. Static critical load vs. crack length, (a) 100 mm CLS with steel (left) and (b) 50 mm without steel, (right); adhesive ADH-1, crack growth from machined notch.
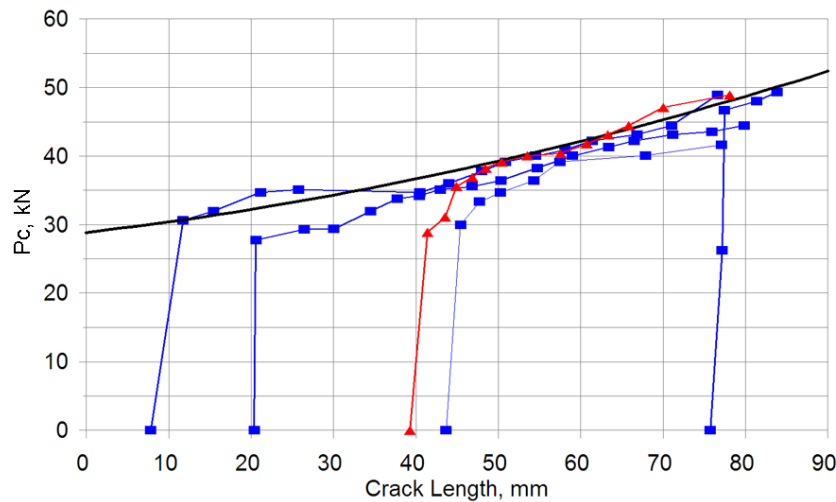
Figure 88. Static critical load vs. crack length, effect of starter crack release film length (blue) and fatigue crack length (red) compared to trend from Figure 18 (a) with no starter crack (black), long CLS with steel.

7.2.4 Cracked Lap Shear Fatigue Tests

Fatigue crack growth testing was conducted at 2-4 Hz under load control at R-values (R = min load/max load) of 0.1 (tensile-tension) and -1 (reversed loading). Crack length was monitored periodically at low magnification on a "white-out" coated surface. Individual tests were run at a constant Pmax in most cases, so the crack growth data tend to fall in groups related to the value of Pmax. Figure 90 gives the crack growth rate, da/dN, as a function of Pmax/Pc on a log-log plot for long CLS specimens with steel and short specimens without steel. Points plotted are for individual measured crack length intervals, da, corresponding to the associated cycle interval, dN. The data are separated by crack length interval, as the mode mixity varies with crack length, discussed later. While most mixed mode testing is done for a relatively constant mode mixity, Reference 38 reports results for a single-lap geometry with varying mode mixity along the crack path. There is an apparent separation with crack length of some of datasets under reversed loading, with shorter cracks propagating more slowly than longer cracks at the same Pmax/Pc ratio, for shorter cracks with the long CLS with steel geometry under reversed loading. Data for

124

other cases do not separate clearly by crack length. Data for reversed loading mostly fall above data for tension-tension, indicating about 10x faster crack growth under reversed loading at the same Pmax/Pc ratio for both specimen geometries. Crack growth is also somewhat faster for the long specimen geometry with steel than for the short specimens at similar Pmax/Pc ratios. These results are considered further in the final section.
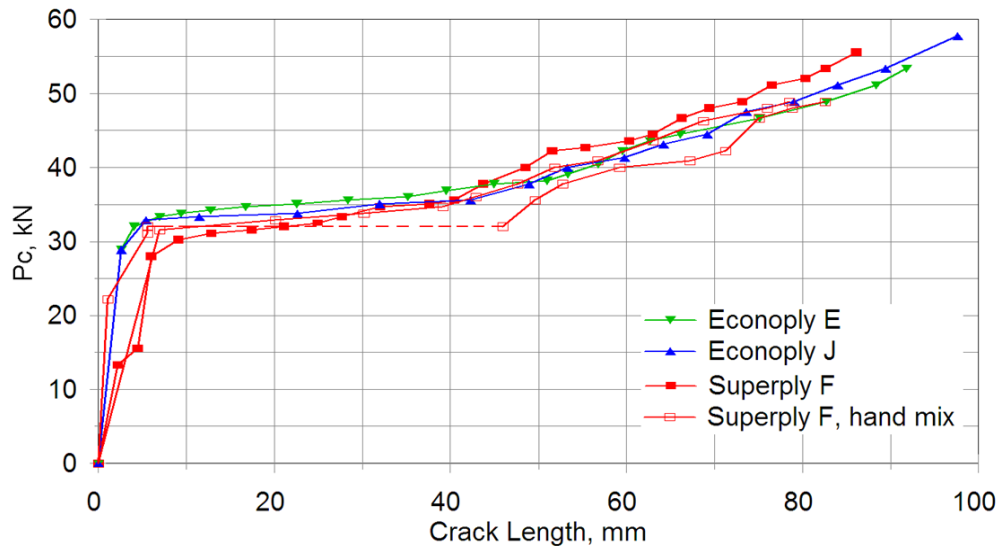
Figure 89. Effect of laminate peel-ply type and adhesive mixing method (machine mixed unless noted) on static crack growth resistance from machined notch; dashed line indicates unstable crack jump.

7.2.5 Comparison of Different Adhesives

This section compares the three adhesives used in this study (Section 3.1.3), ADH-1, ADH-5 and ADH-6, for a limited range of tests; the adhesive thickness was 3.8 mm for these tests, compared with the 2.4 mm used for the remainder of the tests, which affects the results [56]. Table 15 gives mode I G_{Ic} results from DCB tests; data are reduced using Eq. (1). The DCB results in Table 15 show adhesive ADH-6 at much higher toughness than ADH-1, with ADH-5 intermediate. Crack starter films were located at mid-thickness, and cracks for the three adhesives tended to stay in the mid-thickness area, with the most significant undulation for ADH-5. Crack growth in mode I is mid-thickness, so this test provides a measure of the inherent adhesive toughness.

Cracks in the CLS mixed mode test are forced near one interface by the shear stress component, which gives direction to the stress field so that cracks propagating under the local maximum tensile stress grow at some angle to the crack direction [15]. Static (Figure 91) and fatigue (Figure 92) data using the short specimen geometry without steel are now more similar for the three adhesives compared with Table 16; in fact, the static loads for the most brittle system, ADH-1, are the greatest of the three. The local mode of crack growth on path B (Figures 75 and 80) produces a rough fracture surface and high crack resistance for brittle adhesives compared to path C in the strand interface (Figure 81). The data for ADH-1 fall slightly below the trend in Figure 87 for ADH-1 with the thinner 2.4 mm thick adhesive, as expected [2,15,33].

Fatigue crack growth in terms of Pmax/Pc is similar for ADH-1 and ADH-6 on crack paths B and A, respectively; slightly poorer for ADH-5 on path C.

Table 15. DCB adhesive G_{Ic} results, 3.8 mm adhesive thickness [15].

Adhesive	Average G_{IC}, J/m^2
ADH-1	581
ADH-5	938
ADH-6	1626
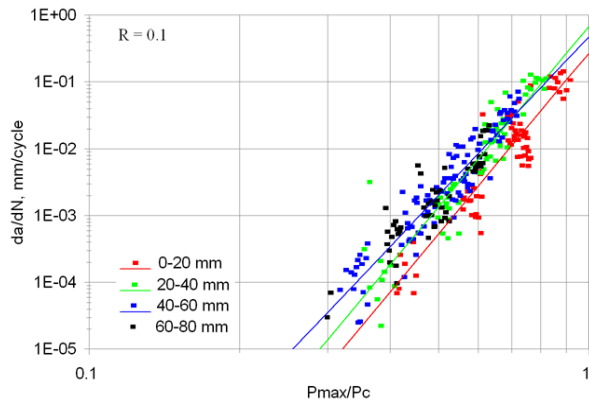
(a) Long CLS with steel, R = 0.1   (b) Short CLS, no steel, R = 0.1
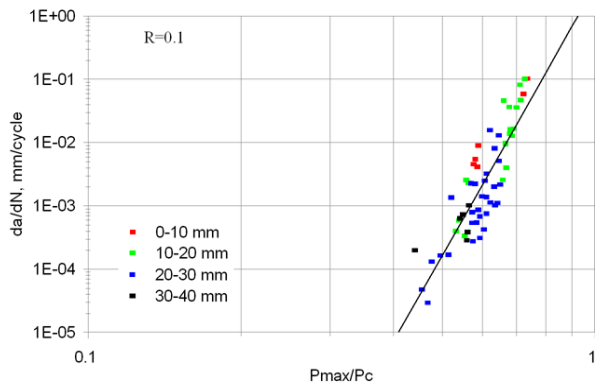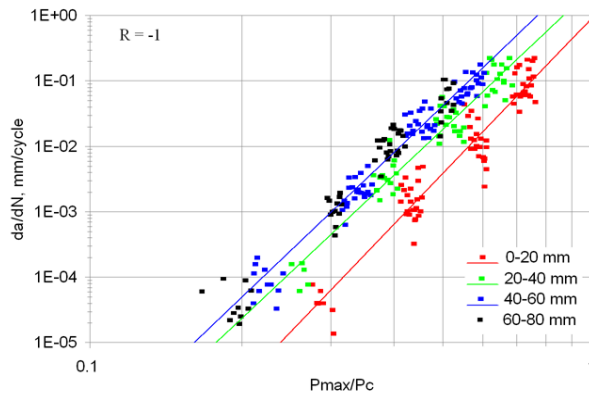
(c) Long CLS with steel, R = -1   (d) Short CLS, no steel, R = -1
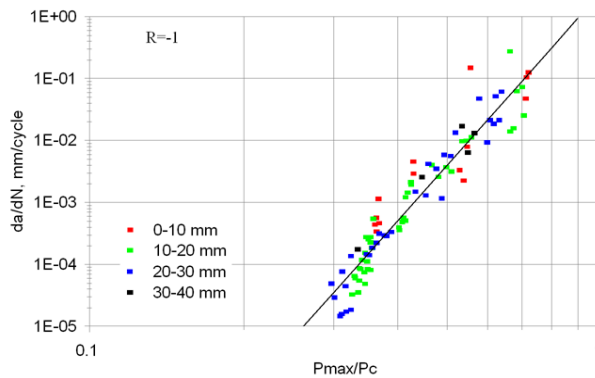
Figure 90. Fatigue crack growth data in terms of P_{max}/P_c for CLS specimens at R = 0.1 and -1. Data differentiated by crack length.

Table 16. Line Fit Equations for Figure 90.

Coupon	Figure	Crack Length Range, mm	Best Fit Equation, mm/cycle
Long CLS w/steel, R = 0.1	90(a)	0 – 20	$da/dN = 0.27\,(Pc/Pmax)^{8.99}$
		20 – 40	$da/dN = 0.67\,(Pc/Pmax)^{8.98}$
		40 – 80	$da/dN = 0.47\,(Pc/Pmax)^{7.89}$
Short CLS, R = 0.1	90(b)	0 – 40	$da/dN = 2.96\,(Pc/Pmax)^{14.14}$
Long CLS w/steel, R = -1	90(c)	0 – 20	$da/dN = 0.99\,(Pc/Pmax)^{8.03}$
		20 – 40	$da/dN = 2.77\,(Pc/Pmax)^{7.26}$
		40 – 80	$da/dN = 6.70\,(Pc/Pmax)^{7.35}$
Short CLS, R = -1	90(d)	0 - 40	$da/dN = 2.45\,(Pc/Pmax)^{9.27}$
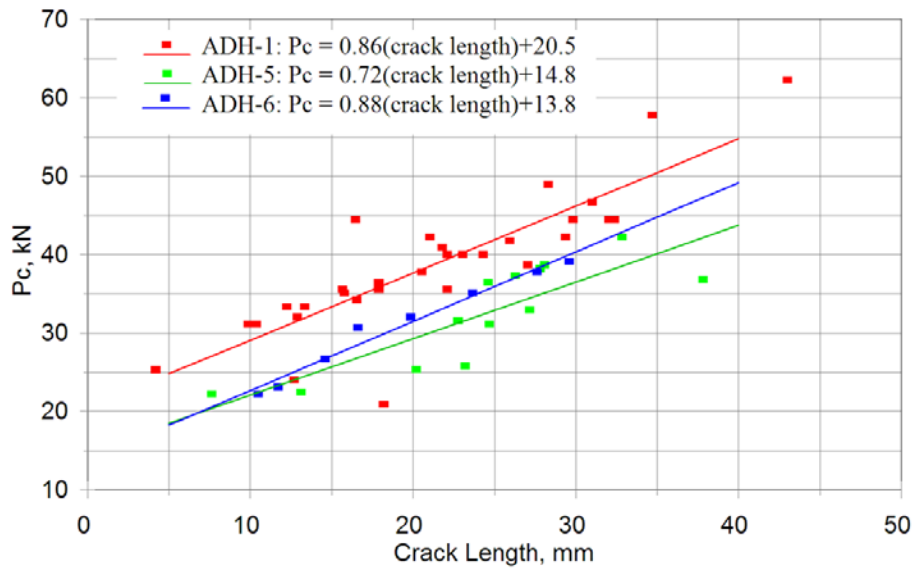
Figure 91. Static G_c values vs G_{II}/G_I; Average G_{Ic} at $G_{II}/G_I = 0$ from DCB tests, and CLS data at higher G_{II}/G_I ratios, 50 mm long specimens, 3.8 mm adhesive thickness.
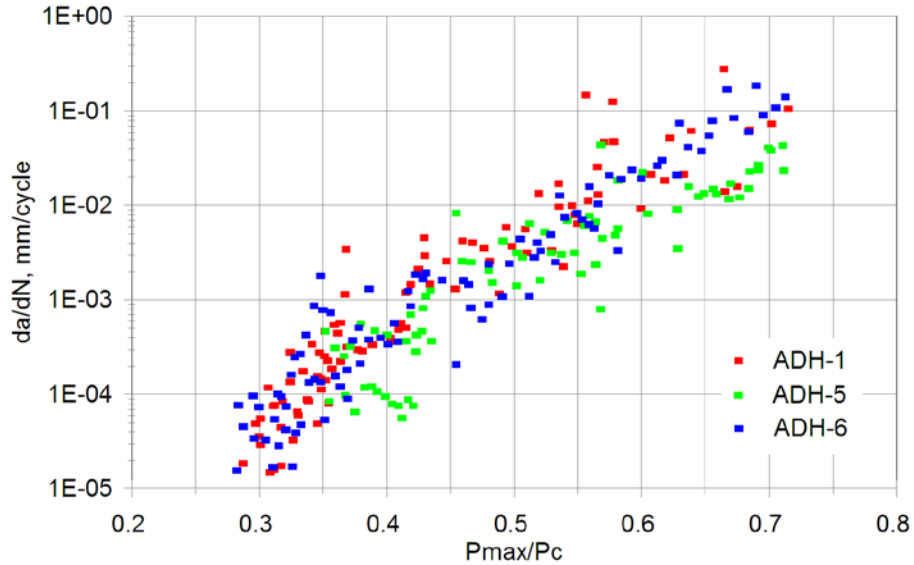
Figure 92. Comparison of reversed loading fatigue crack growth rates for three adhesives (short CLS specimen, no steel, 3.8 mm adhesive thickness).

7.2.6 Discussion

The CLS specimen geometries shown in Figure 18 proved very functional in an experimental sense: they were convenient to prepare and test using the grip system in Figure 18(b), crack growth was generally stable, following paths A, B or C illustrated in Figure 75 for the three adhesives studied, and results were reproducible, with significant but acceptable scatter. Various FEA efforts to date show mode mixities (G_{II}/G_T) in the approximate ranges of 0.4-0.6 for the short geometry and 0.5-0.9 for the long geometry with steel, based on VCCT based finite element modeling. However, significant inconsistencies were observed between the CLS geometry apparent mode mixities and those for the better established MMB, DCB and ENF flexural test geometries, in terms of correlating the fracture energies. This inconsistency apparently relates to grip fixity effects for the non-symmetric CLS test (the symmetric CLS specimen gives similar results to the MMB tests when analyzed by VCCT, but crack growth is unstable, Figure 86).

7.3 Core Materials

Limited static and fatigue results have been obtained for flexural loading of sandwich panel coupons fabricated by resin infusion. Figures 93-95 show the test geometry (four-point bending with an in-house fabricated fixture, following ASTM C393), structure of the Nextcore structured core and core/interface based failure modes. The cores tested were two densities of PVC foam, balsa, and a structured fiberglass/foam core. Cores were approximately 25 mm thick with 2.3 mm thick face sheets consisting of two plies of OCV 1800 triax glass fabric with Epoxy EP-1 resin, $V_f = 0.53$. The test results in Figure 96 show a strong sensitivity to core material and density. The structured core is difficult to define in terms of density, which may depend on details of the infusion process.
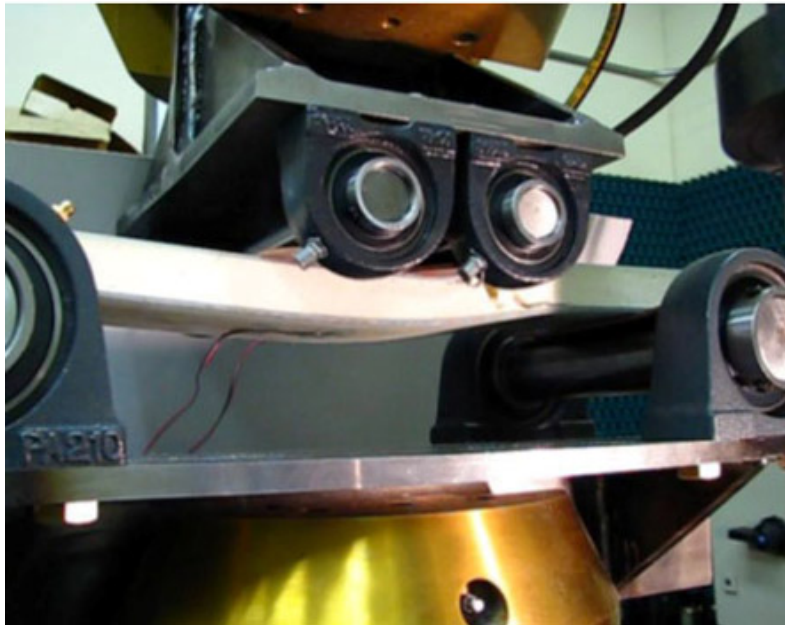
Figure 93. Sandwich panel fatigue test fixture (top) and with failed sandwich panel (bottom).

Figure 94. Nextcore Structure
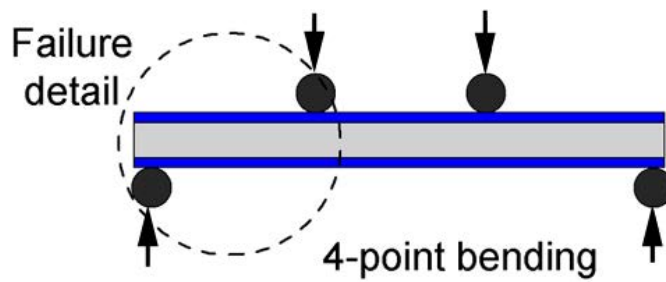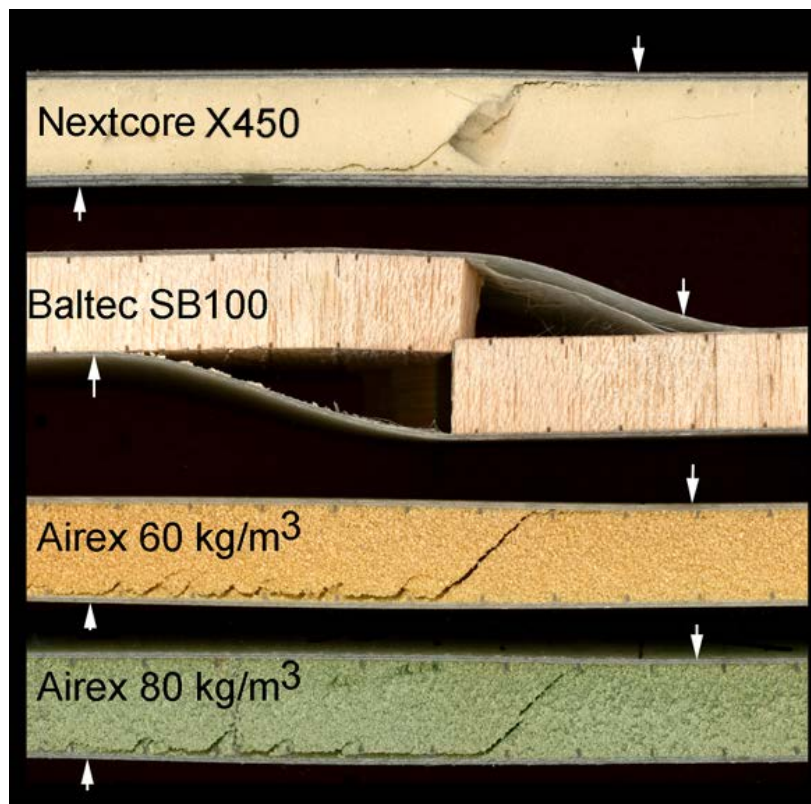
Figure 95. Failure modes for four core materials.
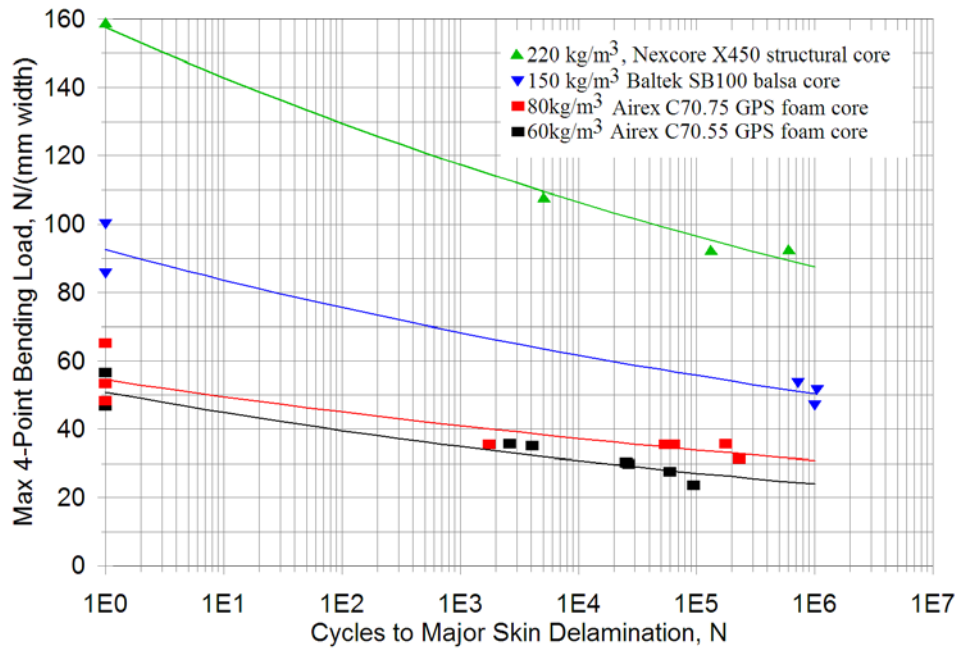
Figure 96. Flexural fatigue S-N data for sandwich panels with four core materials.

Intentionally Left Blank

8. Comparison of Fatigue Trends for Various Blade Materials

Composite structures like blades are complex in construction, containing ply drops for thickness tapering as well as other material transitions such as core materials and close-outs and intersections of spar-caps, webs and shells, and root connections. Establishing the true in-situ fatigue resistance of a material in a blade would require representative substructure testing with realistic loads, and designed to fail in the particular mode of interest. Coupon testing can include only a limited range of details, usually under uniaxial loading and with machined edges.

Material transition areas are prone to delamination between plies under fatigue loading. The database and associated reports [1,2,6,21] contain extensive results for delamination testing with standard geometries as well as mini-substructure coupons containing ply drops, and comparing the performance of various resin systems [2,16,21]. Most wind turbine blades also contain adhesives and core materials which are fatigue sensitive. Data for blade adhesives under fatigue loading have been presented in recent reports and papers [2,6]. Fatigue trends for these various blade components are compared to standard laminate fatigue behavior in this section.

Tables 17 and 18 [14] compares fatigue data trends from various database materials [1]. Included in Table 17 are laminates of increasing complexity: aligned strand, UD fabric and MD laminates, all based on the same strands and resins. Additional laminate trends are given for the transverse direction, biax fabrics and triax fabrics. In Table 18 data are given for structured coupons containing ply drops, where ply delamination is the dominant damage [2], as well as adhesives and core materials. Comparison of fatigue exponent B (Eq. 1), and the million cycle fatigue strain, gives some indication of the most fatigue critical areas of blades. Eq. (1) can be normalized as a function of the static tensile strength, UTS (determined at 0.0254 mm/s displacement rate), which does not affect the exponent. This allows approximate comparison of critical fatigue conditions based on analysis predictions of critical loads for particular failure modes. The properties must be viewed in the context of actual blade stress distribution and the presence of flaws.

As the laminate complexity increases from AS to UD fabric to MD, the fatigue S-N curves steepen, reflected in higher absolute values for exponent B, and lower million cycle strain. This trend is particularly strong for the VE and UP resins. Resin-dominated failures for neat resin, transverse direction laminate and biax laminates (Table 17) all show similar, relatively low fatigue exponents, B, compared to MD laminates and UD fabric laminates with VE and UP resins. The lower exponent B range is also observed for resin dominated delamination growth at ply drops (static delamination resistance in opening and shearing modes is significantly higher for EP1 than for UP1, with vinyl ester VE1 intermediate [2]). Resin dominated exponents indicate relatively flat S-N behavior compared to some UD and MD laminates, but the million cycle fatigue strains are lower, particularly in the transverse direction. Triax constructions have steeper S-N S-N trends in the range of the MD laminates, representing a two stage failure process in some cases, between the biax and UD layers [2,6]. The epoxy based adhesive lap shear joint fatigue exponents are relatively low, similar to the resin dominated transverse and biax trends for epoxy resin; the bulk adhesive exponent B is very low at -0.044, but joints usually fail predominantly by delamination in the laminate surface [15].

Table 17. Comparison of tensile fatigue (R = 0.1) trends for various blade materials. (a) Laminates with a progression of reinforcement structure from aligned strand to multidirectional, three resin types (B and n for stress-cycles fits).

Material Form	Resin	UTS, MPa	A, MPa	B	n	10^6 Cycle Strain, %
UD Aligned Strand (AS) Laminates, PPG 2400 Tex, Hybon 2026 Finish						
AS	EP5	1369	1573	-0.072	13.9	1.20
AS	VE4	1340	1952	-0.088	11.4	1.23
AS	UP5	1382	2153	-0.123	8.13	0.79
UD Fabric H Laminates (contain PPG 2400 Tex/Hybon 2026 Strands)						
$(0)_2$ Fabric H	EP1	995	1259	-0.088	11.4	0.88
$(0)_2$ Fabric H	VE4	912	2266	-0.170	5.88	0.53
$(0)_2$ Fabric H	UP5	884	1715	-0.173	5.78	0.39
MD Laminates, UD Fabric H and Biax Fabric T						
$[(\pm45)_2/(0)_2]s$	EP1	704	1378	-0.130	7.69	0.79
$[(\pm45)_2/(0)_2]s$	VE4	628	1228	-0.146	6.85	0.53
$[(\pm45)_2/(0)_2]s$	UP5	663	1151	-0.151	6.62	0.42
Transverse Direction Fabric H, UD Laminates						
$(0)_6$ Fabric H	EP5	52.4[1]	97.3	-0.114	8.77	0.124
Neat Resin and Adhesive						
Epoxy EP1 Resin	EP1	41.0[2]	82.9	-0.081	12.3	0.77
Bulk Adhesive EP135G3/EKH1376G	ADH1	44.5[2]	57.6	-0.044	22.7	0.79
Biax Fabric M ($\pm45^O$/mat) Laminates						
$(\pm45/m)_3$ Fabric M	EP1	224	225	-0.092	10.9	0.53
$(\pm45/m)_3$ Fabric M	VE1	239	239	-0.090	11.1	0.44
$(\pm45/m)_3$ Fabric M	UP1	208	202	-0.098	10.2	0.41
Triax Fabric W						
$(\pm45/0)s$ Fabric W	EP1	585	1287	-0.143	6.99	0.70

[1]First cracking stress; [2]0.2% offset yield stress

Table 18. Fatigue trends for blade structural details including delamination at ply drops, adhesive joints and skin/core sandwich structures.

Material Form	Resin	Strength	A	B	n	10^6 Cycle Strain, %
Delamination at thick ply drops[2]						
1 ply drop, Fabric D	EP1	189 kN				0.55
2 ply drop, Fabric D	EP1	135 kN		-0.120	8.3	0.39
4 ply drop, Fabric D	EP1	106 kN		-0.099	10.1	0.35
1 ply drop, Fabric D	UP-1	135 kN				0.39
Thick Adhesive Lap Shear Joints[3]						
Hexion Adhesive EP135G3/EKH1376G	N/A	13.9 MPa	22.7 MPa	-0.109	9.17	N/A
3M W1100	N/A	13.8 MPa	29.13 MPa	-0.135	7.41	N/A
Triax Skin/Core Sandwich 4-Point Bending Flexural Fatigue[4]						
Airex C70.55 GPS, 60 kg/m^3 core	EP1	50.25 N/mm	73.34 N/mm	-0.091	11.0	N/A
Airex C70.75 GPS, 80 kg/m^3 core	EP1	55.67 N/mm	46.43 N/mm	-0.026	38.9	N/A
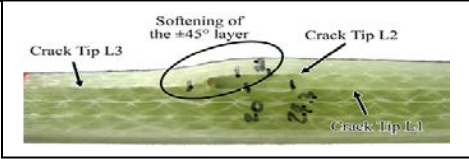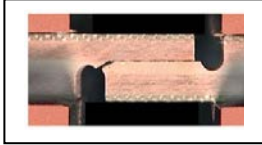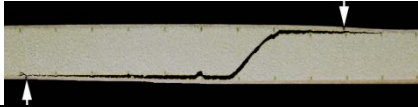
[2]Ply drop strength is Force (kN) at 30-mm delamination length.

[3]Thick adhesive apparent lap shear strength, MPa, 3.25 mm thick adhesive, 25 mm overlap length, 5 mm thick UD Fabric D/EP-1 adherends.

[4]Sandwich Flex Fatigue per ASTM C393, 25 mm thick core, 1.6 mm thick triax glass/epoxy face-sheets. Strength is applied force, N/mm-width, at major core delamination.

Intentionally Left Blank

9. Environmental Effects on Properties

9.1 Overview

This section addresses the effects of environmental factors including seawater and temperature changes on strength, stiffness and fatigue properties for a narrow range of database [1] materials; more fundamental treatment of environmental effects in an associated MSU study is available [3]. Included here are UD laminates of glass fabric H infused epoxy (EP-1) and vinyl ester (VE-7) resins (Table 3), and a UD prepreg carbon/epoxy, Gurit SparPreg UC600. (See Section 3.3.4 for test details.) The glass laminates are representative of typical infused blade laminates with resins of different moisture affinity. The carbon prepreg provides a comparison to a higher performance material with a higher temperature epoxy resin. To address more complex structure, data are also presented for seawater effects on a baseline adhesive joint coupon where laminate, adhesive and interface effects could be present. Moisture effects were investigated for synthetic seawater fully saturated conditions (50°C conditioning) except for the adhesive joint, where the conditioning time was the saturation time for the laminate adherend.

The selection of test methods and materials parameters was based on an earlier moisture/temperature test program with distilled water conditioning [6] using low (glass) fiber content laminates (approximately 36% fiber by volume) and a range of resins, with VARTM processing (two-sided molds). That study indicated particular moisture sensitivity for ortho-polyester and epoxy resins, with reduced sensitivity for iso-polyesters and vinyl esters, for resin sensitive properties like longitudinal and transverse compression and shear. Higher temperature resistant epoxies (higher T_g), like the prepreg system UC600, generally show reduced moisture effects for the temperature range of interest for blades

9.2 Laminate Static Property Results

Figure 97 (a)-(q) and Table 19 give unidirectional laminate data. The glass laminate data, Figure 91 (a)-(l), are given for each material at three test temperatures, 5, 20 and 40°C, after conditioning to equilibrium weight at 50°C, as well as control materials which were stored in dry laboratory air. Control coupon moisture contents were below 0.1%. The thicker transverse and compression coupons required much longer conditioning time to reach saturation, typically thousands of hours [3]. The carbon/epoxy data (Figure 97 (m)-(q)) are compared to the glass/epoxy data for testing at 20°C only. Both epoxy resin materials have similar equilibrium weight gains, while the vinyl ester laminates pick up only about half as much moisture.

Comparing the control properties at 20°C in Table 19, for the similarly infused epoxy and vinyl ester laminates, the epoxy shows slightly higher longitudinal tensile strength, while the vinyl ester longitudinal compressive strength is significantly higher. The transverse compressive strength is higher for the vinyl ester, while the transverse tensile strengths and all modulus values are similar. Comparing control prepreg carbon/epoxy with infused glass/epoxy at 20°C, the longitudinal modulus is about 3x higher for the carbon and the longitudinal tensile strength about 2x higher, as expected [2], the longitudinal compressive strength is about 1.6x higher. The transverse modulus is about 2x higher for the glass, but the transverse tensile strengths are about the same.

9.2.1 Modulus

The effects of seawater conditioning on the longitudinal tensile modulus were insignificant for all materials and test conditions, Figures 97(a, b, m). The transverse tensile modulus was reduced slightly by moisture for the glass/epoxy, reaching a maximum reduction of 16% compared to the dry control at 40°C test temperature (97g). The combined effect of temperature and moisture at 40°C reached a reduction in transverse modulus of 25% relative to the dry control at 5°C for the epoxy, Figure 97(c) and Table 19. Changes in the transverse tensile modulus for the glass/vinyl ester system were not significant over the testing range (97h). The dry, 5°C longitudinal tensile modulus was slightly higher for the epoxy resin compared to the vinyl ester (97a, b), while transverse tensile modulus values were about the same (97g, h).

9.2.2 Longitudinal Tensile Strength

The longitudinal tensile strength of the carbon/epoxy was not significantly affected by seawater saturation at 20°C, Figure 97(o). Generally, the longitudinal tensile strength of infused glass fiber laminates is reduced by increasing test temperature and moisture content [6]. In this test series, the glass/epoxy showed the greatest strength reduction due to seawater, reaching about 26% at 40°C test temperature (97c). The vinyl ester system showed a corresponding reduction of only 2% (97d). The maximum reduction in longitudinal tensile strength due to combined temperature (40°C) and seawater, relative to the 5° dry control cases, was about 33% for epoxy (97c) and 14% for vinyl ester (97d), the latter due almost entirely to the temperature increase (see Table 19).

9.2.3 Longitudinal Compressive Strength

The longitudinal compressive strength is generally the most critical property for moisture and temperature effects [6]. However, here the effects were generally less than those for longitudinal tensile strength. The carbon/epoxy at 20°C test temperature did not show any significant reduction, Figure 97(q). Longitudinal compressive strengths for the vinyl ester were generally higher than for the epoxy, and slightly less sensitive to the seawater saturation. The maximum strength reduction due to seawater was about 16% at 40°C (97e), while the corresponding value for vinyl ester was 15% at 20°C (97f). The maximum reduction in longitudinal compressive strength due to combined seawater and temperature (40°C) relative to 5°C dry was 33% for epoxy and 22% for vinyl ester, Figure 97(e and f) and Table 19. The reason for the somewhat greater than expected effect of seawater on the vinyl ester in longitudinal compression, relative to other properties, may be that the control compressive strengths (and strains) were significantly higher for the vinyl ester.

9.2.4 Transverse Tensile Strength

The transverse tensile strengths show relatively little temperature sensitivity, but significant reductions due to seawater for the epoxy, with little temperature or moisture sensitivity for the vinyl ester, Figures 97(i) and (j) and Table 19. The maximum combined reduction from seawater and temperature, compared to the 5°C dry strength, is about 35% for the epoxy. The carbon/epoxy prepreg, Figure 97(u), shows an 18% reduction in transverse tensile strength at 20°C.

9.2.5 Transverse Compressive Strength

Transverse compressive strengths tend to show very consistent data trends, higher absolute strength and low scatter relative to transverse tension, apparently due to resin dominated yielding as opposed to flaw sensitive cracking failure modes, Figure 97 (k and l) vs (i and j). The seawater saturated cases at different temperatures all show a 22%-25% reduction relative to controls for epoxy and corresponding 5% to 9% reduction for vinyl ester, indicating the reduced seawater sensitivity for the vinyl ester. Temperature effects are also greater for the epoxy. The maximum

Table 19. Static Environmental Test Data

Composite system	Test	V_F	Test Temperature	Conditioned, Dry or Weight Gain	Stress average, MPa	Stress, Std. Dev. MPa	% of dry value	Average modulus, GPa	Modulus Std. Dev., GPa	% of dry value
Glass/Epoxy	Longitudinal tensile [0]₂	0.58	5°C	Dry	1049	34.2		43.6	1.96	
			20°C	Dry	1000	26.1		44.3	0.62	
			40°C	Dry	955	40.0		44.1	1.08	
			5°C	0.72%	862	18.6	82	41.7	0.92	96
			20°C	0.72%	798	34.9	80	43.5	1.16	98
			40°C	0.72%	705	9.6	74	42.3	0.61	96
Glass/Vinyl Ester		0.56	5°C	Dry	999	66.8		41.3	1.38	
			20°C	Dry	952	41.0		41.6	1.58	
			40°C	Dry	885	20.0		41.0	0.97	
			5°C	0.40%	943	25.2	94	42.1	1.57	102
			20°C	0.40%	912	31.7	96	41.8	1.66	100
			40°C	0.40%	863	17.2	98	41.6	1.62	102
Glass/Epoxy	Transverse tensile [90]₆	0.57	5°C	Dry	58.6	2.2		16.3	0.64	
			20°C	Dry	54.8	3.3		15.4	0.51	
			40°C	Dry	55.2	1.6		14.6	0.26	
			5°C	0.72%	43.3	1.5	74	15.4	0.79	94
			20°C	0.72%	42.3	1.2	77	14.6	0.75	95
			40°C	0.72%	38.2	1.2	69	12.3	0.37	84
Glass/Vinyl Ester		0.58	5°C	Dry	62.9	4.4		16.4	1.04	
			20°C	Dry	58.4	6.9		17.4	0.56	
			40°C	Dry	64.3	4.8		16.8	0.20	
			5°C	0.40%	59.6	4.1	95	17.2	1.06	105
			20°C	0.40%	53.5	3.0	92	16.2	0.87	93
			40°C	0.40%	55.3	1.3	86	15.5	0.71	92
Glass/Epoxy	Longitudinal compression [0]₆	0.57	5°C	Dry	-752	34.8				
			20°C	Dry	-737	29.1				
			40°C	Dry	-602	36.8				
			5°C	0.72%	-690	12.8	92			
			20°C	0.72%	-654	15.4	89			
			40°C	0.72%	-506	17.1	84			
Glass/Vinyl Ester		0.58	5°C	Dry	-992	50.4				
			20°C	Dry	-905	51.4				
			40°C	Dry	-856	24.5				
			5°C	0.40%	-904	30.3	91			
			20°C	0.40%	-770	34.3	85			
			40°C	0.40%	-772	25.5	90			
			40°C	0.40%	-176	5.0	91			

Table 19. Static Environmental Test Data (cont)

Composite system	Test	V_F	Test Temperature, °C	Conditioned, Dry or Weight Gain	Stress average, MPa	Stress, Std. Dev. MPa	% of dry value	Average modulus, GPa	Modulus Std. Dev., GPa	% of dry value
Glass/Epoxy	Transverse compression [90]$_6$	0.57	5	Dry	-209	3.96				
			20	Dry	-184	6.65				
			40	Dry	-162	4.46				
			5	0.72%	-164	7.24	79			
			20	0.72%	-143	5.62	78			
			40	0.72%	-122	3.41	75			
Glass/Vinyl Ester		0.58	5	Dry	-227	4.9				
			20	Dry	-213	6.0				
			40	Dry	-194	6.9				
			5	0.40%	-215	6.2	95			
			20	0.40%	-199	6.8	93			
			40	0.40%	-176	5.0	91			
Carbon/Epoxy	Longitudinal tensile [0]$_2$	0.57	20	Dry	2044	36		123	0.9	
			20	0.80%	1993	77	98	124	1.9	101
	Longitudinal 0-degree compression [(90/0)]$_{2S}$	0.57	20	Dry	-1194	90		61.0	0.9	
			20	0.80%	-1206	89	101	62.3	1.2	102
	Transverse tensile [90]$_8$	0.57	20	Dry	55.7	6.6		7.7	0.1	
			20	0.84%	45.4	4	82	7.4	0.2	96
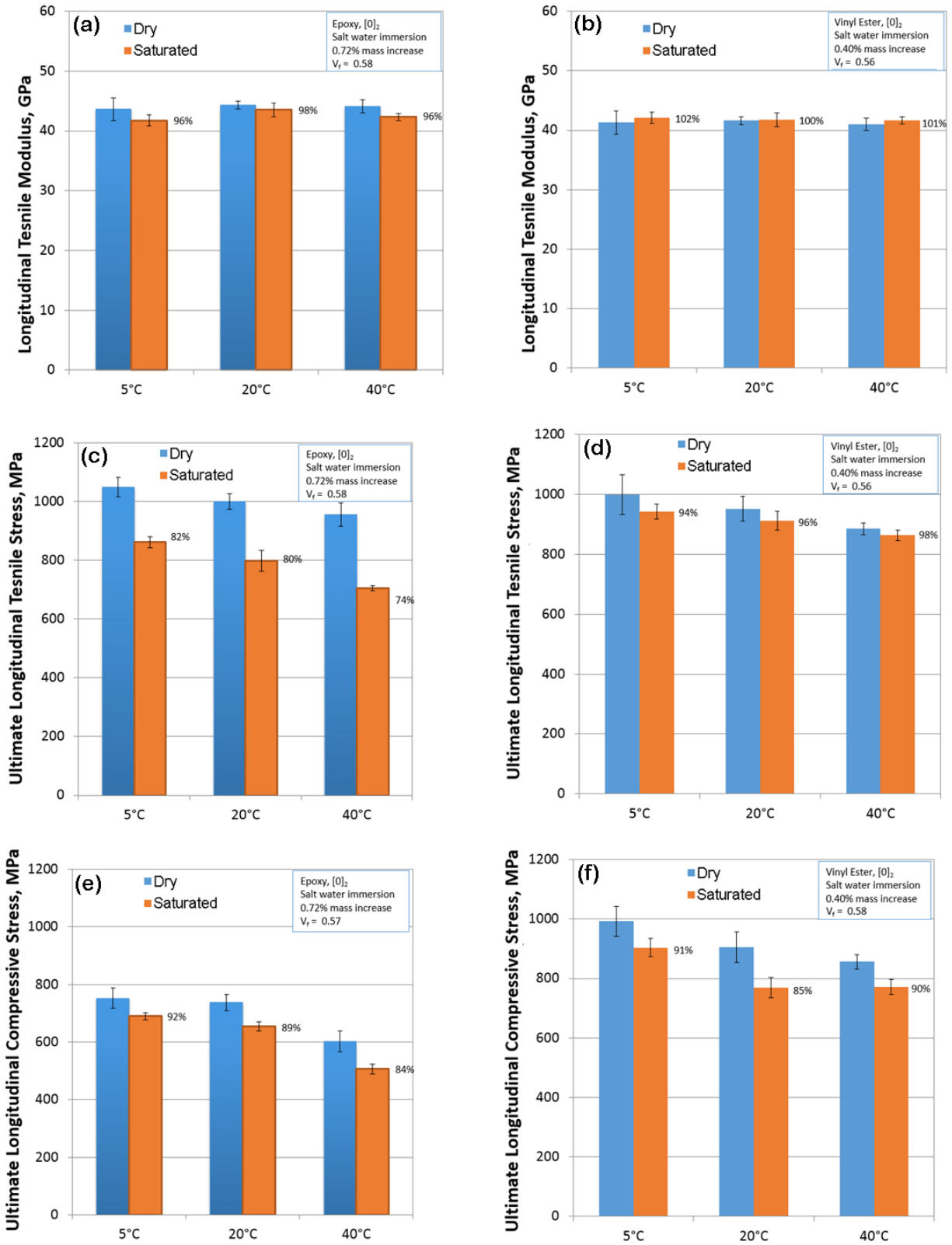
Figure 97 (a)-(f). Static environmental test data
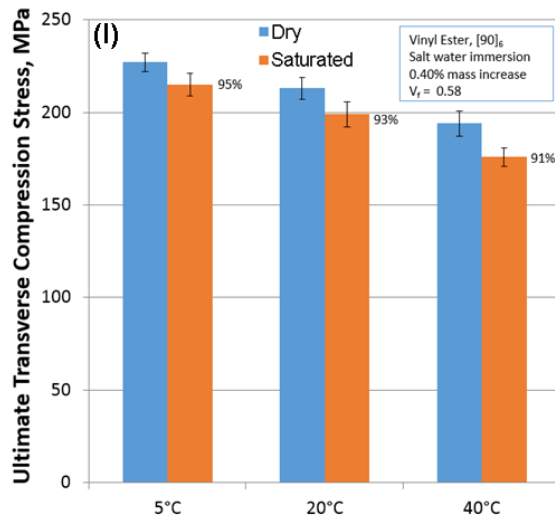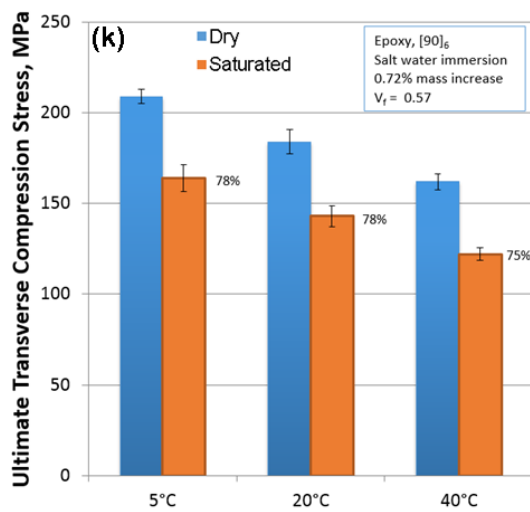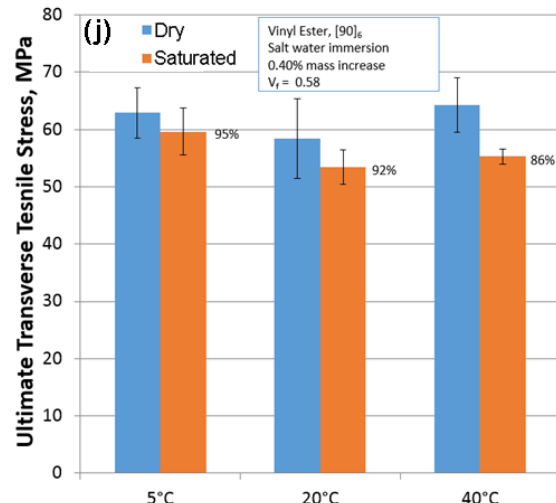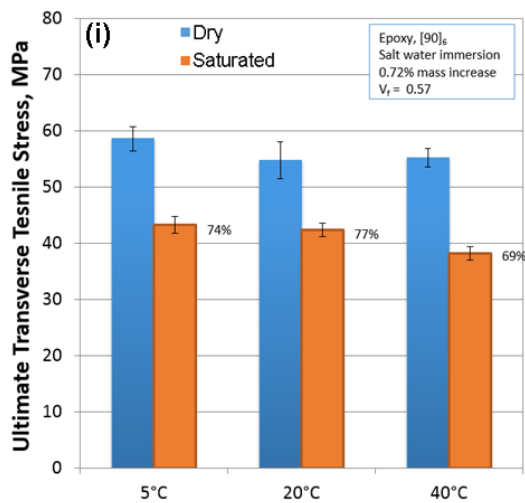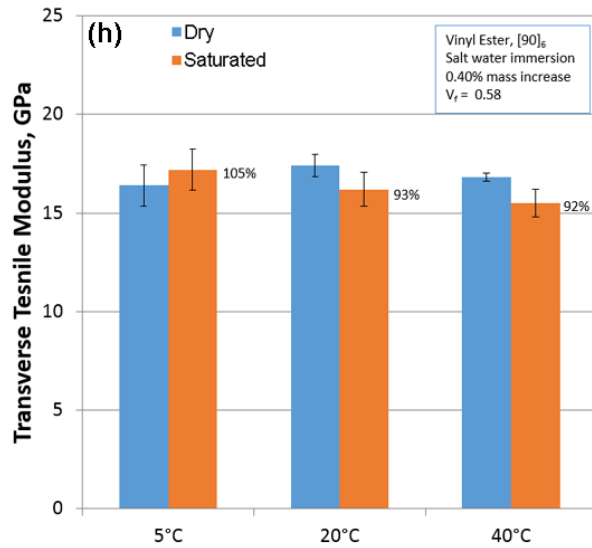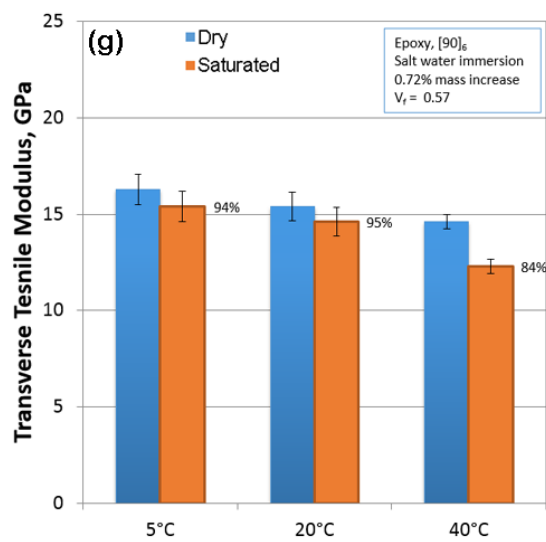
Figure 97 (g)-(i). Static environmental test data
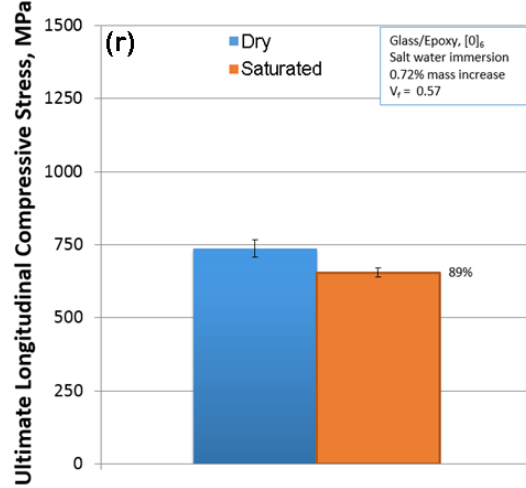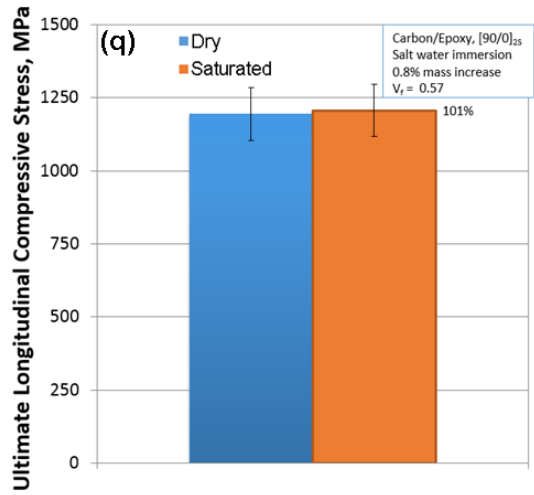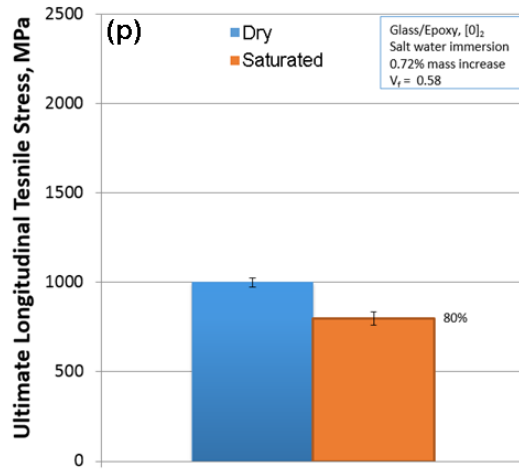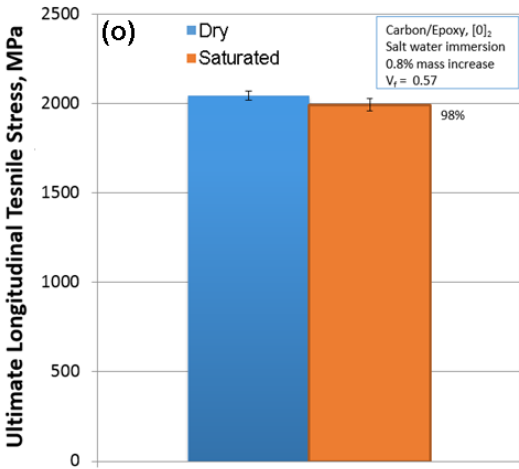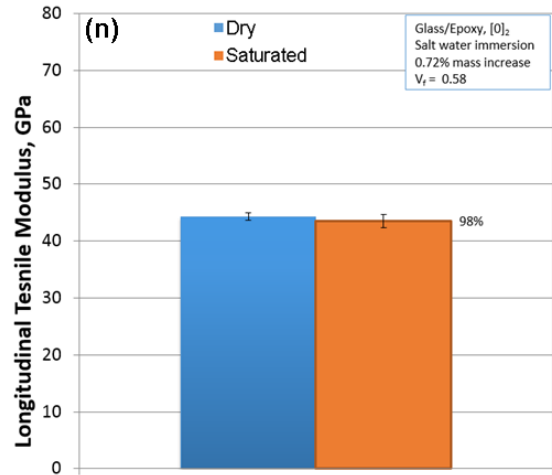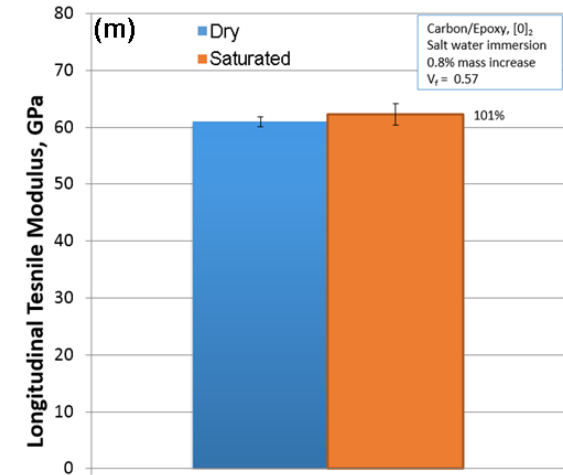
Figure 97 (m)-(r). Static environmental test data

144
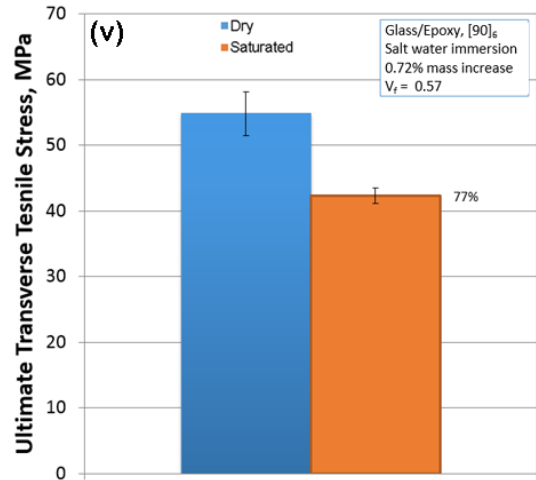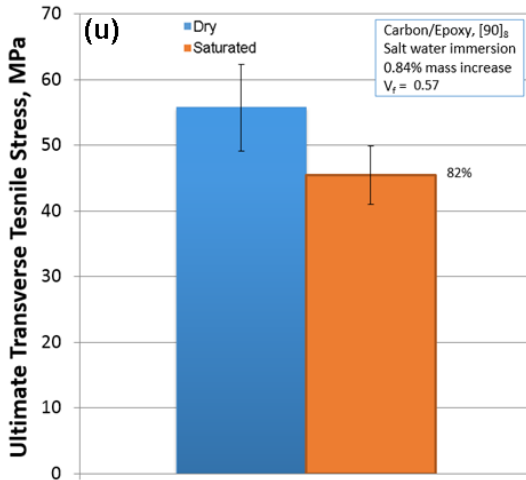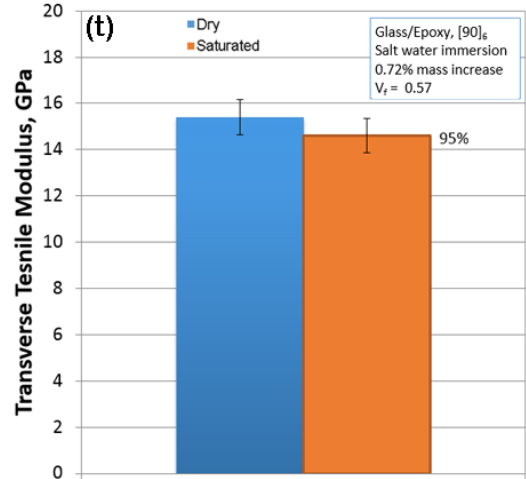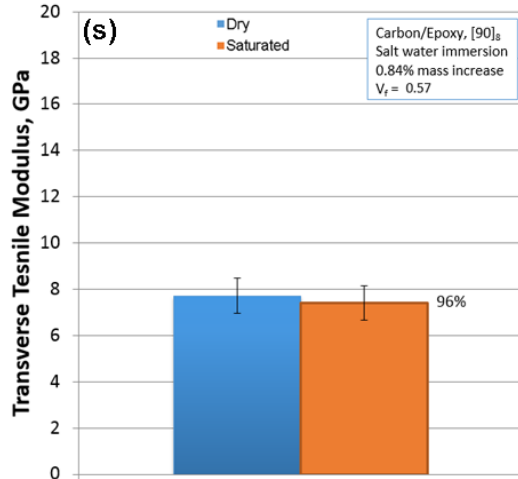
Figure 97 (s)-(v). Static environmental test data

strength reduction for combined seawater and temperature exposure relative to the 5°C dry controls are 42% for the epoxy and 22% for the vinyl ester, Table 17.

9.3 Laminate Fatigue Results

Tensile and compressive fatigue results were obtained for selected laminates following standard testing procedures. Coupons were conditioned to saturation in 50°C synthetic seawater, which was then applied to coupon surfaces during the duration of the test (Figure 23). Figure 98 compares the tensile fatigue S-N data for the two-ply UD fabric H glass fabric and epoxy EP-1 (Tables 2 and 3) in control and saturated conditions, while Figure 99 compares $\pm45^{O}$ DB laminates with fabric P/EP-1. The UD laminate data in Figure 98 show reduced fatigue resistance for static and low cycle fatigue tests consistent with Table 17, converging at higher cycles.

The $\pm 45^O$ laminates show significantly higher saturation moisture content and reduced fatigue stresses for the conditioned and wet tested laminates compared with the controls. Stress-strain curves for the DB laminates, controls and conditioned, are compared in Figure 100. The 50% strain increase criterion is applied for fatigue failures (Figure 53). As expected, the DB laminates, with resin dominated properties, are much more seawater sensitive than are the UD laminates. The significantly increased weight gain at saturation for the DB vs UD laminates (1.4% vs 0.72%) is associated with resin cracking along the stitch lines for the DB laminates during conditioning.

A comparison of tensile fatigue resistance for 2-ply UD (fabric H) laminates between the epoxy EP-1 and vinyl ester VE-7 resins for dry and seawater immersed conditions is presented in Figure 101. Fatigue trends are similar, and the higher fatigue strength for the epoxy is consistent with the static longitudinal ultimate strength data in Table 17. UD laminates with both resin systems are insensitive to seawater at higher cycles in tensile fatigue.

Tensile and compressive fatigue results for the SparPreg UC600 UD carbon/epoxy are shown in Figures 102 and 103. S-N curves are much less steep than glass/epoxy for both tensile and compressive fatigue (see Fig. 47) and very little moisture sensitivity is evident for either type of loading compared to the infused glass/epoxy laminates (Figures 98, 99).

The effects of seawater on the notched lap shear adhesive joint coupon are given in Figures 104 and 105 (coupon shown in Figure 24). The coupons were conditioned for the time equivalent to the saturation time for a single adherend immersed in seawater (1632 hours), so the overall joints were not at saturation, which would have taken very long conditioning times due to the added thickness compared to a single adherend. Tensile and reversed loading fatigue results in Figure 97 show a reduction in strength at low test cycles, tending to converge at high cycles, similar to the pattern shown for the UD laminate adherends alone, Figure 99. As noted for dry adhesives, reversed loading shows reduced lifetime compared to tensile fatigue loading [2], see Figure 73. Figure 105 gives dry and saturation seawater conditioned tensile fatigue data for the neat adhesive; the saturation moisture gain is about 2.6% for the neat (epoxy based) adhesive, similar to the neat EP-1 epoxy resin in the laminate adherends (2.9%). The seawater conditioned adhesive data are scattered, but show a reduction in fatigue strength of about 25% relative to the controls. After conditioning (not to saturation), drying of sectioned samples of the adherend and adhesive showed moisture weight losses of about -0.65% for the adherend and -1.2% for the adhesive, well below their saturation values of 0.72% and 2.6%, respectively.
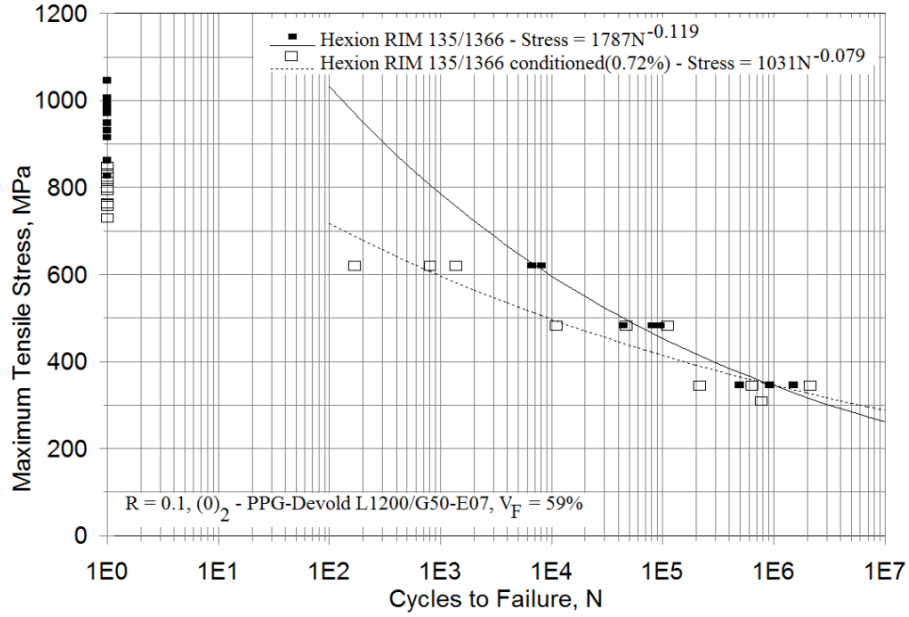
Figure 98. Tensile fatigue S-N data for UD fabric H/EP-1 laminates, comparing control conditioned and tested laminates with saturated seawater conditioned and tested laminates.
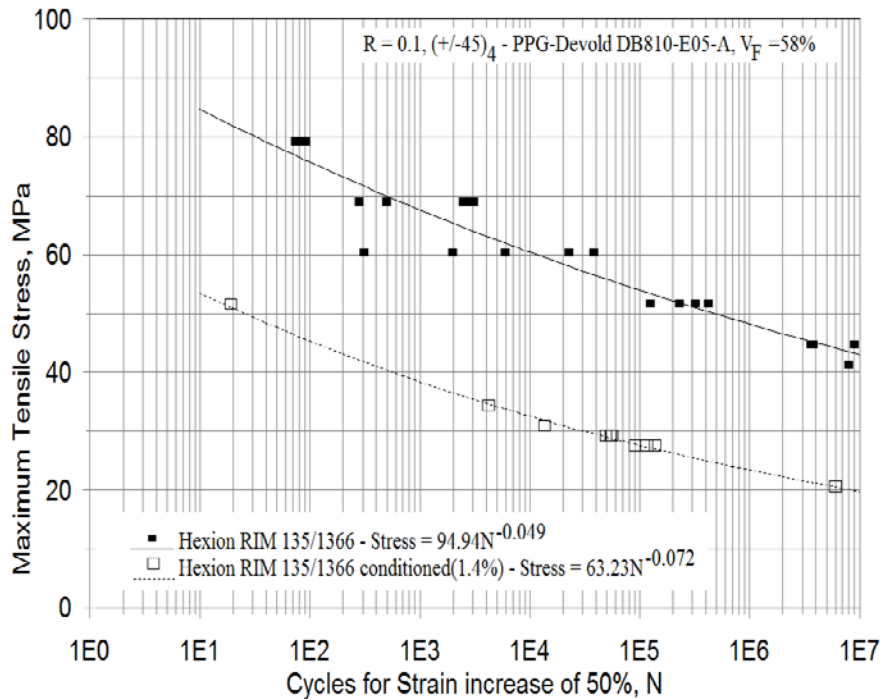
Figure 99. Tensile fatigue S-N data for DB fabric P/EP-1 laminates, comparing control conditioned and tested with saturated seawater conditioned and tested.
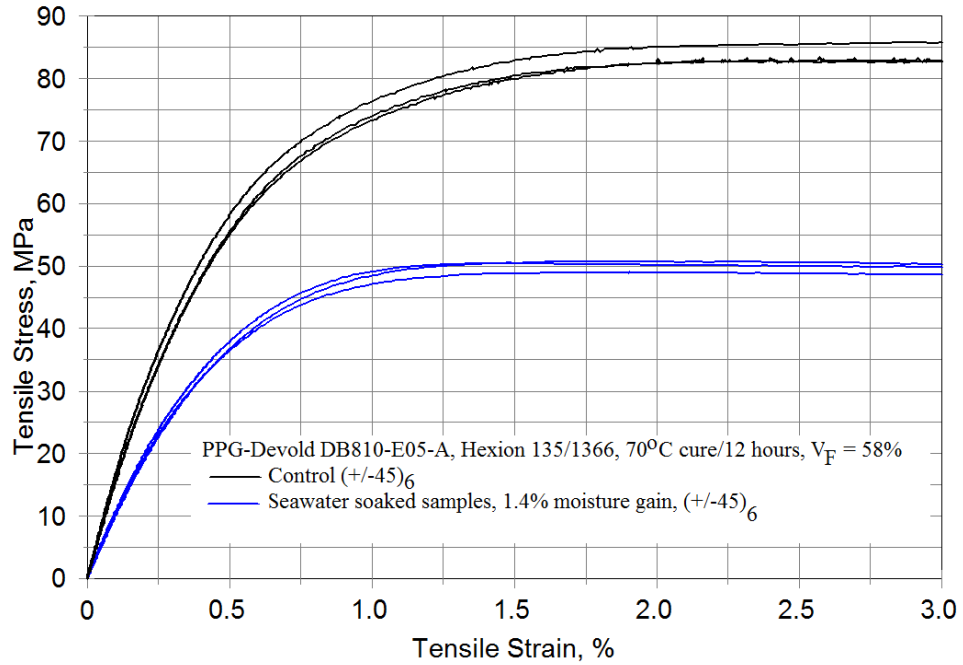
Figure 100. Tensile stress-strain curves for control and seawater saturated ±45° DB coupons from Fig. 97(b).
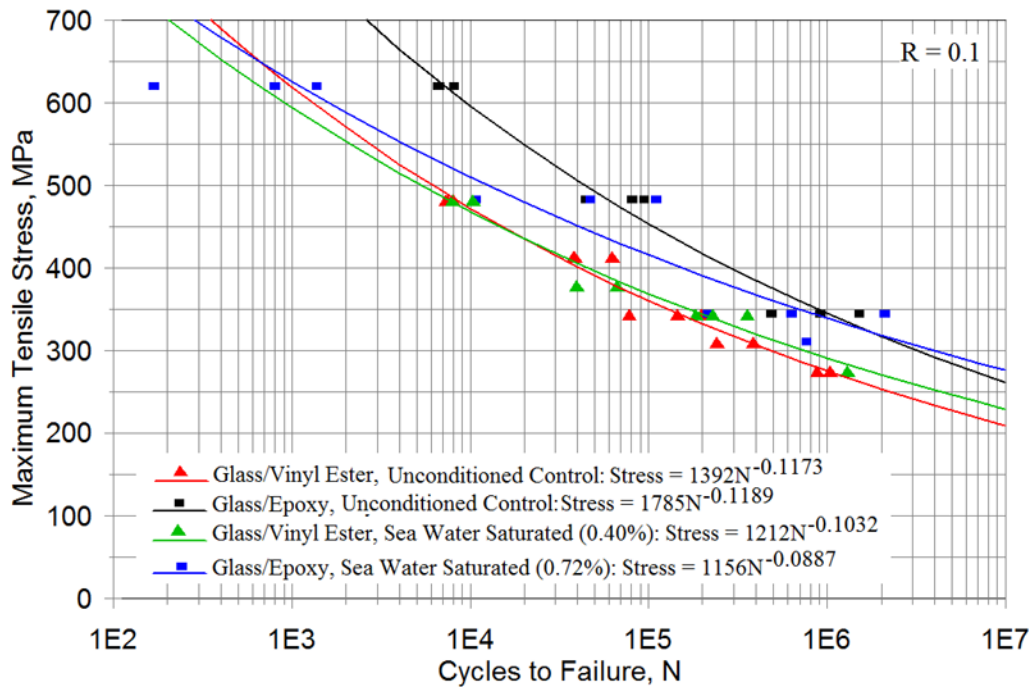
Figure 101. Tensile fatigue data for infused glass/epoxy and glass/vinyl ester dry and seawater saturated UD laminates, 20°C testing.
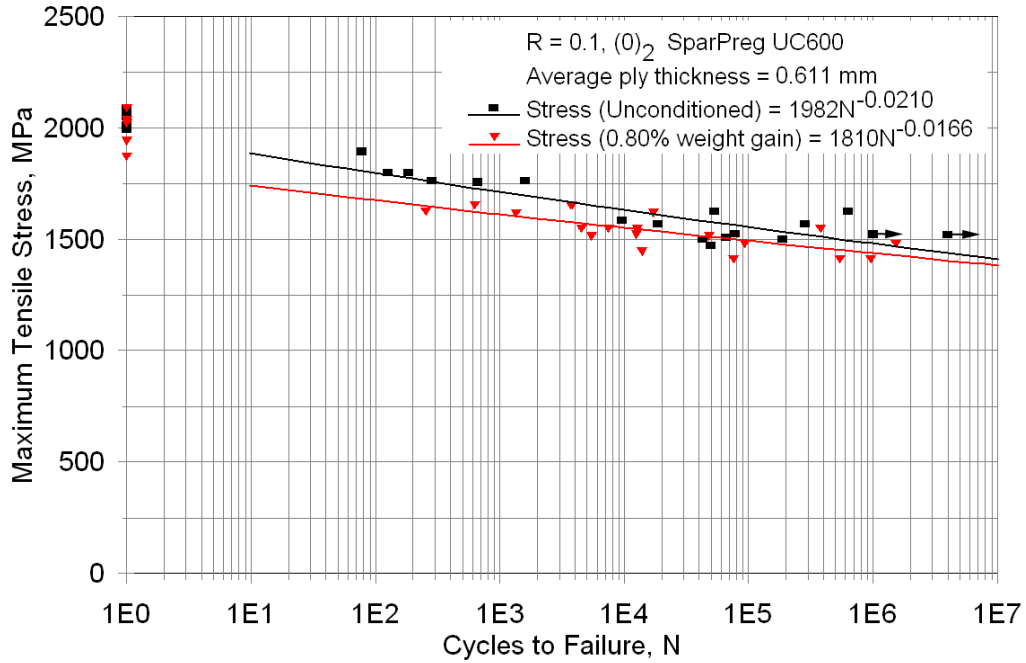
Figure 102. Tensile fatigue data for SparPreg carbon/epoxy dry and seawater saturated UD laminates.
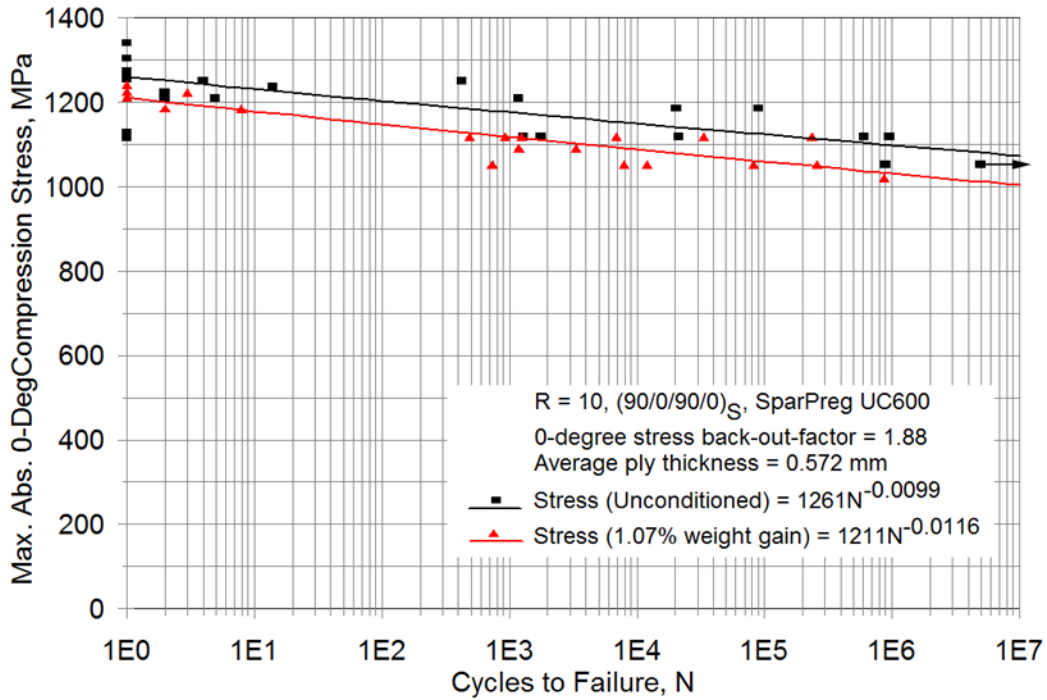
Figure 103. Compression fatigue data for SparPreg carbon/epoxy dry and seawater saturated UD laminates.

149
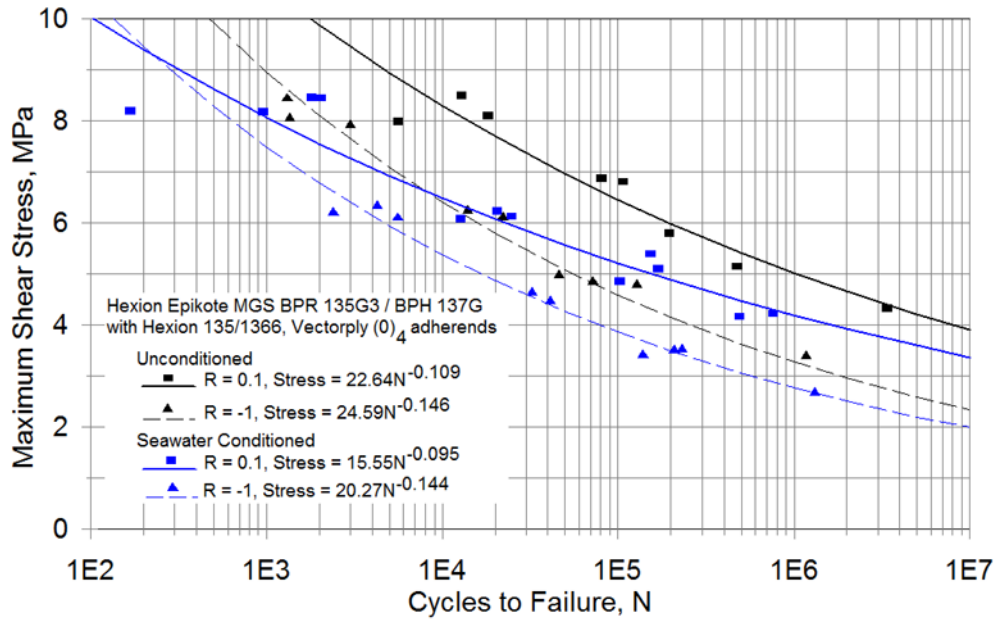
Figure 104. Notched lap shear adhesive joint coupons (Fig. 23), dry control and seawater conditioned tensile and reversed loading fatigue data.
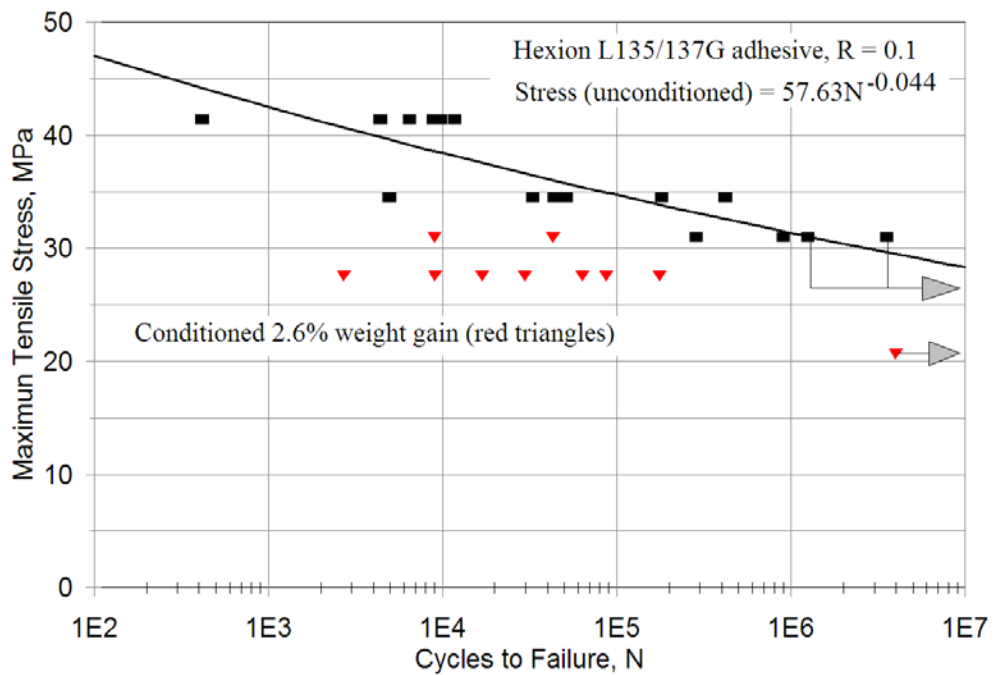
Figure 105. Neat adhesive dry control tensile fatigue behavior, with limited seawater saturated data shown for comparison.

150

10. Conclusions

Section 4. Static properties: Thick laminates and LUR Tests

Static strength and stiffness properties are not widely available for thick infused laminates in the three primary directions, particularly cases with strong nonlinear response which affects the cyclic stress-strain behavior. Test methodology and results are given for tension, compression and shear coupons sectioned from a 93 mm thick epoxy infused baseline unidirectional fabric laminate for which internal curing temperature was monitored and controlled to prevent exothermal heating effects. Thickness-direction properties are shown to be deficient relative to the transverse direction properties which are generally assumed to approximately represent them.

Loading-unloading-reloading (LUR) tests of $\pm 45^O$ laminates have been conducted over a range of increasing tension and compression and reversed direction loads to explore the nonlinear stress-strain (and permanent strain) response, with the results also reduced to shear stress-strain curves. Nonlinear trends are difficult to reduce to simple properties, so complete graphical data are reported as well as modulus and residual property changes. The most notable trend outside of increasing nonlinearity at higher stresses is that the reverse2 scheme (compression followed by tension) is stiffer than the others on the compression side. The LUR approach allows nonlinear response to be represented in a manner which is consistent with cyclic fatigue stress-strain data in Section 6. These results are applicable in various materials models which require unloading.

Section 5. Laminate Tensile Fatigue: Fabric Architecture, Aligned Strands and Resin Effects

Detailed results are presented exploring the effects of fabric structure and resin type on the tensile fatigue resistance. Using aligned strand structure as a baseline, the efficiency of stitched fabric reinforcement is quantified for static and fatigue properties. The fabric efficiency is generally good for an epoxy resin, but poor in fatigue for a vinyl ester and polyester; the latter traced to sensitivity to cracking along the transverse fabric backing strands. The vinyl ester resin laminates varied with the particular UD fabric tested, approaching the epoxy performance only for fabric D and for aligned strand laminates. Laminates with the epoxy resin show little effect of broad variations in fabric weight or construction, or strand fiber and sizing, for glass fibers. A urethane resin shows similar fatigue to the epoxy with fabric H. Commercial (RodPack) precured aligned strand laminates also showed improved fatigue resistance compared to baseline UD fabric materials under tensile, compressive and reversed loading.

Section 6. ±45 Laminates: Creep/Fatigue Interaction

The various tests carried out in this study indicate the importance of the resin viscoelastic response in shear for double bias ($\pm 45^O$) glass fabric reinforced, resin infused laminates loaded under tension or compression in the axial (0°) direction. S-N fatigue results at seven R-values tested are generally best represented in terms of strain increases; failure follows shortly after the maximum strain begins to increase rapidly, represented here by a 50% maximum absolute strain increase. Where the waveform includes tension, the strain increase is associated with the appearance of resin cracking, which can open under the transverse tension condition, growing parallel to the fiber direction, and with associated local ply delamination. Most of the strain increases are associated with tensile or compressive creep, which is a manifestation of resin shear deformation, although significant stiffness loss resulting from resin cracking contributes to

the strain increase. The results have been combined into a cumulative strain based axial and shear constant life diagrams for design and analysis purposes.

Residual tests and stress-strain data gathered during fatigue and LUR (Section 4.2) tests consistently show decreasing (low strain) modulus as the tests progress, except in some compression fatigue tests. Stiffness increases are observed in some cases at higher strains in residual and LUR tests.

Square wave reversed loading results at a particular stress condition show a steady creep response on each cycle, both in tension and compression, in reversed loading. The strains agree with creep test results as long as the strains remain low. A departure from the creep test strains occurs as damage develops, led by the tensile side loading, but also occurring on the compression side. The point where this departure occurs, and strains increase rapidly, falls within a consistent cumulative time range; the cycles simply vary proportionally to the frequency. Thus, the lifetime is cumulative time, rather than cycle number, dependent. Results $\pm45^O$ laminates with a urethane resin show greater creep and fatigue strains, and reduced tensile fatigue resistance for $\pm45^O$ laminates, compared to those with the baseline epoxy.

Section 7. Adhesive and Core Material Fatigue

This study has explored static and fatigue crack growth in thick adhesive joints with fiberglass laminate adherends, for three adhesive systems with a broad range of G_{Ic} values. Data have been presented for mixed shear and opening mode loading conditions, and for tension-tension and reversed loading fatigue. The several versions of the CLS test geometry allow fully reversed and compression loading, in addition to tension. Widely used flexural test geometries (DCB, MMB, and ENF) have been used to obtain static crack growth properties and as a baseline for comparison to the CLS test results. Crack paths and damage characteristics have been characterized using microscopy for CLS and flexural geometries.

Cracks were shown to propagate along four potential paths depending on adhesive and geometry: a. cohesive in the adhesive, mid adhesive for pure mode I, but otherwise near one laminate adherend interface; b. cohesive in the adhesive, but partially involved with cracking from the laminate resin peel-ply surface features; c. inside the laminate resin, along the top fiberglass strand surface; and d. inside the laminate, below the top (fabric) ply. Transitions from (a) and (b) to (c), involving unstable growth, were observed for flexural geometries after a short period of stable crack growth under static loading. Stable growth was observed for most CLS tests. The crack tip area for the more brittle adhesive (ADH-1) showed a zone of one to two mm ahead of the fully formed crack tip, where micro-cracking and hackling damage were present; the damage extended for the order of 0.1 to 0.2 mm into the adhesive thickness from the interface.

Static test results for the flexural geometries followed a trend of the total SERR, G_T, with mode mixity, which was similar to interlaminar cracks in a similar laminate to the adherends, with increasing G_T as the mode II component increased; SERR levels were of generally similar magnitude. Thus, comparable static crack resistance is expected for cohesive cracks in the adhesive, or for cracks which transition into the laminate surface or interior. The CLS static crack growth resistance was insensitive to the type of peel-ply, and to crack starter method, whether grown from the notch, from a Teflon starter film, or from a mixed mode fatigue crack.

Fatigue crack data were obtained for two CLS specimen geometries for adhesive ADH-1 under tension-tension and reversed loading. Crack growth rates, da/dN, were represented as the maximum load normalized by the static critical load at the same crack length. Cracks followed a power law relationship, propagating more rapidly under reversed loading than tension-tension for the same Pmax/Pc. Data were separated according to crack length, presumably reflecting an increased mode II component for longer cracks.

Comparisons of the three adhesives indicate adhesive ADH-6 with a much higher static G_{Ic} from DCB tests with the crack at mid-thickness, compared to ADH-1, and with ADH-5 intermediate. Mixed-mode CLS tests showed generally similar crack resistance for all three adhesives, highest for ADH-1, with cracks propagating near the interface. CLS fatigue cracks propagated at a similar speed for the same Pmax/Pc ratio for all three adhesives.

General applicability of the CLS results requires adequate modeling of the test geometry.

Section 8. Comparison of Fatigue Trends for Various Blade Materials

As the laminate complexity increases from aligned strand to UD fabric to MD, the fatigue S-N curves steepen, reflected in higher absolute values for exponent B, and lower million cycle strain. This trend is particularly strong for the VE and UP resins. Resin-dominated failures for neat resin, transverse direction laminate and biax laminates (Table 17) all show similar, relatively low fatigue exponents, B, compared to MD laminates and UD fabric laminates with VE and UP resins. The lower exponent B range is also observed for resin dominated delamination growth at ply drops (static delamination resistance in opening and shearing modes is significantly higher for resin EP1 than for UP1, with vinyl ester VE1 intermediate [2]). Resin dominated exponents indicate relatively flat S-N behavior compared to some UD and MD laminates, but the million cycle fatigue strains are lower, particularly in the transverse direction. Triax constructions have steeper S-N trends in the range of the MD laminates, representing a two stage failure process in some cases, between the biax and UD layers [2,6]. The epoxy based adhesive lap shear joint fatigue exponents are relatively low, similar to the resin dominated transverse and biax trends for epoxy resin; the bulk adhesive exponent B is very low at -0.044, but joints usually fail predominantly by delamination in the laminate surface [15].

Section 9. Environmental Effects on Properties

This section addresses the effects of environmental factors including seawater and temperature changes on strength, stiffness and fatigue properties for baseline materials. Included here are UD laminates of glass fabric H infused epoxy (EP-1) and vinyl ester (VE-7) resins (Table 3), DB fabric P/EP-1 laminates and a UD prepreg carbon/epoxy, Gurit SparPreg UC600. The glass laminates are representative of typical infused blade laminates with resins of different moisture affinity. The carbon prepreg provides a comparison to a higher performance material with a higher temperature epoxy resin. To address more complex structure, data are also presented for seawater effects on a baseline adhesive joint coupon where laminate, adhesive and interface effects could be present. Moisture effects were investigated for synthetic seawater fully saturated conditions (50^OC conditioning) except for the adhesive joint, where the conditioning time was the saturation time for the laminate adherend (1632 hours).

Both epoxy resin UD materials (glass infused and carbon prepreg) have similar weight gains at saturation, while the vinyl ester resin laminates pick up only about half as much moisture. Comparing the control properties for the similarly infused epoxy and vinyl ester laminates, the epoxy shows slightly higher longitudinal tensile strength, while the vinyl ester longitudinal compressive strength is significantly higher. The transverse compressive strength is higher for the vinyl ester, while the transverse tensile strengths and all modulus values are similar. Comparing control prepreg carbon/epoxy with infused glass/epoxy at $20^{O}C$, the longitudinal modulus is about 3x higher for the carbon and the longitudinal tensile strength about 2x higher, as expected [2], the longitudinal compressive strength is about 1.6x higher. The transverse modulus is about 2x higher for the glass, but the transverse tensile strengths are about the same.

Seawater saturation had little effect on the carbon/epoxy except in the transverse tension strength. The highest test temperature ($40^{O}C$) and saturated conditions produced the greatest strength reductions for the infused glass laminates. The longitudinal modulus was unaffected by the environment for all conditions tested. No significant reductions were found for the VE resin in transverse tensile modulus or strength, with only small or moderate reductions for all other properties. The epoxy resin laminates showed greater reductions in strength for all directions compared to the VE resin, up to 33%-35% relative to the $5^{O}C$ control case. DB ± 45 laminates show significantly higher saturation moisture content and greater strength and fatigue resistance reductions compared with UD laminates.

Fatigue results were obtained for saturated and control conditions at $20^{O}C$ for UD materials in the longitudinal direction as well as for DB laminates. The carbon/epoxy UD laminates showed very high fatigue resistance in longitudinal tension and compression, and very small effects of seawater saturation. The infused glass fabric UD laminates were more fatigue sensitive than carbon in the longitudinal direction as expected. The fatigue strength was reduced by seawater at low cycles, but converged toward the control data at higher cycles. The DB glass/epoxy laminates were very seawater sensitive in static and fatigue loading over the entire lifetime range. Adhesive joint coupon lifetimes were moderately reduced by seawater conditioning (not to saturation) and testing at R = 0.1 and -1, with the lifetimes again converging on those for control conditions at high cycles.

References

1. Mandell, J.F. and Samborsky, D.D., "DOE/MSU Fatigue of Composite Materials Database, 2015 update, http://energy.sandia.gov/energy/renewable-energy/wind-power/materials-reliability-standards/

2. Mandell, J.F., Samborsky, D.D., Agastra, P., Sears, A.T. and Wilson, T.J., "Analysis of SNL/MSU/DOE Fatigue Database Trends for Wind Turbine Blade Materials," Sandia Contractor Report SAND2010-7052, 2010.

3. Miller, D.A., Dept. Mechanical Engineering, Montana State Univ., 2015, www.montana.edu/composites main web portal

4. Nijssen, R.P.L., "Fatigue Life Prediction and Strength Degradation of Wind Turbine Rotor Blade Composites," Contractor Report SAND2006-7810P, Sandia National Laboratories, Albuquerque, NM, 2006.

5. Mandell, J.F. and Samborsky, D.D., "Analysis of the DOE/MSU Database: Fatigue of Composite Materials for Wind Turbine Blades," Final Report DOE Grant DE-FG04-01AL67287, 2004.

6. Mandell, J.F., Samborsky, D.D. and Cairns, D.S. "Fatigue of Composite Materials and Substructures for Wind Turbine Blade," Contractor Report SAND2002-0771, Sandia National Laboratories, Albuquerque, NM, (2002).

7. Mandell, J.F. and Samborsky, D.D., "DOE/MSU Composite Material Fatigue Database: Test Methods, Materials, and Analysis," Contractor Report SAND97-3002, Sandia National Laboratories, Albuquerque, NM (1997).

8. Wahl, N.K., Mandell, J.F., Samborsky, D.D., "Spectrum Fatigue Lifetime and Residual Strength for Fiberglass Laminates," Report SAND2002-0546, Sandia National Laboratories, Albuquerque, NM (2002).

9. Mandell, J.F., Samborsky, D.D., Combs, D.W., Scott, M.E. and Cairns, D.S., "Fatigue of Composite Material Beam Elements Representative of Wind Turbine Blade Substructure," Report NREL/SR-500-24374, National Renewable Energy Laboratory, Golden, CO (1998).

10. Mandell, J.F., Reed, R.M. Jr. and Samborsky, D.D., "Fatigue of Fiberglass Wind Turbine Blade Materials," Contractor Report SAND92-7005, Sandia National Laboratories, Albuquerque, NM (1992).

11. Griffin, D., "Blade System Design Study Part II: Final Project Report (GEC)," Contractor Report SAND2009-0686, Sandia National Laboratories, Albuquerque, NM (2009).

12. Samborsky, D.D., Mandell, J.F., and Miller, D.A., "Creep/Fatigue Behavior of Resin Infused Biaxial Glass Fabric Laminates**",** 2013 AIAA SDM Conference, Wind Energy Session, Boston, paper 10.2514/6.2013-1630, April 8-11, 2013.

13. Samborsky, D.D., Mandell, J.F. and Miller, D.A., "Creep/Fatigue Response of Resin Infused Biaxial (Double Bias) Glass Fabric Laminates in Reversed Loading," 2014 AIAA SciTech conference, 32nd ASME Wind Energy Symposium, Baltimore.

14. Samborsky, D.D., Mandell, J.F. and Miller, D., "The SNL/MSU/DOE fatigue of composite materials database: recent trends," 2012 AIAA SDM conference, Honolulu, AIAA-2012-1573.

15. Sears, A.T., Samborsky, D.D., Agastra, P. and Mandell, J.F., "Fatigue results and analysis for thick adhesive notched lap shear test," 2010 AIAA SDM, Wind Energy Session, Orlando, AIAA-2010-2821.

16. Samborsky, D.D., Agastra, P. and Mandell, J.F.,"Fatigue Trends for Wind Blade Infusion Resins and Fabrics," 2010 AIAA SDM, Wind Energy Session, Orlando, AIAA-2010-2820.

17. Samborsky, D.D., Mandell, JF, and Miller, DA, "Effects of Fiber Alignment and Resin Creep on the Fatigue of Resin Infused Wind Turbine Blade Laminates**,"** CAMX Conf., October 2014, Orlando.

18. Brondsted, P. and Nijssen, R.P.L., eds., *Advances in Wind Turbine Blade Design and Materials,* Woodhead Publishing Limited, 2013, Cambridge, UK.

19. Harris, B. ed., *Fatigue in Composites*, Elsevier, 2003 (ISBN: 978-1-85573-608-5).

20. Nijssen, R.P.L. and Brondsted, P., "Fatigue as a design driver for composite wind turbine blades," in *Advances in Wind Turbine Blade Design and Materials,* Brondsted, P. and Nijssen, R.P.L., eds., Woodhead Publishing Limited, 2013, Cambridge, UK, pp. 175-209.

21. Mandell, J.F., Samborsky, D.D. and Miller, D.A., "Effects of resin and reinforcement variations on fatigue resistance of wind turbine blades," in *Advances in Wind Turbine Blade Design and Materials,* Brondsted, P. and Nijssen, R.P.L., eds., Woodhead Publishing Limited, 2013, Cambridge, UK, pp.210-250.

22. Nijssen, R. P. L., "OptiDAT - Fatigue of Wind Turbine Blade Materials Database," 2006, (www.wmc.eu/optimat_blades).

23. Mishnaevsky, L., Brondsted, P., Nijssen, R., Lekou, D.J. and Philippidis, T.P., "Materials of large wind turbine blades: recent results in testing and modeling," Wind Energy, 15, 2011 83-97.

24. Philippidis, T.P. and Vassilopoulos, A.P., "Fatigue of composite laminates under off-axis loading," Int. J. Fatigue, 1999, no. 21, pp.253-262.

25. Philippidis, T.P. and Eliopoulos, E.N., "Verified material model incorporating progression of damage due to static loading and the effect of fatigue on residual strength and stiffness," 2011 (www.upwind.eu/media/732/Deliverable_D3_3_4).

26. Van Paepegem, W., De Baere, I., and Degrieck, J., "Modeling the nonlinear stress-strain response of glass fibre-reinforced composites. Part I: Experimental Results," *Comp Sci Techn,* 66 (2006) 1455-1464.

27. Tamuzh, V., Andersons, J., Aniskevich, K., Jansons, J. and Korsgaard, J., "Creep and damage accumulation in orthotropic composites under cyclic loading," Mechanics of Composite Materials, 34, 1998, 321-330.

28. Mandell, J.F. and Meier, U., "Effects of stress ratio, frequency and loading time on the tensile fatigue of glass-reinforced epoxy," *Long Term Behavior of Composites, ASTM STP 813,*T. K. O'Brien, Ed., ASTM, Phil., 1983, pp. 55-77.

29. Nijssen , R., Stammes, E. and Westphal, T., "Material and subcomponent research for improved rotor blade design," Second Technical Conf. on Wind Turbine Rotor Blades, Essen, Germany, June, 2010.

30. Raijmaekers, Westphal, T., Stammes, E. and Nijssen, R., "Effect of temperature and frequency on fatigue life: literature study and tension fatigue experiments," Proc. EWEA, 2009.

31. Epaarachchi, J.A., "The effect of viscoelasticity on fatigue behavior of polymer matrix composites," in *Creep and Fatigue in Polymer Matrix Composites*, R. Guedes, Ed., Woodhead, Cambridge UK, 2011, 492-511.

32. Kensche, C., "Final report on tube testing," Optimat Blades OB_TG2_R038 rev. 0, 2006 (www.wmc.eu/optimatblades.php).

33. Dillard, D.A., Advances in Structural Adhesive Bonding," CRC Press, New York, Woodhead Publishing Ltd. 2010, Ch. 13.

34. Choupani, N., JAST, 3 (2006) 185-193.

35. Bing, Q. and Sun, C. T., "Effect of Transverse Normal Stress on Mode II Fracture Toughness in Fiber Composites," 16th Inter. Conf. Composite Materials, Kyoto, 2007.

36. Nijssen, R. P. L., Westphal, T., Stmmes, E., Sari, J., "Strength and Fatigue of Wind Turbine Rotor Laminates and Substructures," 2010 AIAA/ASME Wind Energy Symposium, AIAA-2010-1189.

37. Rybicki E. F. and Kanninem M. F., Eng. Fract. Mech., 9 (1977) 931–938.

38. Quaresimin, M., and Ricotta, M., Composites Sci. and Tech., 66 (2006) 647-656.

39. Mall, S. and Yun, K.T., J. Adhesion, 1987, vol. 23, pp. 215-231.

40. Li, S., Thouless, M. D., Waas, A. M., Schroeder, J. A., and Zavattiere, Experimental Fracture Mechanics, 73 (2006) 64-78.

41. De Moura, M. F. S. F., Goncalves, J. P. M., Chousal, J. A. G., Campilho, R. D. S. G., Int. J. Adhesion and Adhesives, 28 (2008) 41

42. Chai, H., Int. J. Solids and Structures, 40 (2003) 6023-6042.

43. Browning, C., Husman, G., Whitney, J. "Moisture effects in epoxy matrix composites," Composite Materials: Testing and Design. Philadelphia, PA: ASTM, 1977.

44. Springer, G., " Environmental Effects on Composite Materials," Journal of composite materials, 1981.

45. Weitsman, Y. J., Fluid Effects in Polymers and Polymeric Composites," Springer, 2012 ISSN 0941-5122.

46. Cormier, L., Nijssen, R.P.L., Raijmaekers, S., "Temperature and Frequency Effects on the Fatigue Properties of Unidirectional Glass Fiber-Epoxy Composites," 2012 AIAA SDM Conf., paper AIAA2012-1574.

47. Li, X. and Weitsman, J., Composites: Part B, 35 (2004) 451-459

48. Russell, A. J. and Street, K. N., in "Delamination and Debonding of Materials, STP 876," W. S. Johnson, Ed., ASTM, Phil., 1985, 349-370.

49. Reeder, J. R. and Crews, J. H. J., AIAA Journal, 28 (1990) 1270-1276.

50. Adams, D., "Back-out Factors," High-Performance Composites, May, 2006.

51. Daniel, I. M. and Ishai, O., "Engineering Mechanics of Composite Materials," Oxford University Press, 1994, p347.

52. Peterman, J. and Schulte, K., "Strain based service time estimation for angle ply laminates," *Composites Sci. and Tech.*, 62 (2002) 1043-1050.

53. Plumtree, A., Melo, J. and Dahl, J., "Damage evolution in a [±45]2s CFRP laminate under block loading conditions," *Inter. J. of Fatigue*, 32 (2010) 139-145.

54. Rotem, A., "Stiffness change of a graphite epoxy laminate under reverse fatigue loading," *J Composites Tech and Research*, 11 (1989) 59-64.

55. Tanaka, K., and Tanaka, H., "Stress-Ratio Effect on Mode II Propagation of Interlaminar fatigue Cracks in Graphite/Epoxy Composites," *Composite Materials: Fatigue and Fracture (Sixth Volume), ASTM STP 1285*, E.A. Armanios, Ed., ASTM, 1997, pp. 126-142.

56. Samborsky, D.D., Mandell, J.F. and Miller, D.A., "Mixed Mode static and Fatigue Crack Growth in Wind Blade Paste Adhesives," 2011 AIAA SDM Conference, paper AIAA2011_943549, April, 2011.

57. Corleto, C.R. and Bradley, W.L., in Composite Materials: Fatigue and Fracture, Second Volume, ASTM STP 1012, P. A. Lagace, Ed., ASTM, Phil., 1989, 201-221.

58. Broek, D., Elementary Fracture Mechanics, Ch. 8, 4th Ed., Martinus Nijhoff, Dordrecht, The Netherlands, 1986.

Distribution

| 1 | MS0899 | Technical Library | 9536 (electronic copy) |

Sandia National Laboratories